Novel Polybenzimidazoles for the Development of Proton Exchange Membrane Fuel Cells

A Thesis Submitted for the degree of

DOCTOR OF PHILOSOPHY

By

Harilal

School of Chemistry
University of Hyderabad
Hyderabad-500 046
INDIA

January 2022

Dedicated

to

my Family

DECLARATION

I hereby certify that the matter embodied in the thesis entitled "***Novel Polybenzimidazoles for the Development of Proton Exchange Membrane Fuel Cells***" is the result of investigations carried out by me in the School of Chemistry, University of Hyderabad, Hyderabad, India under the supervision of **Prof. Tushar Jana** and it has not been submitted elsewhere for the award of any degree or diploma or membership, etc.

In keeping with the general practice of reporting scientific investigations, due acknowledgements have been made wherever the work described is based on the findings of other investigators. Any omission or error that might have crept in is regretted. This research work is free from Plagiarism. I hereby agree that my thesis can be deposited in shodganga/INFLIBNET. A report on plagiarism statistics from the University of Hyderabad Librarian is enclosed.

January 2022

Harilal

CERTIFICATE

This is to certify that the work incorporated in this thesis entitled "***Novel Polybenzimidazoles for the Development of Proton Exchange Membrane Fuel Cells***" submitted by **HARILAL** bearing registration number **15CHPH19** in partial fulfillment of the requirements for award of Doctor of Philosophy in the School of Chemistry is a bonafide work carried out by him under my supervision and guidance and the same has not been submitted elsewhere for any degree. This thesis is free from plagiarism and has not been submitted previously in part or in full to this or any other University or Institution for award of any degree or diploma.

Parts of this thesis have been published in the following publications:

1. **Harilal**; Nayak, R.; Ghosh, P. C.; Jana, T. ***ACS Appl. Polym. Mater.*** 2020, *2*, 3161-3170.
2. **Harilal**; Shukla, A.; Ghosh, P. C.; Jana, T. ***ACS Appl. Energy Mater.*** 2021, *4*, 1644-1656.

He has also made presentation in the following Conferences:

1. 15th International Conference on Polymer Science and Technology (**SPSI MACRO-2018**) (**Poster presentation**)
2. 16th Annual In-House Symposium (**CHEMFEST-2018**) (**Poster presentation**)
3. 17th Annual In-House Symposium (**CHEMFEST-2019**) (**Oral presentation**)

Further the student has passed the following courses towards fulfillment of course work requirement for Ph.D degree:

SI.No.	Course No.	Title of the Course	No. of Credits	Grade/Status
1.	CY-801	Research Proposal	3	B^+/Pass
2.	CY-802	Chemistry pedagogy	3	B/Pass
3.	CY-805	Instrumental Methods A	3	C/Pass
4.	CY-806	Instrumental Methods B	3	C/Pass

Prof. Tushar Jana
(Thesis Supervisor)

28/1/22

Prof. TUSHAR JANA
School of Chemistry
University of Hyderabad
HYDERABAD-500 046. INDIA.

Dean
School of Chemistry

Dean
SCHOOL OF CHEMISTRY
University of Hyderabad
Hyderabad-500 046

PREFACE

The present thesis entitled *"Novel Polybenzimidazoles for the Development of Proton Exchange Membrane Fuel Cells"* is divided into seven chapters. ***Chapter 1*** provides a brief introduction of fuel cells, working principle of proton exchange membrane fuel cell (PEMFC), properties of proton exchange membrane (PEM) and their types, and applications. The most advanced application of phosphoric acid loaded polybenzimidazole (PA/PBI) membrane as a PEM in high temperature PEM fuel cell (HT-PEMFCs) has also been discussed. ***Chapter 2*** entails the source of materials, methods and experimental techniques used for the whole thesis working chapters. ***Chapter 3*** demonstrates the development of cross-linked polybenzimidazole base PA loaded PEM with the aid of polymeric bromomethyl polyphenylene oxide (BrPPO). The effects of BrPPO on the properties of PBI cross-linked PEM are studied in depth in order to understand the suitability of these PEMs. ***Chapter 4*** deals with the synthesis and characterization of different pendant-types of pyridine-bridged polybenzimidazoles (PyPBI) from a simple, efficient, economically less expensive and scalable process. These newly synthesized PyPBI are converted to PEM by doping in H_3PO_4 and finally PEM properties of various PyPBI structure are analysed. ***Chapter 5*** entails a novel series of sterically hindered pyridine-functionalized arylether-linked random copolymers with systematically varied composition and functionality from a sustainable approach for the use as HT-PEM and effect of composition on the PEM performance is studied. ***Chapter 6*** describes the development of various new kinds of microporous proton exchange membranes from various three-dimensional (3D) iptycene-based polybenzimidazoles (PBIs) by altering the chemical structure of monomers and also studied HT-PEM properties of these polymer membranes. ***Chapter 8*** summarizes the findings of the present investigations, presents a concluding remark and the future scope and upcoming challenges.

January 2022

Harilal

Acknowledgements

The research work discussed in this thesis has been kept in track and seen through to completion with the encouragement and support of countless number of people including my friends, colleagues and well wishers. It is a pleasant task to express my thanks to all those who contributed in various ways to the success of this research and made it an unforgettable memory for me.

First and foremost, I want to express my sincere gratitude to my Ph.D. supervisor Prof. Tushar Jana, for his tremendous cooperation, criticism, encouragement and kind guidance on my research study. He has been quite helpful to me in both consciously and unconsciously, how a scientific problem can be analyzed and solved and how good polymer chemist can do this job. More importantly, I always enjoyed our conversations on a variety of topics, within and beyond the science, which broadened my understanding of the world and taught me how to be a better person. I am also indebted to him for the allowing me to work in a creative environment that not only resulted in this thesis work, but also provided challenges and opportunities that broadened my experience significantly. I am always very proud of being a part of Tushar Jana research group.

Then I would like to thank our collaborator Prof. Prakash Chandra Ghosh, Department of Energy Science & Engineering, Indian Institute of Technology Bombay (IITB) for his helpful suggestions, comments and allowing me to avail the PEM performance testing facilities.

I would like to thank the former and present Dean, School of Chemistry, for their constant inspiration and for allowing me to avail the facilities. I am extremely thankful individually to all the faculty members of the school for their kind help and cooperation at various stages of my stay in the campus. I am also grateful to all my former teachers for their help.

I am very grateful to the members of my thesis doctoral committee - Prof. P. Ramu Sridhar and Dr. Debashis Barik for their constant advice and encouragement throughout my thesis research work.

It is a pleasure to acknowledge the financial support from the National Fellowship for Higher Education (NFHE), UGC, New Delhi that made the work for this thesis possible.

I would also like to express my sincere gratitude to Mr. Sunil and Mr. Durga Prasad of School of Chemistry, UoH for their help with FESEM, TEM imaging.

I am deeply indebted to all my teachers starting from my school to the university for their wonderful teaching and education throughout my academics.

It is my honor to have worked with all the former and current members from Tushar Jana group. Malkappa, Shuvra, Raju, Balakondareddy, Narasimha, Rambabu, Moumita, Suchismita, Nilanjan, Anupam, Prasannatha, Somdatta, Arunava, Akhil Gorre, Krishna, Konda Reddy, Ramesh, Venkanna, Amaranadh, Mithun and Mutyala Naidu, Srinivas, Sandip Manna, Shailendra, Viswanathan, Radhika and Arindam – thank everyone for helping me to complete my doctorate and I enjoyed the time working with you. Additionally, this work could of course not have been finalized without non-teaching staff at the School of Chemistry taking care of the various facilities as well as administrative tasks that has been extremely helpful throughout the years spent working here. Hence, many thanks to Mr. Durgesh and Thurab for their help in recording NMR spectra.

I am really lucky for my close association with 'the gang' of HCU like Ramavath Babu, Manish, Senthilnathan, Swaminath, Ravi, Harikrishna, Golla Ramesh, Mou Mandal, Saddam Hossain, Apurba De, Tanmaya Kumar, Velpuri Vekateswara Rao, Manzoor, Mohan, and so many others in HCU with whom I have some wonderful memories in campus throughout my Ph.D. life.

I would also like to express my sincere thanks to all my close friends Raghunath, Mahender, Venkatesh, Teja, Ravi, Harishiva Prasad, Krishna, Narendar, Vital, Ramesh, Rajashekar Goud, Yakoof Pasha, Jeevitha Reddy, Ravinder and other school friends for their help and encouragement in various stages of my life.

Finally, I would like to express my deepest gratitude to my parents – my beloved Mother Laxmamma and Father Bugya Nayak, without their sacrifice and mental support I would not have reached to this stage of my life. I am greatly

indebted from the bottom of my heart to my Mother and Father for their spiritual guidance and stay as a philosopher of my life. My Mother deserves special mention for her inseparable support and prayers.

My special thanks to my wife Shirisha for continuous support. First, I'm sorry that I haven't been able to give you enough time and secondly, thanks a lot for bearing me as your husband and giving me the most beautiful, handsome and lovely gift: Dhruthi Rathod, Dhevansh Rathod my daughter and son.

January 2022 **Harilal**

University of Hyderabad,

Hyderabad-500 046

India

Common Abbreviations

AFM	Atomic force microscopy
OPBI	Poly(4,4'-diphenylether-5,5'-bibenzimidazole)
FA	Formic acid
DMAc	*N*,*N*′-dimethyl acetamide
DMSO	Dimethyl sulfoxide
DMF	*N*,*N*′-dimethyl formamide
DMA	Dynamic mechanical analyzer
DCA	Dicarboxylic acid
EIS	Electrochemical impedance spectroscopy
TMC	Total monomer concentration
FTIR	Fourier transforms infrared spectroscopy
NMR	Nuclear magnetic resonance
TEG	Triethylene glycol
IV	Inherent viscosity
MW	Molecular weight
OBA	4,4′-Oxybis(benzoic acid)
NMR	Nuclear magnetic resonance
NMP	N-methyl-2-pyrrolidone
NASA	National Aeronautics and Space Administration
PA	Phosphoric acid
PPA	Polyphosphoric acid
PBI	Polybenzimidazole
PyPBI	Pyridine bridge polybenzimidazole
PyTAB	2,6-Bis(3′,4′-diaminophenyl)-4-phenylpyridine
PSD	Pore-size distribution
MEA	Membrane electrode assembly

XPS	X-ray photoelectron spectroscopy
PEMFC	Proton exchange membrane fuel cell
PEM	Proton exchange membrane (membrane only)
SEM	Scanning electron microscopy
SCXRD	Single crystal x-ray diffraction
TEM	Transmission electron microscopy
ADL	Acid doping level
T_g	Glass transition temperature
TGA	Thermogravimetric analyzer
HT	High-temperature
MSA	Methane sulfonic acid
XRD	X-ray diffraction
FC	Fuel cell
WU	Water uptake
WS	Water swelling

CONTENTS

Declaration	**i**
Certificate	**ii**
Preface	**iii**
Acknowledgements	**iv-v**
Common Abbreviations	**vi-vii**
Chapter 1 Introduction	**1-23**
1.1. Introduction	**1**
1.2. Fuel cell	**2**
1.3. The origin of Fuel Cell development	**2**
1.4. Principle of Fuel Cell	**3**
1.5. Fuel Cell Types	**4**
1.6. Polymer Electrolyte Membrane Fuel Cell (PEMFC)	**5**
1.6.1. PEMFC operation mode	**6**
1.6.2. Proton Exchange Membrane (PEM) or Polymer Electrolyte Membrane	**7**
1.6.3. Modified PFSA Membranes	**8**
7.1. High temperature PEMFC	**9**
8.1. Polybenzimidazoles (PBIs)	**10**
1.8.1. Solubility and Molecular Weight determination of PBI	**11**
1.8.2. Polybenzimidazole-based HT-PEMs	**12**
1.8.3. Proton conduction mechanism of acid-loaded PBI membranes	**14**
1.9. Scope of the Thesis	**16**
References	**17-23**

Chapter 2 Materials and Experimental Methods 24-35

2.1. Source of Materials 24

2.2. Characterization Methods 24

2.2.1. Viscosity measurement 24

2.2.2. Solubility test 25

2.2.3. Stability Test in H_3PO_4 25

2.2.4. Acid Doping Level (ADL) 26

2.2.5. Water Uptake, PA Uptake, Swelling Ratio and Swelling Volume in Water and PA 26

2.2.6. Oxidative (or) Chemical Stability 27

2.2.7. Proton Conductivity and Durability Study 27

2.2.8. Phosphoric Acid Retention Test 29

2.2.9. Fabrication of Membrane Electrode Assembly (MEA) 30

2.2.10. Fuel Cell Performance Evaluation 30

2.2.11. Thermogravimetric Analysis (TGA) 31

2.2.12. Brunauer–Emmett–Teller (BET) Measurement 31

2.2.13. Powder X-ray Diffraction (PXRD) 31

2.2.14. Single Crystal X-ray Diffraction (SC-XRD) 31

2.2.15. Dynamic Mechanical Analysis (DMA) 32

2.2.16. Universal Testing Measurement (UTM) 32

2.2.17. ATR-FTIR Spectroscopy 33

2.2.18. Nuclear Magnetic Resonance Spectroscopy (NMR) 33

2.2.19. Absorption Spectroscopy 33

2.2.20. X-ray Photoelectron Spectroscopy (XPS) 33

2.2.21. Field Emission Scanning Electron Microscope (FESEM) 34

2.2.22. Transmission Electron Microscope (TEM) 34

2.2.23. Atomic Force Microscope (AFM) 34

References 34-35

Chapter 3 Cross-Linked Polybenzimidazole Membrane for PEM Fuel Cells 36-55
3.1. Introduction 36-37
3.2. Experimental section 38-39
3.2.1. Synthesis of PyOPBI-cross-linked-BrPPO polymer (CrL-PyOBI) and membrane fabrication 38
3.3. Results and Discussion 40-51
3.3.1. Chemical crosslinking of PyOPBI 40
3.3.2. Solvent resistance test 42
3.3.3. Morphology of the membrane 43
3.3.4. Oxidative resistance 43
3.3.5. Thermal stability 44
3.3.6. Acid loading and dimensional stability of membrane 45
3.3.7. Proton conductivity 46
3.3.8. Mechanical properties 48
3.3.9. Fuel cell performance studies 50
3.4. Conclusion 52
References 52-55
Chapter 4 Pyridine-Bridged Polybenzimidazole for Use in High-Temperature PEM Fuel Cells 56-81
4.1. Introduction 56-58
4.2. Experimental section 58-62
4.2.1. Synthesis of arylether dicarboxylic acid monomers 58
4.2.2. Synthesis of polymers 59-61
4.2.3. Preparation of free-standing membrane 61-62
4.3. Results and Discussion 63-78
4.3.1. Synthesis of aryl ether type PyOPBI polymers and their stability in polar solvents 63-65
4.3.2. Spectroscopic characterization of PyOPBIs 65-67

4.3.3. Impact of pendant-type molecular architecture of arylether linked PyOPBIs on the stability in PA 67-68
4.3.4. Thermal stability 68-69
4.3.5. Morphology of the membranes 69
4.3.6. Oxidative stability 70
4.3.7. Membrane thermomechanical properties 71
4.3.8. Water uptake and swelling ratio of the membranes 72
4.3.9. Phosphoric acid loading and swelling of the membranes 72-73
4.3.10. Proton conductivity 74-75
4.3.11. Phosphoric acid retention and proton conductivity Stability 75-76
4.3.12. Fuel cell performance 77-78
4.4. Conclusions 78
References 79-81
Chapter 5 Copolymers of Pyridine-bridged Polybenzimidazole for the use in High Temperature PEM Fuel Cell 82-102
5.1. Introduction 82-84
5.2. Experimental section 84-86
5.2.1. Synthesis of copolymers 84-85
5.2.2. Preparation of proton exchange membranes 86
5.3. Results and Discussion 87-100
5.3.1. Synthesis and structural characterization of copolymers 87-90
5.3.2. Thermal stability and mechanical properties of the copolymer membranes 90-92
5.3.3. Oxidative stability of the membranes 92-93
5.3.4. Membrane Morphology 93-95
5.3.5. Water uptake, acid doping level and swelling of Membranes 95-97
5.3.6. Proton conductivity and acid retention of membranes 97-98
5.3.7. H_2/O_2 fuel cell performance of the membranes 99-100

5.4. Conclusion 100
References 101-102
Chapter 6 Rational Design of Microporous Polybenzimidazole Framework for Efficient Proton Exchange Membrane Fuel Cell 103-136
6.1. Introduction 103-105
6.2. Experimental section 105-110
6.2.1. Synthesis of iptycene containing arylether diacid monomers 105-107
6.2.2. Synthesis of polymers 107-109
6.2.3. Proton exchange membrane preparation 109-110
6.3. Results and Discussion 111-132
6.3.1. Design strategy 111-113
6.3.2. Synthesis and structural confirmation of monomers and polymers 113-117
6.3.3. Solubility behaviour of 3D iptycene-PyPBI 117-118
6.3.4. Polymer chain packing and microporosity 118-119
6.3.5. Morphology of the membranes 120-121
6.3.6. Chemical stability screening 121-123
6.3.7. Thermal stability and thermomechanical properties 123-125
6.3.8. Phosphoric acid loading and dimensional stability of membranes 125-127
6.3.9. Proton conductivity 127-130
6.3.10. Fuel cell performance test 130-131
6.3.11. Photophysical Properties 132
6.4. Conclusion 132-133
References 133-136

Chapter 7 Summary and Conclusion 137-143
Appendix I 144-150
Appendix II 151-161
Appendix III 162-174
Appendix IV 175-221
Publications & Presentation 222-223

Chapter 1

Introduction

1.1. INDRODUCTION

This thesis is devoted to the development of including synthesis and characterization of various polybenzimidazoles (PBIs)-based proton exchange membranes (PEMs) and their potential as promising materials for the use in high temperature proton exchange membrane fuel cells (HT-PEMFCs). The thread which connects all the working chapters of current thesis is polybenzimidazoles (PBI)-based proton exchange membranes (PEMs). The Chapter 1 gives the insights about fuel cells and also describes various PBI polymer synthesis at the outset and then investigates into the details of PEM and its utility in HT-PEMFCs.

1.2. Fuel Cell

The most significant factor that determines the sustainable development of a modern industrialized society is energy utilization. Energy is an essential supply at times, where the power of the human being is not enough to be used in sectors such as transportation, communication, agriculture and industry. There is a need for energy for a country to develop, strengthen, progress and maintain its civilization. Presently all countries are largely depending on fossil fuel for the energy production, and these fossil fuels are not renewable energy resources. To supply the energy demands of the rapidly growing global population, it is very important to upgrade to an alternative, clean and sustainable energy resources those do not negatively affect the environment in long run. Importantly, increased energy consumption, rising global awareness on environmental protection and reduction of storage of existing conventional fossil fuel based energy sources have led to intensification of research on alternative/renewable energy sources such as sunlight, biomass, wind, geothermal energy, hydropower and hydrogen energy.[1] Studies show that hydrogen (H_2) energy is a good, clean and reusable sustainable energy source among these. There is no impact in the environment due to the fact that water vapor is released from the reaction of H_2 on combustion. High flame speed and ignition ability, low deflagration energy, wide flaring and combustion limits, high energy density, and low pollutant exhaust gas emissions make hydrogen energy the most attractive renewable energy resource.[2,3] The device which can convert hydrogen energy to electrical energy is fuel cells (FCs). FCs are clean, quiet, flexible and eco-friendly energy conversion technology with high conversion efficiency. This technology uses only chemicals (O_2

and H_2) to generate only electrical energy, heat and water. Over the past years, the attention of it increases drastically, especially when major automotive companies introduce their fuel cells products to the world transportation sector. Toyota started selling their hydrogen fuel cell car the 'Mirai', while other automotive companies; Honda (Clarity), Mercedes (B-Class Fuel cell) and Hyundai (Tucson) are also in the focus on manufacturing their own hydrogen-powered zero emission fuel cell vehicles (FCVs).[4-7] These FCVs are ranging from cars, minivans, buses, tricycles, bicycles, forklifts, and drones (**Figure 1.1**). Considering the zero emissions released by FCs when the fuel used is hydrogen and the huge range of applications they can cover, FCs can be considered as the preferred energy conversion device of the 21st century. Therefore, progress in the research and improvements in FCs technologies will be highly attractive for both academic and industrial fields.

Figure 1.1. Commercialization of hydrogen-powered zero emission vehicles.[4-7]

1.3. The origin of Fuel Cell development

A brief search on research history of FCs shows that these devices have been known since more than 160 years. The basic electrochemical principle of fuel cells was first reported by Swiss

researcher Christian Friedrich Schoenbein; however, Sir William Robert Groove (an English lawyer turned scientist) accidentally developed the very first conceptual documented fuel cell in the year 1839 by showing that the electrochemical dissociation of water was almost reversible using platinized platinum (Pt) electrodes in dilute sulphuric acid electrolyte. Mond and Langer named for the first time this kind of device "fuel cell in 1889. Wilhelm Ostwald (Nobel Laureate) experimentally tested various different fuel cell components (electrodes, electrolytes, fuels, and oxidant compounds) in 1893 and William Jacques demonstrated the very first fuel cell with practical applications in 1896.[8] At the same time, the first large scale industrial development of fuel cell happened in the early 1960s, General Electric (GE) Company developed fuel cells with polymer resin-based ion exchange membranes, which were the basis of the fuel cells used for the generation of electricity in the U.S. Apollo Gemini space program (1950−1970).[9] Since then, considerable fuel cell research and development activities and capital investment from various industrial and government enterprises have been extensive upgrade leading to the production of several prototypes and commercial products with a wide range of applications such as portable and stationary power generation, uninterruptible power supplies, auxiliary power units (APUs) and automotive power trains.[10]

1.4. Principle of Fuel Cell

In principle, a FC operates like a traditional battery. Unlike a battery, it does not run down or require recharging, and produces energy in the form of electricity and heat as long as fuel is supplied. Fuel cells are usually arranged in a modular fashion into a cell stack to generate the desired output voltage and power capacity for the application. Generally, the stacking involves connecting multiple unit cells in series via electrically conductive interconnects. Different stacking arrangements have been developed. It is important to emphasize that all fuel cells need a number of auxiliary devices to function. The common physical fuel cell structure is composed of four main components through which electrochemical conversion process occurs, these are an anode (negative electrode), a cathode (positive electrode), an electrolyte, and an external circuit called the load. The anode will continuously be supplied with pure fuel [mostly hydrogen (H_2)], meanwhile the cathode is fed with the oxidant in the ambient air or pure oxygen (O_2). H_2 is

separated into positive and negative ions on the anode. The intermediate membrane electrolyte lets the positive ions (often protons) be transmitted to the cathode and behaves as an insulator for the electrons flow. These electrons, which pass through the cathode side through an electrical circuit, where they participate on the other side of the membrane (anode semireaction), thus generating electric current that is used to power an electrochemical device. The hydrogen ions, electrons and O_2 atoms combine at the cathode in an exothermic reaction to produce water molecules. A continuous electricity production can be achieved by continuous feeding of the fuel. **Figure 1.4** depicts a schematic of a polymer electrolyte FC (PEMFC) operation diagram.[11] The electrochemical reactions are shown below:

At the anode reaction: $2H_2 \rightarrow 4H^+ + 4e$ (1)

At the cathode reaction: $O_2 + 4H^+ + 4e^- \rightarrow 2H_2O$ (2)

Overall cell reaction: $2H_2 + O_2 \rightarrow 2H_2O$ + electrical energy + heat

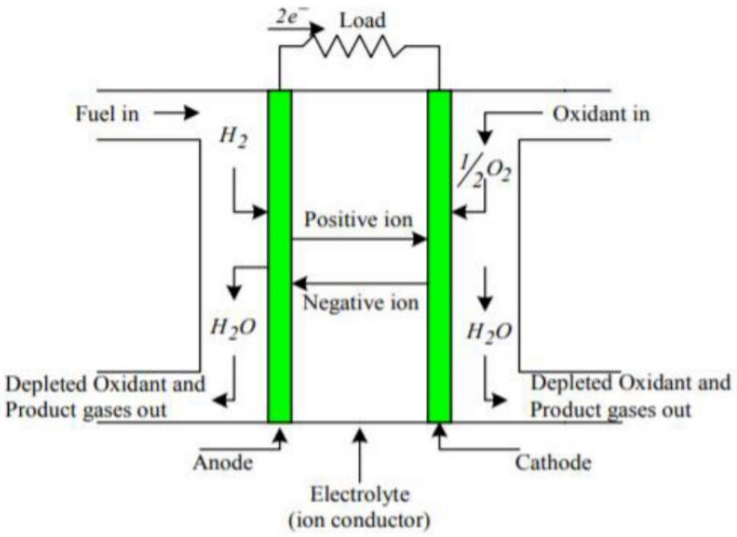

Figure 1.4. Schematic representation of a general fuel cell operation diagram[11].

1.5. Fuel Cell Types

A variety of FCs have been classified according to their operating temperature, nature of the electrolytes, energy efficiency, fuel cell structure (e.g., scale of the system and target application)

and costs, etc. Often five types of fuel cells have received major attention of researchers and these are: (1) alkaline fuel cell (AFC), (2) phosphoric acid fuel cell (PAFC), (3) molten carbonate fuel cell (MCFC), (4) solid oxide fuel cell (SOFC), (5) phosphoric acid fuel fell (PAFC) and (6) proton-exchange or polymer electrolyte membrane fuel cells (both names abbreviated PEMFCs). The main differences of these five types of FCs are operating temperatures, electrodes and electrolyte types. A detailed illustration of all these FCs is shown in **Figure 1.5**. [12] Among them, PEMFC is recognized as a potential candidates for replacing the traditional thermodynamic internal combustion engines owing to their ultralow emission, high power density, quick start-up and market applications; therefore, it is given priority for in-depth research in this thesis. In the following section, we have discussed various aspects of PEMFC.

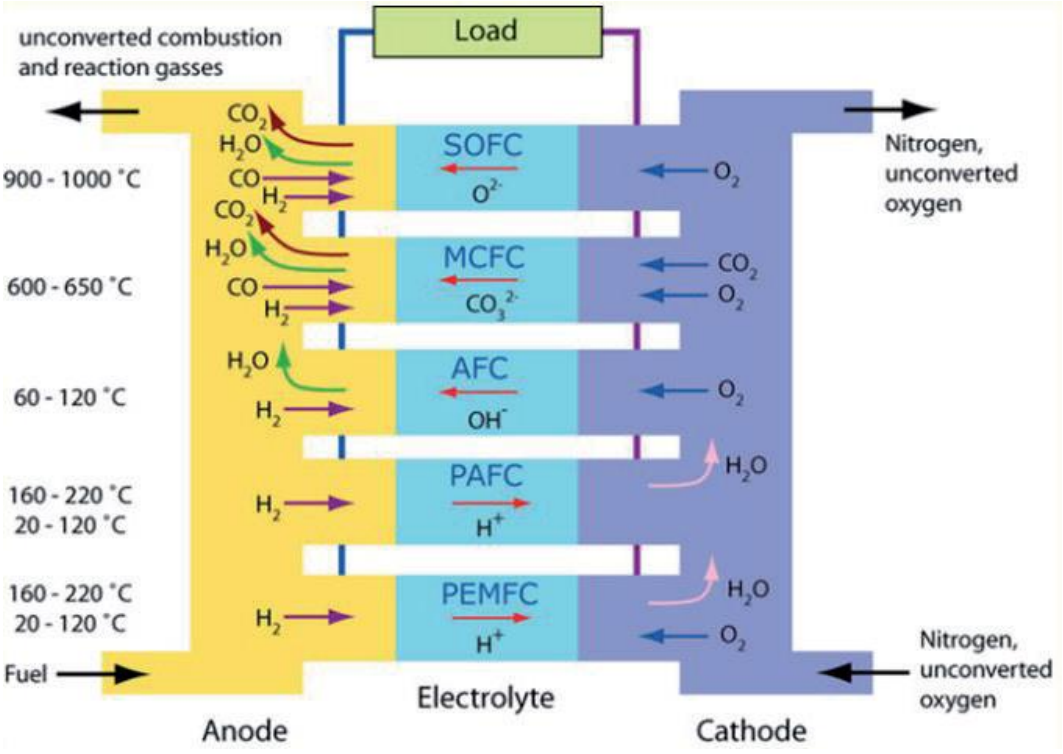

Figure 1.5. Various types of FCs structures and their operation temperatures[12].

1.6. Polymer Electrolyte Membrane Fuel Cell (PEMFC)

PEMFC get their name because the electrolyte used in such cells is a polymeric membrane. In the literature reports, several abbreviations such as PMFC (polymeric membrane fuel cell) and

PEFC (polymer electrolyte fuel cell) exist for this type of fuel cell. The polymer electrolyte membrane (PEM) is an important constituent of PEMFC. It plays a crucial role in determining the efficiency of a PEMFC by selectively transporting protons from anode to cathode. The first application of a PEM in a FC was in the 1960s as an auxiliary power source in the Gemini space flights.[9] At present, PEMFCs are considered to be a promising power source for the development of clean and efficient energy conversion technology in the 21st century because of their advantages including high energy/power densities, low/zero emission, silent operation, broad range of applications ranging from household devices, automobile vehicles, to power grid stations, and capability to supply power and heat even in remote areas.[13] At present, the global fuel cell market is developing rapidly and several automobile makers have started to commercialize green FCVs at affordable prices aiming at the middle-income population. Therefore, researches are going on to find a promising polyelectrolyte material to be used as a membrane in PEMFC.

1.6.1. PEMFC operation mode

PEMFCs can operate in different temperature ranges, typically 60-90 ^{o}C (known as low-temperature PEMFCs[14]) and 100-200 ^{o}C (high-temperature PEMFCs[15]) depending on the proton-conducting membrane used as electrolyte. A deeper work in the basic scheme of a PEMFC operative principle is unveiled in **Figure 1.6** which shows an exploded view of a PEMFC single-cell.[16] Two ending plates, together with anodic and cathodic flow fields, hosting a series of channels to deliver both hydrogen and oxygen sandwiched to form the membrane electrode assembly (MEA) which is the key component of a PEMFC. The MEA is constituted by a proton conductive membrane sandwiched between two gas diffusion layer (GDL) electrodes which host the catalytic layers. Different kinds of catalytic layers are present in anode and cathode. In the MEA, the electrochemical reactions (**Eqs. 1 and 2**) take place with delivery of electricity and release of heat. The membrane has different roles which include conducting protons from the anode to the cathode but insulating electrons so that they move in the external circuit, separating hydrogen from oxygen, and physically supporting the anodic/ cathodic catalysts.

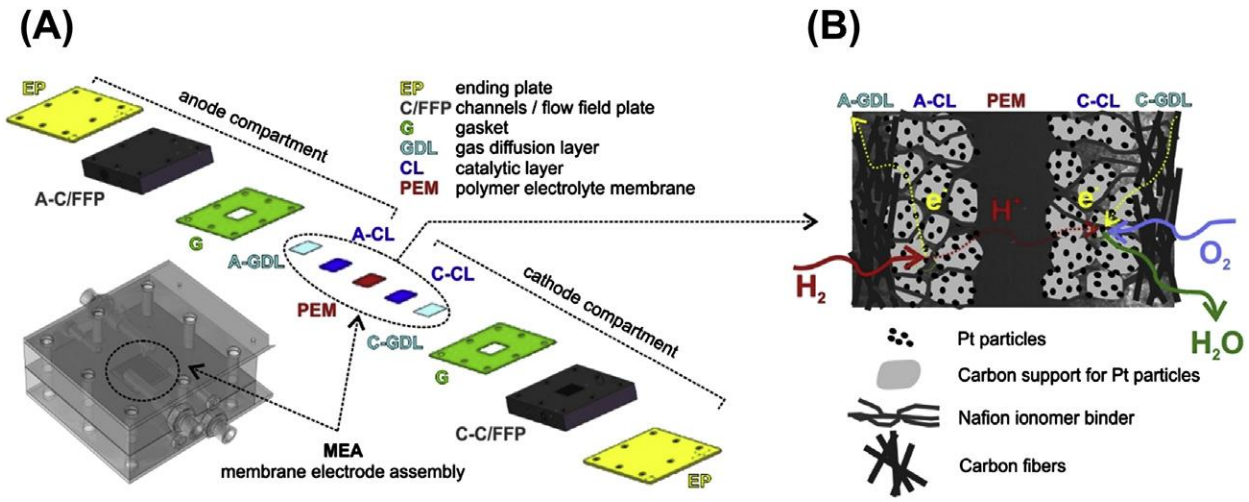

Figure 1.6. (**a**) Exploded view of a PEMFC single-cell. (**b**) Scheme of an MEA.[16]

1.6.2. Proton Exchange Membrane (PEM) or Polymer Electrolyte Membrane

PEM is made from ionomers, which is a polymer consisting of a small but significant proportion of the constitutional units has ionic or ionizable groups[17]. PEM is a very thin, hard and robust plastic like polymeric material with reasonably good proton conductivity. Among the important components constituting PEMFCs, the PEM plays a key role in the cell's performance enhancement. As shown in **Figure 1.6**, the PEM is fitted in the middle of each cell unit. One of its sides faces is connected with the anode catalyst layer which is responsible for hydrogen oxidation reaction (HOR) to produce electrons and protons. The other side of the PEM faces is attached to the cathode catalyst layer which is responsible for the oxygen reduction reaction (ORR) to produce water and heat. The PEM should be specially designed for selective diffusion of H^+ to give high ionic conductivity or other wards low ionic resistance for reducing voltage loss across the membrane. Various methods have been reported for the preparation of PEMs including solution casting,[18-21] sol–gel method,[22, 23] doctor blade casting,[19,20] solvent evaporation,[21] stencil printing,[19] nip-roller[19] and slot dye extrusion.[19,23] Common themes critical to all high performance PEMs include (i) synthetically scalable, (ii) good electrolytic property (i.e. high ion mobility), (iii) negligible electrical conductivity, (iv) resistive to permeation of uncharged gases, (v) good thermal

stability, (vi) good mechanical strength and durability, (vii) being environmentally friendly and cost-effective and so on. Depending on the materials and preparation approaches, various types of PEMs have been described in the literature to make a contemporary HT-PEMFC stack. Among various, the main PEM categories include (1) modified perfluorosulfonic acid (PFSA) membranes and (2) phosphoric acid (H_3PO_4) doped PBI membranes.

1.6.3. Modified PFSA Membranes

The most famous and commonly used commercial membrane material for low-temperature PEMFCs (LT-PEMFCs) is perfluorinated sulfonic acid (PFSA, notably Nafion®) polymer (**Figure 1.7**) owing to its high proton conductivity and excellent thermochemical stability. However, many severe drawbacks such as sluggish electrode kinetics, low operation temperature, cumbersome water management, high cost and which functions only in a highly hydrated state compel the researchers to find alternative PEMs for PEMFC.[24-26] Soon, it was realized that PEMs working at a higher temperature (>100 °C) can successfully resolve all the issues of perfluoro-sulfonated PEMs. In the literature so far, many modified PFSA (nonfluorinated hydrocarbon) polymeric materials such as sulfonated polyimides (SPI)[27-30], polyether sulfones (PAES)[30-34], sulfonated polyether ketones (SPEEK), poly (arylene piperidine)s (PAPs), polyesters and their respective copolymers were introduced as alternative PEM candidates to PESA membranes. However, the operating temperature of modified PFSA polymer membranes is still not high enough to satisfy the requirement for HT-PEMFCs very well because most of them can only work smoothly in the temperature range from 100 to 120 ^oC. Another problem associated with modified PFSA membranes is the high humidity level required to maintain high proton conductivity at the high temperature for HT-PEMFC operation. On the other hand, water droplets which are building up underneath the gas diffusion layer (GDL) and the flow channels can partially block the gas supply of the cell. Therefore balancing the water content is a delicate task for LT-PEMFCs.

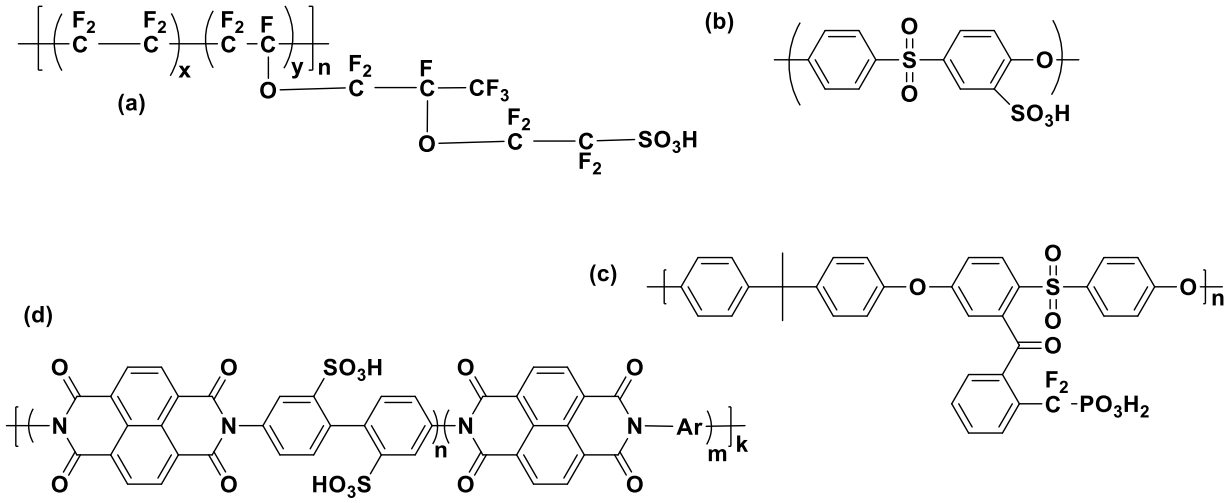

Figure 1.7. (**a**) Structure of Nafion and few representative examples of proton-conducting polymers designed as PEM materials as alternative to Nafion: (**b**) sulfonated poly(arylene ether sulfone), (**c**) polysulfone, (**d**) sulfonated naphthalenic polyimide. (Taken from references 27-34)

1.7. High temperature PEMFC

In recent years, HT-PEMFCs have attracted much attention because of their numerous advantages under high-temperature which ranges from 100−200 °C operating conditions over LT-PEMFCs. Improved electrode kinetics, high tolerance to fuel contaminants such as carbon monoxide (CO), simple system design, better co-generation of heat and water management system are found to be main advantages and reasons for the interest of researchers in HT-PEMFC throughout the world. The main component that makes it possible for PEM fuel cells to operate at higher temperatures is the polymer membrane in the MEA.[35, 36] Great efforts have been and are being made to develop proton conducting polymer membranes and other materials for operation at temperatures above 100 ^{o}C. In spite of the wide spectrum of investigation on PEMs so far, only phosphoric acid (H_3PO_4)-loaded PBI (PA/PBI) is the state-of-the-art PEMs with operation temperature up to 200 ^{o}C because of their low-cost and excellent thermal-chemical properties in

the temperature range from 100 to 300 ºC without humidification.[37] In the following sections we will discuss about PBI-based membranes in more detail.

1.8. Polybenzimidazoles (PBIs)

Polymers with benzimidazole groups as part of the structural repeat unit comprise a big family of engineering plastics known as polybenzimidazoles (PBIs).[38] PBIs are aromatic nitrogen-heterocyclic rigid backbone macromolecules and are typically identified with excellent thermo-mechanical and oxidative resistance properties. These outstanding properties make them particularly suitable for various challenging high-temperature applications in the form of fibers or coatings, like protective garments for fire fighters, membranes etc.[39] The first polybenzimidazoles were reported by Marvell and Vogel from Illinois University in the early 1960s and later commercialized by Celanese company in 1983 using PBI as the trade acronym for poly[2,2'-(m-phenylene)-5,5'-bibenzimidazole] polymer[38,]. PBI has been used by NASA in the Apollo missions as part of the astronauts' clothing, but it was not until 1995 that it was used in fuel cells by Wainright et al.[40] This stimulated to produce PBI in large scale and commercialized it across the worldwide. The PBIs are synthesized from condensation polymerization reaction of aromatic diamines and dicarboxylic acid derivatives in solid state by heating of higher temperature in solution by using polyphosphoric acid (PPA) where PPA has been used as a both solvent as well as catalyst and a large number of combinations of these monomers have been tested so far. Few representative diamine, diacids and PBI structure are shown in **Figure 1.8**.[37, 41, 42] However, many PBIs reported in the literature are not accessible via the PPA route due to the poor solubility of the dicarboxylic acid or due to pronounced side-crosslinking reactions in hot PPA. These can instead be obtained from polycondensation in Eaton's reagent which is mixture of methanesulfonic acid (MSA) and phosphorous pentoxide (P_2O_5).[42] The different PBI derivatives obtained from various monomers often differ in their physical and chemical properties because of the different chemical backbone structures.

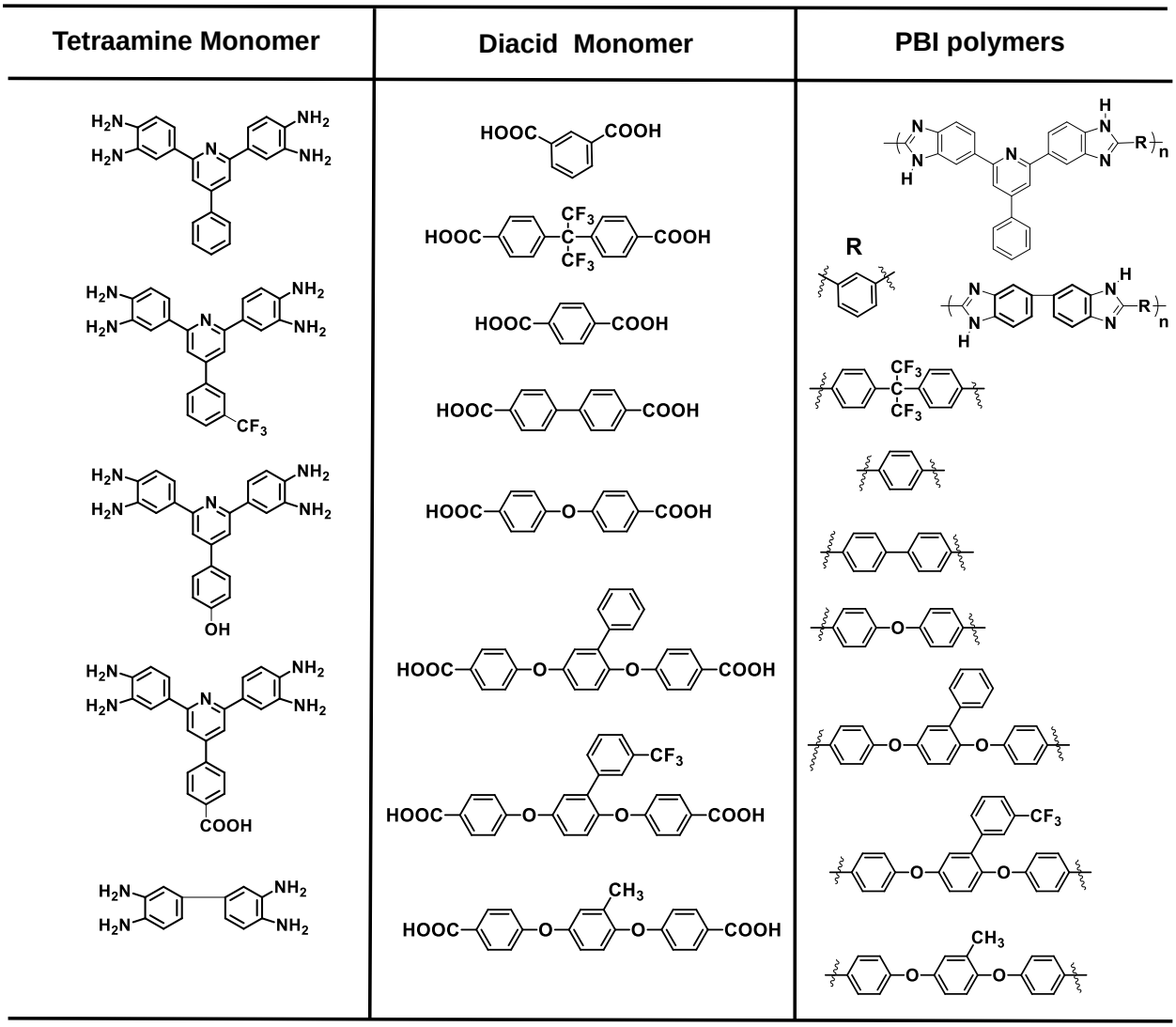

Figure 1.8. Various structures of monomers (diamine, diacid) and PBIs.[37, 41, 42]

1.8.1. Solubility and Molecular Weight determination of PBI

In addition to the acidic solvent systems used for the homogeneous polycondensation reactions (PPA and/or Eaton's reagent), a small number of high-boiling polar aprotic solvents dissolve many of the PBI derivatives reported in the literature. For most of the PBIs, DMAc (N,N-dimethylacetamide) is widely used and gives polymer solutions with suitable viscosity for dry spinning of fibers.[38] Other options are DMF (N,N-dimethylformamide), NMP (N-methyl-2-

pyrrolidone) and DMSO (dimethyl sulfoxide). Alternatively, ethanol containing a few weight percent of a hydroxide salt (e.g. NaOH or KOH) readily dissolves m-PBI or AB-PBI.[35]

The molecular weight of the PBI polymers is typically estimated from Ubbelohde viscometry of polymer solutions using concentrated sulfuric acid as the solvent. The molecular weight of PBIs is normally calculated from intrinsic viscosity [η], obtained from one point measurement using Mark−Houwink–Sakurada equation.[37]

$$[\eta] = K\bar{M}_v^a$$

where K = 5.2×10^{-5} dL/g and a = 0.92 and $[\eta] = \frac{\eta_{sp}+3\ln\eta_{rel}}{4C}$ where $\eta_{sp} = 1-\eta_{rel}$ and $\eta_{rel} = {}^{t}/_{t_o}$ where t and t_o are the time flow for the polymer solution and solvent, respectively. However, it may be noted that inherent viscosity (I.V) values are often need to estimate the molecular weight of PBI polymers. Higher I.V value indicates higher molecular weight PBI.

1.8.2. Polybenzimidazole-based HT-PEMs

In 1995, Wainright *et al*. explored the application of H_3PO_4-loaded polybenzimidazole (PBI) membrane (PA/PBI) for HT-PEMFCs for the first time.[40] After the pioneering work, many investigators including our research group have evaluated PA-loaded PBI as a prominent HT-PEMs candidates and considered as substitute to Nafion and Nafion-like for high temperature fuel cell operation.[43-54] PA-loaded PBIs provide the necessary characteristics for good performance in HT-PEMFCs in comparison with Nafion such as high electrode kinetics, high CO tolerance, simplified thermal, water management systems and enhanced efficiency of the waste heat utilization. PBI is a basic polymer (pK_a = 5.5) with excellent thermal, mechanical and chemical stability that can form an acid–base complex with a strong acid like H_3PO_4. PBIs can be doped with many different acids like HNO_3, HCl, H_2SO_4 and $HClO_4$ to work as the proton donors. In all the cases, the conductivity depends on the amount of acid present in the membrane. However, phosphoric acid (H_3PO_4, PA) has been proved to be a superior dopant because the membranes doped with it always have high conductivity, excellent thermal stability and very low vapour pressure at high temperature and after it was reported as a promising proton conducting electrolyte working at temperatures up to 200 °C.[55] The major issues associated with PA-loaded PBI (PA-

PBI) membranes include catalyst poisoning due to the leaching of acid and membrane degradation due to the harsh operating conditions and undesirable electrochemical reactions.

Along with H_3PO_4-loaded PBI membranes without modification,[56–60] several modified PBIs have also been reported with enhanced membrane performance. The varieties of PBI include include H_2SO_4 loaded PBI membranes,[61] poly(2,5-benzimidazole) (ABPBI) based membranes,[50, 57,62–66] pyridine based PBI membranes,[42–46, 67-69] sulfonated PBI membranes,[70–72] polysiloxane doped PBI membranes,[73] fluorine and fluoropolymer doped PBI membranes,[72, 74–76] arylether based-PBI membranes,[42–46, 77,78] ABPBI and PBI based composite membranes,[79–90] phenylindane containing PBI membranes,[91] imidazole loaded PBI membranes,[92] poly(imide benzimidazole) based membranes,[93] and methylated PBI membranes.[94] Likewise many more modification techniques have been explored to improve the membrane quality, thermal and mechanical properties. Recently, our research group also has made various designs and modular synthetic efforts by (i) constructing novel PBI structures, (ii) blending with appropriate polymers, (iii) making composites like (ionic and covalent cross-linking as well as organic-inorganic composites) and (iv) developing elegant membrane fabrication techniques in order to enhance PBI solubility, flexibility and acid doping capability and so on. Some of these modified structures of PBI have been discussed in Chapter 3, 4, 5, 6 and representative structures are shown in **Figure 1.9**.

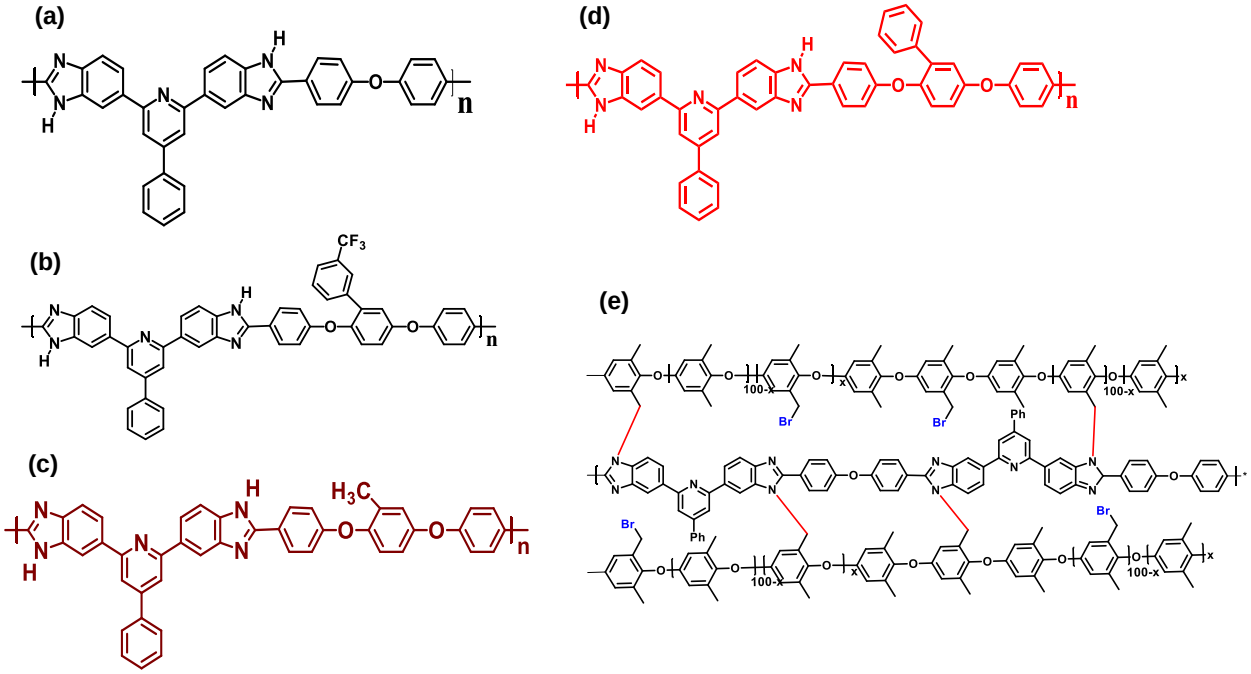

Figure 1.9. Various structures of synthetically modified PBI: Functionalised pyridine based polybenzimidazoles (a), pendant-type arylether-linked PyPBIs (b, c and d), cross-linked polybenzimidazoles (e). (Acquired from reference 42, 46).

1.8.3. Proton conduction mechanism of acid-loaded PBI membranes

The performance of polybenzimidazole-based PEMs depends on several factors including the quantity and distribution of the loaded acid,[95] type of casting solvent used,[96] extent and type of crosslinking between PBI polymer chains,[97-99] and chemical structural properties and micromorphology of the pristine and acid-loaded PBI.[100] Proton conductivity of acid-loaded PBI follows mainly 2-types of mechanisms: Vehicular and Grotthuss. The proton conductivity mechanism of acid-loaded PBIs is mainly governed by a Grotthuss mechanism route. According to this mechanism, proton transfer hopping between two molecules such as acid–acid, acid–water, or acid-imidazole ring through the formation and concomitant cleavage of covalent bonds involving neighboring molecules (**Figure 1.10**). In the other mechanism, the proton moves through solvated structures which are surrounded by water molecules and this is called as vehicle mechanism. The proton diffuses through the membrane dragged by a "vehicle" which is H_3O^+

when the membrane is hydrated.[35] When the PBIs doped with phosphoric acid, the composite system will further encounter several drawbacks, including leaching out of phosphoric acid from the membrane, poisoning of cathode Pt electro catalyst by PA, self-dehydration of H_3PO_4 at higher temperatures, low loading level of PA, and it loses the mechanical stability by PA particularly at high PA concentrations and high temperatures. To address these problems, several authors has developed inorganic additives,[101-104] polymer blends,[105-110] and doping with different electrolytes[111-112] and the synthesis of PBIs with different structures.[113-114]

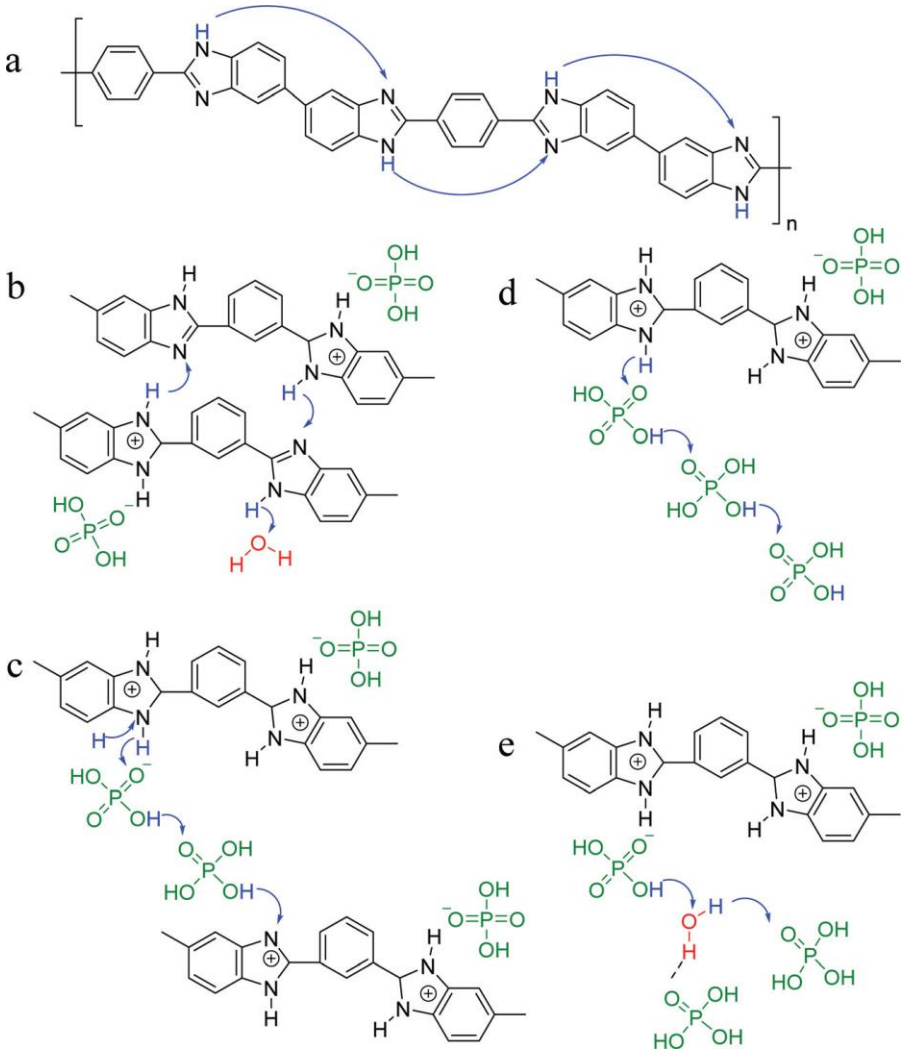

Figure 1.10. (a) Chemical structure of m-PBI; (b) H_3PO_4 protonated PBI with no free acid molecules; proton transfer along (c) acid–PBI-acid, (d) acid–acid, and (e) acid–H_2O. (Acquired from reference 35)

1.9. Scope of the Thesis

The present thesis aims to develop novel membranes suitable for high temperature proton exchange membranes fuel cells (HT-PEMFCs). Special emphasis has been devoted to the study of new type of membrane architecture (porosity and connectivity), properties, membrane processing and scalable synthetic process. The first working chapter (**chapter 1**) describes the optimization and balance of properties in the previously described polymer pyridine bridged oxy-PBI (PyOPBI) through cross-linking with brominated poly phenylene oxide (BrPPO) in order to prepare membranes which can be evaluated in single cell and fabricated on a wider scale to achieve the bring the attractive properties of PyOPBI into application. A huge volume of literature is available on the PBI type conducting materials, we found out that there are many issues which were not properly addressed with and discussed in the literature adequately. However no attempts have been made to resolve membrane processability, acid leaching, long-term membrane stability and durability. To mitigate these bottlenecks, in second working chapter (**chapter 4)**, we synthesized a series of novel PBIs with flexible aryl ether backbones and bulky substituents by polycondensation reaction in a rapid and operationally simple reaction medium following the goal to prepare membranes which can be evaluated in fuel cell and fabricated on a wider scale in order to bring the attractive properties of novel PBIs into application. The third working chapter (**chapter 5**) entails the identification and better understanding of a suitable and versatile reinforcement concept for creating robust membranes based on fluorinated PBI called Ph(CF_3)-PyOPBI. To achieve this, the established homogeneously suitable hydrophilic-hydrophobic copolymers of Ph(CF_3)-PyOPBI with PyOPBI are discussed in-depth and chosen for later systematic optimization in combination with Ph(CF_3)-PyOPBI. In the last five years or so, iptycene (i.e., triptycene and pentiptycene)-containing porous polymer membranes caught tremendous attention as a novel type of potential electrolytes due to their high internal surface area, intrinsic microporosity and tunable functionality. But surprisingly there is no report on the iptycene-based PBI as HT-PEM in the literature yet, possibly because of the scant availability of appropriate polymerizable iptycene building blocks and relatively complex structure determination. Taking consideration into these aspects, In the fourth working chapter (**chapter 6**), for the first time, we report a reliable, scalable, high-yield and cost-efficient strategy to synthesize a novel class of 3D

pentiptycene and triptycene containing advanced hierarchical microporous PBIs with the goal to prepare thin, robust, and highly conductive membranes that can be manufactured on a large scale and evaluated in fuel cells and conditions close to application. Therefore the structure of this thesis involves development of new generation polymer electrolyte membranes based on PBI for the use as potential PEM in HT-PEMFC. More detailed scope of each working chapter of this thesis has been described in the introductory part of the individual chapters.

REFERENCES

1. Kirubakaran, A.; Jain, S.; Nema, R., **2009**, *13*, 2430-2440.
2. Staffell, I.; Scamman, D.; Abad, A. V.; Balcombe, P.; Dodds, P. E.; Ekins, P.; Shah, N.; Ward, K. R., **2019,** *12*, 463-491.
3. Çetinkaya, M.; Karaosmanoğlu, F., **2003**; pp 25-40.
4. Nuvera https://www.nuvera.com/ (accessed February 2018).
5. Toyota Mirai https://ssl.toyota.com/mirai/fcv.html (accessed February 2018).
6. Ballard Fuel Cells http://www.ballard.com/markets (accessed February 2018).
7. Tucson Fuel Cells http://www.hyundaihydrogen.ca/ (accessed February 2018).
8. Bossel, U.; Schönbein, C. F.; Grove, W. R. In The Birth of the Fuel Cell*: 1835-1945:* 1839 to 1868 Between Christian Friedrich Schoenbein (discoverer of the Fuel Cell Effect) and William Robert Grove (inventor of the Fuel Cell), European Fuel Cell Forum: 2000.
9. Litster, S.; McLean, G., PEM fuel cell electrodes. *J. Power Sources* **2004,** *130*, 61-76.
10. Steele, B. C.; Heinzel, A., Materials for fuel-cell technologies. In Materials for sustainable energy: a collection of peer-reviewed research and review articles from nature publishing group, World Scientific: **2011**; pp 224-231.
11. Kirubakaran, A.; Jain, S.; Nema, R., *Int. j. latest trends eng.* **2009**, *1*, 157-161.
12. Tanç, B.; Arat, H. T.; Baltacıoğlu, E.; Aydın, K. *Int. J. Hydrog. Energy* **2019,** *44*, 10120-10128.
13. Zhang, H.; Shen, P. K. *Chem. Soc. Rev.* **2012,** *41*, 2382-2394.
14. Passalacqua, E.; Lufrano, F.; Squadrito, G.; Patti, A.; Giorgi, L. *Electrochim. Acta* **2001**, *46*, 799-805.

15. Li, Q.; He, R.; Jensen, J. O.; Bjerrum, N. J. *Chem. Mater.* **2003**, *15*, 4896-4915.
16. Miranda, P. E., Science and Engineering of Hydrogen-Based Energy Technologies: Hydrogen Production and Practical Applications in Energy Generation. Academic Press: 2018.
17. Hess, M.; Jones, R. G.; Kahovec, J.; Kitayama, T.; Kratochvíl, P.; Kubisa, P.; Mormann, W.; Stepto, R.; Tabak, D.; Vohlídal, J. *Pure Appl. Chem.* **2006,** *78* (11), 2067-2074.
18. Chen, H.; Wang, S.; Li, J.; Liu, F.; Tian, X.; Wang, X.; Mao, T.; Xu, J.; Wang, Z. *J Taiwan Inst Chem Eng.* **2019**, *95*, 185-194.
19. Hooshyari, K.; Javanbakht, M.; Adibi, M. *Electrochim. Acta* **2016**, *205*, 142-152.
20. Harris, T. A.; Walczyk, D. F. *J. Manuf. Process.* **2006**, *8*, 8-20.
21. Das, A.; Ghosh, P.; Ganguly, S.; Banerjee, D.; Kargupta, K. *J. Appl. Polym. Sci.* **2018**, *135*, 45773.
22. Pandey, R. P.; Shahi, V. K. *Int. J. Hydrog. Energy* **2015**, *40*, 14235-14245.
23. Osborn, S. J.; Hassan, M. K.; Divoux, G. M.; Rhoades, D. W.; Mauritz, K. A. *Macromolecules* **2007,** *40*, 3886-3890.
24. Authayanun, S.; Mamlouk, M.; Scott, K.; Arpornwichanop, A. *Applied energy* **2013,** *109*, 192-201.
25. Kim, Y. S. *ACS Appl. Polym. Mater.* **2021**, *3*, 1250-1270.
26. Kusoglu, A.; Weber, A. Z. **2017**, *117*, 987-1104.
27. Asano, N.; Aoki, M.; Suzuki, S.; Miyatake, K.; Uchida, H.; Watanabe, M. *J. Am. Chem. Soc.* **2006**, *128*, 1762-1769.
28. Yin, Y.; Suto, Y.; Sakabe, T.; Chen, S.; Hayashi, S.; Mishima, T.; Yamada, O.; Tanaka, K.; Kita, H.; Okamoto, K.-i. *Macromolecules* **2006**, *39*, 1189-1198.
29. Lee, H. S.; Badami, A. S.; Roy, A.; McGrath, J. E. *J. Polym. Sci. Part A Polym. Chem.* **2007**, *45*, 4879-4890.
30. Yamazaki, K.; Kawakami, H. *Macromolecules* **2010**, *43*, 7185-7191.
31. Wang, F.; Hickner, M.; Ji, Q.; Harrison, W.; Mecham, J.; Zawodzinski, T. A.; McGrath, J. E. *Macromol. Symp.* **2001**; pp 387-396.

32. Titvinidze, G.; Wohlfarth, A.; Kreuer, K. D.; Schuster, M.; Meyer, W. H. *Fuel Cells* **2014,** *14*, 325-331.
33. Lee, H.-F.; Britton, B.; Huang, Y.-C.; Peckham, T. J.; Hsu, Y.-Y.; Tseng, Y.-C.; Huang, P.-C.; Lee, C.-C.; Chang, M.-Y.; Holdcroft, S. *J. Mater. Sci.* **2016**, *51*, 9805-9821.
34. Schuster, M.; Kreuer, K.-D.; Andersen, H. T.; Maier, J. *Macromolecules* **2007,** *40*, 598-607.
35. Haider, R.; Wen, Y.; Ma, Z.-F.; Wilkinson, D. P.; Zhang, L.; Yuan, X.; Song, S.; Zhang, J. *Chem. Soc. Rev.* **2021,** *50*, 1138-1187.
36. Rath, R.; Kumar, P.; Unnikrishnan, L.; Mohanty, S.; Nayak, S. K. *Polym. Rev.* **2020,** *60*, 267-317.
37. Aili, D.; Yang, J.; Jankova, K.; Henkensmeier, D.; Li, Q. *J. Mater. Chem. A* **2020,** *8*, 12854-12886.
38. Vogel, H.; Marvel, C. *J. Polym. Sci.* **1961,** *50*, 511-539.
39. Chung, T.-S. *J. Macromol. Sci., Rev. Macromol. Chem. Phys.* **1997,** *37*, 277-301.
40. Wainright, J.; Wang, J. T.; Weng, D.; Savinell, R.; Litt, M. *J. Electrochem. Soc.* **1995,** *142*, L121.
41. Vogel, H.; Marvel, C., Polybenzimidazoles. *J. Polym. Sci., Part A: Gen. Pap.* **1963,** *1*, 1531-1541.
42. Sana, B. *Ph.D Thesis*; University of Hyderabad: Hyderabad, India, **2018**.
43. Maity, S.; Jana, T. *Macromolecules* **2013**, 46, 6814−6823.
44. Maity, S.; Jana, T. *Polym. Int.* **2015**, 64, 530−540.
45. Sana, B.; Jana, T. *Polymer* **2018**, 137, 312−323.
46. Harilal; Nayak, R.; Ghosh, P. C.; Jana, T. *ACS Appl. Polym. Mater.* 2020, 2, 3161−3170.
47. Singha, S.; Jana, T. *ACS Appl. Mater. Interfaces* **2014**, 6, 21286−21296.
48. Hazarika, M.; Jana, T. *ACS Appl. Mater. Interfaces* **2012**, 4, 5256−5265.
49. Sannigrahi, A.; Ghosh, S.; Maity, S.; Jana, T. *Polymer* **2011**, 52, 4319−4330.
50. Sannigrahi, A.; Arunbabu, D.; Sankar, R. M.; Jana, T. *Macromolecules* **2007**, 40, 2844−2851.

51. Mukhopadhyay, S.; Das, A.; Jana, T.; Das, S. K. *ACS Appl. Energy Mater.* **2020,** *3*, 7964-7977.
52. Koyilapu, R.; Subhadarshini, S.; Singha, S.; Jana, T. *Polymer* **2021,** *212*, 123175.
53. Harilal; Shukla, A.; Ghosh, P. C.; Jana, T. ACS Appl. Energy Mater. 2021, 4, 1644-1656.
54. Mukherjee, N.; Das, A.; Dhara, M.; Jana, T. *Polymer* **2021,** *236*, 124315.
55. Daud, N. A. B.; Lotf, E. A.; Sha'rani, S. S.; Nasef, M. M.; Ahmad, A.; Ali, R. R. In *Efforts to Improve PBI/Acid Membrane System for High Temperature Polymer Electrolyte Membrane Fuel Cell (HT-PEMFC)*, E3S Web of Conferences, EDP Sciences: 2019; p 01002.
56. Ma, Y.-L.; Wainright, J.; Litt, M.; Savinell, R. *J. Electrochem. Soc.* **2003,** *151*, A8.
57. Kim, H. J.; An, S. J.; Kim, J. Y.; Moon, J. K.; Cho, S. Y.; Eun, Y. C.; Yoon, H. K.; Park, Y.; Kweon, H. J.; Shin, E. M. *Macromol. Rapid Commun.* **2004,** *25*, 1410-1413.
58. Lobato, J.; Canizares, P.; Rodrigo, M. A.; Linares, J. J.; Manjavacas, G. *J. Membr. Sci.* **2006,** *280*, 351-362.
59. Lobato, J.; Canizares, P.; Rodrigo, M.; Linares, J.; Aguilar, J. *J. Membr. Sci.* **2007,** *306*, 47-55.
60. Yu, S.; Zhang, H.; Xiao, L.; Choe, E. W.; Benicewicz, B. *Fuel Cells* **2009,** *9*, 318-324.
61. Wu, X.; Scott, K. *Fuel Cells* **2012,** *12*, 583-588.
62. Asensio, J. A.; Borrós, S.; Gómez-Romero, P. *Electrochem.Commun.***2003,** *5*, 967-972.
63. Wannek, C.; Lehnert, W.; Mergel, J. *J. Power Sources* **2009,** *192*, 258-266.
64. Zheng, H.; Petrik, L.; Mathe, M. *Int. J. Hydrogen Energy* **2010,** *35*, 3745-3750.
65. Gulledge, A. L.; Gu, B.; Benicewicz, B. C. *J. Polym. Sci.,Part A: Polym. Chem.* **2012,** *50*, 306-313.
66. More, M.; Sunda, A. P.; Venkatnathan, A. *RSC Advances* **2014,** *4*, 19746-19755.
67. Daletou, M.; Gourdoupi, N.; Kallitsis, J. *J. Membr. Sci.* **2005,** *252*, 115-122.
68. Xiao, L.; Zhang, H.; Jana, T.; Scanlon, E.; Chen, R.; Choe, E. W.; Ramanathan, L.; Yu, S.; Benicewicz, B. *Fuel Cells* **2005,** *5*, 287-295.
69. Molleo, M.; Chen, X.; Ploehn, H. J.; Benicewicz, B. C. *Fuel Cells* **2015,** *15*, 150-155.

70. Ponce, M.; Boaventura, M.; Gomes, D.; Mendes, A.; Madeira, L.; Nunes, S. *Fuel Cells* **2008,** *8*, 209-216.
71. Mader, J. A.; Benicewicz, B. C. *Fuel Cells* **2011,** *11*, 222-237.
72. Villa, D. C.; Angioni, S.; Barco, S. D.; Mustarelli, P.; Quartarone, E. *Adv. Energy Mater.* **2014,** *4*, 1301949.
73. Harms, C.; Wilhelm, M.; Grathwohl, G. *ECS Transactions* **2009,** *25*, 1669.
74. Qian, G.; Smith Jr, D. W.; Benicewicz, B. C. *Polymer* **2009,** *50*, 3911-3916.
75. Qian, G.; Benicewicz, B. C. *Polym. Sci., Part A: Polym. Chem.* **2009,** *47*, 4064-4073.
76. Li, X.; Qian, G.; Chen, X.; Benicewicz, B. *Fuel Cells* **2013,** *13*, 832-842.
77. Dai, H.; Zhang, H.; Zhong, H.; Jin, H.; Li, X.; Xiao, S.; Mai, Z. *Fuel Cells* **2010,** *10*, 754-761.
78. Angioni, S.; Righetti, P.; Quartarone, E.; Dilena, E.; Mustarelli, P.; Magistris, A. *Int. J. Hydrogen Energy* **2011,** *36*, 7174-7182.
79. Lobato, J.; Cañizares, P.; Rodrigo, M. A.; Úbeda, D.; Pinar, F. J. *J. Membr. Sci* **2011,** *369*, 105-111.
80. Zheng, H.; Mathe, M. *J. Power Sources* **2011,** *196*, 894-898.
81. Eguizábal, A.; Lemus, J.; Urbiztondo, M.; Garrido, O.; Soler, J.; Blazquez, J.; Pina, M. *J. Power Sources* **2011,** *196* (21), 8994-9007.
82. Lobato, J.; Cañizares, P.; Rodrigo, M. A.; Úbeda, D.; Pinar, F. J. *ChemSusChem* **2011,** *4*, 1489-1497.
83. Linlin, M.; Mishra, A. K.; Kim, N. H.; Lee, J. H. *J. Membr.Sci.***2012,** *411*, 91-98.
84. Chu, F.; Lin, B.; Qiu, B.; Si, Z.; Qiu, L.; Gu, Z.; Ding, J.; Yan, F.; Lu, J. *J. Mater. Chem.* **2012,** *22*, 18411-18417.
85. Stewart, K. A.; Missan, H. P. S. *ECS Trans.* **2013,** *50*, 1167.
86. Pinar, F. J.; Cañizares, P.; Rodrigo, M. A.; Ubeda, D.; Lobato, J. *RSC Adv.* **2012,** *2*, 1547-1556.
87. Yang, J.; Aili, D.; Li, Q.; Cleemann, L. N.; Jensen, J. O.; Bjerrum, N. J.; He, R. *ChemSusChem* **2013,** *6*, 275-282.

88. Ghosh, P.; Halder, D.; Ganguly, S.; Banerjee, D.; Kargupta, K. *Int. J. Plast. Technol.* **2014,** *18*, 403-408.

89. Aili, D.; Allward, T.; Alfaro, S. M.; Hartmann-Thompson, C.; Steenberg, T.; Hjuler, H. A.; Li, Q.; Jensen, J. O.; Stark, E. J. *Electrochim. Acta* **2014,** *140*, 182-190.

90. Rao, S. S.; Hande, V. R.; Sawant, S. M.; Praveen, S.; Rath, S. K.; Sudarshan, K.; Ratna, D.; Patri, M. *ACS Appl. Mater.Interfaces* **2019,** *11*, 37013-37025.

91. Li, X.; Chen, X.; Benicewicz, B. C. *J. Power Sources* **2013,** *243*, 796-804.

92. Lin, B.; Chu, F.; Yuan, N.; Shang, H.; Ren, Y.; Gu, Z.; Ding, J.; Wei, Y.; Yu, X. *J. Power Sources* **2014,** *252*, 270-276.

93. Yuan, S.; Guo, X.; Aili, D.; Pan, C.; Li, Q.; Fang, J. *J. Membr.Sci.* **2014,** *454*, 351-358.

94. Cho, H.; Hur, E.; Henkensmeier, D.; Jeong, G.; Cho, E.; Kim, H. J.; Jang, J. H.; Lee, K. Y.; Hjuler, H. A.; Li, Q. *Eur. Polym. J.* **2014,** *58*, 135-143.

95. Conti, F.; Bertasi, F.; Wackerl, J.; Dams, P.; Di Noto, V.; Lehnert, W.; Korte, C. *ECS Trans* **2016,** *72*, 157.

96. Nayak, R.; Sundarraman, M.; Ghosh, P. C.; Bhattacharyya, A. R. *Eur. Polym. J* **2018,** *100*, 111-120.

97. Krishnan, N. N.; Joseph, D.; Duong, N. M. H.; Konovalova, A.; Jang, J. H.; Kim, H.-J.; Nam, S. W.; Henkensmeier, D. *J. Membr. Sci.* **2017,** *544*, 416-424.

98. Özdemir, Y.; Özkan, N.; Devrim, Y. *Electrochim. Acta* **2017,** *245*, 1-13.

99. Søndergaard, T.; Cleemann, L. N.; Becker, H.; Aili, D.; Steenberg, T.; Hjuler, H. A.; Seerup, L.; Li, Q.; Jensen, J. O. *J. Power Sources* **2017**, *342*, 570-578.

100. Ivanova, O.; Lüke, W.; Majerus, A.; Krutyeva, M.; Szekely, N.; Pyckhout-Hintzen, W.; Appavou, M.-S.; Monkenbusch, M.; Zorn, R.; Lehnert, W. *J. Membr. Sci.* **2017,** *533*, 342-350.

101. Li, M.-Q.; Shao, Z.-G.; Scott, K. *J. Power Sources* **2008,** *183*, 69-75.

102. Quartarone, E.; Mustarelli, P.; Carollo, A.; Grandi, S.; Magistris, A.; Gerbaldi. *Fuel Cells* **2009,** *9*, 231-236.

103. Mustarelli, P.; Quartarone, E.; Grandi, S.; Carollo, A.; Magistris, A. *Adv. Mater.* **2008,** *20* (7), 1339-1343.

104. Liu, Y.-L. *J. Membr. Sci.* **2009,** *332* (1-2), 121-128.

105. Qingfeng, L.; Hjuler, H. A.; Bjerrum, N. *J. Appl. Electrochem.* **2001,** *31*, 773-779.

106. Lin, H.-L.; Chen, Y.-C.; Li, C.-C.; Cheng, C.-P.; Yu, T. L. *J. Power Sources* **2008,** *181*, 228-236.

107. Lin, H.; Hsieh, Y.; Chiu, C.; Yu, T.; Chen, L. *J. Power Sources* **2009,** *193*, 170-174.

108. Kerres, J.; Schönberger, F.; Chromik, A.; Häring, T.; Li, Q.; Jensen, J. O.; Pan, C.; Noyé, P.; Bjerrum, N. *Fuel Cells* **2008,** *8*, 175-187.

109. Li, Q.; Jensen, J. O.; Pan, C.; Bandur, V.; Nilsson, M.; Schönberger, F.; Chromik, A.; Hein, M.; Häring, T.; Kerres, J. *Fuel Cells* **2008,** *8* (3-4), 188-199.

110. Li, M.; Scott, K. *Electrochim. Acta* **2010,** *55*, 2123-2128.

111. Larson, J.; Hamrock, S.; Haugen, G.; Pham, P.; Lamanna, W.; Moss, A. B. *J. Power Sources* **2007,** *172*, 108-114.

112. Noyé, P.; Li, Q.; Pan, C.; Bjerrum, N. J. *J. Polym. Adv. Technol.* **2008,** *19*, 1270-1275.

113. Kim, T.-H.; Lim, T.-W.; Lee, J.-C. *J. Power Sources* **2007,** *172*, 172-179.

114. Yu, S.; Xiao, L.; Benicewicz, B. *Fuel Cells* **2008,** *8*, 165-174.

Chapter 2

Materials and Experimental Methods

This chapter describes the source of materials, detailed experimental procedures, all the characterization techniques and the instruments used in working Chapters 3 to 6.

2.1. Source of Materials

Pd/C catalyst (10 wt% Pd on active carbon), 2-phenylhydroquinone, 2-methylhydroquinone, anthracene (99 %) and phosphorus pentoxide (P_2O_5) were procured from Aldrich and used as received. Hydrazine monohydrate, glacial acetic acid, hydrobromic acid (48 %), ammonium acetate (96 %), acetic anhydrate (97 %), hydrogen peroxide (H_2O_2), sodium bicarbonate ($NaHCO_3$), anhydrous magnesium sulphate (MgSO4) and sodium dithionite were purchased from Fisher Scientific. Xylenes, N, N-dimethylformamide (DMF), potassium carbonate, dimethyl sulphoxide (DMSO), sulphuric acid (99.8 %), *N*-methyl-2-pyrrolidone (NMP), orthophosphoric acid (85 %) and N, N-dimethylacetamide (DMAc) were bought from Finar chemicals and used as received. Formic acid (FA), 4-fluoro benzonitrile, hydrochloric acid (HCl), p-benzoquinone, methane sulfonic acid (CH_3SO_3H), sulphuric acid (99.8%), Trifluoromethanesulfonic acid (TFSA), sulphuric acid (99.8%) and potassium hydroxide (KOH) was obtained from Avra chemicals. Fuming nitric acid was purchased from Faiz chemicals, India. 4-fluoro-2-methylbenzonitrile and 4-fluoro-2-(trifluoromethyl)benzonitrile and other reagents were obtained from SRL, India. Eaton's reagent, (3-trifluoromethyl)-phenylhydroquinone and PyTAB were synthesized using the procedure reported in the previous literature.[1-6] All chemicals were used without further purification.

Synthesis of monomers, polymers, preparation of membranes and all other sample preparation details are described in the individual chapters for the better clarity.

2.2. Characterization Methods

2.2.1. Viscosity Measurement

The inherent viscosity (I.V) of the polymer solutions was measured using a Cannon Ubbelohde capillary dilution viscometer (model F725) at 30 °C. Polymers were dissolve in 98% sulfuric acid at a concentration of 0.2 g/L. The insoluble precipitate was passed through a 0.25 µm PTFE syringe filter before injecting into the viscometer. The I.V values were determined from the flow time data as previously described. Results are averaged from 3 duplicates.

The equation for calculating IV (dL/g) is given by

$$IV = \frac{\ln(\frac{t}{t_o})}{C} \qquad (2.1)$$

where C is the polymer solution concentration of 0.2 g/dL, and t and t_0 are the flow times of the polymer solution and sulfuric acid, respectively. The molecular weight of PBIs is normally calculated from intrinsic viscosity [η], obtained from one point measurement using Mark−Houwink–Sakurada equation.

$$[\eta] = K\bar{M}_v^a \qquad (2.2)$$

where K = 5.2×10^{-5} dL/g and a = 0.92 and $[\eta] = \frac{\eta_{sp}+3\ln\eta_{rel}}{4C}$ where $\eta_{sp} = 1-\eta_{rel}$ and $\eta_{rel} = {}^{t}/_{t_o}$ where t and t_o are the time flow for the polymer solution and solvent, respectively.

2.2.2. Solubility Test

The solubility of all the synthesized polymers was observed in various common organic solvents like dimethylacetamide (DMAc), N, N-dimethyl sulphoxide (DMSO), formic acid (FA), methane sulfonic acid (MSA), N-methyl-2-pyrrolidone (NMP) and phosphoric acid and the solubility test was carried out up to 2 wt%. The solubility was first carried out at room temperature and then followed by heating condition. The weight losses were obtained by weighing the membranes before and after solubility test. The remaining weight was calculated by the following formula:

$$Remaining\ weight(\%) = \frac{W_b - W_a}{W_b} \times 100\% \qquad (2.3)$$

Where W_b and W_a are the weight of dry membranes before and after being immersed in solvents, respectively.

2.2.3. Stability Test in H_3PO_4

All the polymer membranes were immersed into H_3PO_4 (85%) for 72 h at 100 °C. Then the samples were taken out and washed with deionized water for several times. Finally, the membranes

were dried for 24 h at 110 °C. The weight losses were obtained by weighing the membranes before and after solubility test. The remaining weight was calculated by the following equation.

$$\text{Remaining weight} = \frac{W_b - W_a}{W_b} \times 100\% \qquad (2.4)$$

Where W_b and W_a are the weight of dry membranes before and after being immersed in phosphoric acid (PA), respectively.

2.2.4. Acid Doping Level (ADL)

The ADL of all the polymer membrane samples were achieved by immersing the membranes in a phosphoric acid solution at room temperature for 72 hrs until equilibrium sorption occurred. Then the membranes were removed from the petridish, and their surface acid was wiped with a tissue paper and titrated against standardized 0.1N NaOH solution using Autolab Metrohm 702 titrator. ADL of the membrane is expressed as the mole number of PA per molar repeat unit of all polymer membranes. The measurement was performed in triplicate with five same-size membrane samples to ensure the reproducibility of the results. The PA loading levels reported in the 3, 4, 5 and 6 chapters are the average values of the three measurements. The ADL was calculated according to following equation:

$$ADL = \frac{(W_{doped} - W_{undoped})/M_{PA}}{(W_{undoped})/M_{Polymer}} \qquad (2.5)$$

Where M_{PA} and $M_{Polymer}$ refer the molecular weight of phosphoric acid and repeat unit of PBI polymer component, respectively. $W_{undoped}$ and W_{doped} represent the weight of doped and undoped samples, respectively.

2.2.5. Water Uptake, PA Uptake, Swelling Ratio and Swelling Volume in Water and PA

For PA uptake, water uptake, swelling ratio and swelling volume measurements in both water and phosphoric acid, initially the membranes were dried thoroughly in vacuum oven at 100 °C for 48 hours. Specifically, three dried membranes of each type of PBI membranes were cut in 4×4 cm^2 size specimens and the weights of individual specimens were separately noted. The specimens were immersed in both phosphoric acid and water at 30 °C for 3 days. The solution was

renewed twice in a 24 h period. After three days, the doped membranes were carefully removed from the solvent vial and their surface wiped many times using laboratory tissue paper. The membranes were quickly weighed to record the loaded mass and dimensions, in triplicate. Swelling ratio, swelling volume, PA and water uptake were calculated as the following equations.

$$\text{PA and Water uptake (\%)} = \frac{W_w - W_d}{W_d} \times 100\% \quad (2.6$$

$$\text{Swelling ratio in PA and water (\%)} = \frac{L_w - L_d}{L_d} \times 100\ \% \quad (2.7)$$

$$\text{Swelling Volume in PA and water (\%)} = \frac{V_w - V_d}{V_d} \times 100\ \% \quad (2.8)$$

Where, W_w, L_w and V_w are the weight, length and volume of the wet membranes, respectively and W_d, L_d and V_d are the weight, length and volume of the dry membranes, respectively. These measurements were carried out in triplicate independently and the average values with error bar were calculated to check for reproducibility.

2.2.6. Oxidative (or) Chemical Stability

The oxidative chemical stability of all the polymer membranes was measured using Fenton reagent (3 wt.% H_2O_2 solution with 4 ppm Fe^{2+}) at 70 ºC. The dry membrane samples were put into freshly prepared Fenton's solution and taken out periodically every 24 h, washed thoroughly with Milli-Q deionized water and dried at 100 °C under vacuum for 24 h and mass was measured. The oxidative stability was determined in terms of the remaining mass percentage of membrane samples after being exposed to a Fenton's reagent.

2.2.7. Proton Conductivity and Durability Study

The proton conducting ability of all the phosphoric acid (H_3PO_4)-doped proton exchange membranes (PEMs) were investigated using alternating-current (A.C) impedance spectroscopy over the frequency range of 1 Hz to 100 KHz. The resistance was measured using a Autolab Impedance analyser (model: PGSTAT302N) bearing a four-probe cell (The opposite electrode and the reference electrode are connected to a Pt electrode, and the first reference electrode and the working electrode are connected to another Pt electrode). The rectangular membranes (1 cm × 5

cm) were sandwiched between the four platinum electrodes of the conductivity test cell (**Figure 2.1**) two outer electrodes 1.5 cm apart supply current to the cell, while the two inner electrodes 0.5 cm apart on opposite sides of the membrane measure the potential drop across the electrodes. Prior to the measurement the whole test cell along with the membrane was heated at 100 ºC for 2 hours inside the oven, to remove water from the membrane completely and to reached constant weight. After which cell was shifted into the desiccator for allowing cooling to room temperature. All conductivity measurements were conducted under anhydrous conditions over the temperature range of 30-180 °C (tested every 30 min). Proton conductivity (σ) was calculated according to the following equation.

$$\sigma = L / R \times A \qquad (2.9)$$

where σ represented the proton conductivity in S cm^{-1}, L was referred to the distance of adjacent electrodes (cm), R was the membrane resistance (Ω) obtained from Nyquist plots, A is stand for the cross-sectional area of the membranes (cm^2). **Figure 2.2** shows a schematic diagram of Nyquist plot. The durability of all polymers PA-doped membranes was monitored in a same way at 160 ºC under anhydrous conditions.

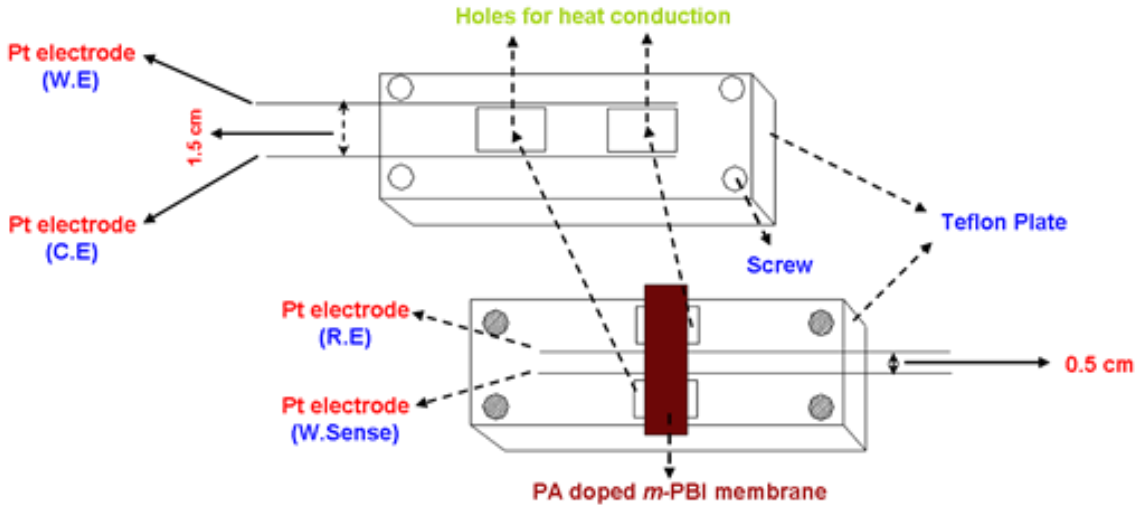

Figure 2.1 *Conductivity cell used to measure proton conductivity of PA-loaded membranes. The two parts as shown in the figure are clamped together by screws and the cell was kept inside a programmable oven to control temperature (Taken from reference 7, 8).*

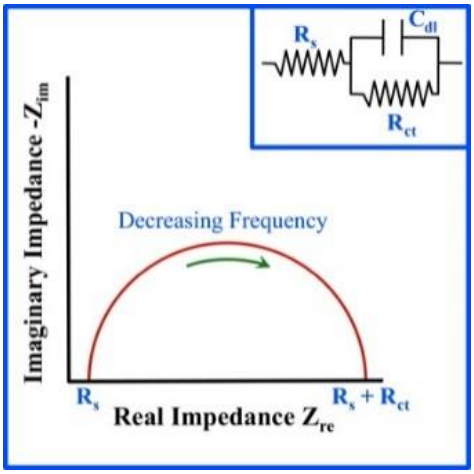

Figure 2.2 *Schematic representation of Nyquist plot. (Adopted from google image)*

Activation energy (Ea) is calculated via the Arrhenius equation from conductivity values using equation:

$$\ln(\sigma_T) = ln\sigma_0 - \frac{E_a}{RT} \qquad (2.10)$$

Where E_a is the activation energy for the proton conductive transform, σ_0 corresponds to the proton conductivity (S cm^{-1}) at zero Kelvin temperatures, R is the gas constant (8.314 J mol^{-1} K^{-1}), and T refers to absolute temperature (K).

2.2.8. Phosphoric Acid Retention Test

The phosphoric acid (H_3PO_4) retention test was performed for the dried H_3PO_4-loaded membranes according to the previous literature.[9, 10] The acid loaded membranes were mopped with tissue paper to remove excess acid and their initial weights noted down. The membranes were allowed to hang over boiling water vapour condition (100° C) for a period of 3 hours (**Figure 2.3**) and the weight of the membrane was recorded (*Wi*) every one hour after wiping off the leached acid and condensed water from the membranes. The weight loss ratio of acid in the membranes was calculated using the following equation:

$$R\ (\%) = \frac{W_o - W_i}{W_a} \text{ x } 100\ \% \qquad (2.11)$$

Where, W_0 is the initial weight of the PA doped membrane, W_i is the weight of the PA doped membrane after leaching at different times and *Wa* is the original weight of PA present in the membranes calculated from the PA doping level of the membranes. The measurement was performed at least 3 times and the average values are reported. The proton conductivity of the acid leached samples was measured from 30 °C to 160 °C immediately after 5 hours of leaching experiment as described above in the previous section.

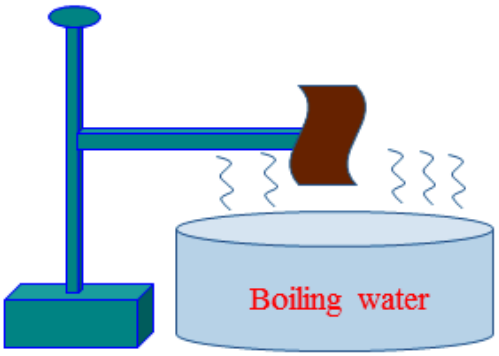

Figure 2.3 *Schematic representation of acid retention test performed in the wet laboratory. (Adopted from S. Singha thesis, UOH, 2015)*[8]

2.2.9. Fabrication of Membrane Electrode Assembly (MEA)

The MEA were fabricated using the method reported elsewhere.[11] In brief, the catalyst slurry was prepared by 40 wt% platinum supported on carbon using solvent as isopropyl alcohol and 10 wt% poly-tetrafluoroethylene (PTFE) solution as binder. The electrodes were fabricated by brush coating of the above prepared slurry on the commercial gas diffusion layer with loading of 0.6 mg cm^{-2}. Further the synthesized membrane was uni-axially sandwiched between the electrodes to form MEA.

2.2.10. Fuel Cell Performance Evaluation

MEA was assembled in a single cell (indigenously engineered) with 4 cm^2 serpentine flow field area made up of graphite plates along with current collector and end plates. The cell was further stabilized/activated for 1 h and then tested for polarization (I-V characteristics). High pure

H_2 and O_2 with the stoichiometry of 1.2 and 3 at ambient pressure were supplied as a fuel and oxidant on anode and cathode side respectively for HT-PEM-FC test. Polarization experiments were carried out from 120 to 180 ^oC after stabilizing the fuel cell in an DC electronic load PRODIGIT Instrument Professional, Taiwan (Model: 3354F).

2.2.11. Thermogravimetric Analysis (TGA)

The TGA of all the prepared PEMs were performed on a TA-Q500 (TA instrument) in the presence of N_2 atmosphere at a flow rate of 50 mL min^{-1}. All the membrane samples were preheated in a vacuum oven at 100 °C for 24 h to remove the residual solvent and any absorbed water before the measurement. TGA profiles of membranes were collected over a temperature range between 30 ^oC to 700 ^oC with a scanning rate of 10 °C/min^{-1}. Each polymer sample was taken approximately 5-10 mg in these experiments and tested for at least 3 times with the same sample.

2.2.12. Brunauer–Emmett–Teller (BET) Measurement

N_2 gas adsorption experiment of all the polymer samples (in chapter 6) were performed on a Quantachrome Quadrasorb automatic gas adsorption analyzer (ADIQC000-4). Prior to surface area analysis, the samples were activated at 120 °C for 20 hours. The porosity of polymer networks were measured by N_2 adsorption-desorption of an activated sample at 77 K. The Brunauer-Emmet-Teller (BET) surface area of the polymers were determined by multipoint BET analysis.

2.2.13. Powder X-ray Diffraction (PXRD)

The PXRD patterns of all polymer membrane samples were recorded using a Rigaku Philips (model PW 1830) powder diffraction instrument. The samples were placed on a glass slide, and the diffractograms were recorded with nickel-filtered Cu-K_α radiation source (λ = 1.5406 Å) operated at 40 kV and 50 mA current in the angular 2θ range of 5-60° with a scanning rate of 0.6° 2θ/min at room temperature.

2.2.14. Single Crystal X-ray Diffraction (SC-XRD)

All the newly synthesized monomers were (in chapter 6) recrystallized from 1, 4-dioxane at room temperature. Single crystal X-ray data for crystals of compounds were recorded on a Rigaku Oxford Diffraction CCD single crystal diffractometer using graphite monochromatic Mo Kα (λ = 0.71073 Å) radiation at 293K. Unit cell measurement, data collection, integration, scaling, and absorption corrections were performed using Rigaku Oxford Diffraction. Multiscan absorption corrections were applied using SADABS-2014. The structure was solved by direct methods using SHELXS-97 and refined with the full matrix least squares method using SHELXL-2014[12] present in the program OLEX2 Software. All of the non-hydrogen atoms were refined anisotropically. Hydrogen atoms on the O atoms were introduced on calculated positions and included in the refinement riding on their respective parent atoms. The packing diagram of the crystal was generated using *PLATON* software. All the crystal structures, the fully refined final structures, were deposited to CSD. In addition, full crystallographic details can be obtained free of charge from the Cambridge Crystallographic Data Center (CCDC) via www.ccdc.cam.ac.uk/data_request/cif (CCDC 2099945, 2070384, 2070350 and 1951204 for **4c**, **4d**, **8c** and **8d**, respectively).

2.2.15. Dynamic Mechanical Analysis (DMA)

The thermo-mechanical properties of all prepared polymer membranes were performed by a dynamic mechanical analyser (DMA, Q-800, TA Instruments) at room temperature. Membrane samples were cut to rectangular dimension (25 × 5 × 0.08 mm) and loaded between the two DMA tension clamp points. Prior to the test, the membrane samples were equilibrated at 100 °C overnight to remove the water from the membrane. The samples were heated from from 100 to 450 °C with a ramping rate of 4 °C/min at an oscillation frequency of 1 Hz. The glass-transition temperature (T_g) and chain relaxation behaviours of polymer membranes was determined from the position of the maximum (peak) on the tan δ vs temperature plot.

2.2.16. Universal Testing Measurement (UTM)

Tensile strength and elongation at break measurements of all the acid-doped and undoped casted membranes (in the chapter 3 & 6) were done by a Universal Testing Machine (UTM, Instron Model 5965-5kN) using a strain rate of 1 mm/min. The samples were cut into a dumbbell shaped

specimen according to the ASTM D653 standard and fixed between the two holders and pulled at a cross-head strain speed of 10 mm/min. The stress-strain curves measurements were carried out under ambient conditions and tested each sample minimum 3 times to check for the reproducibility. Tensile strength, and elongation at break were calculated using the Bluehill-3 material testing software.

2.2.17. ATR-FTIR Spectroscopy

Background corrected attenuated total reflection Fourier transform infrared (ATR-FTIR) spectra of all the prepared samples were recorded on a Nicolet iS5 ATR-FTIR (Thermo scientific, India) spectrometer in the range of 4000-400 cm^{-1} with a nominal resolution of 4 cm^{-1} using 32 scans and analysed by OMNIC spectra software.

2.2.18. Nuclear Magnetic Resonance Spectroscopy (NMR)

The synthesized compounds (monomers and polymers) NMR spectra were obtained on a Bruker Avance-500 MHz (^{1}H: 500 MHz; ^{13}C: 100 MHz. ^{19}F: 376 MHz) spectrometer at room temperature and using DMSO-d_6 and $CDCl_3$ as a solvent, and tetramethyl silane (TMS) as an internal chemical shift reference. Chemical shifts (δ) are reported in ppm. The degree of crosslinking of PyOPBI-Crosslinked membranes was estimated from ^{1}H NMR spectroscopy (chapter 3). Solid-state ^{13}C CPMAS NMR spectra were obtained at ambient temperature with Bruker AV 400 MHz NMR spectrometer operating at 500 MHz at a spinning rate of 5 kHz and a contact time of 2 ms and mentioned in Chapter 6.

2.2.19. Absorption Spectroscopy

Absorption spectra were recorded on a JASCO (V-750) UV-visible spectrometer. All the polymers (in chapter 6) were dissolved in DMSO and the spectra were recorded. The concentration of the sample solutions was taken as1mg/mL.

2.2.20. X-ray Photoelectron Spectroscopy (XPS)

XPS analyses of the powdered samples (carried out for Chapters 5 and 6) were performed on an Omicron Nanotech ESCA+ (Oxford Instruments, Germany).

2.2.21. Field Emission Scanning Electron Microscope (FESEM)

The cross-sectional morphology images of the fracture prepared membranes were observed through field-emission scanning electron microscopy (FESEM) (Carl Zeiss Ultra-55 using EHT detector at accelerating voltage of 5 kV) analysis. Before cross-sectional analysis, all the membrane samples were cryogenically fractured in liquid nitrogen (N_2). Prior to the measurements, all samples were need to be sputtered with a thin film of gold to avoid charging effects during SEM analysis. The surface morphology and cross section microstructure of the membranes was visualized from field-emission scanning electron microscopy (FESEM).

2.2.22. Transmission Electron Microscope (TEM)

The polymer samples (chapter 6) were prepared first, prior to TEM analysis by dispersing in a very diluted solution of suitable solvent followed by drop casting on carbon coated copper (200 mesh) grids and dried and then the images were captured using FEI (Technai Model No. 2083) TEM machine at an accelerating voltage of 200 kV.

2.2.23. Atomic Force Microscope (AFM)

AFM studies (in the chapter 6) were carried out on NT-MDT Model Solver Pro M microscope using a class 2R laser of 650 nm wavelength having a maximum output of 1 mW. All calculations and image processing were carried out by using NOVA 1.0.26.1443 software provided by the manufacturer. The images were recorded in in tapping mode using a super sharp silicon cantilever (NSG 10-DLC) with a diamond-like carbon tip (NT-MDT, Moscow).

REFERENCES

(1) Liu, J. G.; Wang, L. F.; Yang, H. X.; Li, H. S.; Li, Y. F.; Fan, L.; Yang, S. Y. *J. Polym. Sci. A Polym. Chem.* 2004, 42, 1845-1856.

(2) Maity, S.; Jana, T. *Macromolecules* 2013, 46, 6814−6823.

(3) Maity, S.; Jana, T. *Polym. Int.* **2015**, 64, 530−540.

(4) Sana, B.; Jana, T. *Polymer* **2018**, 137, 312−323.

(5) Harilal; Nayak, R.; Ghosh, P. C.; Jana, T. *ACS Appl. Polym. Mater.* 2020, 2, 3161−3170.

(6) Maglio, G.; Palumbo, R.; Tortora, M.; Vignola, M. C. *Polym. Adv. Technol.* 1996, 7, 385-392.

(7) Sannigrahi, A. *Ph.D Thesis*; University of Hyderabad: Hyderabad, India, **2010**.

(8) Singha, S. *Ph.D Thesis*; University of Hyderabad: Hyderabad, India, **2015**.

(9) Pu, H.; Liu, L.; Chang, Z.; Yuan, J. *Electrochimica Acta* **2009,** *54*, 7536-7541.

(10) Pu, H.; Qin, Y.; Tang, L.; Teng, X.; Chang, Z. *Electrochimica Acta* **2009,** *54*, 2603-2609.

(11) Harilal; Shukla, A.; Ghosh, P. C.; Jana, T. *ACS Appl. Energy Mater*. **2021**, *4*, 1644-1656.

(12) Sheldrick, G. M. SHELXL. Program for Refinement of Crystal Structures; Universitat Go ¨ttingen: Germany, 2014.

Chapter 3

Cross-Linked Polybenzimidazole Membrane for PEM Fuel Cells

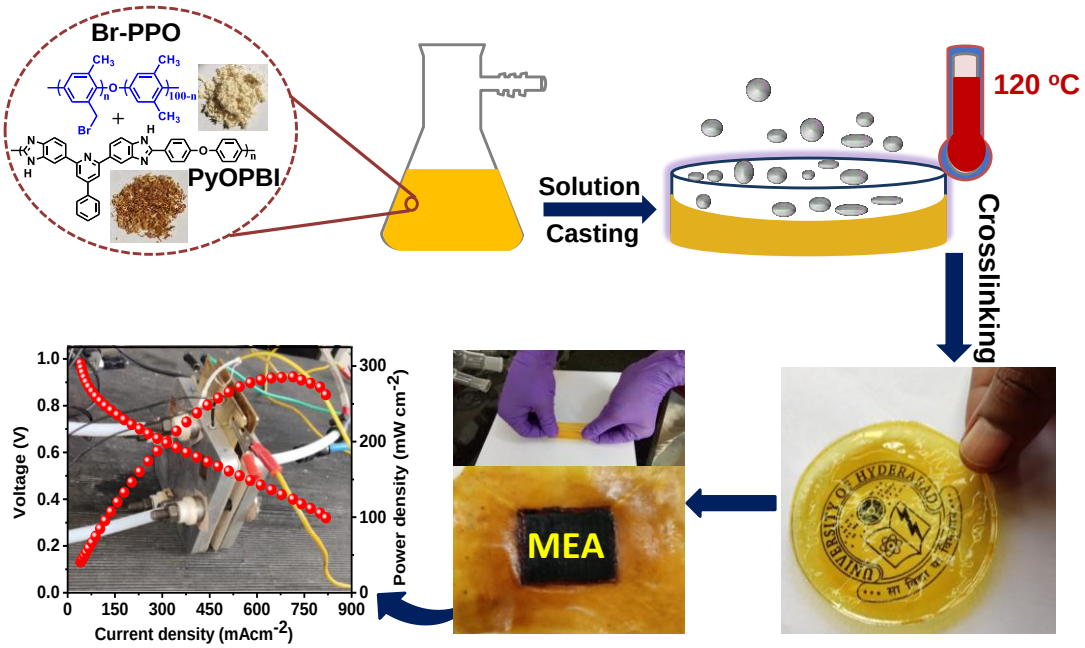

In this chapter, we have fabricated a series of cross-linked pyridine-bridge polybenzimidazole (PyPBI) proton exchange membranes (PEMs) with high conductivity, superior mechanical robustness and very good fuel cell performance.

Harilal; Nayak, R.; Ghosh, P. C.; Jana, T. *ACS Appl. Polym. Mater.* **2020,** *2*, 3161-3170.

3.1. INTRODUCTION

In recent years, proton exchange membranes fuel cells (PEMFCs) have attracted huge attention due to their many advantages including high power density, non-polluting nature and high-energy conversion efficiency.[1-3] PEM is the core component of PEMFCs which acts as a solid electrolyte barrier for transferring protons and prevents permeation of fuels between anode and cathode. Over the years, perfluoro sulfonated polymer membranes have become benchmark PEMs because of their several unique properties including high proton conductivity and good thermo-mechanical stabilities.[4] However, many severe drawbacks such as slow electrode kinetics, low operation temperature and high cost of these membranes compel the researchers to find alternative PEMs.[5-8] Soon, it was realized that PEMs working at a higher temperature (>100 °C) can successfully resolve all the issues of perfluoro sulfonated PEMs.[9-17] In literature so far many polymers such as poly (arylene piperidine) (PAPs), sulfonated polyimides (SPI), sulfonated polyether ketones (SPEEK), polyether sulfones (PAES), and polyesters were introduced as high temperature PEM candidates.[18-21] Despite all such research trials, a significant of efforts are still needed to provide a commercial PEMs with optimum fuel cell performance.

Phosphoric acid (PA) loaded polybenzimidazole (PBI) membranes have become most promising high temperature PEMs as these membranes display high proton conductivities, excellent thermal, mechanical and chemical stabilities along with high tolerance to fuel impurities and hence display high cell efficiency.[22-24] However, few limitations: (i) deterioration of membrane mechanical strength at high PA loading and (ii) acid leaching from membrane; raises serious concerns about the use of these type of PEMs.[25, 26] Hence, the current focus in the preparation of PBI based PEMs is therefore to overcome these limitations. Many investigators including our research group have made various efforts by: (i) synthesizing novel PBI structures, (ii) blending with suitable polymers and (iii) making nanocomposites and (iv) developing novel membrane fabrication technique to resolve these issues.[7-14, 27-30]

Very recently, we have developed a new kind of readily processable PBI structure (named as PyPBI) from a readily accessible and less expansive tetraamine [2, 6-bis (3, 4'-diamino phenyl)-4-phenyl pyridine (PyTAB)] monomer. These pyridine bridged PBIs (PyPBIs) membranes showed remarkable improvement in various PEM properties in comparison to traditionally synthesized polybenzimidazoles (PBIs).[31, 32] Nevertheless, we

observed a drawback with PyPBI membranes in regard to their limited stability in PA medium. These membranes are found to be stable up to 60% PA during the PA doping process, but dissolved completely in > 60% PA may be due to the presence of highly basic pyridine ring in the polymeric backbone and large intermolecular distance between polymeric chains. This instability can have serious consequences as it is well known that the membranes doped with 85% PA often yield higher proton conductivity which inevitably enhances the fuel cell performance. As we wish to keep the backbone structure since it has many advantages over conventional PBI structure but also want to resolve the stability problem, we tried to figure out the possible reason for instability and find out a solution. We traced that the large inter-chain distance which enhances the free volume of the PyPBI chains is the main driving force for the high solubility and low stability of PyPBI in PA. To reduce the free volume of polymer chain without altering the structure, the only possible solution is to cross-link the chains therefore we wish to test this idea in case of PyPBI in this work.

In general, ionically cross-linked chains show poor thermal stability whereas covalently cross-linked chains with small-molecular cross-linkers tend to be brittle. A good number of cross-linked PBI membranes with varieties of cross-linkers have been reported in recent times.[33-39] Results from these studies show that the cross-linked membranes with high acid doping level exhibit almost zero performance decline during the test period. These observations suggest crosslinking is a promising approach towards the enhancement of PEM properties of PA-doped PBI membranes.

With all these backgrounds and our hypothesis, we have cross-linked PyPBI chains with bromomethyl polyphenylene oxide (BrPPO) to tighten its free volume in order to improve various PEM properties and fuel cell performance. Various characterization techniques including nuclear magnetic resonance (NMR), attenuated total reflection flourier transformed infrared (ATR FT-IR) spectroscopy and thermogravimetric analysis (TGA) technique are employed to gain insights into the interactions between the PyPBI and the BrPPO membranes before and after crosslinking. Different crosslinking degrees are obtained by changing BrPPO/PyPBI molar ratio in the crosslinking solutions. Thereafter structure, morphology, physicochemical properties, oxidation stability, mechanical strength and fuel cell performance of membranes are systematically investigated to understand the effects of covalent crosslinking reaction.

3.2. Experimental Section

Source of materials and all the details of various characterization techniques used in this chapter are described in the **chapter 2**.

3.2.1. Synthesis of PyOPBI-cross-linked-BrPPO polymer (CrL-PyOBI) and membrane fabrication

Scheme 3.1 presents the synthetic routes for the preparation of CrL-PyOPBI polymer. First, one of the precursor PyOPBI was synthesized in the laboratory by polymerizations of 2,6-bis (3′,4′-diamino phenyl)-4-phenylpyridine (PyTAB) and 4,4′-oxybis (benzoic acid) (OBA) with polyphosphoric acid (PPA) [**Scheme 3.1(A)**] using our previously reported method.[31, 32] The yield was found as 95%. ^{13}C NMR (101 MHz, DMSO-d_6) δ (ppm) 158.20, 157.46, 153.01, 152.48, 149.93, 145.46, 144.95, 138.60, 136.59, 136.21, 133.77, 129.57, 129.10, 127.84, 126.22, 119.84, 116.09, 111.74. Spectrum is given in the supporting information **Appendix I Figure 3.1**.

A targeted degree of bromination on PPO was carried out using reported protocol [40] as depicted in **Scheme 3.1 (B)**. Typically, PPO, AIBN and NBS were reflex in chlorobenzene to obtain BrPPO. Detail procedure is described in supporting information. The yield of resulting BrPPO was found as 86%, and the degree of bromination (DB) was 28.6% which was calculated from the ^{1}H NMR spectrum. The ^{13}C-NMR spectra of BrPPO is given in **Appendix I Figure 3.2**.

PyOPBI membranes were covalently cross-linked with BrPPO by mixing the two polymer solutions in DMAc at 80-120 ^{o}C as shown in **Scheme 3.1 (C)**. The preparation steps of the crosslinking process and membrane fabrication are presented in **Scheme 3.2**. BrPPO and PyOPBI were dissolved in DMAc by keeping the total solid contents 2 wt % and the mixture was stirred for 24 h. The amount of BrPPO in the crosslinking solutions were varied as 12.5, 25.0 and 37.5 wt % with respect to PyOPBI wt %. The mixed solution was then poured on a clean glass petridis and baked at 80 °C for 5 h followed by baking at 120 °C for 24 h. During the baking process, the solvent evaporation and dynamic covalent crosslinking networks generate simultaneously. After the baking, the membranes were allowed to cool down to room temperature, peeled off from the glass petridis and washed thoroughly with hot deionized water (at 80 ^{o}C) to remove residual solvent. The membranes were dried under vacuum at 100 °C for 24 h to obtain homogeneous transparent cross-linked membranes and were designated as CrL-

PyOPBI-12.5 (**P1**), CrL-PyOPBI-25 (**P2**) and CrL-PyOPBI-37.5 (**P3**) where the numerical number referred to the theoretical crosslinking degree expected from the initial content of the bromomethyl group of BrPPO to -NH groups of PyOPBI by assuming complete conversion. The obtain membranes thickness were in the range of 30-50 μm thick. The pristine PyOPBI membrane was also prepared by the following route: a solution of 2 wt % PyOPBI was prepared by dissolving PyOPBI in DMAc and then was cast onto a glass petridis directly and baked at 100 °C for 12 h. The obtained homogeneous membrane was dried at 100 °C for 12 h.

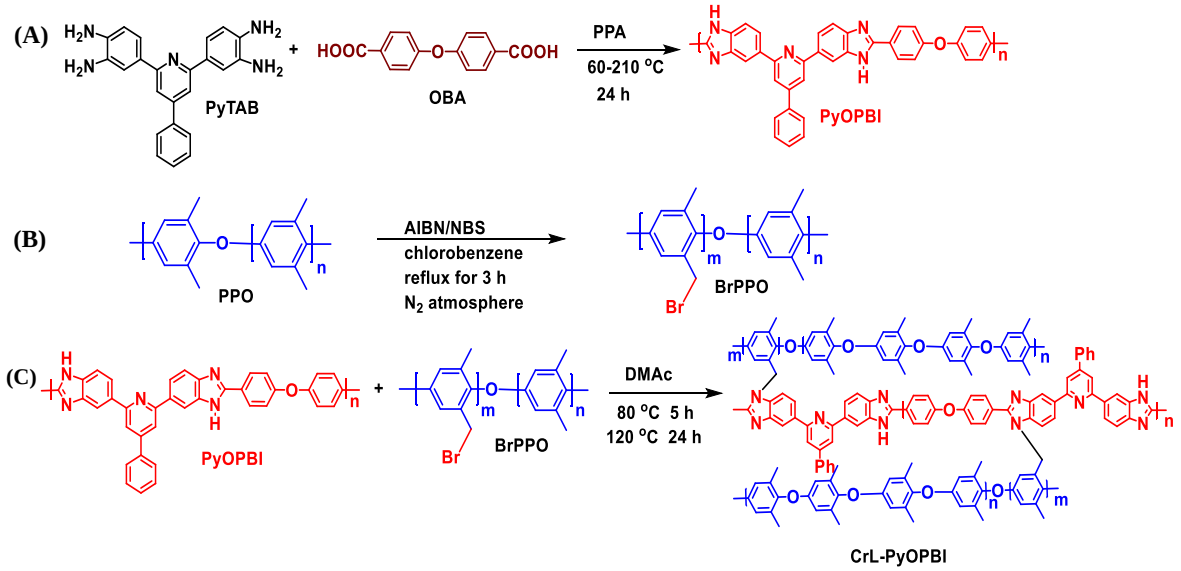

Scheme 3.1. Synthesis of (A) PyOPBI, (B) BrPPO and (C) the formation of the cross-linked polymer (CrL-PyOPBI) through the alkylation reaction between PyOPBI and BrPPO.

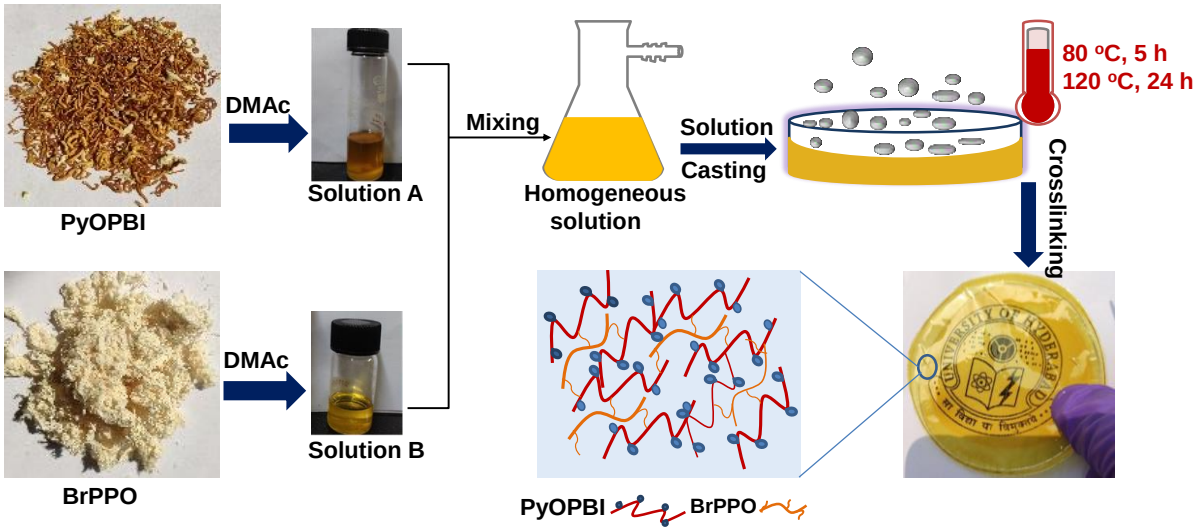

Scheme 3.2. Schematic depiction for the preparation of the cross-linked membranes.

3.3. Results and discussion

3.3.1. Chemical crosslinking of PyOPBI

In order to enhance the stability of pyridine bridged oxy-polybenzimidazole (PyOPBI) membrane in PA medium; BrPPO copolymer is introduced into PyOPBI matrix via a simple nucleophilic N-substituted reaction methodology at 80-120 ^{o} C using dimethylacetamide (DMAc) as the solvent. First, BrPPO was prepared through a facile free radical reaction between a PPO and brominating agent NBS. The degree of bromination is calculated from the peak integral of ^{1}H NMR found to be ~28.6 %. The functionalized benzyl bromide of BrPPO react with imidazole protons of PyOPBI when mixed in DMAc solvent at 80-120 ^{o}C for 24 h to form crosslinking structure as depicted in **Scheme 3.2**. Covalent crosslinking is often used to increase the stability of membranes under harsh environments so to prevent the dissolution of the membrane in high polar solvents. As illustrated in **Scheme 3.1**, the cross-linked membranes were prepared from PyOPBI and BrPPO with various weight % of BrPPO such as 12.5, 25.0 and 37.5 wt % with respect to PyOPBI. All the obtained membranes are homogeneous and transparent with a slightly yellow colour. The cross-linked membranes are designated as **P1**, **P2**, and **P3** for 12.5, 25.0 and 37.5 BrPPO wt % in the membrane, respectively. **Figure 3.1** shows the ^{1}H-NMR spectra of PyOPBI, BrPPO and cross-linked membranes in DMSO-d_6. As seen from the figure, the chemical shifts at 7.3-8.6 ppm represent the aromatic protons of PyOPBI and the characteristic peak at 13.1 ppm is assigned for the imidazole protons. The singlet proton signal at 2.0 and 4.3 ppm in BrPPO are attributed to the methyl groups and benzyl bromide proton (-CH_2Br), the signals at approximately 6.5-6.90 ppm are identified as phenyl protons, which matches well with previous literature.[40] The spectra of the cross-linked membranes unambiguously display changes in the chemical shifts from both the pristine PyOPBI and BrPPO. On keen observation, it is found that the methylene peak of -CH_2Br and aromatic peaks move to the downfield around 5.4 ppm (shown as CH_2-N in the figure) and 6.9-7.2 ppm which is probably due to the more electrophilic environment because of benzimidazole groups in PyOPBI, the new peaks at 2.2-2.23 ppm is attributed to the methyl groups of BrPPO in cross-linked membrane.[42] In addition, we noticed that the intensity of imidazole proton at 13.1 ppm N-H decreases (almost vanished) in the cross-linked membranes, especially in the case of the membranes containing higher percentage of BrPPO. This again attribute that the bond formation between -CH_2Br of BrPPO and imidazole of PyOPBI. The

degree of crosslinking (DC) is estimated from the peak integral ratio of -CH_2Br to aromatic peaks.

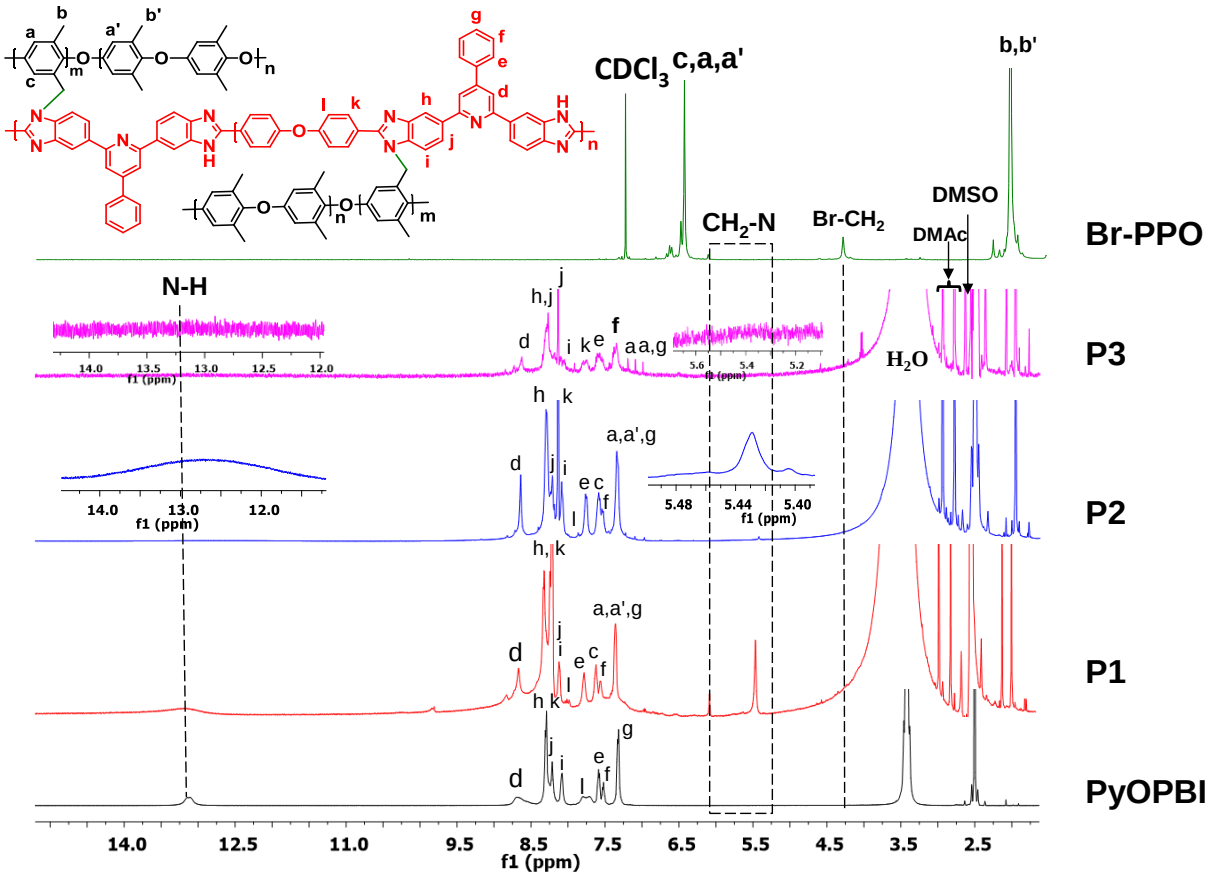

Figure 3.1. ^1H NMR spectra of PyOPBI, cross-linked membranes and Br-PPO. In case of **P2** and **P3** spectra, the proton of imidazole NH signal (at 13.1 ppm) and N-CH_2 (at 5.4 ppm) are zoomed to show the appearance and disappearance of signals.

Further information obtained from FTIR spectra (**Appendix I Figure 3.3**) suggesting the chemical bond formation between PyOPBI and BrPPO. The typical characteristic peaks for the symmetrical and asymmetrical stretching vibrations of C-O-C (aromatic ether) at 1185 and 1310 cm^{-1}, stretching of phenyl group at 1470 and 1595 cm^{-1} and a noticeable stretching vibration of -CH_2 group at 2924 cm^{-1} can be observed in spectra of all cross-linked membranes. These peaks intensity increases with BrPPO content in the polymer matrix which proves the possible chemical bond formation occurring between PyOPBI and BrPPO during the membrane preparation. [43, 44]

3.3.2. Solvent resistance test

The solvent stability of pristine PyOPBI membrane and cross-linked membranes were examined in DMAc and 85 wt % phosphoric acid (PA) for 72 h duration at room temperature. Expectedly, the pristine PyOPBI completely dissolved in DMAc as well as in 85 wt% PA within 1 h which is in agreement with our earlier observation.[31] Interestingly, when BrPPO is incorporated into PyOPBI membrane matrix to make cross-linked structure, the resulting membranes (**P1**, **P2** and **P3**) show robust solvent stability both in DMAc and 85% PA at room temperature. This can be clearly monitored from the pictures of the membranes before and after the test from the **Figure 3.2**. This result confirms that indeed the crosslinking network has been constructed in between PyOPBI and polymer cross-linker BrPPO successfully which enhance the stability in solvents. The stability in solvents is calculated as the remaining mass percentage (R) of the samples, using equation[45] R (%) $= \frac{W_i - W_o}{W_i} \times 100$ where W_i represents the weight of the dry membrane and W_o indicates the weight of the dry membrane after dipping the sample for 72 h in solvent. The results both R (%) value and the visual observations (**Figure 3.2**) clearly prove that the significant change in the stability in both DMAc and 85% PA the membrane after crosslinking with BrPPO. Particularly at higher crosslinking density (**P3**), weight loss upon exposure to solvent is less than 5% attributing huge enhancement of stability owing to the crosslinking.

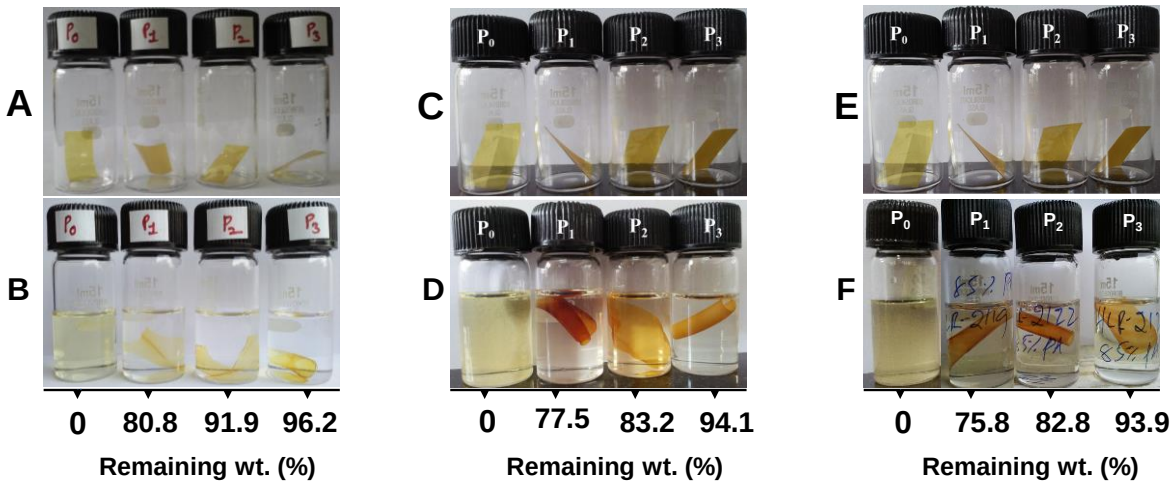

Figure 3.2. Remaining weight (%) of membrane samples and photographs before (A, C and E) and after (B, D and F) immersed in DMAc (A and B) and PA (C and D) at room temperature and PA (E and F) at 100 ^{o}C for 72 h. P_o indicates the pristine PyOPBI.

3.3.3. Morphology of the membrane

The cross-sectional morphology obtained from FESEM studies of the cross-linked membranes containing different BrPPO contents are shown in **Appendix I Figure 3.4**. All cross-linked PEM membranes exhibit a honeycomb network structure consisting of nano-fibers which is increasing with more BrPPO content.[46] This distinct morphology in the case of cross-linked membranes is the direct consequence of crosslinking. Both the pristine polymers (PyOPBI and BrPPO) do not show any significant morphological features as seen from the **Appendix I Figure 3.4** (A and E).

Further investigation on cross-linked membranes structure using PXRD **[Appendix I Figure 3.4 (F)]** reveals the more or less amorphous nature. Pristine PyOPBI shows a broad peak at 2θ=21° which indicates the convolution of an amorphous region in accordance with our previous observation.[31] A strong peak appears at 14.8° in case of BrPPO indicates π-π stacking of the aromatic rings. As can be seen from the **Appendix I Figure 3.4 (F),** the cross-linked polymer interchain spacing decreases after cross-linking between PyOPBI and BrPPO which also indicates that the closer chain packing and more compact chemical structure of cross-linked membranes.[46-48] The 2θ values of the cross-linked membranes lies in between PyOPBI and BrPPO attributing the presence of new structural entity as seen in FESEM images.

3.3.4. Oxidative resistance

During the long-term fuel cell operation, the heteroatom containing polymeric chain can be attacked by hydroxyl ($OH^{\cdot}$) and hydroperoxyl ($OOH^{\cdot}$) unstable free radicals resulting in degradation of the polymer membrane. Hence, radical induced degradation of PEMs is one of the most important issue needs to be addressed. In the present work, the oxidative resistance of fabricated membranes was determined by measuring the remaining weight of the membranes after immersion into Fenton's reagent (3% H_2O_2 containing 4 ppm $FeSO_4$) at 70 ^oC over 140 hours as a function of time as shown in **Figure 3.3**. It could be seen that all of the covalently cross-linked membranes exhibit much impressive chemical stability than the pristine PyOPBI. Also, the chemical stability gradually increased with increase in weight percentage of BrPPO in the polymer matrix. This enhancement in oxidative stability may be attributed to the formation of dense crosslinking structure between the PyOPBI and the BrPPO chains, which could retard chain scission. This result clearly suggested that the cross-linked membranes have

high tolerance to the Fenton reagent. Similar enhancement of oxidative stability of PBI based membranes has been reported earlier. [49,50]

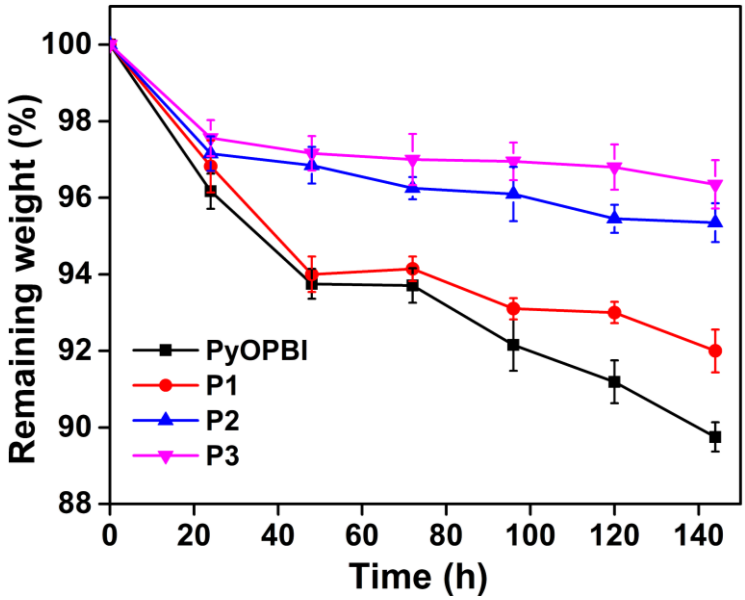

Figure 3.3. The membrane degradation in 3% H_2O_2 containing 4 ppm Fe^{2+} at 70 °C

3.3.5. Thermal stability

Thermogravimetric analysis (TGA) were performed on undoped and doped (loaded with PA) membranes to get more insights on the membrane structure and thermal stability which is essential information for the application in high temperature PEMFC. **Appendix I Figure 3.5 (A)** represents the thermogram of the undoped membranes including both PyOPBI and BrPPO. It is observed that all the membranes show a 5-10 % mass loss up to 300 ^oC due to the presence of moisture and DMAc solvent. Among all the membranes, PyOPBI show higher thermal stability as compared to the cross-linked membranes (P1, P2 and P3). Above 300 °C, the thermal stability of cross-linked membranes are lower than that of pristine PyOPBI due to the thermal degradation of less stable bromomethyl groups of BrPPO which adds to the ramping of polymer degradation. **P3** exhibits least thermal stability among the cross-linked membranes due to the higher content of BrPPO.

PyOPBI membrane was doped with 60 wt.% PA as beyond 60 wt % the membrane dissolves in PA whereas the cross-linked membranes were doped in 85 wt % PA. **Appendix I Figure 3.5 (B)** represents the thermogram for PA-doped membranes (PyOPBI, P1, P2 and P3). It is observed that the undoped and PA-doped membranes display almost similar thermal

profile. The first mass loss between 30 ºC-180 ºC is attributed to the loss of moisture and dehydration of PA to form pyrophosphoric acid.[50] The mass loss between of 300 to 400 °C is mainly due to the degradation of the polymer backbone and the continuous dehydration of the pyrophosphone acid to polyphosphoric acid which is in agreement with earlier reported results.[51, 52]. **Appendix I Figure 3.5 (B**) also indicates that PA-doped cross-linked membranes exhibit poor thermal stability compared to PA-doped PyOPBI membrane due to the presence of higher PA in the PA-doped cross-linked membranes. Overall, TGA studies show good thermal stabilities of the cross-linked membrane and hence these results indicate that the cross-linked membranes meet the thermal requirement of PEMs to be applied in PEMFCs.

3.3.6. Acid loading and dimensional stability of membrane

The amount of PA loaded and swelling of the membrane greatly influence the proton conductivity, mechanical properties and cell performance of the resulting PEM. A high PA loading of PBI membrane is an imperative requirement for achieving higher proton conductivity. However, presence of excess acid (PA) molecules can also deteriorate the mechanical strength and induce the dimensional instability during long-term operation of the cell at elevated temperatures.

Many reports suggested that covalently crosslinking provide more compact chemical structures,[53, 54] which can restrain the PA doping level and dimensional swelling. In this work, in order to prevent the PyOPBI membrane dissolution at higher acid concentrations, we used BrPPO as a polymeric crosslinking agent to form a robust covalent inter-chain linkage between PyOPBI via simple N-substituted reaction. To examine the effect of the crosslinking on PA doping level (loading) and dimensional swelling of the cross-linked membranes were immersed in 85 wt.% PA solutions at room temperature for 72 h. The acid doping level (ADL) is measured as moles of PA per PBI repeat unit and plotted as a function of doping times [**Figure 3.4 (A)**]. The volume swelling is also measured and plotted against doping time [**Figure 3.4 (B)**]. It is observed that the incorporation of BrPPO lead to an enhancement of the PA doping level in case of cross-linked membranes. The doping level (ADL) increases rapidly first 15 h and then saturates [**Figure 3.4 (A)**]. It is to be noted that the ADL values of all cross-linked samples are higher than pristine PyOPBI, in-fact the highest value of ADL (~ 18) obtained in case of **P1** which has the lowest crosslinking density (~12.5%). The ADL value decreases with

increasing crosslinking density (ADL is 14.2 in case of **P3**) is due to more compact chemical structure (which confirmed by PXRD pattern) leading to decrease in PA loading capacity. Similar observation is made from the **Figure 3.4 (B)** where **P1** and **P2** show higher volume swelling compared to pristine PyOPBI but **P3** shows less dimensional stability owing to the compact structure because of higher crosslinking. Few snapshots of the PA loaded cross-linked membranes are shown in the **Appendix I Figure 3.6** to demonstrate the flexibility and mechanical robustness of the membranes. More detailed discussion on the mechanical strength is included in the later section.

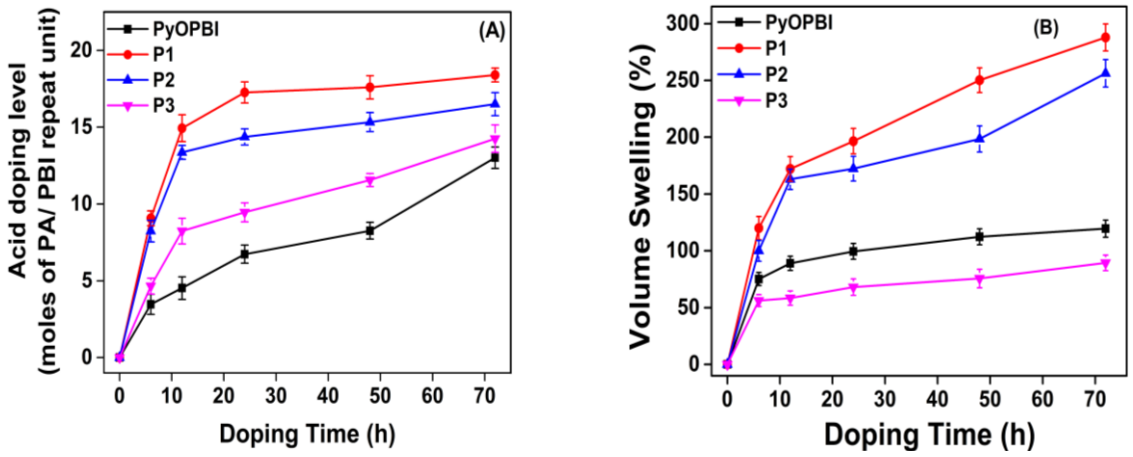

Figure 3.4. Acid doping level (ADL) (A) and volume swelling (B) of PyOPBI and cross-linked membranes as a function of doping time. Each data points are the average of three independent measurements. ADL is measured as PA moles per PyOPBI repeat unit. PyOPBI is doped with 60% PA for 3 days whereas all cross-linked membranes were doped with 85% PA for 3 days.

3.3.7. Proton conductivity

The targeted proton conductivity of PEMs for most of the applications such as automotive applications is approximately 0.1 S cm^{-1}.[55] In the present article, we wish to achieve proton conductivity beyond 0.1 S cm^{-1} by employing crosslinking method as described above. The conductivity measurements of PEMs developed in this were performed under anhydrous condition in the temperature range of 30 to 180 °C. Prior to performing the experiments the pristine PyOPBI membrane was soaked in 60 wt. % PA and cross-linked membranes were soaked in 85 wt. % PA for 72 hours, and dried completely in vacuum over at 100 °C. **Figure 3.5 (A)** displays proton conductivity as a function of temperature of doped PyOPBI and cross-

linked membranes. This figure clearly shows that the proton conductivity of PyOPBI membrane is much lower than all the cross-linked membranes. Among cross-linked membranes, **P1** displays the highest conductivity (0.12 S/cm^{-1} at 180 ^{o}C) where as **P3** shows the lowest conductivity (0.037 S/cm^{-1} at 180 ^{o}C) but still higher than the pristine PyOPBI. The conductivity trend is **P1** > **P2** > **P3** which is in agreement with the trend of PA loading capacity (P1 > P2 > P3) of these membranes. We believe the enhanced proton conductivity for the cross-linked membranes is achieved due to the presence of porous honeycomb structure in the cross-linked membranes as seen from the morphology (**Appendix I Figure 3.4**) which allows membrane to absorb more PA, and higher PA uptake leads to higher proton conductivity.

Proton conductivity of the membranes were also monitored at 160 °C after every 2-hour interval over 72 hours to understand the long-term proton conductivity stability of the membranes which decides the end use of the membranes in PEMFCs. **Figure 3.5 (B)** represents the plot of long-term proton conductivity stability at 160 ^{o}C. It is observed that PyOPBI membrane shows decrease in conductivity till 9 hours and beyond that the conductivity remains constant. Whereas the cross-linked membranes show a noticeable decrease in proton conductivity till 24 hours and there after it remains constant. The initial significant decrease in proton conductivity of the membranes is due to the exudation of free PA and water molecules from the membrane.[46, 56-58] Even after initial decrease, the conductivities of the **P1**, **P2** and **P3** are much higher than that of PyOPBI which suggests that the incorporation of BrPPO with PyOPBI effectively improve long-term proton conductivity.

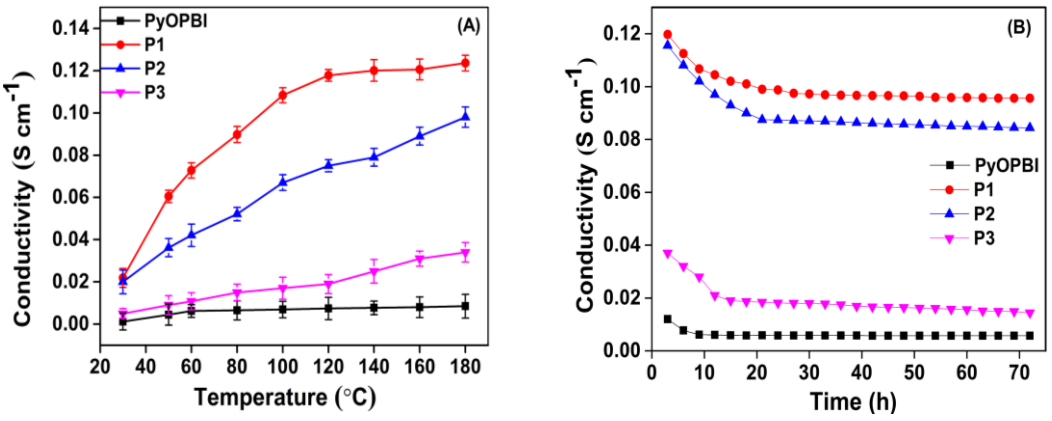

Figure 3.5. (A) Proton conductivity of PA-doped PyOPBI and cross-linked membranes at different temperatures, (B) Stability of conductivity (isothermal) of the membranes measured at 160 °C for 72 h.

3.3.8. Mechanical properties

Mechanical property of membrane determines the durability of a working PEMFC and hence various research groups devoted their efforts toward optimizing the mechanical properties for PEM. The mechanical properties of the PyOPBI and its cross-linked membranes were measured using dynamic mechanical analysis (DMA) and universal testing machine (UTM). Dynamic mechanical analysis experiments for the membranes were performed from 100-400 °C and results are obtained as temperature dependent storage modulus, loss modulus and tan δ which are represented in **Figure 3.6**. It is evident from **Figure 3.6 (A)**, the storage modulus (E') of the cross-linked membranes are superior to that of pristine PyOPBI membrane over the entire temperature region and also value of E' increases with increasing crosslinking density (**P1 > P2 > P3**). The enhanced storage modulus in cross-linked membranes is due to the more compact structure and better interfacial interaction between polymer chains which making them more rigid and stiffer compared to the pristine PyOPBI. Their arrested mobility enhances the storage modulus of the membranes which indicating that the membranes are sufficiently in enough robust for high temperature PEM application. As the crosslinking increases, the tan δ value decreases (**Appendix I Figure 3.7**) due to compact morphology of the membrane owing to the strong covalent bond between the bromomethyl groups of BrPPO and the -N-H of PyOPBI. It is also to be noted from both tan δ and loss modulus measurements that the T_g value decreases as **P3** < **P2** < **P1** < PyOPBI (**Figure 3.6** and **Appendix I Figure 3.7**) because increasing crosslinking density. This is simply because of covalent crosslink network tightening the structure among the polymer matrix as a result of which polymer chains free volume declines considerably and so it takes lower temperature to cause segmental motion of the polymer chains and hence glass-transition temperature decreases.

The membrane must withstand high pressure during cell preparation and operation otherwise it can easily break resulting into the failure of the cell. Therefore, we verified the mechanical properties (stress- strain) of membranes before and after PA doping using UTM **(Figure 3.6 C & D)**. Tensile strength (σ_b) and elongation at break (ε_b) obtained from stress vs. strain plot which predict the overall mechanical robustness of membranes are tabulate in the **Table 3.1**. The dried PyOPBI membrane shows a tensile strength of 41.3 MPa and an elongation at break value of 6.2%. Generally, in case of covalently cross-linked polymer the main chain is pulled by the cross-linked structure resulting enhanced interaction between the

chains which improves the tensile strength of the membrane. **Figure 3.6 (C)** shows that the cross-linked membranes have better tensile strength, with values of 48.4 MPa, 62.5 MPa and 104.9 MPa for the P1, P2 and P3 membranes, respectively in comparison to pristine PyOPBI. Also elongations at break values of cross-linked membranes are quite similar to PyOPBI. **Figure 3.6 (D)** represents the plot of stress vs strain plots of the PA-doped membranes. It is observed from the figure that the PA-doped cross-linked membranes display higher or comparable elongation at break (ε_b) and tensile strength than PA doped PyOPBI.

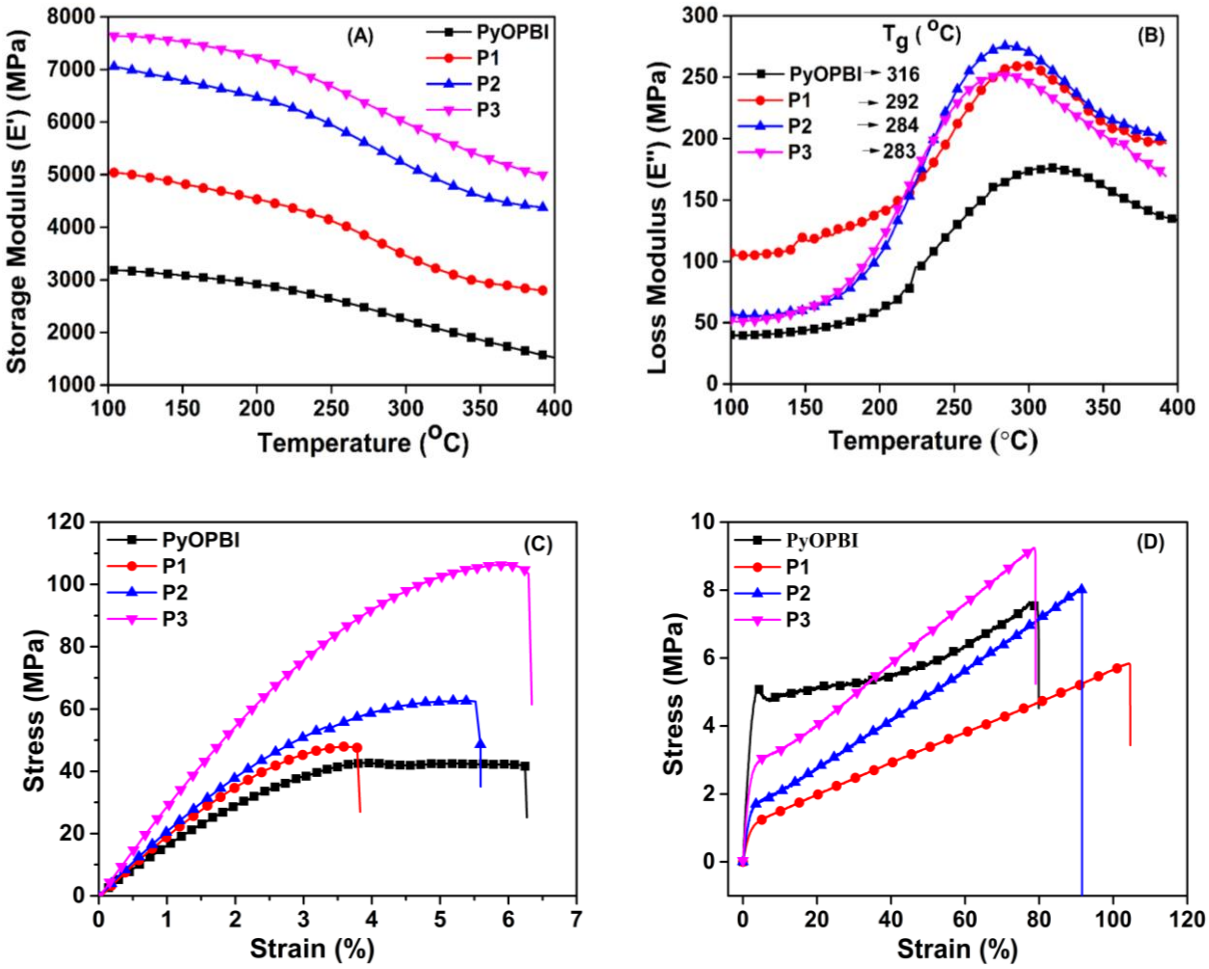

Figure 3.6. Thermo-mechanical properties of PyOPBI and cross-linked membranes from DMA. (A) and (B) represent temperature depended storage modulus and loss modulus plots, respectively. The T_g values obtained from tan δ and loss modulus are shown inside the figure. Stress-strain plots of undoped (C) and doped (D) PyOPBI and cross-linked membranes.

Table 3.1. Various tensile properties and cell performance data of PA doped membranes. Data in the first two columns are extracted from Figure 6 (D) and the data of last three columns are obtained from the Figure 3.7.

Membranes	Tensile stress (MPa)	Tensile strain (%)	OCV (V)	Peak power density (mW cm^{-2})	Current density (mA cm^{-2}) at 0.3 V
PyOPBI	7.6	79.2	0.88	96.4	321.5
P1	5.8	104.5	0.98	289	848.7
P2	8.0	91.4	0.95	144.2	480.7
P3	9.2	79	0.91	84.6	282.5

3.3.9. Fuel cell performance studies

The single cell performance of PA-doped PyOPBI and cross-linked membranes were measured at 160 °C with non-humidified gases. The power density and polarization curves of the single cell obtained from these membranes are shown in **Figure 3.7**. And various important cell performance data extracted from **Figure 3.7** plots are tabulated in **Table 3.1**. Open circuit voltage (OCV) values of cross-linked membranes vary between 0.91-0.98V. This relatively high OCV values are quite satisfactory and suggesting a low hydrogen and oxygen gas permeability across the membrane in case of cross-linked membranes. However, PyOPBI displays relatively low OCV value (0.88V) which indicates gas crossover behaviour across the membrane caused by mechanical damage such as membrane thinning and pin-hole formation.[59] It is also to be noted that OCV values varies as crosslinking densities changes indicating the influence of crosslinking on the membrane performance. A photograph of MEA made of **P1** membrane was taken after the cell performance is shown in the inset of **Figure 3.7** clearly indicates the dimensional stability of the membrane. The maximum power densities of **P1**, **P2** and **P3** membranes are 289, 144.2 and 84.6 mW cm^{-2}, respectively (**Table 3.1**). The maximum power density of the **P1** membrane is ~ 3 times higher than the maximum power density of pristine PyOPBI (96.4 mW cm^{-2}). The current density of the **P1**, **P2**, and **P3** membranes at 0.3

V are 848.7, 480.7, 282.5 mA cm^{-2}, respectively (**Table 1**). The current density at 0.3 V of the **P1** membrane is 2.6 times higher than the pristine PyOPBI (321.5 mA cm^{-2}). The higher power density, OCVs and the current density of the cross-linked membranes than pristine PyOPBI are the manifestation of their high ADLs and the remarkably higher proton conductivities as discussed in the previous section. This single cell performance of cross-linked membranes decreases with increasing crosslinking density which is again in agreement with the proton conductivity results. However, in the present study the **P3** membrane exhibits little lesser fuel cell performance than that of pristine PyOPBI membrane. The precise reason for this decrease is difficult to establish at this moment, however, one possible reason might be the some deleterious effect of the decomposing/degrading phosphoric acid at the electrolyte/electrode interface at temperatures >160 °C.[60] The overall performance demonstrate that these cross-linked membranes have potential as PEM for the use in HT-PEMFC.

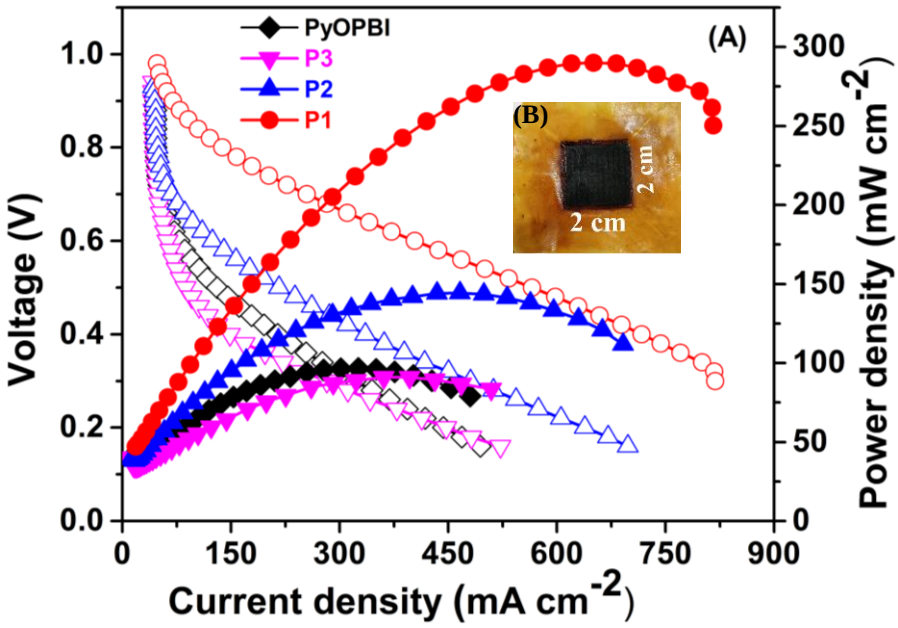

Figure 3.7. (A) Cell performance (power density curve shown by filled symbol and polarization curve shown by open symbol) of PA loaded pristine PyOPBI and cross-linked membranes (**P1**, **P2** and **P3**) at 160 °C with non-humidified H_2 and O_2. The Pt catalyst loading of the electrodes is 0.5 mg cm^{-2} , H_2 gas flow rates at anode was 0.3 mL min^{-1} and O_2 gas flow rate at cathode was 0.5 mL min^{-1}. (B) Insets show the photograph of **P1** membrane (4 cm^2) after cell performance analysis.

3.4. Conclusion

In conclusion, we demonstrated a novel facile thermal crosslinking technique to crosslink PyOPBI membranes with the aid of bromomethyl polyphenylene oxide (BrPPO) in order to boost their acid retention ability with appreciable proton conductivity at elevated temperatures. The obtained BrPPO-cross-linked PyOPBI membranes are thermally stable (up to 400 ^{o}C) with enhanced chemical resistance and displayed better mechanical properties due to significant reductions of inter-chain spacing. Though with increasing amount of BrPPO in the cross-linked membranes, the extend of PA loading decreased a bit, however, the proton conductivity of the PA doped cross-linked membrane found to be higher than that for the PA doped PyOPBI membrane and a maximum conductivity of 0.123 S cm^{-1} is observed. Fuel cell performances of the membranes were tested at 160 ^{o}C with non-humidified gas. The cross-linked membrane displayed a higher power density and current density than that with pristine PyOPBI membrane.

Appendix I

Synthesis of BrPPO and ^{13}C NMR spectra of BrPPO, PyOPBI polymers and photographs of PA loaded membranes are included in Appendix I (page no. 144-150)

REFERENCES

1. Liu, X.; Li, Y.; Xue, J.; Zhu, W.; Zhang, J.; Yin, Y.; Qin, Y.; Jiao, K.; Du, Q.; Cheng, B.; Zhuang, X.; Li, J.; Guiver, M. D. *Nat. Commun.* **2019**, 10, 842-854.
2. Park, C. H.; Lee, S. Y.; Hwang, D. S.; Shin, D. W.; Cho, D. H.; Lee, K. H.; Kim, T.-W.; Kim, T.-W.; Lee, M.; Kim, D. S.; Doherty, C. M.; Thornton, A. W.; Hill, A. J.; Guiver, M. D.; Lee, Y. M. *Nature* **2016**, 532, 480-483.
3. Liu, B.; Guiver, M. D. Wiley, **2012**; Chapter 9.
4. Han, R.; Wu, P., *ACS Appl. Mater. Interfaces* **2018**, *10*, 18351-18358.
5. Li, Q.; He, R.; Jensen, J. O.; Bjerrum, N. J. *Chem. Mater* **2003**, *15*, 4896-4915.
6. Notter, D. A.; Kouravelou, K.; Karachalios, T.; Daletou, M. K.; Haberland, N. T. *Energy Environ. **Sci.*** **2015**, *8*, 1969-1985.
7. Araya, S. S.; Zhou, F.; Liso, V.; Sahlin, S. L.; Vang, J. R.; Thomas, S.; Gao, X.; Jeppesen, C.; Kær, S. K. *Int. J. Hydrogen Energ.* **2016**, *41*, 21310-21344.

8. Xiao, L., H, Zhang, E. Scanlon, LS Ramanathan, E.-W. Choe, D. Rogers, T. Apple, and BC Benicewicz. *Chem. Mater* **2005**, *17*, 5328-5333.
9. Asensio, J. A.; Sánchez, E. M.; Gómez-Romero, P. *Chem. Soc. Rev.* **2010**, *39*, 3210-3239.
10. He, R.; Li, Q.; Bach, A.; Jensen, J. O.; Bjerrum, N. J. *J. Membr. Sci.* **2006**, *277*, 38-45.
11. Pan, C.; He, R.; Li, Q.; Jensen, J. O.; Bjerrum, N. J.; Hjulmand, H. A.; Jensen, A. B. *J. Power Sources* **2005**, *145*, 392-398.
12. Nawn, G.; Pace, G.; Lavina, S.; Vezzù, K.; Negro, E.; Bertasi, F.; Polizzi, S.; Di Noto, V. *Macromolecules* **2015**, *48*, 15-27.
13. Quartarone, E.; Angioni, S.; Mustarelli, P. *Materials* **2017**, *10*, 687.
14. Li, Q.; He, R.; Jensen, J.; Bjerrum, N. *Fuel Cells* **2004**, *4*, 147-159.
15. Li, Q.; He, R.; Gao, J.-A.; Jensen, J. O.; Bjerrum, N. J. *J. Electrochem. Soc.* **2003**, *150*, A1599-A1605.
16. Zhang, J.; Xie, Z.; Zhang, J.; Tang, Y.; Song, C.; Navessin, T.; Shi, Z.; Song, D.; Wang, H.; Wilkinson, D. P. *J. Power Sources* **2006**, *160*, 872-891.
17. Hossain, S.; Abdalla, A. M.; Jamain, S. N. B.; Zaini, J. H.; Azad, A. K. *Renew. Sustain. Energy Rev* **2017**, *79*, 750-764.
18. Jiang, J.; Zhu, X.; Qian, H.; Xu, J.; Yue, Z.; Zou, Z.; Yang, H. *Sustainable Energy & Fuels* **2019,** *3*, 2426-2434.
19. Peighambardoust, S. J.; Rowshanzamir, S.; Amjadi, M. *Int. J. Hydrogen Energ.* **2010,** *35*, 9349-9384.
20. Bai, H.; Peng, H.; Xiang, Y.; Zhang, J.; Wang, H.; Lu, S.; Zhuang, L. *J. Power Sources* **2019,** *443*, 227219.
21. Wong, C.; Wong, W.; Ramya, K.; Khalid, M.; Loh, K. S.; Daud, W.; Lim, K. L.; Walvekar, R.; Kadhum, A. A. H. *Int. J. Hydrogen Energy* **2019**, *44*, 6116-6135
22. Lysova, A.; Stenina, I.; Volkov, A.; Ponomarev, I.; Yaroslavtsev, A. *Solid State Ionics* **2019**, *329*, 25-30.
23. Kallem, P.; Eguizabal, A.; Mallada, R.; Pina, M. P. *ACS Appl. Mater. Interfaces* **2016**, *8*, 35377-35389.
24. Subianto, S. *Polym. Int.* **2014,** *63*, 1134-1144.
25. Chen, X.; Qian, G.; Molleo, M. A.; Benicewicz, B. C.; Ploehn, H. J. *J. Polym. Sci. B* **2015**, *53*, 1527-1538.

26. Liao, J.; Li, Q.; Rudbeck, H.; Jensen, J. O.; Chromik, A.; Bjerrum, N.; Kerres, J.; Xing, W. *Fuel Cells* **2011**, *11*, 745-755.
27. Singha, S.; Jana, T. *ACS Appl. Mater. Interfaces* **2014**, *6*, 21286-21296.
28. Hazarika, M.; Jana, T. *ACS Appl. Mater. Interfaces* **2012**, *4*, 5256-5265.
29. Sannigrahi, A.; Ghosh, S.; Maity, S.; Jana, T. *Polymers* **2011**, *52*, 4319-4330.
30. Sannigrahi, A.; Arunbabu, D.; Sankar, R. M.; Jana, T. *Macromolecules* **2007**, *40*, 2844-2851.
31. Maity, S.; Jana, T. *Macromolecules* **2013**, *46*, 6814-6823.
32. Sana, B.; Jana, T. *Polymers* **2018**, *137*, 312-323.
33. Yang, J.; Li, Q.; Cleemann, L. N.; Jensen, J. O.; Pan, C.; Bjerrum, N. J.; He, R. *Adv. Energy Mater.* **2013**, *3*, 622-630.
34. Liu, C.; Wang, X.; Li, Y.; Zhang, S.; Wang, J.; Jian, X. *J. Polym. Res.* **2017**, *24*, 23.
35. Kerres, J.; Atanasov, V. *Int. J. Hydrog. Energy* **2015**, *40*, 14723-14735.
36. Liu, F.; Wang, S.; Chen, H.; Li, J.; Tian, X.; Wang, X.; Mao, T.; Xu, J.; Wang, Z. *ACS Sustain Chem Eng* **2018**, *6*, 16352-16362.
37. Özdemir, Y.; Özkan, N.; Devrim, Y. *Electrochim. Acta* **2017**, *245*, 1-13.
38. Li, X.; Ma, H.; Wang, P.; Liu, Z.; Peng, J.; Hu, W.; Jiang, Z.; Liu, B.; Guiver, M. D. *Chem. Mater.* **2020**, *32*, 1182−1191
39. Krishnan, N. N.; Joseph, D.; Duong, N. M. H.; Konovalova, A.; Jang, J. H.; Kim, H.-J.; Nam, S. W.; Henkensmeier, D. *J. Membr. Sci* **2017**, *544*, 416-424.
40. Liu, L.; He, S.; Zhang, S.; Zhang, M.; Guiver, M. D.; Li, N. *ACS Appl. Mater. Interfaces* **2016**, *8*, 4651-4660.
41. Nayaka, R.; Sundarramana, M.; Ghosh, P. C.; Bhattacharyya, A. R. *Euro. Polym. J.* **2018**, *100*, 111–120.
42. Li, X.; Wang, P.; Liu, Z.; Peng, J.; Shi, C.; Hu, W.; Jiang, Z.; Liu, B. *J. Power Sources* **2018**, *393*, 99-107.
43. Tashvigh, A. A.; Luo, L.; Chung, T.-S.; Weber, M.; Maletzko, C. *J. Membr. Sci* **2018**, *551*, 204-213.
44. Tashvigh, A. A.; Chung, T.-S. *J. Membr. Sci* **2018**, *560*, 115-124.
45. Wang, S.; Zhao, C.; Ma, W.; Zhang, N.; Zhang, Y.; Zhang, G.; Liu, Z.; Na, H. *J. Mater. Chem. A* **2013,** *1*, 621-629.

46. Liu, F.; Wang, S.; Chen, H.; Li, J.; Tian, X.; Wang, X.; Mao, T.; Xu, J.; Wang, Z. *ACS Sustainable Chem. Eng* **2018**, *6*, 16352-16362.
47. Arrieta, C.; David, E.; Dolez, P.; Vu-Khanh, T. *Polymer composites* **2011,** *32*, 362-367.
48. Xu, C.; Cao, Y.; Kumar, R.; Wu, X.; Wang, X.; Scott, K. *J. Mater. Chem.* **2011,** *21*, 11359-11364.
49. Wang, S.; Zhao, C.; Ma, W.; Zhang, N.; Liu, Z.; Zhang, G.; Na, H. *J. Power Sources* **2013**, *243*, 102-109.
50. Yang, J.; Aili, D.; Li, Q.; Cleemann, L. N.; Jensen, J. O.; Bjerrum, N. J.; He, R. *ChemSusChem* **2013**, *6*, 275-282.
51. Wang, S.; Zhang, G.; Han, M.; Li, H.; Zhang, Y.; Ni, J.; Ma, W.; Li, M.; Wang, J.; Liu, Z. *Int. J. Hydrog. Energy* **2011,** *36*, 8412-8421.
52. Angioni, S.; Righetti, P.; Quartarone, E.; Dilena, E.; Mustarelli, P.; Magistris, A. *Int. J. Hydrog. Energy* **2011**, *36*, 7174-7182.
53. Shen, C.-H.; Jheng, L.-C.; Hsu, S. L.-C.; Wang, J. T.-W. *J. Mater. Chem.* **2011**, *21*, 15660-15665.
54. Yang, J.; Xu, Y.; Liu, P.; Gao, L.; Che, Q.; He, R. *Electrochim. Acta* **2015**, *160*, 281-287.
55. Hickner, M. A.; Ghassemi, H.; Kim, Y. S.; Einsla, B. R.; McGrath, J. E. *Chemical reviews* **2004**, *104*, 4587-4612.
56. Lee, K.-S.; Spendelow, J. S.; Choe, Y.-K.; Fujimoto, C.; Kim, Y. S. *Nature energy* **2016**, *1*, 16120.
57. Yu, S.; Zhang, H.; Xiao, L.; Choe, E. W.; Benicewicz, B. *Fuel Cells* **2009**, *9*, 318-324.
58. Liu, F.; Wang, S.; Chen, H.; Li, J.; Tian, X.; Wang, X.; Mao, T.; Xu, J.; Wang, Z. *ACS Sustainable Chem. Eng* **2018**, *6*, 16352-16362.
59. Marrony, M.; Barrera, R.; Quenet, S.; Ginocchio, S.; Montelatici, L.; Aslanides, A. *J. Power Sources* **2008**, *182*, 469-475.
60. Li, Q.; Jensen, J. O.; Savinell, R. F.; Bjerrum, N. J. *Prog. Polym. Sci.* **2009**, *34*, 449-477.

Chapter 4

Pyridine-Bridged Polybenzimidazole for Use in High-Temperature PEM Fuel Cells

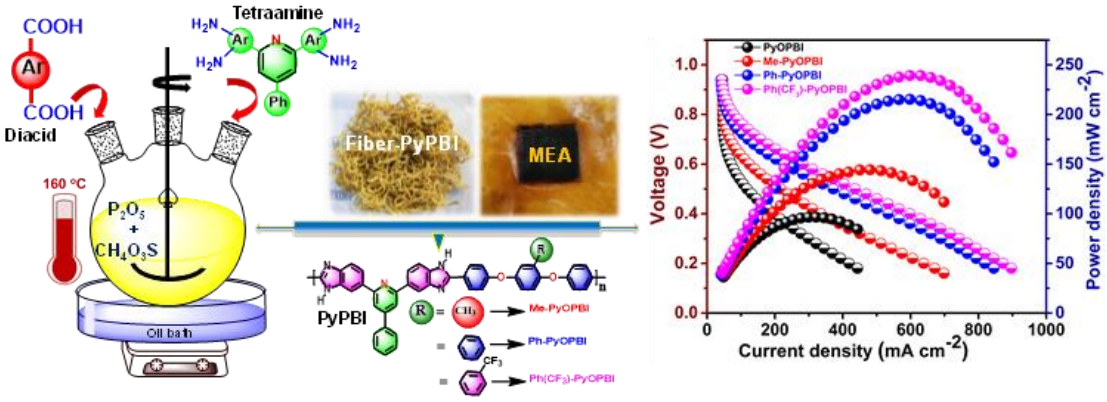

In this chapter, we demonstrated an innovative approach for the synthesis of novel PyPBIs structure in a simpler and scalable process. The PEMs obtained from these PyPBIs are found to have much superior physical properties such as thermal, mechanical, acid loading, oxidative stability, proton conductivity and more importantly higher fuel cell performance than the conventional PyOPBI.

Harilal; Shukla, A.; Ghosh, P. C.; Jana, T. *ACS Appl. Energy Mater.* **2021,** *4*, 1644-1656.

4.1. INTRODUCTION

A sustainable carbon dioxide emission-free transportation system is of great interest in the present era and the development of devices for such system is big challenge for both academics and industrial researchers all over the world.[1] In this context, significant efforts in identifying alternate energy sources such as proton exchange membrane fuel cells (PEM-FCs) have been devoted in recent times.[2-5] PEM-FCs have attracted more and more attention because of their high electrochemical energy conversion efficiency, lack of harmful exhaust and quiet operation.[6-8] In a PEM-FC, the key component is the dense solid ion-exchange membrane which serves as both the proton transport medium and the separator for isolating the gases between the electrodes. A facile proton conduction plays a vital role in the performance of PEM-FC and hence significant amount of investigations have been directed towards improving it.[9] To date, the most frequently used PEM is Nafion in light of its excellent thermal-chemical stability and high proton conductivity.[10, 11] However, difficult water and heat managements, sluggish electrode kinetics and low tolerance to carbon monoxide has thrown up need for alternative PEM.[12]

Past several years, efforts have been devoted to develop PEM for the use in high temperature (>100 ^{o}C) and low humidity conditions to eliminate the shortcomings of Nafion.[13,14] Among several HT-PEM studied so far, the most promising one is the phosphoric acid (PA) loaded polybenzimidazole (PBI), in which PA molecules act as proton carrier by forming dense hydrogen bonded network to facilitate proton hopping.[15-18] Despite their impressive advantages, still they have confronted with some limiting factors such as the acid leaching during the long-term cell operation, limited proton conductivity, and severe weakening of mechanical integrity in the operational environment.[19, 20] In addition, the tedious synthetic process and low solubility of the PBI polymers restricted the scale-up of PBI manufacturing and the membrane fabrication, respectively.[21] In order to overcome these concerns, several efforts have been explored to develop PA doped PBI HT-PEM materials by various design strategies and synthetic methods. Over the years it is understood that any successful development of PA doped PBI must meet several criteria such as: (i) synthetically scalable, (ii) good solubility, (iii) high proton conduction, (iv) good thermal stability, (v) high mechanical strength, (vi) environmentally friendly and so on. In recent years, many reports have come in the literature which made efforts to fulfil these prerequisites. Among these the prominent are: pyridine and imidazole dicarboxylic acids based PBIs[22-24], arylether type acid-

based PBIs[25-27] hyper branched based PBIs[28] and etc. Litt et.al. demonstrated that poly(2,5-benzimidazole) usually referred to as ABPBI, is readily polymerizable from a single monomer viz. 3,4-diaminobenzoic acid, absorbs better phosphoric acid and exhibited higher proton conductivity.[29-31] Unfortunately, most of these newly designed PBI based PEM could not satisfied all of the essential properties as stated above, in particular proton conductivity and chemical-mechanical stabilities. In addition, persistent challenges such as complicated synthetic procedures, crosslinking during polymerization[32], poor solubility and processability have become new concerns. A large number of current PBIs were synthesized in polyphosphoric acid (PPA) solvent which requires longer reaction time (typically 18-24 h) and high reaction temperatures (180-220 °C).[21, 33, 34,]

Very recently, our research group reported a novel kind of readily accessible and less expensive nitrogen-rich heterocyclic tetraamine, 2,6-bis(3',4'-diaminophenyl)-4-phenylpyridine (PyTAB) based homo and copolymer of PBI, named as PyPBI, as PEM candidates and had fulfilled most of the needs for application in HT-PEMFCs.[35-38] The good solubility, higher affinity with PA, superior mechanical and chemical properties and readily synthesizable raw materials make PyPBI membranes as a sustainable alternative to conventional PBI polymeric materials. However, questions remain regarding the structural instability in highly concentrated PA and the PEM performance. PyPBI membranes are stable up to 60% H_3PO_4 solution during the PA doping process but more than this concentration the membranes are found to be completely dissolved. This may be due to the presence of highly basic pyridine ring in the polymeric backbone which get protonated by PA, leading to an increased density of cationic groups and thus excessive absorption of bulk PA. Stability is a serious obstacle as it is well known that the membranes doped with 85% PA often yield higher proton conductivity which inevitably enhances the fuel cell performance. Therefore, the study of main chain chemical stability needs to be focused on. In this regard, recently we have attempted to functionalize the backbone with various functionalities and also introduce crosslinking in the chains, and we could improve the stability of the PyPBI in concentred PA quite significantly.[37, 38]

Herein, we hypothesize that introduction of bulky groups in the PyPBI backbone may result in more open “sponge like” structure which can hold considerable amount of PA and maintain original shape. In order to design “sponge-like” microstructure, one has to choose the polymer structure in such a way that the microstructure should provide “free volume” and a

rugged framework to maintain the mechanical strength. Therefore, it is expected that the introduction of a bulky group in the flexible backbone structure is likely the most suitable strategy. Taking into consideration of all these aspects, we have design suitable arylether based dicarboxylic structure with bulky groups and then polymerized these with PyTAB to get the PyPBI with sponge like microstructure. These synthesized polymers were characterized thoroughly using various spectroscopic, thermal and mechanical techniques. PEMs were made from these polymers and studied extensively to check the chemical stability, proton conductivity and fuel cell performance.

4.2. EXPERIMENTAL SECTION

The source of all the materials and the various characterization techniques used in this chapter are described in the **Chapter 2**.

4.2.1. Synthesis of arylether dicarboxylic acid monomers

The dicarboxylic acid monomers 4,4'-([1,1'-biphenyl]-2,5-diylbis(oxy))dibenzoic acid (Ph-COOH), 4,4'-((2-methyl-1,4-phenylene)bis(oxy))dibenzoic acid (Me-COOH) and 4,4'-((3'-(trifluoromethyl)-[1,1'-biphenyl]-2,5-diyl)bis(oxy))dibenzoic acid [Ph(CF_3)-COOH] were synthesized in a similar fashion to previous report and by applying some more modifications.[39] The reaction scheme for the synthesis of these three monomers are shown in **Scheme 4.1**. A typical synthetic protocol of Me-COOH was as follows: in a 250 mL three-necked round bottom flask 12.5 g (0.0673 mol) of solid 2-methyl hydroquinone, 16.7 g (0.138 mol) 4-fluoro benzonitrile, 18.6 g of K_2CO_3 and 180 mL of a dry DMF solvent were added. The reaction mixture was heated to 150 °C and left to stir at this temperature under reflux for 8 h. The solvents (DMF) was removed under vacuum and the resultant solid crude dicyano compound was grounded, washed several times with water and acetone. The crude product was recrystallized from acetone, filtered, and dried under vacuum at 100 °C. This gave the pure product, as white crystals 24.8 g, Yield: 89% (m.p 195 °C). The white crystals of 4, 4'-(1, 4-phenylenedioxy-2-phenyl) dibenzonitrile 11.9 g (0.0307 mol) and 130 g of KOH were suspended in 462 mL of ethanol/water solution (v/v: 1/1) and the reaction mixture was refluxed for 24 h at 90 °C. After cooling, the solution was acidified with HCl at pH = l and the white precipitate was filtered, washed with water, dried at 140 °C and then crystallized from dioxane (12.6 g, 80% yield; m.p 262 °C). ^{1}H NMR (500 MHz, DMSO-d_6): δ (ppm) 2.12 (3H, s), 7.12 (1H, s), 6.95-7.16 (6H, m), 7.93 (2H, d), 7.97 (2H, d), 12.8 (1H, s). ^{13}C NMR (101 MHz,

DMSO-d_6): δ (ppm) 167.20, 161.78, 152.41, 149.62, 132.18, 125.75, 123.40, 122.97, 119.54, 117.60, 16.23. The synthesis of Ph-COOH and Ph(CF_3)-COOH diacids were the similar as Me-COOH and the chemical structures were confirmed by NMR techniques (^{1}H, ^{13}C, and ^{19}F) in DMSO-d_6 solvent and all the spectra including Me-COOH are given in the **Appendix II-Figure 4.1** and **Figure 4.2**.

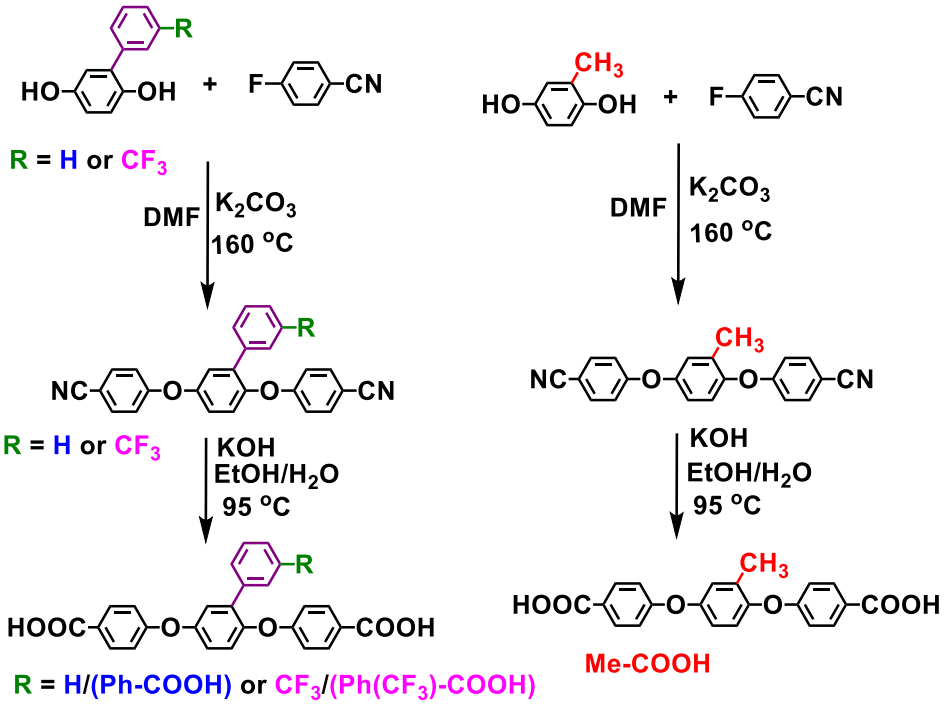

Scheme 4.1. Synthetic scheme used for making various aryl ether based dicarboxylic acid monomers.

4.2.2. Synthesis of polymers

The aryl ether type PyPBIs namely, Me-PyOPBI, Ph-PyOPBI, Ph(CF_3)-PyOPBI and PyOPBI) were typically prepared through a condensation polymerization process of different aryl ether dicarboxylic acids monomers (Ph-COOH, Ph(CF_3)-COOH ,Me-COOH and OBA) with PyTAB as shown in **Figure 4.1**. It should be noted that the molar ratios of diacid and PyTAB monomers were kept as 1:1 for all polymer synthesis in this work. A typical synthetic protocol of Me-PyOPBI was as follows: 2.0 g (5 mmol) of Me-COOH, 2.214 g (5 mmol) of PyTAB and 10 mL Eaton's Reagent (PPMA- which is 1:1 mixture of P_2O_5 and $MeSO_3H$, preparation detail is given in supporting information) were added in a 50 mL three-necked mercury sealed round-bottomed flask equipped with a mechanical stirrer, a nitrogen inlet and

an outlet. Afterward, the mixture was stirred using overhead mechanical stirrer and gradually heated up to 100 °C for 2 h and another 2 h stirring was continued at 140 °C in continuous nitrogen atmosphere. Thereafter, the final polymerization temperature of the reaction medium was raised up to the 180 °C and kept for 4 h to ensure the complete polymerization. After the complete polymerization process, a brown coloured high viscous polymer solution was slowly transferred into a huge excess of deionized (DI) water with stirring and the collected precipitated polymer (Me-PyOPBI) was filtrated and washed several times with DI water. The obtained fibrous polymer was neutralized with 10 wt % $NaHCO_3$ solution at 40 ^oC overnight and the polymer was rinsed several times with water, dried at 100 °C in a vacuum oven for 24 h to remove the water. A pictorial presentation of the polymerization mixture and the purification process is shown in **Figure 4.1 (b)**. Yield: 95%, ^{1}H NMR (500 MHz, DMSO-d_6): δ (ppm) 13.08 (NH s), 8.64 (1H s), 8.24 (2H m), 8.08 (2H d), 7.96 (2H m), 7.73 (2H m), 7.58 (2H d), 7.23 (1H m), 7.12 (1H s), 2.19 (3H s). ^{13}C NMR (101 MHz, DMSO-d_6): δ (ppm) 157.50, 152.68, 149.90, 138.62, 133.75, 132.42, 132.12, 129.57, 129.00, 127.81, 125.46, 124.88, 122.95, 122.65, 119.10, 118.75, 117.24, 116.08, 16.39.

Synthesis of Ph(CF_3)-PyOPBI. The synthetic procedure of Ph(CF_3)-PyOPBI was the same as that of Me-PyOPBI except that in this case Ph(CF_3)-COOH monomer was used with PyTAB for the polymerization. In this case the polymerization temperature was kept at 140 °C for last 4 h of reaction. The resulting polymer was obtained as fiber-like shape beige tint solid and the yield was 92%. ^{1}H NMR (500 MHz, DMSO-d_6): δ (ppm) 13.05 (NH s), 8.64 (2H d), 8.28 (2H m), 8.20 (2H d), 8.10 (1H s), 7.89 (2H d), 7.69 (2H m), 7.60 (1H m), 7.47 (2H m), 7.34 (1H m), 7.14 (1H d), 6.95 (1H m). ^{13}C NMR (126 MHz, DMSO-d_6): δ (ppm) 157.47, 153.15, 152.50, 149.89, 148.52, 138.57, 137.61, 133.82, 133.48, 130.06, 129.56, 129.05, 127.81, 125.97, 125.62, 123.63, 121.73, 118.92, 117.76, 116.14. ^{19}F NMR (471 MHz, DMSO-d_6): δ (ppm) -61.12.

Synthesis of Ph-PyOPBI. The synthesis of Ph-PyOPBI was the same as the synthesis of Me-PyOPBI using Ph-COOH and PyTAB in the stoichiometric ratio. In this case the polymerization temperature was kept at 160 °C for last 4 h of reaction. The resulting polymer was brown fiber with a yield of 89%. ^{1}H NMR (500 MHz, DMSO-d_6): δ (ppm) 13.00 (NH s), 8.62 (2H d), 8.33 (1H m), 8.27 (2H m), 8.20 (1H m), 8.16 (1H d), 8.14 (2H d), 8.08 (1H m), 7.72 (1H s), 7.57 (1H m), 7.38 (1H m), 7.31 (2H d), 7.12 (1H m). ^{13}C NMR (126 MHz, DMSO-

d_6): δ (ppm) 157.52, 153.17, 152.52, 149.91, 148.47, 138.57, 136.72, 135.63, 133.70, 129.55, 129.29, 129.05, 128.86, 127.82, 125.61, 124.90, 123.56, 122.12, 120.60, 118.96, 117.73, 116.14.

4.2.3 Preparation of free-standing membrane

The 2 (wt %) solution of all the synthesized PyOPBI polymers were prepared by dissolving the weighted amount of these polymers in DMAc in a round bottom flask overnight at 60 ºC followed by filtration using a 0.25 μm PTFE syringe filter for the removal of any undissolved solids. The solutions were left for at least 2 h to allow air bubbles to leave the solution. Afterwards, the resulting homogeneous solution was cast on a clean glass Petri dish and dried in a ventilated oven at 100 °C for 24 h. Thereafter, the obtained homogeneous transparent slightly yellowish coloured membranes were cooled to room temperature and then soaked in deionized water to peel off from the Petri dish and then thoroughly washed with DI water, drying in a vacuum oven at 100 ºC for 12 h. The thickness of the all cast membranes was in the range of 40-50 μm. A schematic presentation of the fabrication steps of these membranes are presented in **Figure 4.1 (c)**.

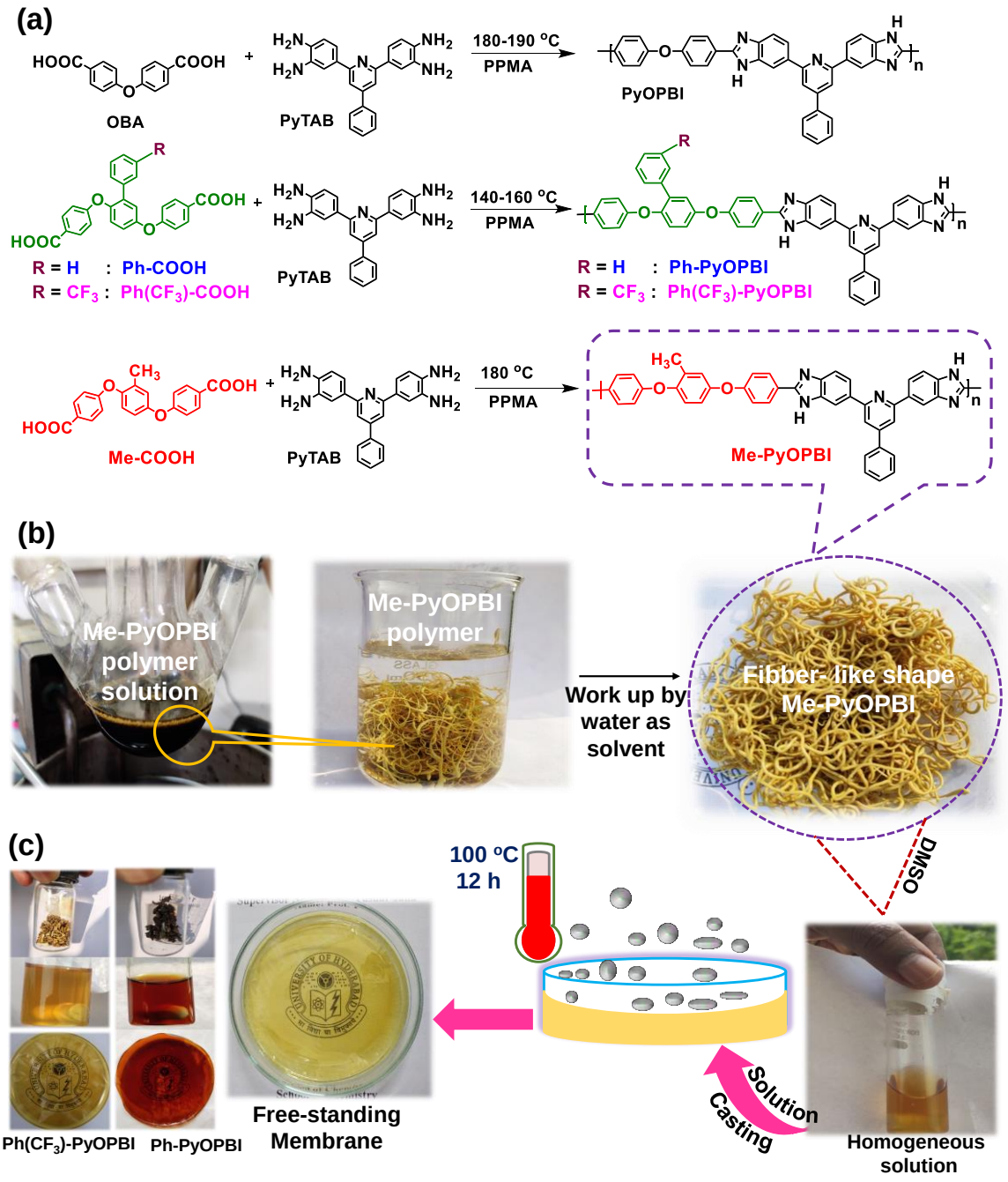

Figure 4.1. (**a**) Reaction schemes for the synthesis of PyOPBI polymers, (**b**) a representative pictorial presentation of polymerization mixture collection and purification process of Me-PyOPBI and (**c**) schematic illustration showing the fabrication of various PyOPBIs membranes by solution casting method. It is to be noted that the colour of the each polymer solutions are quite different and all the polymers formed homogeneous solution.

4.3. RESULTS AND DISCUSSION

4.3.1. Synthesis of aryl ether type PyOPBI polymers and their stability in polar solvents

A significant number of previous studies showed that the polybenzimidazole (PBI) backbone structure has a major influence on the stability of the PBI polymer in phosphoric acid (PA) and the fuel cell performance of PBI based PEM.[40] Generally, it is also noticed that the membrane prepared from high molecular weight PBI displays good thermal, chemical, mechanical stability and also does not get dissolve in concentrated PA readily. However, often high molecular weight PBI tends to show poor solubility and hence preparation of membrane becomes quite difficult. In order to address this concern, recently we synthesized pyridine-bridged PBI (PyPBI) which was obtained by poly-condensing 2, 6-bis (3', 4'-diaminophenyl)-4-phenylpyridine (PyTAB), a tetraamine monomer which was made readily, with varieties of dicarboxylic acids. Several PyPBIs synthesized so far showed good solubility & processability along with very good thermal, mechanical and chemical stabilities.[35-37] However, it was observed that the membranes of PyPBI get dissolved in concentrated (85 %) PA and therefore needs attention. Recently, we addressed this problem by crosslinking the PyPBI chains using BrPPO but this approach hinders the solubility.[38] Therefore, in this work we have synthesized a series of aryl ether based dicarboxylic acids monomers (**Scheme 4.1**) which were further polymerized with PyTAB to get PyOPBIs in order to eliminate the problems as discussed above. The detailed characterizations data of these monomers are given in the experimental section and the all NMR spectra are included in the supporting information Appendix II-**Figure 4.1** and **Figure 4.2**. In order to polymerize these aryl ether based dicarboxylic acid (AEDCA) monomers with PyTAB, we first attempted solution polymerization in polyphosphoric acid (PPA) as a reaction medium. During the polymerization, the sublimation of AEDCA monomers was observed, and the polymerization produced low inherent viscosity (IV) polymers (**Table 4.1)**. The reasons for the low molecular weight (low IV) polymer can be attributed to the low solubility of AEDCA monomers in PPA and the loss in molar ratio between PyTAB and AEDCA caused by the sublimation of the later at the polymerization temperatures (~220 °C) during the polymerization in PPA medium. In order to improve monomer dissolution and reaction rate, additional intermediate temperature polymerization steps were introduced into the polymerization scheme. However, the sublimation of monomer still occurred at higher polymerization temperatures. Considering all these, it was concluded that PPA is perhaps not

a good polymerization solvent for AEDCA monomers as this method failed to yield reasonable high molecular weight PyOPBI for further studies. PPA with added P_2O_5 and PPA with N-methyl-2-pyrrolidone (NMP) were also tested as polymerization solvents and results are similar to that PPA (**Table 4.1**). This study confirmed that PPA is not a suitable medium for AEDCA based PyOPBI polymerization, even with the increase of P_2O_5 content in PPA or the addition of NMP solvent to increase the solubility of the monomers in PPA, we did not observe any improvement in IV values. Another solution polymerization medium was tested in this study is the mixture of P_2O_5 and MSA (PPMA). Eaton et al. proposed PPMA as a convenient alternative to PPA solvent for the synthesis of various polymers.[25, 41] The polymerization of AEDCA based PyOPBI in PPMA was conducted and high molecular weight polymer with the higher inherent viscosity are obtained (**Table 4.1**). After careful optimization of the monomer weight %, reaction time and temperature, the best results obtained with high IV are listed in **Table 4.1** (in last row). A comparison of the reaction condition and the results of **Table 4.1** clearly show that with lower temperature (140-160 °C) and less reaction time (8 h), we could achieve higher IV when PPMA is used as solvent for the polymerization. Therefore, we concluded from our above discussion that the PPMA is the best choice of solvent for AEDCA based PyOPBI polymers.

Table 4.1. Optimization of polymerization conditions to find the suitable solvent in order to make higher IV (molecular weight) aryl ether containing PyOPBI polymers. The IV values of the polymers are written in the parenthesis after the polymer name.

Solvent	Polymerization condition	I.V. (dL/g)
PPA	220 °C, 24 h	Me-PyOPBI (0.17), Ph-PyOPBI (0.14), Ph(CF_3)-PyOPBI) (0.16) and PyOPBI (3.23)
PPA+P_2O_5 [a]	220 °C, 24 h	Me-PyOPBI (0.18), Ph-PyOPBI (0.21), Ph(CF_3)-PyOPBI) (0.23) and PyOPBI (3.13)
PPA+NMP [b]	190 °C, 24 h	Me-PyOPBI (0.16), Ph-PyOPBI (0.19), Ph(CF_3)-PyOPBI) (0.18) and PyOPBI (2.93)
PPMA+ P_2O_5 [c]	140-160 °C, 8 h	Me-PyOPBI (1.59), Ph-PyOPBI (1.93), Ph(CF_3)-PyOPBI) (2.93) and PyOPBI (1.9)

[a] The content of added P_2O_5 was calculated for a PPA concentration of 128 wt%.

[b] N-methyl-2-pyrrolidinone (NMP), the added content was equal to 5 wt% of PPA.

[c] certain amount (~2.5 g) of P_2O_5 was added in the PPMA solution to increase the solubility of monomer in the reaction mixture.

Besides molecular weight, it is well known that the rigid structure and strong intermolecular hydrogen bonding of PBI lead to its poor solubility in organic solvents.[42, 43] However, the dissolution property of PBI can be enhanced by introducing a flexible segment or breaking the intermolecular hydrogen bonding.[44] Solubility tests conducted on the synthesized AEDCA based PyOPBI polymers shows that these polymers can be easily dissolved in common aprotic polar solvents such as NMP, DMSO, and DMAc at room temperature, which is beneficial to producing homogenous self-standing membranes [**Figure 4.1 (c)**]. This good solubility behaviour may be ascribed to the side-chain-type pendent groups and flexible ether bond in PyOPBIs which can enhance the free volume and orientation of the polymer main chains leading to the wider hydrophilic channels in pendant-type PyOPBI, causing in the easy diffusion of solvents between main chains. Therefore, transparent membranes can be fabricated in a mild condition. Therefore, the combination of simple monomer structure, synthetic scalability, relatively easy and excellent solvent solubility made the AEDCA (pendant-type) PyOPBIs promising polymers for making HT-PEM.

4.3.2. Spectroscopic characterization of PyOPBIs

The ATR-FTIR spectra of all the aryl ether based PyOPBI membranes are shown in **Appendix II-Figure 4.3**. Important characteristic stretching bands of PBI structure denoted by dotted lines, are clearly visible in the spectra and these stretching bands have been discussed in many literature previously.[35, 45] The IR stretching bands centred at around 3620 and 3415-3210 cm^{-1} assigned to O-H stretching of physically adsorbed moisture and the stretching vibration of the imidazole N-H group, respectively. The other characteristic bands of benzimidazole polymers appears at around 1596, 1476, and 901 cm^{-1} are because of C=C/C-N, in-plane benzimidazole ring deformation and C-H stretching vibration of the pyridine ring, respectively. Additionally, a prominent band centred at 1165 cm^{-1} corresponded to the Ar-O-Ar linkage demonstrating the successful synthesis of aryl ether containing PyOPBIs. In addition, the characteristic bands of methyl groups are found at around 2960~2840 cm^{-1} in the Me-PyOPBI membrane. Therefore FT-IR characterization demonstrates the chemical structures of the bulky aryl ether containing PyOPBI polymers.

Furthermore, the synthesized polymers chemical structural confirmation was carried out by the multinuclear (^{1}H, ^{13}C, and ^{19}F) NMR spectroscopic techniques. The ^{1}H NMR spectra of Me-PyOPBI, Ph-PyOPBI and Ph(CF_3)-PyOPBI as well as PyOPBI are displayed along with their chemical structure and the peak assignments in **Figure 4.2**. The peaks are matching with the expected chemical structure of the polymers. The chemical shift of the characteristic imidazole -NH proton of all these polymers is centred at δ 13.36 ppm. All other chemical shifts of aromatic protons appear around at δ 7.0-8.61 ppm. Aromatic region proton chemical shifts are also different from polymer to polymer due to their different chemical environments as depicted in peak assignments in **Figure 4.2**. In the case of Me-PyOPBI spectrum, one additional downfield signal at 2.1 ppm is observed compared to other polymers which is attributed to the protons of the methyl group. The ^{13}C NMR spectra of these polybenzimidazoles is shown in **Appendix II-Figure 4.4** along with their polymer repeating units and peak assignment. The ^{13}C NMR spectra is also in good agreement with the predicted chemical structure of all the polymers. The chemical shift of the characteristic imidazole carbon peak of all these polymers are centred at δ 152.6 ppm indicated successful imidazole ring formation.[46, 47] Also the ^{19}F NMR spectrum (**Appendix II-Figure 4.5**) of Ph(CF_3)PyOPBI polymers shows a strong peak at –61.12 for the CF_3 functionality. Together all the spectral characterizations undoubtedly proof the formation of aryl ether linked PyOPBIs.

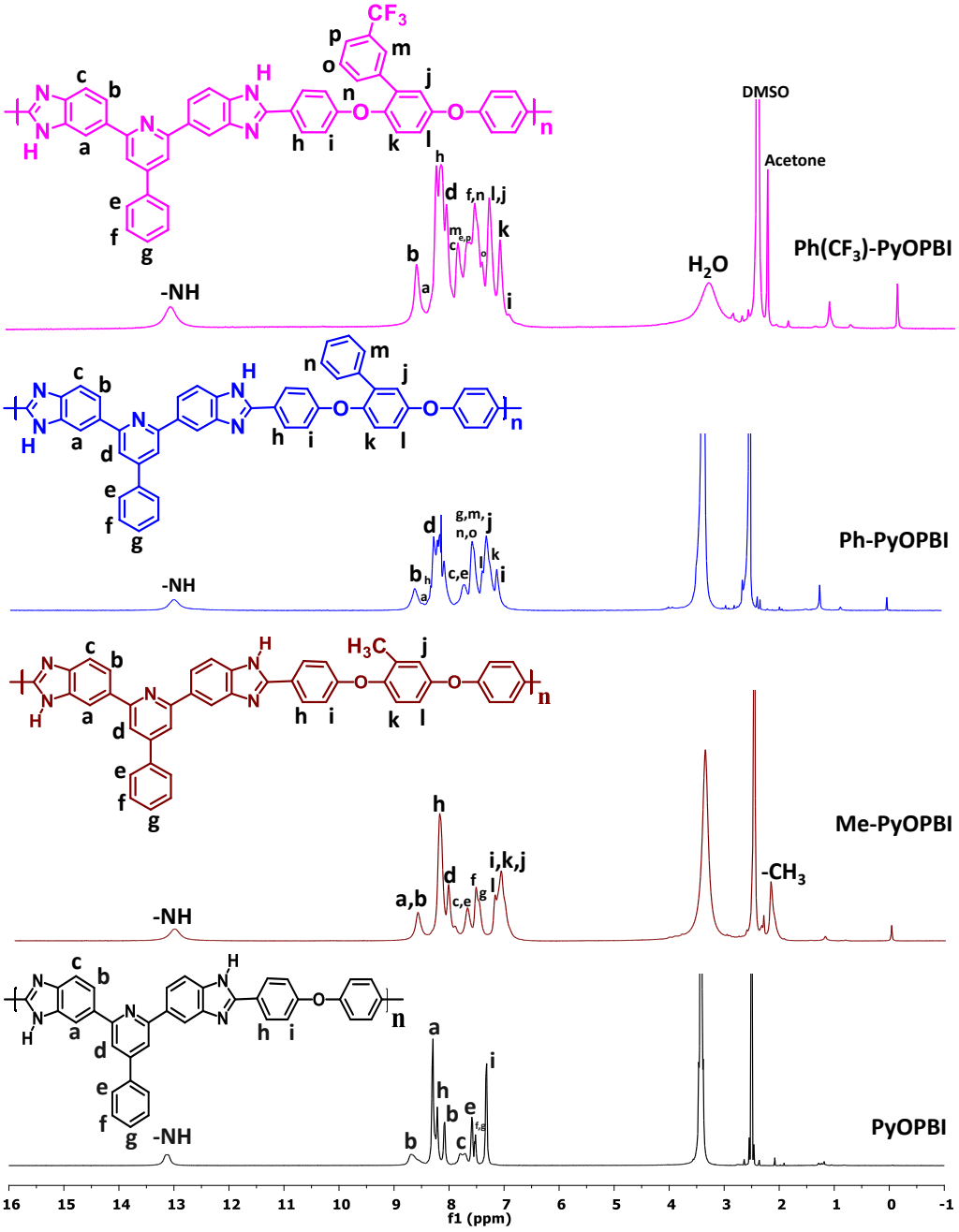

Figure 4.2. ^{1}H NMR spectra of PyOPBI, Me-PyOPBI, Ph-PyOPBI and Ph(CF_3)-PyOPBI recorded in DMSO-d_6.

4.3.3. Impact of pendant-type molecular architecture of arylether linked PyOPBIs on the stability in PA

PBI membranes of good PA stability is required for HT-PEMFC application in view of the high concentration of PA (>85%) and mechanical stress imposed during the fuel cell

assembly and operation processes. In order to verify the stability of the aryl ether linked PyOPBIs, which have pendant-type structure as discussed in earlier sections, the synthesized PyOPBI samples were immersed in the 85% PA solution at 100 °C for 3 days. **Figure 4.3** reveals that the PyOPBI membrane was completely dissolved in PA solution within 1 h whereas other pendant-type PyOPBI membranes did not exhibit any significant changes in PA solution. This can be clearly realized from the pictures of the membranes before and after soaking for 3 days at 100 °C as seen from **Figure 4.3 (a)** and **(b)**, respectively. We also recorded the weight loss of the membranes after three days of PA soaking and plotted them in **Figure 4.3 (c)** as a remaining weight for each of these membranes. The weight loss data clearly show that there is zero (negligible) remaining weight in case of PyOPBI but for all other pendant type PyOPBI between 83% to 97% remaining weights are present even after 3 days treatment in PA at 100 °C. The maximum weight remains in case of Ph(CF_3)-PyOPBI membrane. All these results indicated that the introduction of flexible unsymmetrical bulky pendants-type structure in the backbone of PyOPBI greatly enhances the backbone stability of newly designed PyOPBI polymer (Me-PyOPBI, Ph-PyOPBI and Ph(CF_3)-PyOPBI) membranes. Particularly Ph(CF_3)-PyOPBI, weight loss upon exposure to PA is less than 3% indicating significant increment of stability owing to the pendant trifluoro methyl groups connected to the meta-position of phenyl ring of PyOPBI.

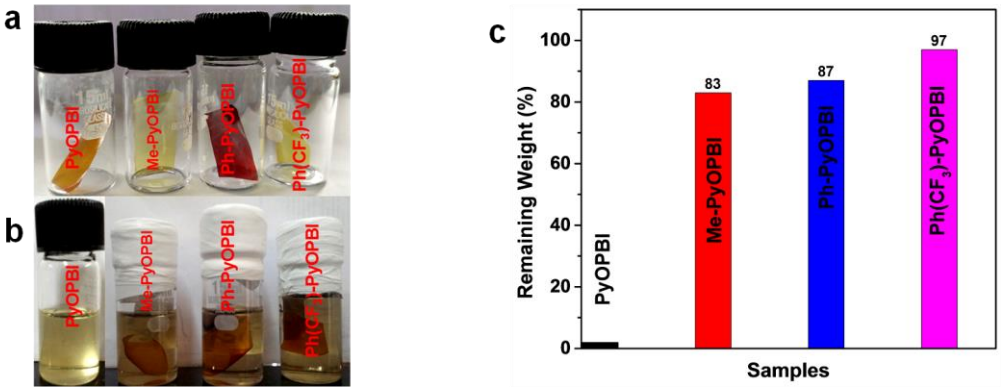

Figure 4.3. Photographs of the membranes before (a) and after (b) the solubility test and membranes remaining weight (c) after the solubility test soaked in PA at 100 °C for 72 h.

4.3.4. Thermal Stability

Good thermal stability of PEM is an essential requirement for long-lifetime (durability) of PEM in the fuel cell when the operating temperature is above 150 °C. The thermal stabilities

of the undoped and the PA-doped PyOPBI membranes were investigated by thermogravimetric analysis (TGA), performed from room temperature to 700 °C under nitrogen atmosphere, and the results are presented in **Appendix II-Figure 4.6**.The TGA thermogram of undoped membranes [**Appendix II-Figure 4.6 (a**)] display clear three steps weight losses below 700 ^{o}C. The initial weight loss region started from 80 °C to 150 °C, which can be attributed to the loss of both physically absorbed moisture and hydrogen-bonded water in the membranes. While the second weight loss region began at around 220-350 °C corresponds to the evaporation of residual DMAc solvent bonded to PyOPBI molecular chains and the third weight loss started from 500 °C is corresponding to the main chain degradation of the PyOPBI polymers.[37] Overall, thermal stability clearly shows the dependence on the structure of the polymers. The pedant type structure clearly increases the thermal stability of the PyOPBIs and the highest stability is shown by Ph(CF_3)PyOPBI polymer owing to the presence of bulky trifluoro group in the backbone. As a result of PA-doping, the thermal behaviour of PyOPBI membranes changed when compare with undoped membranes [see **Appendix II-Figure 4.6 (b)**]. The initial weight loss at 120 ºC is due to the physically adsorbed water molecules onto PyOPBI membranes. Another weight loss from 200 ºC to 400 ºC is observed and assigned to the formation of pyrophosphoric acid and higher-ordered phosphate species at a higher temperature.[48] From these results, it can be concluded that all the synthesized PyOPBI membranes meet the thermal stability requirements for the use in HT-PEMFC.

4.3.5. Morphology of the membranes

FE-SEM images of the cryo-fractured cross-section of membranes were imaged and shown in **Appendix II-Figure 4.7**. It should be noted that the PEM properties of PBI considerably depend on the internal micromorphology.[38] All the membranes exhibited significant change in morphologies compared to the PyOPBI membrane. In pendant-type polymeric membranes, spongy support structures with voids in the membranes are clearly visible which are completely absent in case of PyOPBI. This spongy support feature is more visible in Ph(CF_3)-PyOPBI, which was advantageous to the properties of the membrane, such as proton transportation, mechanical property, stability, and so on.

4.3.6. Oxidative stability

During the electrochemical operation of HT-PEMFC, the PEM is subjected to attack by hydroxyl (OH·) and hydroperoxyl (OOH·) free radicals which causes the membranes degradation.[49] Therefore, the chemical stability, often called as oxidative stability, of the membrane is a key parameter to determine the long-term stability of the PEM. Fenton's test is the well-known method for assessment of the chemical stability of PEM. In this work, Fenton's test was conducted by subjecting the membranes of the similar size in 3% H_2O_2 solution containing 4 ppm $FeSO_4$ at 70 °C for 6 days. The detail of the procedure is explained in the supporting information. The remaining weight loss of samples was recorded as a function of time and shown in **Figure 4.4**. All three unsymmetrical pendant-type PyOPBIs show no substantial weight loss during the six days of the degradation experiment in comparison to PyOPBI. This may be due to the impact of bulky side groups (aryl, methyl and trifluoromethylphenyl) in the main chain of PyOPBI polymers. Among them, the Ph(CF_3)-PyOPBI polymer based membrane degradation is the lowest. This slower rate of degradation of Ph(CF_3)-PyOPBI membrane is related to the less hygroscopic nature of trifluoro moieties polymer and intramolecular/inter chain interaction because of the presence of highly electronegative fluoride. As such, the adding of electron withdrawing groups to phenyl rings appears to enhance their chemical stability by lowering their rate of reaction with HO·radicals. Hence, the results indicate that the as prepared unsymmetrical pendant-type PyOPBI membranes are comparatively more oxidatively stable even in a drastic chemical environment than symmetrical PyOPBI.

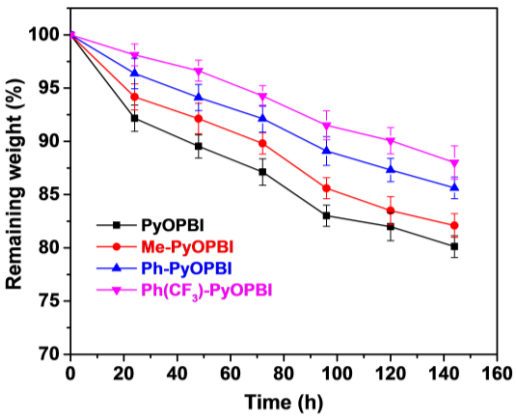

Figure 4.4. Oxidative stability of PyOPBI, Me-PyOPBI, Ph-PyOPBI and Ph(CF_3)-PyOPBI membranes in 3% H_2O_2 containing 4 ppm Fe^{2+} at 70 °C.

4.3.7. Membrane thermomechanical properties

Dynamic mechanical analysis (DMA) measurements were conducted to study the various thermomechanical characteristics of these synthesized arylether-linked polymer membranes when they are deformed under a periodic stress and the temperature dependent results are obtained for storage modulus, loss modulus and tan δ which are represented in Appendix II-**Figure 4.8**. The storage modulus (*E'*) of arylether-linked PyOPBI membranes at different temperatures are extracted from **Appendix II-Figure 4.8 (a)** are shown in **Table 4.2**. The storage moduli values decrease at around 250 ^{o}C owing to the increased segmental motion of the polymer backbone and gradually decrease further with increasing temperature attributing that mechanical strength becomes poorer at higher temperatures. Nevertheless, all the polymer membranes showed good storage moduli values at temperatures less than 350 ^{o}C. **Appendix II-Figure 4.8 (a)** clearly displays that Ph(CF_3)-PyOPBI polymer shows significantly higher storage moduli than that of all other PyOPBI membranes. It could be because of the presence of bulky trifluoromethyl groups which hinder segmental motions of the polymeric chains.

The T_g of all the samples were measured from loss modulus (*E''*) and tan δ plots and the values are tabulated in **Table** 4.**2**. Both *E''* and tan *δ* plots exhibits a well-defined relaxation peak above 340 ^{o}C which is assigned to the molecular-scale segmental motion during the glassy to rubbery transition. The T_g value varies greatly as the structure of the PyOPBI backbone alters indicating the strong influence of the pendant structure of the polymer. The glass transition temperature of Ph(CF_3)-PyOPBI polymer membrane displays highest T_g value (410 °C) which is significantly higher than all other PyOPBI derivatives and this might be due to interaction between the bulky trifluoromethyl group and the –N= of the imidazole moiety of the PyOPBI backbone. Again, it is distinctly clear that T_g value depends on the type of diacid structure was used to make the PyOPBI polymers. Similar trend of T_g values can also be seen from the tan *δ* data.

Table 4.2. Various thermomechanical data and glass transition temperatures of PyOPBI membranes extracted from DMA analysis.

Samples	E' (MPa) at 100 °C	E' (MPa) at 400 °C	T_g (°C) from E''	T_g (°C) from tan δ
PyOPBI	3195	1520	311	348
Me-PyOPBI	3771	2646	351	364
Ph-PyOPBI	3420	2125	328	352
Ph(CF_3)-PyOPBI	6137	1560	391	410

4.3.8. Water uptake and swelling ratio of the membranes

It is widely known that polybenzimidazole is a hygroscopic polymer and it has high affinity to form stronger intermolecular interactions with water molecules which severely influences the dimensional stability of the membrane.[35-37] After immersing the membranes in distilled water for 3 days, we observed that the amount of water uptake (WU) of PyOPBI, Me-PyOPBI, Ph-PyOPBI and Ph(CF_3)-PyOPBI membranes is 13.21, 17.01, 20.55 and 16.56 wt % , respectively (**Appendix II-Figure 4.9**). It is quite evident from the data that the introduction of pendant type side groups in PyOPBI backbone has increased the WU, however Ph(CF_3)-PyOPBI displays the least WU among the pendant type polymers due to the hydrophobic nature owing to the presence of trifluoro functionality in the polymer backbone. The swelling ratio values shown in **Appendix II-Figure 4.9** also follow similar trend like WU. Hence both WU and SR measurements clearly demonstrate the effect of pendant type structure of PyOPBI in comparison to pristine PyOPBI.

4.3.9. Phosphoric acid loading and swelling of the membranes

The membranes need to be loaded with phosphoric acid (PA) to achieve proton conductivity which is the essential requirement for PEMFC applications. The transport of protons is accomplished by dissociation of the phosphoric acid molecules and hence the PA loading/doping level, often called as acid doping level (ADL), determines the proton conductivity of the PEMs. However, excess PA-loading often leads to compromised mechanical properties of the membrane and also interferes membrane properties between two

catalyst layers in the MEA which is detrimental to the fuel cell performance. All the newly synthesised PyOPBI membranes were immersed in 85 wt % PA solution at room temperature for a duration of 3 days for PA loading, whereas PyOPBI membrane was soaked in 60 wt% PA as in higher PA concentration (>60%) the PyOPBI membrane loses mechanical integrity. The acid doping level, which is expressed as PA moles per PBI repeat unit, for all the membranes as a function of doping time is shown in **Figure 4.5 (a)**. The data clearly show that the pendant type PyOPBI membranes load more PA than the PyOPBI. It is also to be noted that all the membranes absorb PA very fast at the beginning and then slowly saturates. After doping for 72 h, ADL (PA uptake in weight %) of Me-PyOPBI, Ph-PyOPBI and Ph(CF_3)-PyOPBI membranes reach 16.04 (382 wt%), 18.20 (410 wt%) and 22.18 (492 wt%), respectively, which are much higher than that of PyOPBI [~12 (298 wt%)] membrane. This is because of the formation of entangled polymer networks owing to the presence of flexible ether linkages which might have enabled the entanglement between molecular chains. Also, the interactions of imidazole and pyridine groups will be helpful to form a stable framework. The side groups with large steric hindrance will disrupt the close polymer chain packing and reduce molecular chain packing density, to increase the "free volume" in the supposed "sponge-like" structure in the pendant-type PyPBIs backbone and hence facilitated absorption of more PA compared to conventional PyOPBI. The highest PA loading is around 20 moles of PA/PBI in case of Ph(CF_3)-PyOPBI which is in agreement with the PA swelling data as discussed in the proceeding section. This result is not unexpected, as pyridine and fluorinated based polymers are known to undergo a higher rate of dynamic hydrogen bonding ability with imidazole and acid molecules.[50] The swelling ratio and swelling volume were also measured and plotted against doping time [**Figure 4.5(b), Appendix II-Figure 4.10**]. Swelling data is consistent with PA loading data as it is expected that higher the PA loading pushes the membrane to swell more.

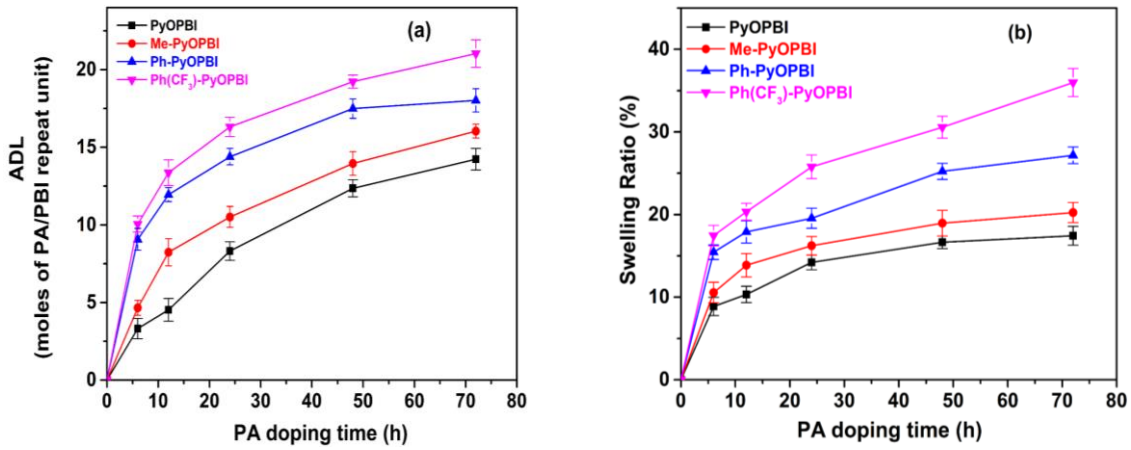

Figure 4.5. Acid doping level (ADL) (**a**) and swelling ratio (**b**) of PyOPBI and pendant-type PyPBI membranes as a function of doping time. Each data points are the average of three independent measurements. ADL is measured as PA moles per PBI repeat unit.

4.3.10. Proton conductivity

Proton conductivity of the PEMs is influenced by several factors such as ADL, polymer structure, PA retention, etc. and this is the most important parameter required to have for the development of efficient PEMFC. Proton conductivity of PyOPBI type PEMs has been reported between 0.001-0.01 S cm^{-1} at 160 °C.[35-37] In the present study, we compare the effect of chemically different monomer units on the proton conductivity of PyOPBI type membranes. Prior to the measurements, the conventional PyOPBI membrane was soaked in 60 wt % PA and all the other synthesized PyOPBIs (Me-PyOPBI, Ph-PyOPBI and Ph(CF_3)-PyOPBI) membranes were soaked in 85 wt % PA for 72 h and dried in oven at 120 °C for 2 h before putting into the alternating current (AC) impedance assembled test cell. The temperature-dependent conductivity of PA-doped membranes are calculated from Nyquist plots (see **Appendix II-Figure 4.11**) at wide temperature range (30 to 180 °C). As described in **Figure 4.6 (a)**, all the PEMs show significant enhancement in proton conductivity as a function of temperature. The conductivity values are 0.078, 0.066 and 0.041 S cm^{-1} at 180 °C in Ph(CF_3)-PyOPBI) Ph-PyOPBI and Me-PyOPBI, respectively. Whereas the proton conductivities of PyOPBI is only 0.007 S cm^{-1} at 180 °C, which is much lower than that of all other pedant type PyOPBI polymers. We believe that the reasons for such high proton conductivity of pendant type polymers are multiple and these are firstly, there are abundant hydrogen bond acceptors (oxygen and nitrogen atoms in the backbone of polymer and trifluoromethyl groups on the chains of polymer, etc.) in Me-PyOPBI, Ph-PyOPBI and Ph(CF_3)-PyOPBI. Secondly, the

strong intermolecular interactions between polymer imidazole units makes the movement of protons facile and more active, which will efficiently increase the proton transfer capacity. The noticeable difference in proton conductivity values suggests that more facile proton transfer pathways are formed among flexible asymmetric bulky arylether containing PyOPBIs-H_3PO_4 adducts than simple PyOPBI owing to the close connection of proton donor (acid group) and acceptor (base group).

In order to understand the conducting mechanism of proton transport in the membranes, we plotted conductivity data using the Arrhenius equation [**Figure 4.6 (b)]** to calculate the activation energy values (E_a) for the proton conduction of all the PA-doped membranes. The calculated activation energies of the PyOPBI, Me-PyOPBI, Ph-PyOPBI, and Ph(CF_3)-PyOPBI membranes are found as 12.71, 13.25, 13.38, and 15.38 kJ mol^{-1}, respectively. These E_a data and the nature of the plots indicate that the proton conduction is mainly follow the Grotthuss conduction mechanism.[51-53] Hence from the above discussion, it is amply clear the impact of bulky pendant side groups on proton conductivity and on proton transfer rate.

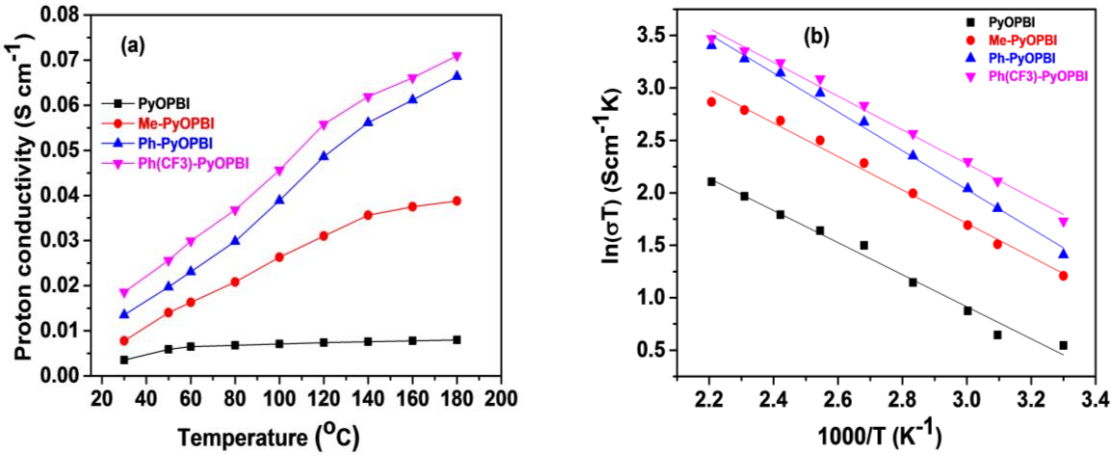

Figure 4.6. Proton conductivity of PA-doped PyOPBI membranes as a function of temperature in non-humidification environment **(a)** and Arrhenius plots of the proton conductivity data in order to find out the activation energy of the PA-doped Py-OPBI membranes **(b)**.

4.3.11. Phosphoric acid retention and proton conductivity stability

During the operation of HT-PEM fuel cell, the phosphoric acid-doped PEMs frequently suffer from acid leaching. In order to test the phosphoric acid retention ability of the PEMs, the acid leaching test was performed with the PA doped membranes by exposing them to water vapour at 100 °C for a period of 3 h and measuring the remaining weight after every 30 minutes.

It was found that all the membranes exhibit a noticeable decrease in weight in the initial 1 h, which is attributed to the discharge of free water and acid molecules from the membranes and then slowly saturates [**Figure 4.7 (a)**]. It is very much clear from this data that the decrease in weight has a strong influence on the polymer structure-the lease weight loss is observed in case of Ph(CF_3)-PyOPBI and the maximum is observed for PyOPBI. The data clearly confirm that the presence of pendant groups in the backbone improves the acid retention capacity of the membrane. It is worth to note that among the all membranes, Ph(CF_3)-PyOPBI polymer absorbed more PA **(Figure 4.5)** and less PA leaches out from the membrane and this may be due to interaction between Ph(CF_3) and PA molecules.

The long-term stability of proton conduction is a major requirement for the practical application of PEM materials. The proton conductivity data of all the PA-doped membranes were recorded at 160 °C after every 2 h interval over 72 h to simulate the PEMs real operating environment. Notably, the proton conductivity values remain constant during the measurements except the initial loss which is because of the loss of water [**Figure 4.7 (b)**]. This results indicate the good durability of the membrane. Even after initial decrease in proton conductivities of these membranes, the conductivities of the Ph(CF_3)-PyOPBI, Ph-PyOPBI and Me-PyOPBI membranes are greater than that of PyOPBI due to their better acid and water retention ability at high temperature, which suggests that the incorporation of flexible ether linkages and asymmetric bulky pendants with polymer backbone would effectively improve the stability and durability of membranes and make them promising candidates for HT-PEMs.

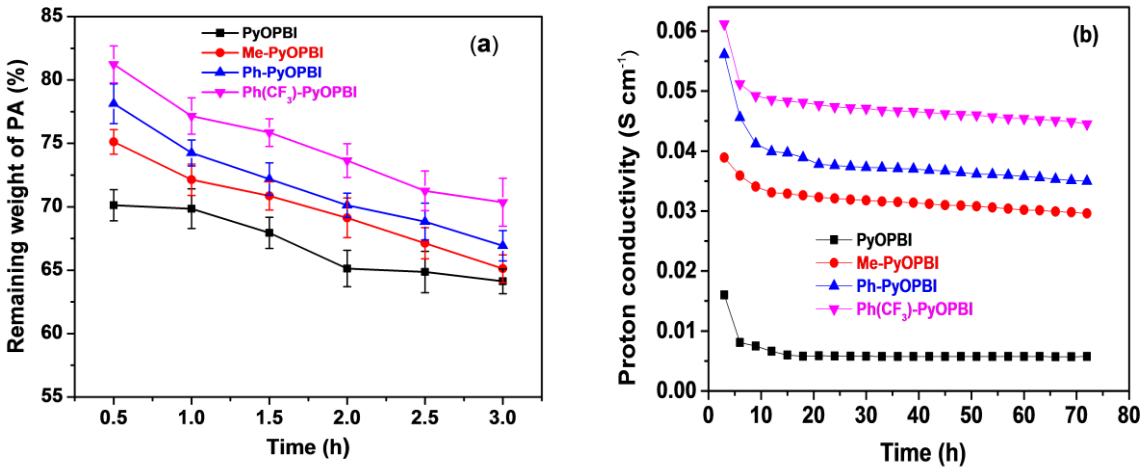

Figure 4.7. The PA stability of the membranes under the water vapour at ~100 °C **(a)** and conductivity stability of the membranes at 160 °C without humidification **(b)**.

4.3.12. Fuel cell performance

The fuel cell performances of all the PA-doped membranes were measured at 160 °C using H_2 and O_2 gas without any humidification. **Figure 4.8** represents the cell performance (polarization and power density curves) data of the membrane electrode assembly (MEA) made from the PEMs of PyOPBIs which are developed in this study. The Ph-PyOPBI, Ph(CF_3)-PyOPBI and Me-PyOPBI membranes show much improved fuel cell performances compared to PyOPBI. This observation is attributed to their superior trade-off between proton conductivity, dimensional stability and good mechanical behaviours. The open circuit voltages (OCV) of all PEMs are above than 0.91V indicating their sluggish fuel gas permeability through the membrane.[54] The peak power density of 93.45 $mW \cdot cm^{-2}$ at a cell voltage of 0.3 V with a current density of 254.5 mA cm^{-2} is obtained for PyOPBI membrane-based MEA. In comparison, the pendant-type PyOPBIs: Ph-PyOPBI, Ph(CF_3)-PyOPBI and Me-PyOPBI, polymer membranes show much better fuel cell performance than that of PyOPBI membrane. Notably, among all the samples, the Ph(CF_3)-PyOPBI membrane-based MEA shows the highest peak power density (PPD) of 240.02 $mWcm^{-2}$ at a voltage of 0.3 V with the current density of 629.5 mA cm^{-2} which is a gain of ~47% in power density than PyOPBI. This improvement of power density is probably due to the enhancement of ADL of the membranes and higher catalytic activity at the electrodes and the high conductivity of the PEM.[16] After the fuel cell test, the single cells were disassembled and the tested membranes were taken out. The PyOPBI membrane exhibited visible mechanical damage between the active area and the clamps **(Appendix II-Figure 4.12)** owing to the low acidic stability of polymer structure that can lead to scission of the polymer main chain. Whereas, the pendant-type structure based PyOPBI membranes such as Ph(CF_3)-PyOPBI did not show any mechanical damage even after completion of the fuel cell test **(Appendix II-Figure 4.12)**. Overall, to achieve an acceptable fuel cell performance is still a challenge, we are improving in our future efforts by optimizing operating parameters such as catalysts, carbon paper thickness, ionomer binder development, operating temperature and MEA fabrication.

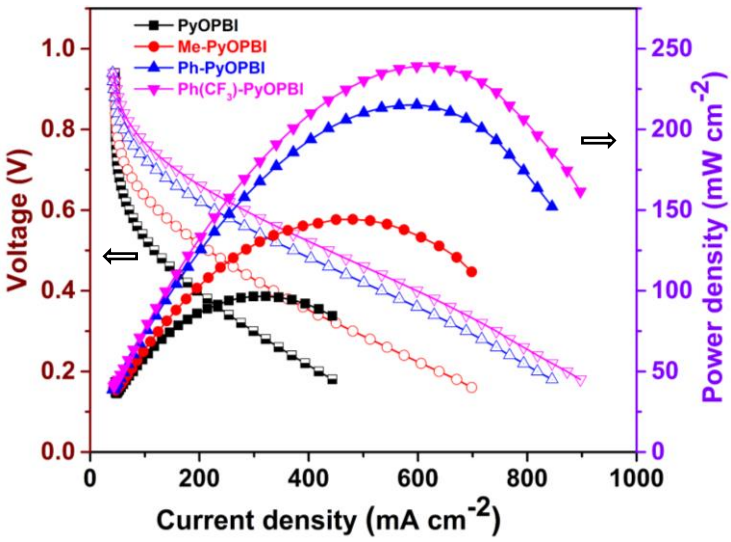

Figure 4.8. HT-PEMFC performance of PA doped PyOPBI, Me-PyOPBI, Ph-PyOPBI and Ph(CF_3)-PyOPBI membranes at 160 ^oC without humidification.

4.4. CONCLUSION

In summary, we demonstrated an innovative approach for the synthesis of novel PBIs structure in a simpler and scalable process. The approach successfully synthesized the pendant-type diacid based PyOPBIs with reaction time less then10 h. We have also explored different solvent mixtures for the identification of a solvent mixture, phosphorous pentoxide/methane sulfonic acid (PPMA) that is found to be the best choice for the synthesis of high molecular weight PyOPBI with ease. The pendant type PyOPBI is found to have much higher acid stability than the conventional PyOPBI. The PEMs obtained from these pendant-type PyOPBIs are found to have much superior physical properties such as thermal, mechanical, acid loading, acid leaching, oxidative stability and more importantly higher proton conductivity than the conventional PyOPBI. In addition the pedant type PyOPBI resulted much higher cell performance than PyOPBI indicating that the insertion of bulky groups in the backbone is indeed helpful. Therefore, we believe that appropriate structural modulation of the PBIs is utmost important in tuning the physical properties of the PBI and also in improving the PEM performance of this type polymer.

Appendix II

^{1}H and ^{13}C NMR spectrums of diacid monomers. FT-IR and ^{13}C NMR spectra of the synthesized PyOPBIs and TGA curves, FESEM cross-section morphology and Thermomechanical properties of pendant-type PyOPBIs are included in the Appendix II (page no. 151-161).

REFERENCE

(1) Armaroli, N.; Balzani, V. *Angew. Chem., Int. Ed*. **2007**, 46, 52−66.

(2) Peighambardoust, S. J.; Rowshanzamir, S.; Amjadi, M. *Int. J. Hydrog. Energy* **2010,** *35*, 9349-9384.

(3) Devanathan, R. *Energy Environ. Sci.* **2008,** 1, 101-119.

(4) Jacobson, M. Z.; Colella, W. G.; Golden, D. M. *Science* **2005**, 308, 1901−1905.

(5) Wang, Y.; Chen, K. S.; Mishler, J.; Cho, S. C.; Adroher, X. C. *Applied Energy* **2011,** 88, 981-1007.

(6) Farooqui, U. R.; Ahmad, A. L.; Hamid, N. A. *Renew. Sust. Energ. Rev*. **2018**, 82, 714-733.

(7) Park, C. H.; Lee, S. Y.; Hwang, D. S.; Shin, D. W.; Cho, D. H.; Lee, K. H.; Kim, T.-W.; Kim, T.-W.; Lee, M.; Kim, D. S.; Doherty, C. M.; Thornton, A. W.; Hill, A. J.; Guiver, M. D.; Lee, Y. M. *Nature* **2016**, 532, 480-483.

(8) Liu, B.; Guiver, M. D. Wiley, Chichester: **2012**.

(9) Zhang, H.; Shen, P. K. *Chem. Rev*. **2012**, 112, 2780-2832

(10) Kusoglu, A.; Weber, A. Z. *Chem. Rev*. **2017**, 117, 987−1104.

(11) Katzenberg, A.; Chowdhury, A.; Fang, M.; Weber, A. Z.; Okamoto, Y.; Kusoglu, A.; Modestino, M. A. *J. Am. Chem. Soc.* **2020,** 142, 3742-3752.

(12) Bazylak, A. *Int. J. Hydrog. Energy* **2009,** 34, 3845-3857.

(13) Li, Q.; He, R.; Jensen, J. O.; Bjerrum, N. J. *Chem. Mater*. **2003**, 15, 4896− 4915.

(14) Bose, S.; Kuila, T.; Nguyen, T. X. H.; Kim, N. H.; Lau, K. T.; Lee, J. H. *Prog. Polym. Sci.* **2011**, 36, 813−843.

(15) Yu, S.; Benicewicz, B. C. *Macromolecules* **2009**, 42, 8640-8648.

(16) Aili, D.; Yang, J.; Jankova, K.; Henkensmeier, D.; Li, Q. *J. Mater. Chem. A* **2020,** 8, 12854-12886.

(17) Berber, M. R.; Nakashima, N. *ACS Appl. Mater. Interfaces* **2019**, 11, 46269-46277.

(18) Aili, D.; Henkensmeier, D.; Martin, S.; Singh, B.; Hu, Y.; Jensen, J. O.; Cleemann, L. N.; Li, Q. *Electrochem. Energy Rev.* **2020**, 1-53.

(19) Chen, X.; Qian, G.; Molleo, M. A.; Benicewicz, B. C.; Ploehn, H. J. *J. Polym. Sci., Part B: Polym. Phys.* **2015**, 53, 1527−1538.

(20) Liao, J.; Li, Q.; Rudbeck, H.; Jensen, J. O.; Chromik, A.; Bjerrum, N.; Kerres, J.; Xing, W. *Fuel Cells* **2011**, 11, 745−755.

(21) Xiao, L.; Zhang, H.; Scanlon, E.; Ramanathan, L.; Choe, E.-W.; Rogers, D.; Apple, T.; Benicewicz, B. C. *Chem. Mater.* **2005,** 17, 5328-5333.

(22) Fang, J.; Lin, X.; Cai, D.; He, N.; Zhao, J. *J. Membr. Sci*. **2016**, 502, 29−36.

(23) Xiao, L.; Zhang, H.; Jana, T.; Scanlon, E.; Chen, R.; Choe, E. W.; Ramanathan, L.; Yu, S.; Benicewicz, B. *Fuel Cells* **2005,** 5, 287-295.

(24) Guan, Y.; Pu, H.; Jin, M.; Chang, Z.; Modestov, A. *Fuel Cells* **2012,** 12, 124-131.

(25) Li, X.; Ma, H.; Shen, Y.; Hu, W.; Jiang, Z.; Liu, B.; Guiver, M. D. *J. Power Sources* **2016**, 336, 391-400.

(26) Ueda, M.; Sato, M.; Mochizuki, A. *Macromolecules* **1985,** 18, 2723-2726.

(27) Li, X.; Ma, H.; Wang, H.; Zhang, S.; Jiang, Z.; Liu, B.; Guiver, M. D. *RSC Advances* **2015,** 5, 53870-53873.

(28) Wang, L.; Wu, Y.; Fang, M.; Chen, J.; Liu, X.; Yin, B.; Wang, L. *J. Membr. Sci.***2020,** 602, 117981.

(29) Litt, M.; Ameri, R.; Wang, Y.; Savinell, R.; Wainwright, J. *Mater Res Soc Symp Proc* **1998,** 548.

(30) Chaudhari, H. D.; Illathvalappil, R.; Kurungot, S.; Kharul, U. K. *J. Membr. Sci.* **2018,** *564*, 211-217.

(31) Nayak, R.; Sundarraman, M.; Ghosh, P. C.; Bhattacharyya, A. R. *Eur. Polym. J.* **2018**, 100, 111-120.

(32) Bhadra, S.; Kim, N. H.; Lee, J. H. *J. Membr. Sci.* **2010**, 349, 304-311.

(33) Quartarone, E.; Angioni, S.; Mustarelli, P. *Materials* **2017**, 10, 687.

(34) Molleo, M.; Chen, X.; Ploehn, H. J.; Fishel, K.; Benicewicz, B. C. *Fuel Cells* **2014**, 14, 16-25.

(35) Maity, S.; Jana, T. *Macromolecules* **2013**, 46, 6814−6823.

(36) Maity, S.; Jana, T. *Polym. Int* **2015,** 64, 530-540.

(37) Sana, B.; Jana, T. *Polymer* **2018**, 137, 312−323.

(38) Harilal; Nayak, R.; Ghosh, P. C.; Jana, T. *ACS Appl. Polym. Mater*. **2020,** 2, 3161-3170.

(39) Maglio, G.; Palumbo, R.; Tortora, M.; Vignola, M. C. *Polym. Adv. Technol* **1996**, *7* (5-6), 385-392.

(40) Yang, J.; Cleemann, L. N.; Steenberg, T.; Terkelsen, C.; Li, Q.; Jensen, J. O.; Hjuler, H.; Bjerrum, N. J.; He, R. *Fuel Cells* **2014,** *14* (1), 7-15.

(41) Eaton, P. E.; Carlson, G. R.; Lee, J. T. *J. Org. Chem.* **1973**, 38, 4071-4073.

(42) Sh Shogbon, C. B.; Brousseau, J.-L.; Zhang, H.; Benicewicz, B. C.; Akpalu, Y. A. *Macromolecules* **2006,** 39, 9409-9418.

(43) Sannigrahi, A.; Arunbabu, D.; Sankar, R. M.; Jana, T. *Macromolecules* **2007,** 40, 2844-2851.

(44) Ghosh, S.; Sannigrahi, A.; Maity, S.; Jana, T. *J. Phys. Chem.B* **2010,** 114, 3122-3132.

(45) Deimede, V.; Voyiatzis, G.; Kallitsis, J.; Qingfeng, L.; Bjerrum, N. *Macromolecules* **2000,** 33, 7609-7617.

(46) Conti, F.; Willbold, S.; Mammi, S.; Korte, C.; Lehnert, W.; Stolten, D. *New J. Chem.* **2013,** 37, 152-156.

(47) Cattaneo, A. S.; Villa, D. C.; Angioni, S.; Ferrara, C.; Quartarone, E.; Mustarelli, P. *J. Phys. Chem. C* **2015,** 119, 18935-18944.

(48) Aihara, Y.; Sonai, A.; Hattori, M.; Hayamizu, K. *J. Phys. Chem. B* **2006,** 110, 24999-25006.

(49) Chang, Z.; Pu, H.; Wan, D.; Liu, L.; Yuan, J.; Yang, Z. *Polym. Degrad. Stab*. **2009**, 94, 1206–1212.

(50) Yang, J.; Xu, Y.; Zhou, L.; Che, Q.; He, R.; Li, Q. *J. Membr. Sci.* **2013**, 446, 318-325.

(51) Agmon, N. *Chem. Phys. Lett*. 1**995**, 244, 456−462.

(52) Vilčiauskas, L.; Tuckerman, M. E.; Bester, G.; Paddison, S. J.; Kreuer, K.-D. *Nat. Chem*. **2012**, 4, 461–466.

(53) Melchior, J.-P.; Majer, G.; Kreuer, K.-D. *Phys. Chem. Chem. Phys*. **2017**, 19, 601−612.

(54) Marrony, M.; Barrera, R.; Quenet, S.; Ginocchio, S.; Montelatici, L.; Aslanides, A. *J. Power Sources* **2008**, 182, 469-475.

Chapter 5

Copolymers of Pyridine-bridged Polybenzimidazole for the use in High Temperature PEM Fuel Cell

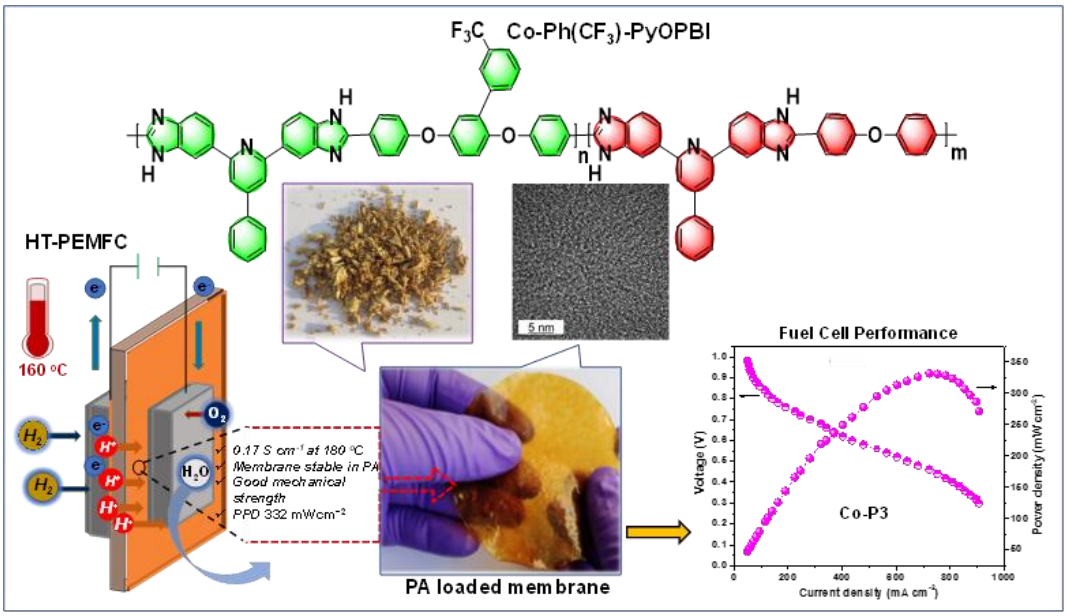

In this chapter, various copolymers of pyridine-bridged polybenzimidazole have been synthesized to develop proton exchange membranes (PEMs) with superior properties and fuel cell performance.

Harilal; Shukla, A.; Ghosh, P. C.; Jana, T. communicated to *ACS Appl. Polym. Mater.*

5.1. INTRODUCTION

The ever-increasing global energy demand and unavoidable environmental issues such as water and air pollution from the combustion of fossil fuels thrown up an urgent demand of developing clean and renewable energy sources.[1] Hydrogen fuel is considered as one of the most ideal candidates to meet this challenge due to its high energy density and clean combustion product only H_2O.[2-5] Hydrogen-fed polymer electrolyte membrane fuel cell (PEMFC) offers a clean and reliable alternative energy source due to their high energy conversion efficiency, low pollutant emissions and mild operating conditions.[6] Currently, exploring new proton-conducting polymeric materials that can serve as a solid electrolyte membranes of PEMFC is a primary focus in this fast-evolving field. At present, few materials offer the high proton conductivity and long working life necessary for commercial application with the main exception being Nafion, a sulfonated tetrafluoroethylene copolymer.[7,8] Despite the success of the Nafion-based polymers as PEM under humidified conditions and at a lower temperature (below 100 °C), the high-temperature PEM operated at a temperature of 100-200 °C could be commercially more viable due to the manifold reasons which include: enhancing electrode kinetics, decreasing CO poisoning of Pt-based electrodes, facile management of water and heat and so forth.[9] Hence, the development of cheaper and yet better-performing novel HTPEM with operating in 100 to 200 °C has been a subject of intense current interest in both academic and industrial communities.

Among several HTPEM candidates studies so far, the phosphoric-acid (PA)-loaded polybenzimidazole (PA/PBI) based PEMs are well documented in the literature on account of their excellent thermal, chemical stability and good proton conductivity (above 100 °C) under anhydrous conditions.[10-14] Nevertheless, although PA/ PBI HTPEM possesses several benefits, further improvements in proton conductivity for more efficient fuel cell is still desired. In general, two elegant strategies have been explored in regard to PBI structure to enhance the proton conductivity of PBI HTPEMs: (i) increasing molecular weight (or) (ii) introducing multiple heteroatoms into polymer backbones. It has been noted that direct casting from a poly(phosphoric acid) (PPA) solution (sol-gel process)[15-17] or replacing PPA with Eaton's reagent (which is 1:1 mixture of P_2O_5 and CH_3SO_3H)[18] are two most effective methods to obtain high molecular weight PBIs. The flipside of high molecular weight PBI is that it suffers poor solubility which is not conducive for processing and making membrane. On the other

hand basicity of PBI can be enhanced by the incorporation of monomer units containing basic N-heterocyclic groups (i.e. triazole, pyridine) in the PBI backbones.[19-21] This eventually increases the availability of the bound phosphoric acid molecules which then resulted in improved proton conductivity of PBI PEMs. The incorporation of basic N-heterocycle groups is also reported to enhance oxidative and thermal stability. Despite their striking advantages, they have still been confronted with some limiting factors. Hence, to overcome the rebarbative disadvantages (tedious synthetic process, high cost, limited processability and fuzzy structures), to date, many researchers including our research group have made various designs and modular synthetic efforts by (i) constructing novel PBI structures, (ii) blending with appropriate polymers, (iii) making composites like (ionic and covalent cross-linking as well as organic-inorganic composites) and (iv) developing elegant membrane fabrication techniques in order to resolve these issues.[22-25]

Recently, we have strategically developed a novel type of readily processable PBI polymer structure called pyridine-bridged (PyPBI) from a readily accessible and low-cost sterically hindered pyridine-functionalized tetraamine (PyTAB) monomer.[26-28] These heteroatom-rich polymeric PyPBI membranes with unique structures showed notable improvement in various PEM properties including thermal, mechanical, chemical stabilities and proton conductivity in comparison to traditional PBI PEMs. Nevertheless, among the various structure of PyPBIs so far we have studied, the pyridine-functionalized poly(fluorophenylene-oxybenzimidazole) Ph(CF_3)-PyOPBI having a well integration of high molecular weight as well as superior solubility and it exhibited high dimensional-mechanical stability with low swelling ratios despite of their relatively high capability of PA loading.[29] We demonstrated that the incorporated side groups (pyridine, CF_3) with large steric hindrance disrupted the close chain packing of PBI to increase the free volume and with the nitrogen atom of the pyridine ring helped in processability and rendering absorption of more PA with less volume swelling compared to conventional PBI. Also, the inclusion of multiple heteroatoms including O and F into polymer backbones can endow Ph(CF_3)-PyOBI with distinctive physical properties. This observations encourage us to further investigate the Ph(CF_3)-PyOBI based PEMs for their performance and create more systems beyond traditional PBIs.

Considering this observation, we hypothesise that introducing a hydrophilic-hydrophobic multifunctional co-network microstructure into PyPBI backbone can integrate the

advantages of micro-phase separation, a "spongelike" morphology, in which hydrophobic regions provide critical mechanical support for the resulting membranes and hydrophilic regions provide ionic nanochannels for proton conduction, in addition to the intermolecular hydrogen bonding among proton donor and acceptor groups to affords higher conductivity of the PEM. Therefore, we herein designed and successfully synthesized a series of sterically hindered pyridine-functionalized arylether-linked random copolymers with systematically varied composition and functionality through a readily doable approach in order to develop a more efficient PEMs. The obtained multifunctional polymeric membranes were characterized and investigated in detail, including thermal and mechanical stability, oxidative stability, proton conductivity, PA retention as well as single-cell performance.

5.2. EXPERIMENTAL SECTION

The source of all the materials and the characterization methods details are used in this chapter are described in the **Chapter 2**.

5.2.1. Synthesis of copolymers

The Ph(CF_3)-PyOPBI polymer was synthesized according to the method reported in our previous studies.[26, 29] Briefly, 2.214 g (5 mmol) pyridine-functionalized tetraamine (PyTAB, which was made in 5 steps from simple aromatic building blocks as previously described, see **Appendix III-Scheme 5.1**) and 2.0 g (5 mmol) arylether diacid [Ph(CF_3)-COOH which was synthesized in 5 steps from simple aromatic building blocks as previously described, see **Appendix III-Scheme 5.2**] monomers with a molar ratio of 1 : 1 in the presence of Eaton's Reagent (15 mL) were taken in a three-necked round bottom flask equipped with an overhead mechanical stirrer under continuous nitrogen atmosphere during the entire polymerization process. The reaction mixture was stirred and heated in a programmable temperature-controlled manner at 100 °C for 2 h, 140 °C for 4 h and finally at 160 °C for 4 h to obtain a highly viscous product. The viscous solution was purified by precipitation into distilled water, neutralized with sodium bicarbonate and washed with distilled water several times and dried in an oven at 120 °C for 24 h (3.97 g, 87.7% yield) [**Appendix III-Figure 5.1 (A)**]. **^{1}H NMR** (500 MHz, DMSO-d_6): δ (ppm) 13.05 (NH s), 8.64 (2H d), 8.28 (2H m), 8.20 (2H d), 8.10 (1H s), 7.89 (2H d), 7.69 (2H m), 7.60 (1H m), 7.47 (2H m), 7.34 (1H m), 7.14 (1H d), 6.95 (1H m). The ^{1}H NMR spectra is shown in **Figure 5.2**.

For the synthesis of PyOPBI [**Appendix III-Figure 5.1 (B)**], the above procedure was followed by using OBA (1.4 g, 5 mmol) instead of Ph(CF_3)-COOH. The heating programme followed was 100 °C for 2 h, 120 °C for 4 h and finally 140 °C for 2 h. The resulting polymer was obtained as fiber-like shape beige tint solid and the yield was 92%. **^{1}H NMR** (500 MHz, DMSO): δ/ppm 13.11(s NH), 8.69 (d 1H), 8.31(s 1H), 8.29 (dd 2H), 8.21 (m 2H), 8.09 (d 1H), 8.08 (d 1H), 7.80 (m 1H), 7.71 (d 2H), 7.59 (d 2H), 7.57 (m 2H), 7.53 (d 2H), 7.52 (d 1H), 7.51 (m 2H), 7.33 (m 1H), 7.32 (dd 2H). The ^{1}H NMR spectra is shown in **Figure 5.2**.

A series of Ph(CF_3)-PyOPBI and PyOPBI copolymers with different contents of fluorophenylene arylether linkages were synthesized by altering the feed molar fraction 25 wt%, 50 wt% and 75 wt% of OBA to Ph(CF_3)-COOH. The obtained copolymers were hereafter referred to as Co-x% Ph(CF_3)-PyOPBI (Co-P1, Co-P2 and Co-P3), where x is the molar percent of PyOPBI in the copolymers. The synthesis procedure for the copolymers was also similar to that for Ph(CF_3)-PyOPBI where OBA was first dissolved followed by Ph(CF_3)-COOH into the Eaton's Reagent. The synthetic process shown in **Figure 5.1(C)**. **Co-P1**: **^{1}H NMR** (500 MHz, DMSO-*d_6*): δ/ppm 13.17(s NH), 8.62 (d 2H), 8.47 (m 1H), 8.29 (m 2H), 8.20 (m 1H), 8.14 (d 1H), 8.07 (s 1H), 8.02 (d 2H), 8.00 (m 2H), 7.87 (m 2H), 7.72 (m 1H), 7.59 (m 2H), 7.53 (m 2H), 7.32 (m 1H), 7.16 (d 2H), 7.10 (m 2H), 6.94 (m 2H). **^{19}F NMR** (471 MHz, DMSO-*d_6*): δ/ppm −61.13. The ^{1}H NMR spectra is shown in **Figure 5.2** and the **^{19}F NMR** is given in **Appendix III-Figure 5.3**.

Co-P2: **^{1}H NMR** (500 MHz, DMSO-*d_6*): δ/ppm 13.24 (s NH), 8.62 (d 2H), 8.46 (m 1H), 8.29 (m 2H), 8.28 (m 1H), 8.16 (d 1H), 8.07 (s 1H), 8.00 (d 2H), 7.99 (d 2H), 7.97 (m 2H), 7.95 (m 1H), 7.87 (m 2H), 7.84 (d 2H), 7.73 (m 1H), 7.58 (m 2H), 7.38 (m 1H), 7.30 (d 2H), 7.10 (m 2H), 6.96 (m 2H). **^{19}F NMR** (471 MHz, DMSO-*d_6*): δ/ppm −61.15. ^{1}H NMR spectra is shown in **Figure 5.2** and the **^{19}F NMR** is given in **Appendix III-Figure 5.4**.

Co-P3: **^{1}H NMR** (500 MHz, DMSO-*d_6*): δ/ppm 13.20 (s NH), 8.61 (d 2H), 8.46 (m 1H), 8.26 (m 2H), 8.15 (d 1H), 8.00 (s 1H), 7.99 (d 2H), 7.86 (m 2H), 7.71 (m 1H), 7.54 (m 2H), 7.40 (m 1H), 7.26 (d 2H), 7.08 (m 2H), 6.88 (m 2H). **^{19}F NMR** (471 MHz, DMSO-*d_6*): δ/ppm −61.15. ^{1}H NMR spectra is shown in **Figure 5.2** and the **^{19}F NMR** is given in **Appendix III-Figure 5.5**.

5.2.2. Preparation of proton exchange membranes

Membranes of Ph(CF_3)-PyOPBI, PyOPBI and their copolymers were prepared by solvent casting at 100 ^oC for 12 h from 2 wt% polymer solutions in 10 mL dimethyl sulfoxide (DMSO). The polymers were dissolved for 48 h at room temperature and then filter through a 0.5 µm Teflon syringe filter onto a clean and smooth bottomed glass Petri dish. The obtained transparent and flexible membranes were carefully peeled from the glass Petri dishes and washed several times with deionized water and dried at 100 °C for 24 h to remove the remaining traces of DMSO solvent. The membranes were stored in the desiccator at room temperature for further characterization. A schematic presentation of the fabrication steps of these membranes are presented in **Figure 5.1 (D)**.

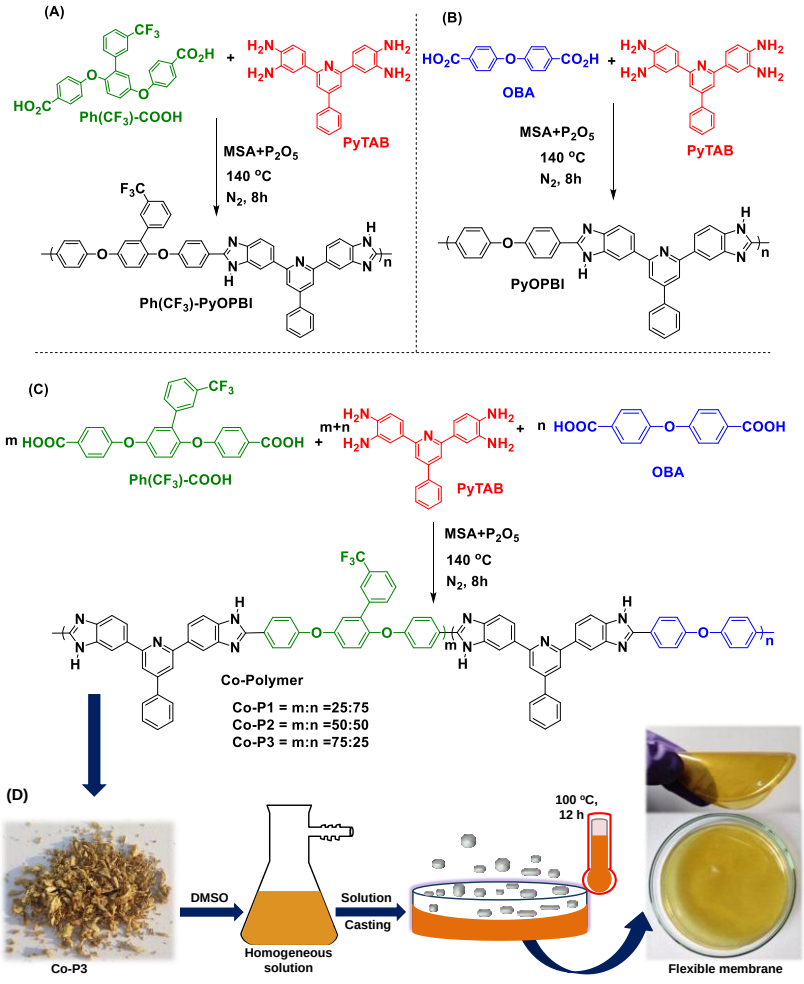

Figure 5.1. Schemes for synthetic procedures of the (**A**) Ph(CF_3)-PyOPBI, (**B**) PyOPBI, (**C**) copolymers (**Co-P1**, **Co-P2**, **Co-P3**) in gram-scale. (**D**) Schematic illustration of the fabrication of Co-P3 membrane by solution casting method.

5.3. RESULTS AND DISCUSSION

5.3.1. Synthesis and structural characterization of copolymers

The proton conductivity and mechanical stability of the PBI based PEMs are the key properties for the long-time operation of PEMFCs. Therefore, the chemical structure design of membrane materials is critical for the overall performance of PEMs. To enhance the proton conductivity and mechanical stability of PEMs, in this work various molecular weights of pyridine functionalized co-polybenzimidazoles based on Ph(CF_3)-COOH, OBA dicarboxylic diacids were synthesized using the procedure as described in the proceeding section (**Figure 5.1**) and are characterized. Intrinsic viscosity of the synthesized polymers were determined in 98 wt% H_2SO_4 and are found to be 2.88, 1.89, 1.91, 1.83 and 2.24 dL/g for polymer Ph(CF_3)-PyOPBI, PyOPBI and Co-P1, Co-P2 and Co-P3, respectively. The combination of chain flexibility and high molecular weight guarantees the requirement of membranes having sufficient mechanical strength for the preparation of strong PA/PBI membranes. The polymer solubility was checked and found that Ph(CF_3)-PyOPBI is much easier to dissolve in DMSO, NMP, formic acid and DMAc under refluxing at 100 ^oC, clearly because of the flexible pendant-type spacer groups of –CF_3–. Dissolution of the copolymers would need slightly higher temperatures or a longer time in the same solvent compared to homo Ph(CF_3)-PyOPBI as a result of the replacement of the flexible aryl fluoro-linkages by the stiff para-phenylene unit in the copolymer structures. Homogeneous and transparent membranes of copolymer could be prepared by solution casting from DMSO solution as shown in **Figure 5.1 (D)**.

The synthesized polymers structures are confirmed by the ^{1}H-NMR and FT-IR spectroscopic techniques. FT-IR spectra of both homo and random copolymers are shown in **Appendix III-Figure 5.6**. The important characteristic stretching bands of the polymer structures marked with purple colour rectangle in the spectra which have been previously discussed in the literature as important FT-IR stretching bands for PBIs.[13,15] The characteristic stretching bands centred at around 3620 and 3415−3210 cm^{-1} are due to the O−H stretching of physically adsorbed moisture and the stretching vibration of the imidazole free N−H group, respectively. Also, the peaks at 1596, 1476, and 901 cm^{-1} are because of C=C/C=N in-plane benzimidazole ring deformation and C−H stretching vibration of the pyridine ring,

respectively. Additionally, the typical characteristic stretching bonds between 1240 and 1165 cm^{-1} corresponded to the ether (Ar−O−Ar) linkage.

The effective formation of imidazole linkages of the polymers is also characterized using NMR spectroscopy (**Figure 5.2**). The peaks are matched well to those of the expected chemical structures. For homo polymer PyOPBI and Ph(CF_3)-PyOPBI, the characteristic peaks appear at 12.98 ppm for N-H of imidazole ring and 13.11 ppm, respectively. All other chemical shifts of aromatic protons appear around at δ 7.0−8.61 ppm which is consistent with our previously reported data. In the NMR spectra of copolymers, signals corresponding to protons of aromatic region are varied with respect to composition due to their different chemical environments as depicted in peak assignments in the **Figure 5.2**. The 'm' peak for Ph(CF_3)-PyOPBI is present in the high chemical shift region because of the effect of the electron-withdrawing –CF_3– group. The peak area at around 7.08 ppm for the protons in the phenyl units (j) increases as the amount of the Ph(CF_3)PyOPBI content in the copolymers is increased when compared with homo Ph(CF_3)-PyOPBI polymer. One can estimate the molar composition of the flexible aryl fluoro-linkage in the copolymers from the ratios of the peak area for 'm' to those for 'd' and 'f'. The calculated mole percentage of Ph(CF_3)-PyOPBI in the copolymers are estimated to be 75.4, 50.4 and 25.0 for Co-P3, Co-P2 and Co-P1, respectively. These obtained values are in good agreement with the molar feed ratios at the start of polymerization. These results indicate efficient random polymerization from the fluorinated comonomer and suggest that the structures of the copolymer repeat unit can be readily controlled by changing the molar ratios of the comonomers i.e. Ph(CF_3)-COOH to OBA.

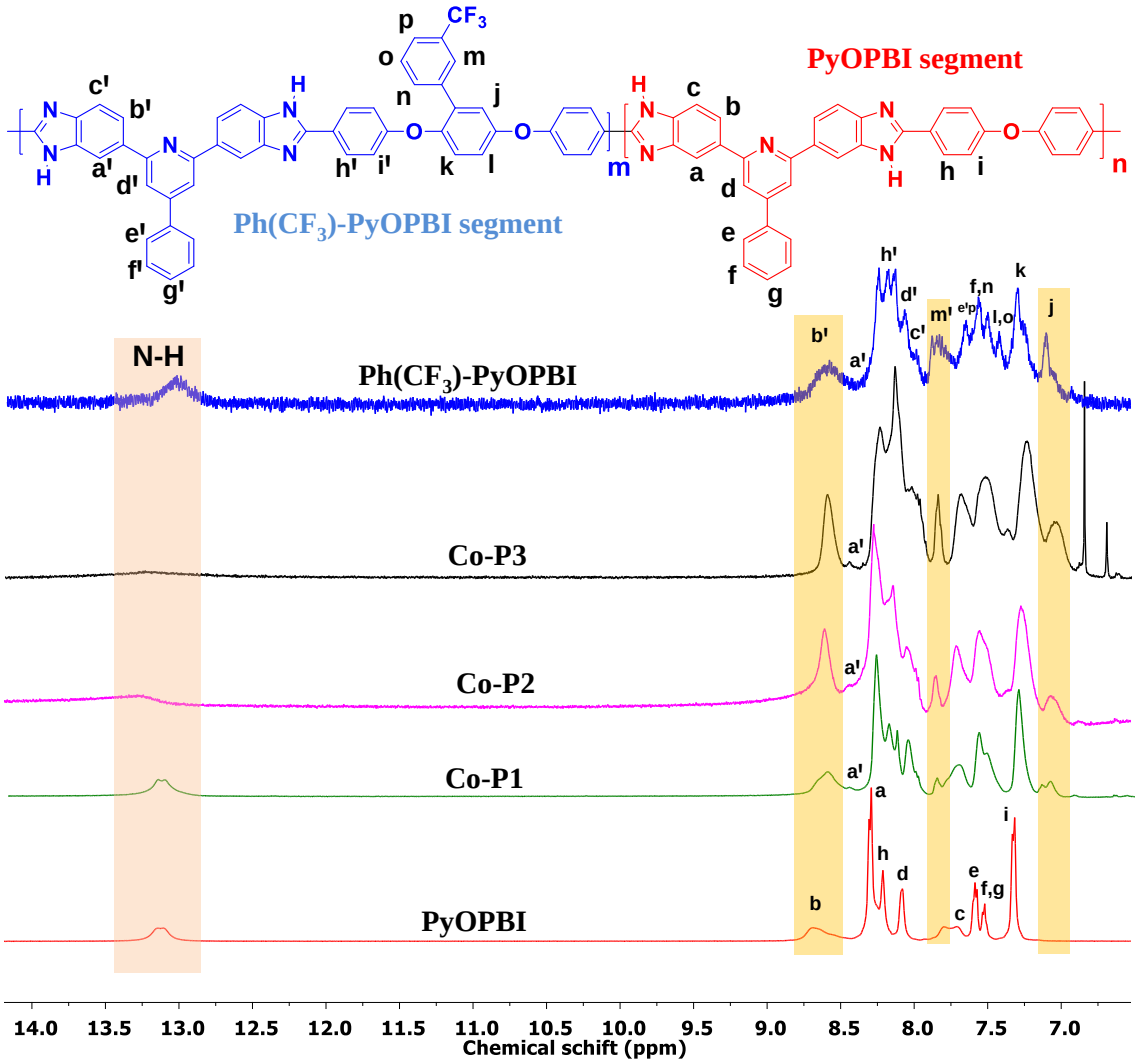

Figure 5.2. ^{1}H NMR spectra of the homo and copolymers with the peak assignments and chemical structure. Spectra were recorded in DMSO-*d*$_6$.

Furthermore, the successful construction of PBIs were also verified by X-ray photoelectron spectroscopy (XPS) survey which led us to a deeper understanding of bond types and elementary compositions. The C, O, N and F elements have been found in XPS full spectra of homo and copolymers **(Appendix III-Figure 5.7**). For carbon spectroscopic signatures, two typical peaks appear at binding energy of 284~289 eV attributing to the C=C, C=N (imidazole), C–F (trifluoromethyl), C=N (pyridine), and C-O bonds (**Figures 5.3**). The two typical N 1s signals concentrated at ~399 and 402 eV can be assigned to different chemical environments of pyridine and imidazole linkage (**Figures 5.3 A, B** and **C**) and peak at 688 eV is assigned to

C-F bond for copolymers. In light of all these spectral results, undoubtedly the formation of arylether-linked pyridine-functionalized copolybenzimidazoles is proved.

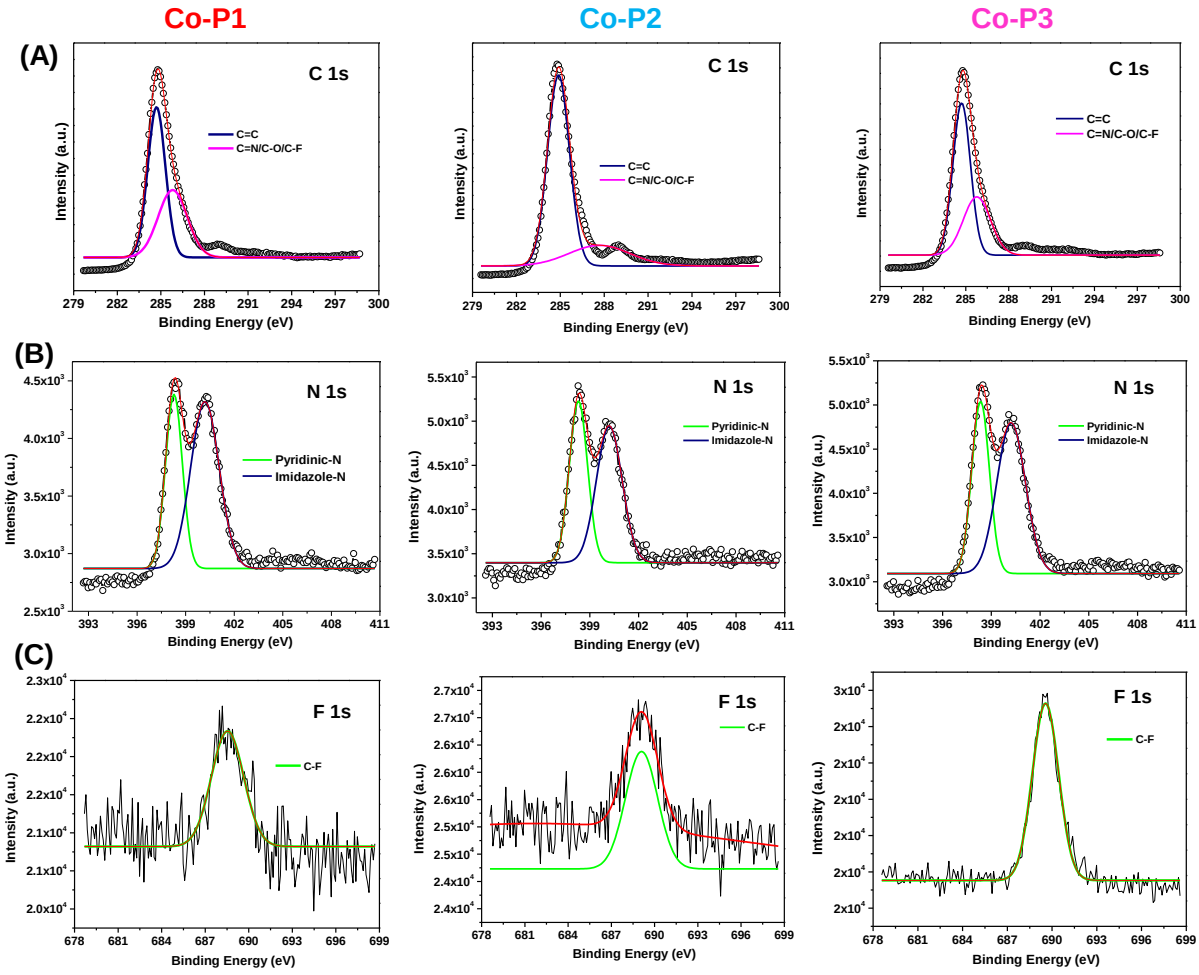

Figure 5.3. High resolution XPS spectra of C1s, N1s, F1s bands of copolymers. Each column is identified with different polymer as noted at the top. (**A**) C1s, (**B**) N1s and (**C**) F1s spectra.

5.3.2. Thermal stability and mechanical properties of the copolymer membranes

Satisfactory thermal and mechanical properties of the PEMs are the two of the main requirements for handling membrane electrode assembly (MEA) and durability of the fuel cell. Therefore, thermogravimetric analysis (TGA) and dynamic mechanical analyser (DMA) tests were carried out to examine the thermal and mechanical properties of the resulting copolymers membranes. **Figure 5.4 (A)** shows the TGA of copolymers and homopolymer membranes in the temperature range 30–700 ºC under N_2 atmosphere. All the membranes displayed mainly three decomposition steps. First, the slight weight loss step from 100 to 160 °C which can be

attributed to the elimination of physically absorbed moisture and bound water present in the membranes whereas the second weight loss region began at around 220−350 °C corresponds to the evaporation of residual DMSO solvent bonded to polymer chains. The third weight loss starting from 500 °C corresponds to the main chain deterioration of the polymer backbone. Among all the membranes, homo Ph(CF_3)-PyOPBI shows higher thermal stability as compared to the PyOPBI and copolymer membranes (Co-P1, Co-P2 Co-P3). It can be seen that copolymer membranes show a similar thermal degradation nature. The thermal stability of copolymer membranes are higher than that of homo PyOPBI due to the high thermal degradation of more stable trifluoromethyl groups of Ph(CF_3)-PyOPBI which adds to the lowering of polymer degradation. Also, the char yield of the copolymers increased with phenyl(trifluoromethyl) aromatic content indicates that the introduction of flexible arylether in the backbone of Ph(CF_3)-PyOPBI greatly enhances the backbone stability of random copolymer membranes. In summary, TGA results indicate that all the copolymer membranes are maintained thermal stability and sufficiently thermostable for further HT-PEMFC applications.

It is evident from **Figure 5.4B** that the storage modulus (E') of the copolymer membranes are higher to that of the homo PyOPBI membrane over the entire temperature region and also the value of E' increases with increasing the amount of the Ph(CF_3)-PyOPBI content in the copolymers (Co-P3 > Co-P2 > Co-P1). The enhanced storage modulus in copolymer membranes due to the presence of bulky arylether fluorophenyle groups which hinder segmental motions of the polymeric chains and form the iterative hydrogen bonding in between polymer chains. The storage moduli values decrease at around 350 °C due to the increased segmental motion of the polymer backbone and gradually decrease further with increasing temperature which indicates that the mechanical strength becoming poorer at higher temperatures. Nevertheless, all the Co-PyOPBI membranes showed good storage moduli values at temperatures less than 400 °C. The glass transition temperature (T_g) values of all the polymers were measured from loss modulus (E″) and tan δ plots and the presented in **Figure 5.4 (C** and **D)**. Both E″ and tan δ plots exhibits a well-defined relaxation peak above 340 °C that is assigned to the molecular-scale segmental motion during the glassy to rubbery transition. The T_g value varies greatly as the structure of the copolymer backbone changes, indicating the strong influence of the rigid arylether pendant-type structure of the copolymer. The T_g value

increases with increasing Ph(CF_3)-PyOPBI content in the chain. The highest T_g ~ 400 °C obtained in case of the Ph(CF_3)-PyOPBI polymer membrane, which is significantly higher than all other polymers and might be because of interaction between the trifluoromethyl, arylether (–O–), pyridinic nitrogen (pyri-N) and imidazole (−NH) of the Ph(CF_3)-PyOPBI backbone. From these TGA and DMA results, it can be concluded that all the prepared membranes meet the thermo-mechanical stability requirements for the use in high-temperature fuel cell as PEM.

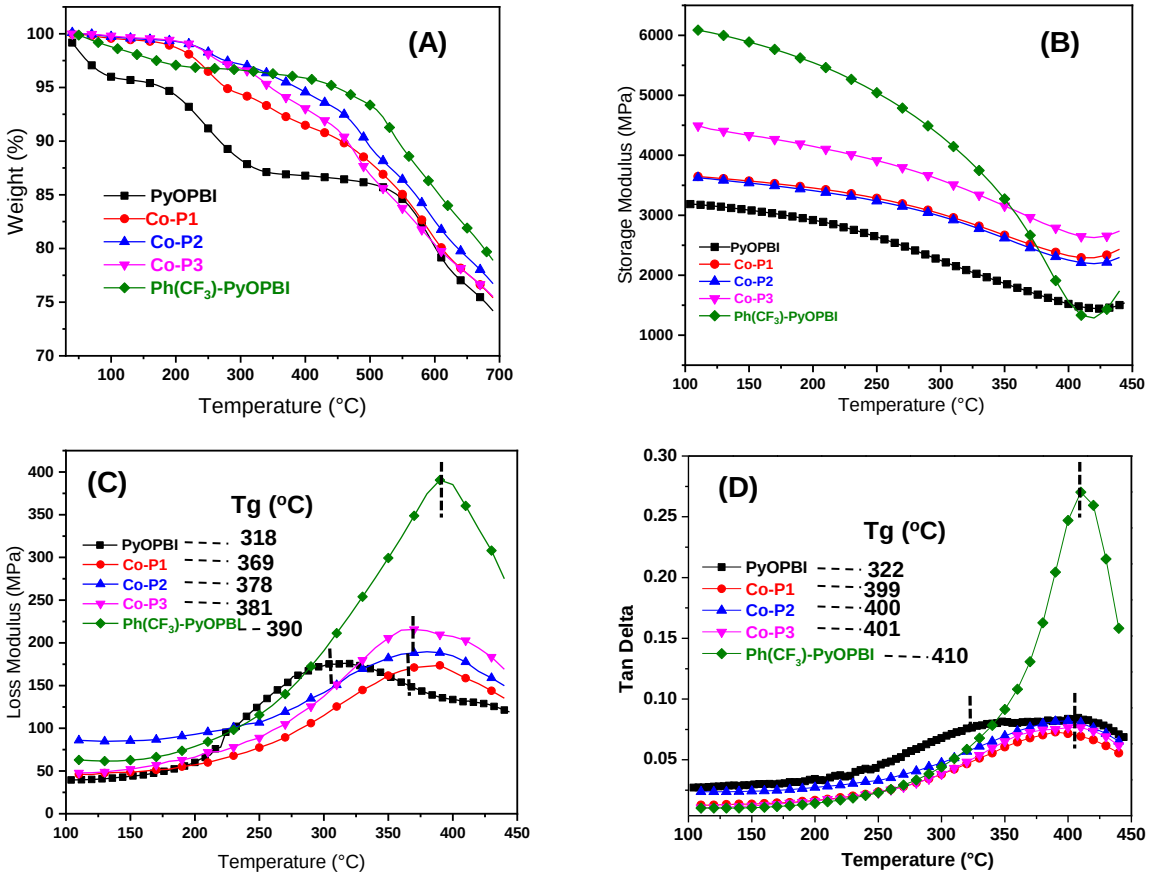

Figure 5.4. (**A**) TGA curves of homo and copolymers measured under N_2. DMA plots of membranes: (**B**) Storage modulus (E'), (**C**) loss modulus (E'') and (**D**) Tan δ plots against temperature. T_g value are indicated by dotted vertical line and list out in (**C**) and (**D**) along with the sample identity.

5.3.3. Oxidative stability of the membranes

During the operation of HT-PEMFC, the polymer membrane will be attacked by hydroxyl ($HO^{\bullet}$) and hydroperoxyl ($HOO^{\bullet}$) free radicals resulting in membrane breakage. Therefore, the oxidative (or chemical) stability is crucial to be evaluated. In the present work,

the oxidative stability is obtained by recording the weight loss as a function of time when membranes are exposed to a Fenton reagent (3% H_2O_2 containing 4 ppm $FeSO_4$) at 70 °C for 6 days. It could be seen from **Figure 5.5**, all copolymer membranes had a sustained weight loss and the weight losses of membranes decreases with higher arylether pendant trifluoromethyl phenyl content with respective to homo PyOPBI. This may be attributed to the hydrophobic trifluoro-methyl side chain which prevent free radical from attacking to the imidazole ring. The result indicated the good oxidative stability of copolymer membranes. [30,31]

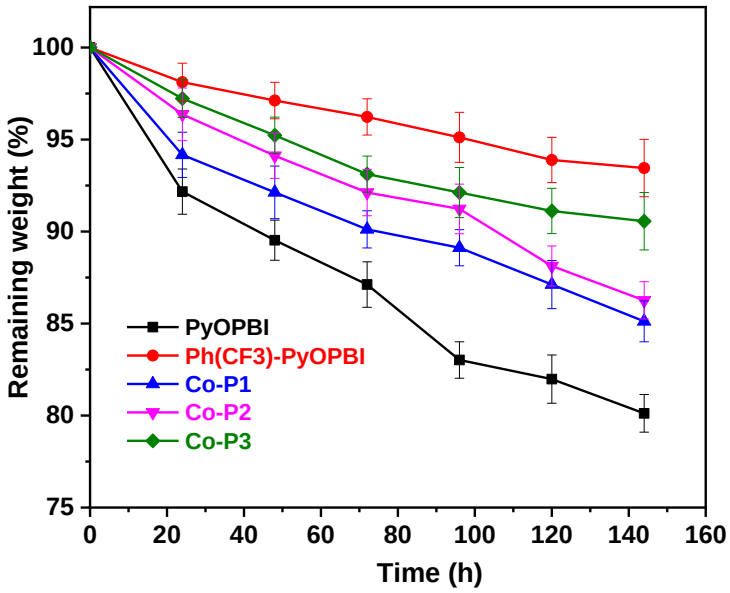

Figure 5.5. Oxidative stability of PyOPBI, Ph(CF_3)-PyOPBI and copolymer membranes in 3% H_2O_2 containing 4 ppm Fe^{2+} at 70 °C.

5.3.4. Membrane Morphology

We used scanning electron microscopy (SEM) and high-resolution transmission electron microscopy (HRTEM) techniques to investigate the microstructure morphological features of the synthesized polymer membranes in order to correlate the morphology and membrane performance. SEM cross-sectional images of the membranes are shown in **Figure 5.6 (A** and **B)**. All copolymer membranes exhibit remarkable change in morphologies compared to the both homo PyOPBI and Ph(CF_3)-PyOPBI membranes. In the copolymer membranes a spongy-like support structures with microcavities are observed which increases as we go from left to right in the **Figure 5.6A** and **B**. This feature is completely absent in the case of PyOPBI (**Appendix III-Figure 5.8**). This distinct morphology feature is advantageous

to the various improvement in the properties of the membrane such as proton transportation, thermal and mechanical stability, and so on.

Figures 5.6 (C and D) show the HR-TEM images of different membranes. The subtle distinct phase separation could be observed over the entire scanning area for all three copolymer membranes compared with the homo PyOPBI (**Appendix III-Figure 5.8**) and Ph(CF_3)-PyOPBI membranes suggesting the presence of aggregation of ionic clusters structures (CF_3···H−N, C−O···H–N=C and pyridinic–N···H–N=C). The bright region is due to the hydrophobic blocks of pendants fluorophenylene PyOPBI chain-rich domain while the dark regions corresponding to the clustering of long arylether-bonded pyridyl and imidazole groups for ion conduction are found to be synergistically interconnected throughout the TEM image with a domain width of approximately 5–10 nm which may facilitate the formation of a continuous long-range proton nanochannels. However, the XPS high-resolution C1s spectra confirmed the presence of numerous polar bonds of C−O/C−N and C−F (284.1-289.4 eV) in copolymers **(Figure 5.3A**) and atomic contents of C, O, N and F are listed in **Appendix III-Table 5.1**. The polarity ratio, defined as the value of (O at.% + F.at % + N at.%)/C at.%, was as high as 22.89 % for Co-P3 demonstrating the strong polar nature of copolymers. This result suggests that the introduction of a flexible arylether trifluorophenylene units in the polymer backbone can significantly enhance phase separation due to presence of numerous polar bonds in the copolymers.

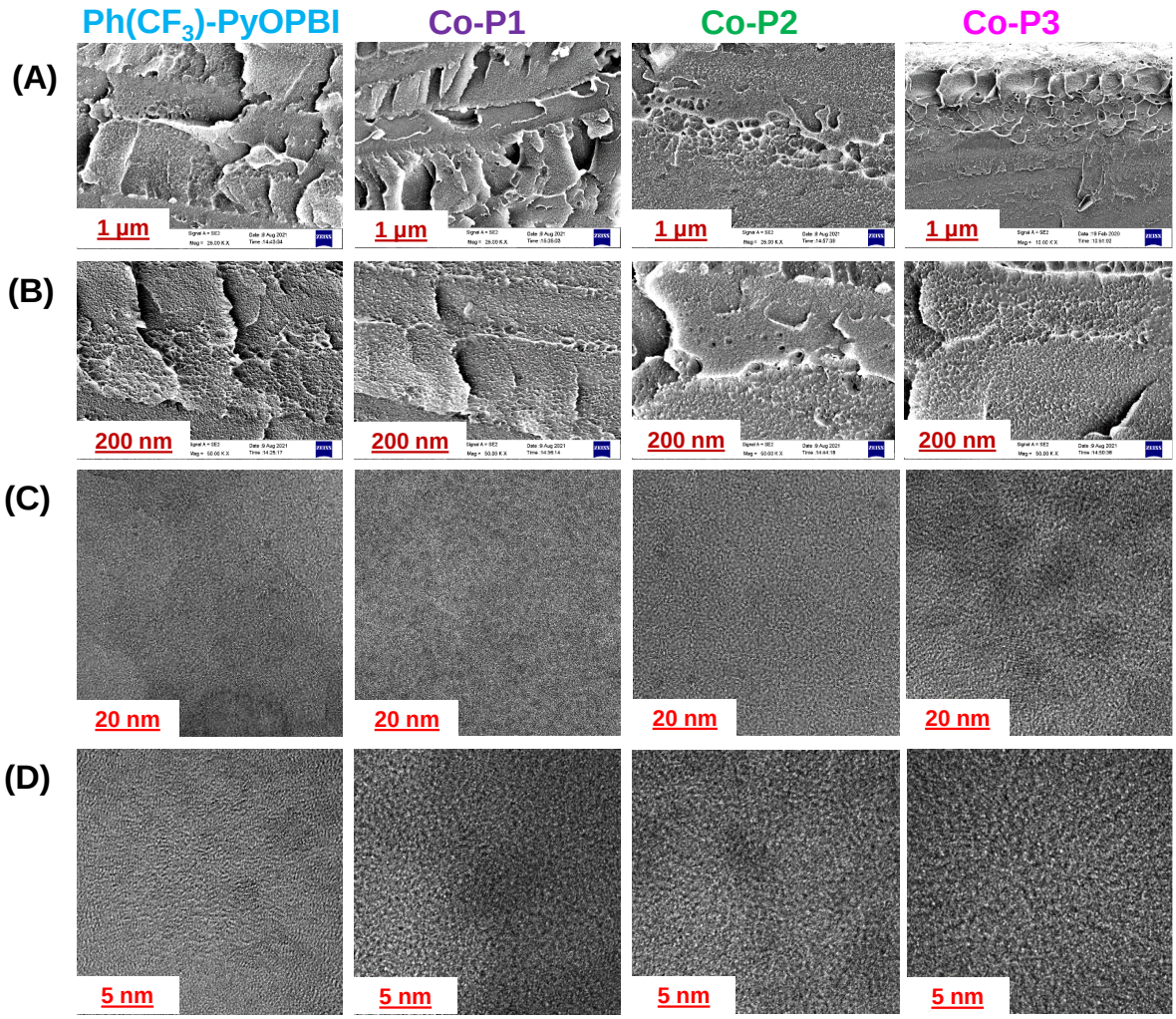

Figure 5.6. Microscopic morphologies of all the polymer membranes. Each column is identified with different polymer as noted at the top. (**A** & **B**) Cross-sectional SEM images with scale bar 1µm and 200 nm, respectively and (**C** & **D**) HR-TEM images with scale bar 20 and 5 nm, respectively.

5.3.5. Water uptake, acid doping level and swelling of membranes

It is widely noted that PBI is a hygroscopic engineering plastic and it has a high affinity to form stronger interactions with water molecules which rigorously impacts the dimensional stability of the membrane. After dipping the membranes in deionized (DI) water for three days, we observed that the amount of water uptake (WU) of PyOPBI, Ph(CF_3)-PyOPBI, Co-P1, Co-P2 and Co-P3 membranes is 16.56, 16.10, 19.12, 20.13 and 21.21 wt %, respectively and the data is shown **Appendix III-Figure 5.9**. It is quite evident from the data that the introduction

of flexible arylether units in polymer backbone has increased the WU; however, Ph(CF_3)-PyOPBI shows less WU compared to copolymers because of the hydrophobic nature owing to the presence of trifluoro functionality in the polymer backbone. The swelling ratio values are also shown in **Appendix III-Figure 5.9** which also follows similar trend like WU. Hence both WU and SR measurements clearly demonstrate the effect of arylether structure of copolymer in comparison to both homo polymers.

Furthermore, Ph(CF_3)-PyOPBI and copolymers (Co-P1, Co-P2, Co-P3) membranes were immersed in concentrated PA (85 wt %) solution at 30 ^oC for a period of three days for PA uptake, whereas homo PyOPBI membrane was dipped in 60 wt% PA as in higher PA concentration (>60 wt%) the PyOPBI membrane loses mechanical strength. The acid doping level (ADL), which is defined as the number of moles of PA per repeat unit of the PBI polymer, for all the membranes is shown in **Figure 5.7 (A)**. The data clearly indicate that the flexible arylether pendant copolymer membranes load more PA than the both homo PyOPBI and Ph(CF_3)-PyOPBI membrane. After loading for 72 h, ADL of Co-P1, Co-P2 and Co-P3 membranes reach, 23.6, 24.6 and 25.4, respectively, which are much higher than homo PyOPBI (14.2) and marginally higher than Ph(CF_3)-PyOPBI (21.9) membranes. This is because of the abundant number of proton accepting and donating functional entities such as arylether (–O–), pyridyl nitrogen (pyri-N) and imidazole associated across the membranes of polymer provides sites for absorption the PA through hydrogen bonding of P=O···H–N, H–O···F–C, O–H···N=C and O–H···O–C interactions [**Figure 5.7 (B)]**. Also, the pendant trifluorophenylene prohibits the polymers from packing efficiently, leading to free volume in the pendant-type PyOPBIs backbone as discussed in the earlier section and hence facilitated absorption of more PA compared to homo polymers in a concentrated H_3PO_4 solution. When the composition ratio of PyOPBI to Ph(CF_3)-PyOPBI is 50 to 75 wt%, the ADL of the polymer is the highest (Co-P3, 25.4 mol of PA/PBI) which is in agreement with the PA swelling data. The swelling ratio was also measured and shown in **Figure 5.7 (A)**. Swelling data are consistent with PA loading data as it is expected that a higher PA loading pushes the membrane to swell more.

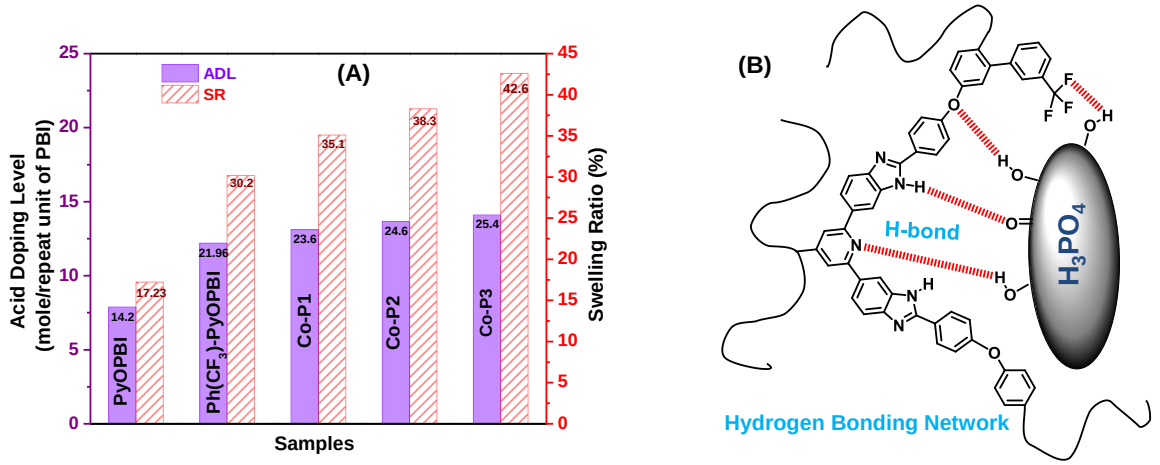

Figure 5.7. (**A**) ADL and swelling ratio of the membranes after doping for 3 days in H_3PO_4. (**B**) Possible bonding interaction pattern of PA molecules with pyridine functionalized-oxy-fluorinated polybenzimidazole membrane.

5.3.6. Proton conductivity and acid retention of membranes

One of the key factors influencing the performance of fuel cell is the proton conductivity of PEMs especially at high temperature (>100 °C). We investigated the temperature-dependent proton conductivity of all the prepared membranes after loading with H_3PO_4 by measuring membranes impedance **(Appendix III-Figure 5.10)**. Prior to the measurements, the homo PyOPBI membrane was soaked in 60 wt % PA and all the other copolymers (Co-P1, Co-P2 and Co-P3) including pristine Ph(CF_3)-PyOPBI membranes were soaked in 85 wt % PA for 3 days and dried in oven at 120 °C for 2 h before putting into a home-made four-point probe conductivity test cell. Then the test cell along with the PA-loaded membranes were heated in a programmed manner from 30 °C to 180 °C and the impedance was measured using a Nyquist plot (**Appendix II-Figure 5.10**) under anhydrous conditions. From the impedance data, proton conductivities were calculated and plotted including error bars **[Figure 5.8 (A)]**. The conductivity measurements were made twice and the average values were reported. As expected, the proton-conductivity of the membranes increases with increase in the acid doping level and temperature. The copolymer Co-P3 exhibits the highest proton conductivity of 0.17 S cm^{-1} at 180 °C whereas PyOPBI display the lowest conductivity of 0.007 S cm^{-1} at 180 °C. The general observation is that conductivity increases with increase the amount of the Ph(CH_3)-PyOPBI content in the copolymers. However, the homopolymer with the maximum aromatic pendant-type trifluoromethyl phenyl content Ph(CF_3)-PyOPBI

exhibited a conductivity of 0.07 S cm^{-1} (less than that of Co-P3) at 180 °C. Considering the quantity of acid loaded Co-P3 contains more moles of acid (25.4) than both pristine PyOPBI (14.2) and Ph(CH_3)-PyOPBI (21.9) yet its conductivity is higher than that of both homopolymers. This may be attributed to forming acid−base pairs, ionic cross-linking and electrostatic attractions and the specific ordering as microphase separated morphology which helped in boosting the proton conduction of Co-P3 in the presence of PA. In fact, all the copolymers display higher proton conductivity then both the homopolymers which attribute that those above-mentioned cases may be the driving forces for such observation.

To prove further the increased conductivity of copolymer, we performed the acid leaching test with the PA-doped membranes by exposing them to water vapour at 100 °C for a period of 3 h and measuring the weight loss ratio of the acid from the membranes after every 30 min. It is clear from the **Figure 5.8 (B)** that all the membranes suffer from acid leaching with time especially within the initial 1 h, which is attributed to the discharge of non-bonded water and acid molecules from the membranes. However, all the copolymer (Co-P1, Co-P2, Co-P3) membranes show a much well controlled leaching behaviour. And the Co-P3 is the best among the three copolymers. Although the percentage loss in the initial 1 h may be rapid, it is still lesser than homo [PyOPBI and Ph(CF_3)-PyOPBI] membrane and also becomes lesser with time. This is suggestive of the role of the flexible pendant arylether polymer chains help to improve the acid molecules from being leached away through strong hydrogen bonding interactions. Hence, the copolymer membranes prove to be worthy candidates for use in HT-PEMFCs.

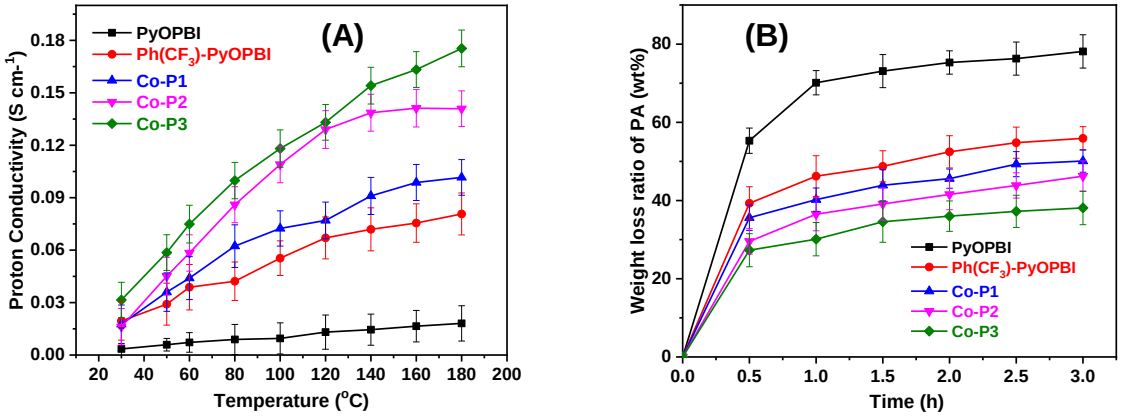

Figure 5.8. (**A**) Proton conductivities and (**B**) acid leaching plots of of the homo and copolymers membranes.

5.3.7. H_2/O_2 fuel cell performance of the membranes

H_2/O_2 fuel cell testing is a direct application-oriented way to assess the properties such as proton conductivity, swelling ratio, PA uptake, acid retention stability, etc. of a PEM, all of which have a significant impact on the fuel cell performance. Given the comprehensive properties of prepared membranes, the single-cell utilizing Co-P2 and Co-P3 membrane were investigated for the performance of PEMs. The single H_2/O_2 fuel cell performance of PA-loaded Co-P2, Co-P3, PyOPBI and Ph(CF_3)-PyOPBI membranes were measured at 160 ^oC without humidification. The polarization and power density curves of the membrane electrode assembly (MEA) made from these PEMs are shown in **Figure 5.9**. The open circuit voltage (OCV) of Ph(CF_3)-PyOPBI, Co-P2 and Co-P3 PEMs is around 0.91V indicating the prepared membranes can effectively block gaseous fuel permeability though PyOPBI membrane exhibits a relatively low OCV (0.85 V) which implies a gas permeability caused by mechanical damage such as membrane pin-hole formation and ruptures. The single H_2/O_2 fuel cell using the Co-P3 PEM yielded a maximum peak power density (PPD) of 332.23 mW cm^{-2} at a cell voltage 0.46 V with current density of 722.25 mA cm^{-2} which is an encouraging result and is better than our previously reported fuel cell performance results for PEMs. In comparison, the Co-P3 PEM shows much better single-cell performance than that of the both homo PyOPBI (108.18 mW cm^{-2} at a voltage 0.46 V with a current density of 209.25 mA cm^{-2}) and Ph(CF_3)-PyOPBI (239.21 mW cm^{-2} at a voltage 0.46 V with current density of 629.5 mA cm^{-2}) under the identical measurement conditions. Also, Co-P2 shows better performance than both homopolymers and little less than Co-P3. This improvement of copolymer power densities is probably due to the enhancement of ADL of the membranes and the high conductivity of the PEM. Hence, the improved fuel cell performance demonstrates that the combination of pendant-type and flexible arylether structures for use in HT-PEMFCs is very useful.

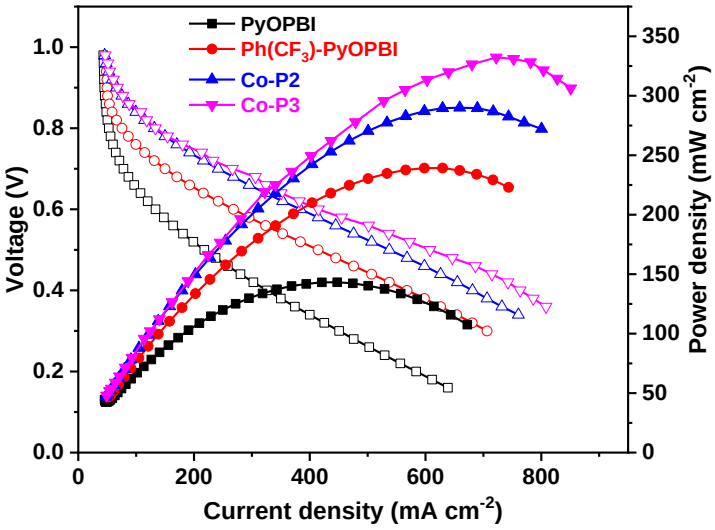

Figure 5.9. HT-PEMFC performance of PA-doped PyOPBI, Ph(CF_3)-PyOPBI, Co-P2 and Co-P3 membranes at 160 °C without humidification.

5.4. Conclusion

In conclusion, a series of pyridine-bridge copolybenzimidazoles have been synthesized, characterized and converted as PEM upon PA loading for the use in HT-PEMFC. Incorporation of the stiff para-phenylene and flexible arylether linkages in the macromolecular structures resulted in copolymers with high molecular weights and sufficient solubility. Compared with homo PyOPBI, introduction of the electron-withdrawing arylether functional groups into the polymeric backbones significantly improved the membrane resistance towards radical oxidation during the Fenton test. Single cell tests based on these membranes were carried out at temperatures of up to 160 ^{o}C with unhumidified H_2/O_2 fuels. The best performance was achieved for the Co-P3 membrane with a peak power density of 332.23 mW cm^{-2} at a cell voltage 0.46 V with current density of 722.25 mA cm^{-2} at 160 ^{o}C and under ambient pressure. The copolymer membrane displayed a higher conductivity, power density and current density than that of homo PyOPBI and Ph(CF_3)-PyOPBI membranes.

Appendix III

^{19}F NMR, FTIR and XPS spectra of copolymer membranes are included in the Appendix III (page no. 162-174).

REFERENCES

1. Armaroli, N.; Balzani, V. *Angew. Chem. Int. Ed.* **2007**, 46, 52-66.
2. Lubitz, W.; Tumas, W. *Chem. Rev.* **2007**, 107, 3900-3903.
3. Shultz, M. J.; Kelly, M.; Paritsky, L.; Wagner, J. *J. Chem. Educ.* **2009**, 86, 1051.
4. Eberle, U.; Felderhoff, M.; Schueth, F. *Angew. Chem. Int. Ed.* **2009**, 48, 6608-6630.
5. Staffell, I.; Scamman, D.; Abad, A. V.; Balcombe, P.; Dodds, P. E.; Ekins, P.; Shah, N.; Ward, K. R. *Energy Environ. Sci.* **2019,** 12, 463-491.
6. Jacobson, M. Z.; Colella, W.; Golden, D. *Science* **2005**, 308, 1901-1905.
7. Zhang, C.; Yue, X.; Luan, J.; Lu, N.; Mu, Y.; Zhang, S.; Wang, G. *ACS Appl. Energy Mater.* **2020**, 3, 7180−7190.
8. Vinothkannan, M.; Hariprasad, R.; Ramakrishnan, S.; Kim, A. R.; Yoo, D. J. *ACS Sustainable Chem. Eng.* **2019**, 7, 12847−12857.
9. Haider, R.; Wen, Y.; Ma, Z.-F.; Wilkinson, D. P.; Zhang, L.; Yuan, X.; Song, S.; Zhang, J. *Chem. Soc. Rev.* **2021**, 50, 1138-1187.
10. Aili, D.; Yang, J.; Jankova, K.; Henkensmeier, D.; Li, Q. *J. Mater. Chem. A* **2020**, 8, 12854-12886.
11. Guo, H.; Li, Z.; Lv, Y.; Pei, H.; Sun, P.; Zhang, L.; Cui, W.; Yin, X.; Hui, H. *ACS Appl. Energy Mater.* **2021**, 4, 8969-8980.
12. Yin, B.; Wu, Y.; Liu, C.; Wang, P.; Wang, L.; Sun, G. *J. Mater. Chem. A* **2021**, 9, 3605-3615.
13. Chen, J.-C.; Chen, P.-Y.; Liu, Y.-C.; Chen, K.-H. *J. Membr. Sci.* **2016**, 513, 270-279.
14. Skorikova, G.; Rauber, D.; Aili, D.; Martin, S.; Li, Q.; Henkensmeier, D.; Hempelmann, R. *J. Membr. Sci.***2020**, 608, 118188.
15. Mader, J. A.; Benicewicz, B. C. *Fuel Cells* **2011**, 11, 222-237.
16. Mader, J.; Benicewicz, B. *Fuel Cells* **2011**, 11, 212-221.
17. Maity, S.; Sannigrahi, A.; Ghosh, S.; Jana, T. *Eur. Polym. J **2013,** 49*, 2280-2292.
18. Chen, J.-C.; Chen, P.-Y.; Lee, S.-W.; Liou, G.-L.; Chen, C.-J.; Lan, Y.-H.; Chen, K.-H. *React. Funct. Polym.* **2016**, 108, 122-129.
19. Özdemir, Y.; Özkan, N.; Devrim, Y. *Electrochim. Acta* **2017**, 245, 1-13.
20. Fang, J.; Lin, X.; Cai, D.; He, N.; Zhao, J. *J. Membr. Sci.***2016**, 502, 29-36.

21. Escorihuela, J.; Sahuquillo, Ó.; García-Bernabé, A.; Giménez, E.; Compañ, V. *Nanomaterials* **2018**, 8, 775.
22. Singha, S.; Jana, T. *ACS Appl. Mater. Interfaces* **2014**, 6, 21286−21296.
23. Hazarika, M.; Jana, T. *ACS Appl. Mater. Interfaces* **2012**, 4, 5256−5265.
24. Sannigrahi, A.; Ghosh, S.; Maity, S.; Jana, T. *Polymer* **2011**, 52, 4319−4330.
25. Sannigrahi, A.; Arunbabu, D.; Sankar, R. M.; Jana, T. *Macromolecules* **2007**, 40, 2844−2851.
26. Maity, S.; Jana, T. *Macromolecules* **2013**, 46, 6814−6823.
27. Sana, B.; Jana, T. *Polymer* **2018**, 137, 312−323.
28. Harilal; Nayak, R.; Ghosh, P. C.; Jana, T. *ACS Appl. Polym. Mater.* **2020**, 2, 3161−3170.
29. Harilal; Shukla, A.; Ghosh, P. C.; Jana, T. *ACS Appl. Energy Mater.* **2021**, 4, 1644-1656.
30. Wang, S.; Zhao, C.; Ma, W.; Zhang, N.; Liu, Z.; Zhang, G.; Na, H. *J. Power Sources* **2013**, 243, 102−109.
31. Yang, J.; Aili, D.; Li, Q.; Cleemann, L. N.; Jensen, J. O.; Bjerrum, N. J.; He, R. *ChemSusChem* **2013**, 6, 275−282.

Chapter 6

Rational Design of Microporous Polybenzimidazole Framework for Efficient Proton Exchange Membrane Fuel Cell

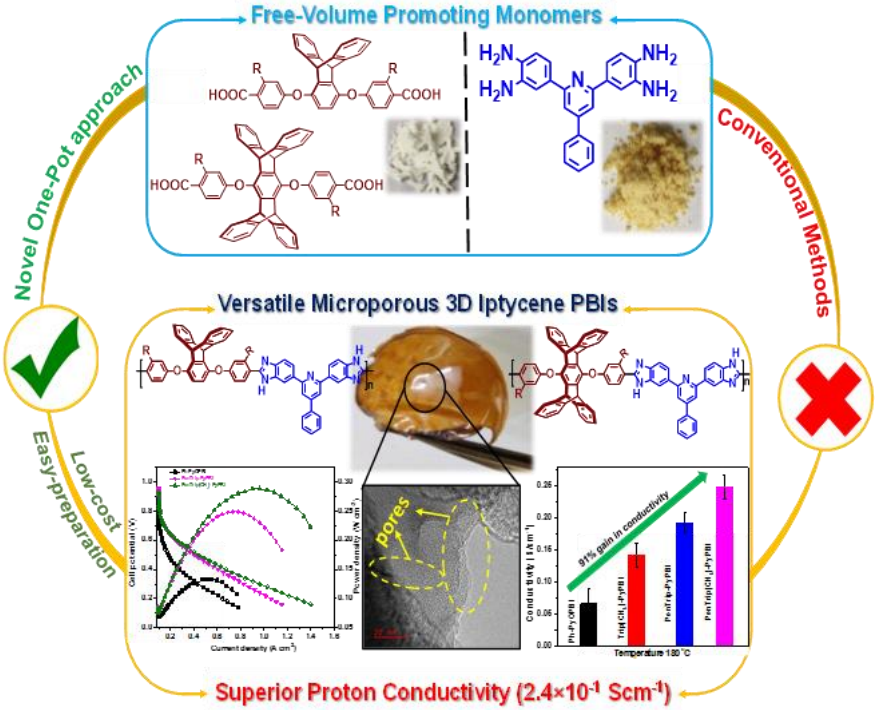

In this chapter, we report a reliable, scalable, high-yield (>95%) and cost-efficient strategy to synthesize a novel class of 3D pentiptycene and triptycene containing oxygen-enriched arylether diacid monomers. These diacids have been further used to synthesize a series of advanced hierarchical microporous 3D iptycene-based PyPBIs in a rapid and operationally simple reaction medium followed by casting as PEMs for the use in HT-PEMFC.

Harilal; Bhattacharyya, R.; Shukla, A.; Ghosh, P. C.; Jana, T. communicated to *J. Mater. Chem. A*

6.1 INTRODUCTION

The increasing demand of sustainable energy as alternative to traditional energy resources has pushed the research and development of new materials into new heights in recent years. In particular, anhydrous proton-conducting polymer membrane materials used in HT-PEM fuel cell in which chemical energy is transformed into electrical energy in a direct, green and efficient way have received significant attentions and has become most sought-after materials in the modern energy systems.[1] Anhydrous proton-conducting polymer membrane material that work above 100 ^{o}C enables fast reaction kinetics and improve cell efficiency.[1] Polybenzimidazoles (PBIs) loaded with phosphoric acid (PA) have been in the limelight for the past few decades in constructing anhydrous PEM.[2,3] Nevertheless, it remains a hard task to form a definite structure by suitably organizing PBI's chains which could have stabilize the PA network. Such a structural entity can limit the swelling of PBI chains in the pool of PA and hence leakage of PA from PBI matrix can be eventually stopped. Swelling of the PBI chains in PA also slows down the proton motion due to the steric hindrance.[4] Due to all of these factors, the PEMs of PBI are often found to be unreliable in yielding sustainable performance and show proton conductivity in the range of 10^{-2} S cm^{-1} which is one order of magnitude lesser than neat PA (~10^{-1} S cm^{-1}). In addition, the intricate method of synthesis and poor solubility of the PBIs circumscribed the scale-up of PBI production.[3] In an attempt to address these issues, to date, much efforts have been pursued by various elegant strategies and synthetic approaches.[5-14] Unfortunately, no noticeably successful strategies have known so far which resolved the above concerns and showed the improvement of properties of PBI based HT-PEMs. As part of this viewpoint, in a recent effort, we have strategically introduced a new kind of alternative PBIs with soluble, readily accessible and processable pyridine functionalized PBIs (PyPBIs) homo and copolymers as PEM candidate that nullified most of the concerns as discussed above.[15–19] However, the overall performance of these PEMs especially in proton conductivity need to be further improved to realize future development.

Notably, it has been reported that the local and translational diffusion of proton carriers significantly affects the rate of proton transfer and hence to improve the proton carrier's ability to transport, flexible organic polymers or high-porosity frameworks would be very much useful as those will be capable of developing built-in channels for a carrier are considered to be promising. Proton-conducting porous polymer membranes hold tremendous attention as a novel type of potential electrolytes owing to their high internal surface area, intrinsic

microporosity and tunable functionality.[20–26] The presence of pores in the membranes pushes the electrolyte uptake and thereby facilitating proton transportation. Hence, to promote effective proton transport, creation of porous materials with interconnecting pores consisting of tailored pore volume, size could be the right approach. In earlier reports porous PBI structures have been created by leaching out low molecular weight porogens from the membrane matrix.[27, 28] However, formation of large pores because of porogens can be the reason for severe damage and carbon monoxide poisoning due to PA bleeding of the membrane.[29] In addition, large pores would help in flow of proton carrier molecules instead of protons. Hence, to overcome these issues, there is an obvious need to develop synthetically novel flexible linkages of PBIs consisting of high internal free volume and an appropriate pore size distribution so as to enable rapid proton transfer and accommodate large amounts of PA. It is however worth noting that, the rational design of such amorphous yet hydrophilic and *template-free* porous PBI framework structures for HT-PEM remains difficult and challenging. It has been reported that iptycene and its derivatives are promising building blocks for constructing supramolecular host or microporous polymers because of their highly 3D interwoven structure, abundant free-volume and are found to be useful in making ion conducting polymer membranes.[30-35] Gong et al. first demonstrated the potential of a triptycene-derived poly(arylene ether sulfone)s as membrane material for PEMs.[34] Swager and co-workers have recently reported a triptycene-based poly(ether ketone) membrane system with large internal molecular free volume that showed increased proton conductivities in low relative humidity and high temperature.[33]

However, as far as we are aware, there has been no report on the iptycene-based PBI as PEM in the literature yet, possibly because of the scant availability of appropriate polymerizable iptycene building blocks and relatively complex structure determination. Therefore, considering the demands on advanced porous PBI microstructure, inspired by the aforementioned advantages of the unique porous network structure of iptycene-containing polymers and one of our current objective in developing proton conductive materials for applications in the HT-PEMFCs, we hypothesized that a polycondensation reaction between two conformationally rigid and large free volume monomers would results in porous benzimidazole-linked polymers that may hold a large amount of PA and at the same time maintain the original shape with a good retention ability of PA. As a proof of this concept, we have carefully chosen monomers like pentiptycene (PenTrip), triptycene (Trip) and pyridine

functionalized tetraamine (PyTAB) to create rigid polymer backbones with enhanced microporosity. Taking consideration into these aspects, herein, for the first time, we report a reliable, scalable, high-yield (>95%) and cost-efficient strategy to synthesize a novel class of 3D pentiptycene and triptycene-containing oxygen-enriched arylether diacid monomers. These diacids have been further used to synthesize a series of advanced hierarchical microporous 3D iptycene-based PyPBIs in a rapid and operationally simple reaction medium consisting of a mixture of CF_3SO_3H, CH_3SO_3H and P_2O_5. The successful synthesis of monomers and polymers are confirmed by a variety of analytical techniques. To our knowledge, no network PBI PEMs have hitherto been reported with 3D iptycene-based (i.e., triptycene and pentiptycene) dicarboxylic acid as primary building blocks. We believe our combination of this strategy which include incorporation of nitrogen-enriched pyridine-functionalized heterocycles, flexible arylether (–O–) and the inefficient chain packing would result as interconnected microchannel walls to accommodate large amounts of PA molecules by strong acid-base interactions and capillary force for fast and efficient proton conduction under anhydrous conditions. We hope, our macromolecular architecture concept would motivate the rational design of a new class of porous polybenzimidazole loaded with electrolyte for advanced energy applications.

6.2 EXPERIMENTAL SECTION

The source of all the materials and reagents used in this work are included in the Supporting Information. In addition, all the characterization methods details are also included in the supporting information.

6.2.1 Synthesis of iptycene containing arylether diacid monomers

A series of iptycene such as pentiptycene and triptycene-containing diacid monomers (**4 c**, **d** and **8 c**, **d**) were synthesized by the hydrolysis of the dicyano intermediates of pentiptycene and triptycene (**3 a**, **b** and **7 a**, **b**) which were generated via the aromatic nucleophilic substitution between pentiptycene and triptycene-hydroquinone (**2** and **6**) and halogenated cyano compounds as portrayed in **Scheme 6.1**. The key intermediates, i.e., pentiptycene and triptycene diquinone (**1** and **5**) and pentiptycene and triptycene-hydroquinone (**2** and **6**) used for synthesis of acid monomers were synthesized according to previously reported methods.[36-38] Two different *ortho*-substituent group (i.e., H and CH_3) were introduced at the position neighbouring to the pentiptycene and triptycene units in order to understand

effect of the relative internal molecular-free volume in the corresponding polymer chains by altering the molecular structures of the arene planes of the pentiptycene and triptycene units. The details of monomer synthetic procedures and characterization are included in the **Appendix IV**.

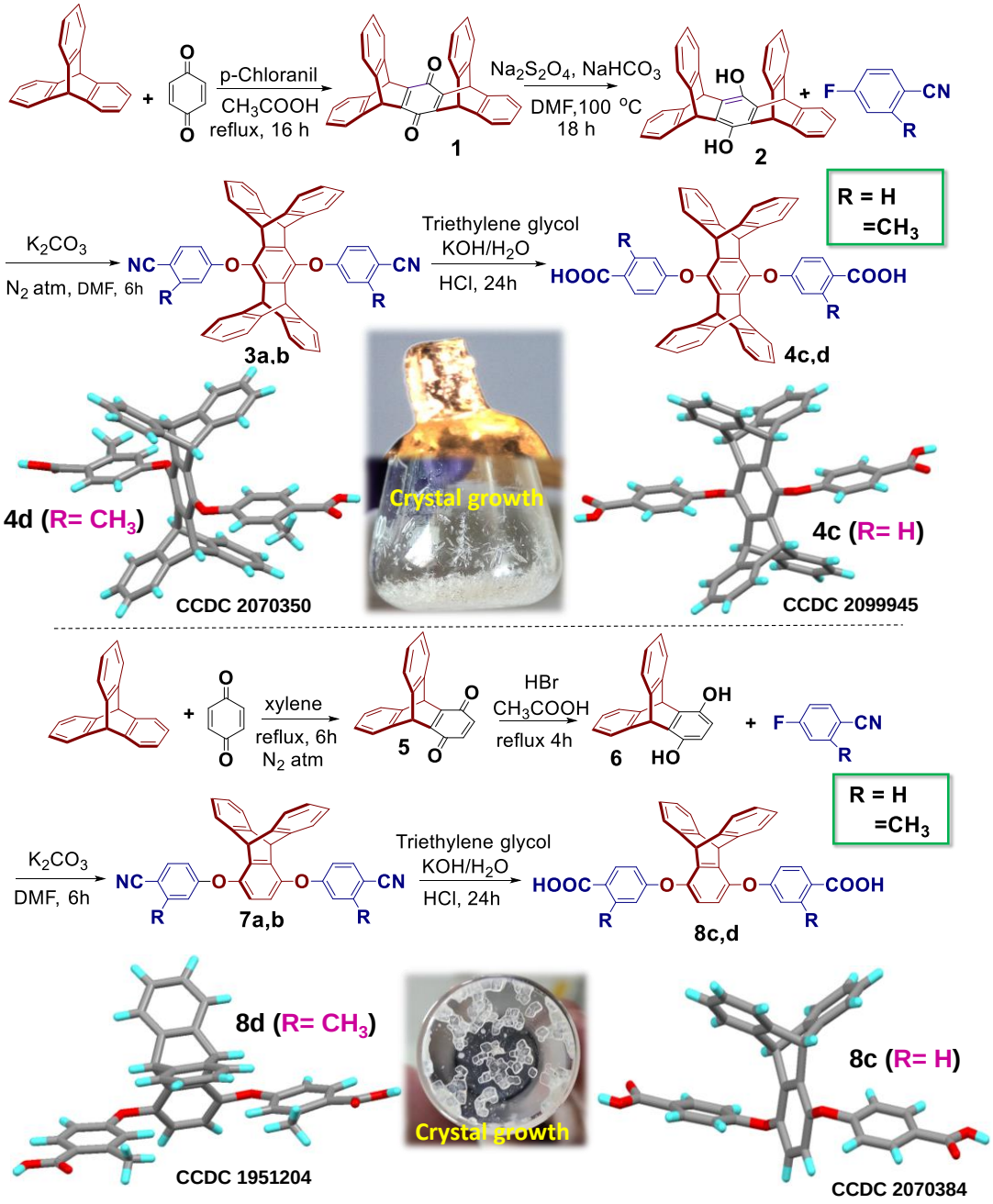

Scheme 6.1. Synthetic route used for constructing various 3D pentiptycene (**4 c, d**) and triptycene (**8 c, d**)-based dicarboxylic acid monomers. Representative photos of single crystals

growth of these molecules in solution are also shown here. Crystal structure (ball-and-stick model) of all the compounds are included in the figure. Carbon, oxygen and hydrogen are represented in light grey, red and light blue color, respectively. Solvent molecules are omitted for clarity.

6.2.2 Synthesis of polymers

We screened various synthetic conditions by altering solvents, temperature and reaction time for the synthesis of iptycene-based PyPBIs (**Appendix IV Table 6.3**). Under optimal conditions, the arylether ladder type iptycene-based PyPBIs namely, Trip-PyPBI, Trip(CH_3)-PyPBI, PenTrip-PyPBI and PenTrip(CH_3)-PyPBI were prepared via a polycondensation reaction of various arylether diacids monomers [Trip-COOH, Trip(CH_3)-COOH, PenTrip-COOH and PenTrip(CH_3)-COOH] with pyridine functionalized tetramine (PyTAB) as presented in **Figure 6.1 (b)**. The molar ratios were kept as 1:1 between aryl-ether dicarboxylic acid and PyTAB monomers for all the polymer synthesis in this work. The general synthetic procedure for the synthesis of PenTrip(CH_3)-PyPBI was carried out in the following way: 3.88 g (5 mmol) of purified PenTrip(CH_3)-COOH (**4d**), 2.0 g (5 mmol) of PyTAB, 5 mL of CF_3SO_3H and 10 mL Eaton's Reagent (PPMA,1:1 mixture of CH_3SO_3H and P_2O_5, see the supporting information for the preparation details of PPMA) were taken in a 50 mL three-necked mercury sealed round bottomed flask equipped with a mechanical overhead stirrer, a nitrogen inlet and an outlet. Then, the mixture was stirred using mechanical stirrer and slowly heated up to 100 °C for 2 h. After this we added 2 g of P_2O_5 in the reaction mixture and another 1 h stirring was continued at 140 °C under N_2 atmosphere. The synthetic condition mentioned in the last row of **Appendix IV Table 6.3** was followed as this condition resulted best yield. After the complete polymerization reaction, a dark brown colour high viscous polymer solution was obtained, slowly poured into deionized (DI) cool water (600 mL) with stirring and the obtained precipitated solid polymer [PenTrip(CH_3)-PyPBI] was filtrated and washed repeatedly with copious amount of water. The residual phosphoric acid in the polymer powder was neutralized with 10 wt % $NaHCO_3$ solution at 40 ^oC overnight and the polymer was washed thoroughly with DI water until the wash water pH reached 7.0, and then dried under reduced pressure at 100 ^oC for 24 h to get 5.76 g (98% yield) of a dark brown solid. Schematic presentation of the polymerization reaction mixture and the purification process are shown in **Figure 6.1 (c)**. **^{1}H NMR** of PenTrip(CH_3)-PyPBI (500 MHz, DMSO-d_6) δ [ppm]: 13.11 (s,

NH), 8.64 (s, 3H), 7.95 (d, 4H), 7.83 (dd, 8H), 7.74 (s, 4H), 7.69 (s, 4H), 7.59 (s, 7H), 8.51 – 5.86 (m, 2H), 7.38 – 7.08 (m, 2H), 7.13 (s, 2H), 7.13 (s, 2H), 7.01 (s, 6H), 6.99 (s, 4H), 7.61 – 5.86 (m, 2H), 6.78 (ddd, 8H), 6.00 (s, 4H). **IR (ATR)**: ν [cm^{-1}] = IR (ATR): ν [cm^{-1}] = 3500-3100 (vibration of O-H from moisture and imidazole ring N−H vibration), 1593-1541 (C=N, C=C vibration), 1450-1397 (in-plane benzimidazole ring vibration), 1211-1160 (asymmetric C−O vibration) and 757 (C−H stretching vibration of pyridine ring).

Synthesis of PenTrip-PyPBI. The synthetic protocol of PenTrip-PyPBI was similar to that of PenTrip(CH_3)-PyPBI. The only difference is that PenTrip-COOH (**4c**) monomer was used with PyTAB in this case for the polymerization. The resulting polymer was obtained as a dark-brown powder in 84% isolated yield. **^{1}H NMR** (500 MHz, DMSO-d_6) δ [ppm]: 13.05 (s, NH), 8.63 (s, 5H), 8.35 (s, 2H), 8.47 – 8.12 (m, 10H), 8.47 – 7.95 (m, 4H), 7.73 (s, 2H), 7.60 (d, *4*H), 7.55 (s, 2H), 7.10 (s, 4H), 6.97 (s, 2H), 6.02 (s, 4H), 2.42 (s, 4H). **IR (ATR)**: ν [cm^{-1}] = 3061 (imidazole ring N−H vibration), 1597-1542 (C=N, C=C vibration), 1455-1398 (in-plane benzimidazole ring vibration), 1217-1163 (asymmetric C−O vibration) and 759 (C−H stretching vibration of pyridine ring).

Synthesis of Trip-PyPBI. The synthetic condition of Trip-PyPBI was similar to the synthesis of PenTrip(CH_3)-PyPBI using Trip-COOH (**8c**) and PyTAB in the stoichiometric ratio. The brown coloured fiber type polymer was obtained with a yield of 89%. **^{1}H NMR** (500 MHz, DMSO-d_6) δ [ppm]: 13.09 (s, NH), 8.64 (s, 2H), 8.63 – 7.93 (m, 10H), 7.96 (s, 5H), 7.96 (s, 2H), 9.96 – 7.15 (m, 8H), 9.96 – 7.02 (m, 4H), 7.74 (s, 2H), 9.96 – 6.97 (m, 2H), 7.59 (s, 3H), 9.96 – 6.15 (m, 2H), 7.43 – 6.61 (m, 6H), 7.28 – 5.86 (m, 5H), 6.03 (s, 2H). **IR (ATR)**: ν [cm^{-1}] = 3300-2750 (imidazole ring N−H vibration), 1593-1541 (C=N, C=C vibration), 1468-1397 (in-plane benzimidazole ring vibration), 1220-1163 (asymmetric C−O vibration) and 760 (C−H stretching vibration of pyridine ring).

Synthesis of Trip(CH_3)-PyPBI. Polymer Trip(CH_3)-PyPBI was synthesized from Trip(CH_3)-COOH (**8d**) and PyTAB at 140 °C by following the synthetic procedure as described in all other cases. The obtained polymer was brown coloured fiber with a yield of 89%. **^{1}H NMR** (500 MHz, DMSO-d_6) δ [ppm]: 13.02 (s, 1H), 8.23 (s, 4H), 8.14 (s, 2H), 7.97 – 7.02 (m, 11H), 7.57 (d, 5H), 7.40 (dd, 6H), 7.34 (s, 5H), 7.12 (s, 4H), 6.96 (d, 4H), 6.91 – 6.85 (m, 6H), 6.16 (s, 2H), 2.13 (s, 6H). **IR (ATR)**: ν [cm^{-1}] = 3300-2750 (imidazole ring N−H vibration),

1593-1541 (C=N, C=C vibration), 1469-1397 (in-plane benzimidazole ring vibration), 1220-1165 (asymmetric C−O vibration) and 760 (C−H stretching vibration of pyridine ring).

6.2.6. Proton exchange membrane preparation

Polymer solutions were prepared by dissolving Trip-PyPBI, Trip(CH_3)-PyPBI, PenTrip-PyPBI and PenTrip(CH_3)-PyPBI into a DMSO over a 24 h period to obtain a clear 2 wt % polymer solution. After filtration through a 0.5 μm PTFE syringe filter, the filtered polymer solutions were poured onto clean glass Petridis and the solutions were slowly evaporated by placing at 100 °C for 12 h in a hot air oven. Homogeneous self-standing membranes were obtained, peeled from the glass Petridis and washed repeatedly with deionized water and dried under vacuum at 120 °C for 12 h to remove traces of residual DMSO. The obtained membranes thickness was around from 60 to 80 μm. These membranes were stored in the desiccator until further use. **Figure 6.1 (d)** displays a pictorial presentation of the various membrane fabrication steps. These membranes were dipped into H_3PO_4 (85%) bath for 3 days to get proton exchange membrane (PEM) (see the details in **Appendix IV**).

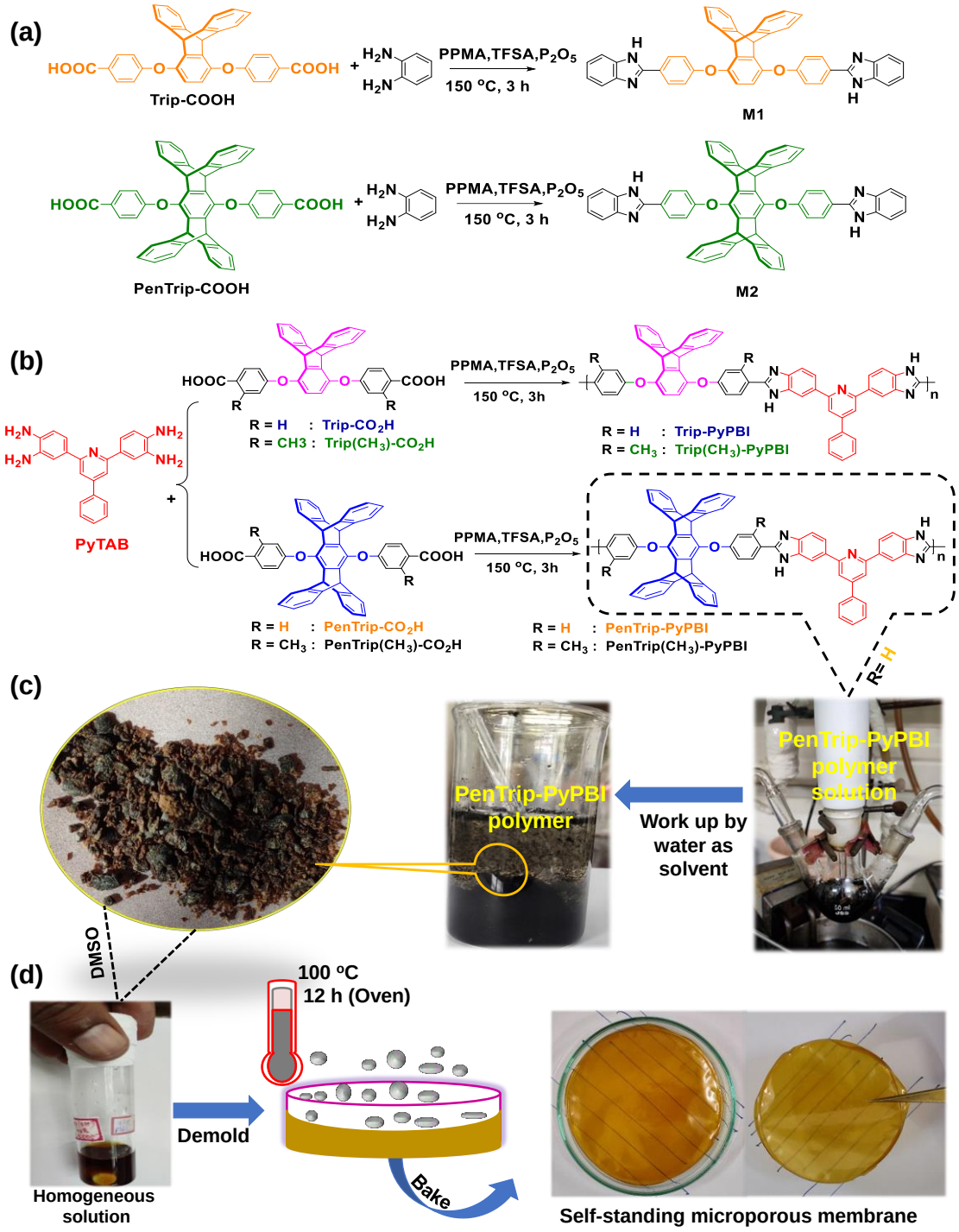

Figure 6.1. Schemes for synthetic procedures of the (**a**) model compounds (**M1** & **M2**), (**b**) 3D iptycene-based PyPBI polymers in gram-scale. (**c**) Representative pictorial presentation of polymerization mixture collection and purification process of PenTrip-PyPBI and (**d**) schematic illustration of the preparation of PenTrip-PyPBI membrane by solution casting process.

6.3. RESULTS AND DISCUSSION

6.3.1 Design strategy

We incorporated 3D iptycene units into the polymer backbone to make inherently stable pyridine functionalized-oxypolybenzimidazoles with hierarchical ultrafine-intrinsic-microporosity and unidirectionally aligned channels in order to have easy passage to neat liquid phosphoric acid (PA). A representative construct of such structure in case of PenTrip(R)-PyPBI is shown in **Figure 6.2a**. Structural features of iptycene monomers are such that it perturbs the efficient packing to form crystalline lattices rather they tend to yield clathrates with included solvent molecules as seen from the single crystal structure of PenTrip(CH_3)-COOH (CCDC No. 2070350) and Trip(CH_3)-COOH (CCDC No. 1951204) (**Figure 6.2c** & **g**, respectively). The total accessible free volume of PenTrip(CH_3)-COOH and Trip(CH_3)-COOH frameworks for solvent molecule were estimated to be 42.1 and 37.7%, respectively of their unit cell volume (**Figure 6.2b** & **f**, respectively) and obtained from the crystallographic packing analysis viewed in the *ab*-plane (**Figure 6.2d** & **e** and **f** & **i**, respectively). An analogy to such a function can be drawn conceptually for crystalline iptycene solids.[39] In order to visualize free-volume in these monomers, we have inscribed an iptycene molecule into a trigonal prism which has high probability to form a dense crystal. The internal free volume (IFV) is shown in the **Figure 6.2b** & **f** geometrically can be defined as the volume between the surface of trigonal prism.[40,41] Therefore, we envisioned that rigid C_{3v}-symmetric iptycene-based dicarboxylic acid building blocks could be potential precursors for construction of microporous polybenzimidazoles. However, one discrete entity is that the micropore walls are engineered to possess flexible arylether, pyridinic linkages and benzimidazole units which pilled-up along the linear direction so that each and every microchannel consists of abundant proton accepters like imidazole and pyridinic nitrogen and proton donor [arylether (–O–)] functionalities. The presence of hydrogen bonding acceptor nitrogen atom in the pyridinic linkage drives the single point hydrogen-bonding interactions with PA. In contrast, the benzimidazole framework structure with both oxygen and nitrogen atoms can develop multiple interactions with the PA molecules through hydrogen bonding so as to stabilize and lock the PA networks in the micropores. Such a precise tailoring of interactions by designing pore architectures has not been achieved with PBI frameworks so far in the literature. Especially, the nitrogen atoms in the pyridine and imidazole units are protonated to create pyridinium and imidazolium cations while $H_2PO_4^-$ anion is obtained by deprotonation of H_3PO_4 so as to facilitate the proton network movement

through charge assisted $H_2PO_4^{-}\cdots{}^{+}H$-N hydrogen bond resulting enhanced proton conductivity. We reasoned that this heterogeneous micropore wall configuration is the structural basis for strong proton networks in the micropores and for creates proton conducting paths to enable fast proton transport. Clearly, our strategy brings the advantages of both uniform-intrinsic-microporosity and PBI functionality into one material and addresses the key fundamental challenges in making PEM from PBIs. As a proof-of-concept, we observed that the intrinsically microporous 3D iptycene-based PBI frameworks exhibit ultrafast proton conductivity over a wide range of temperatures from 30 °C to 180 °C without external humidification as discussed later section in this article.

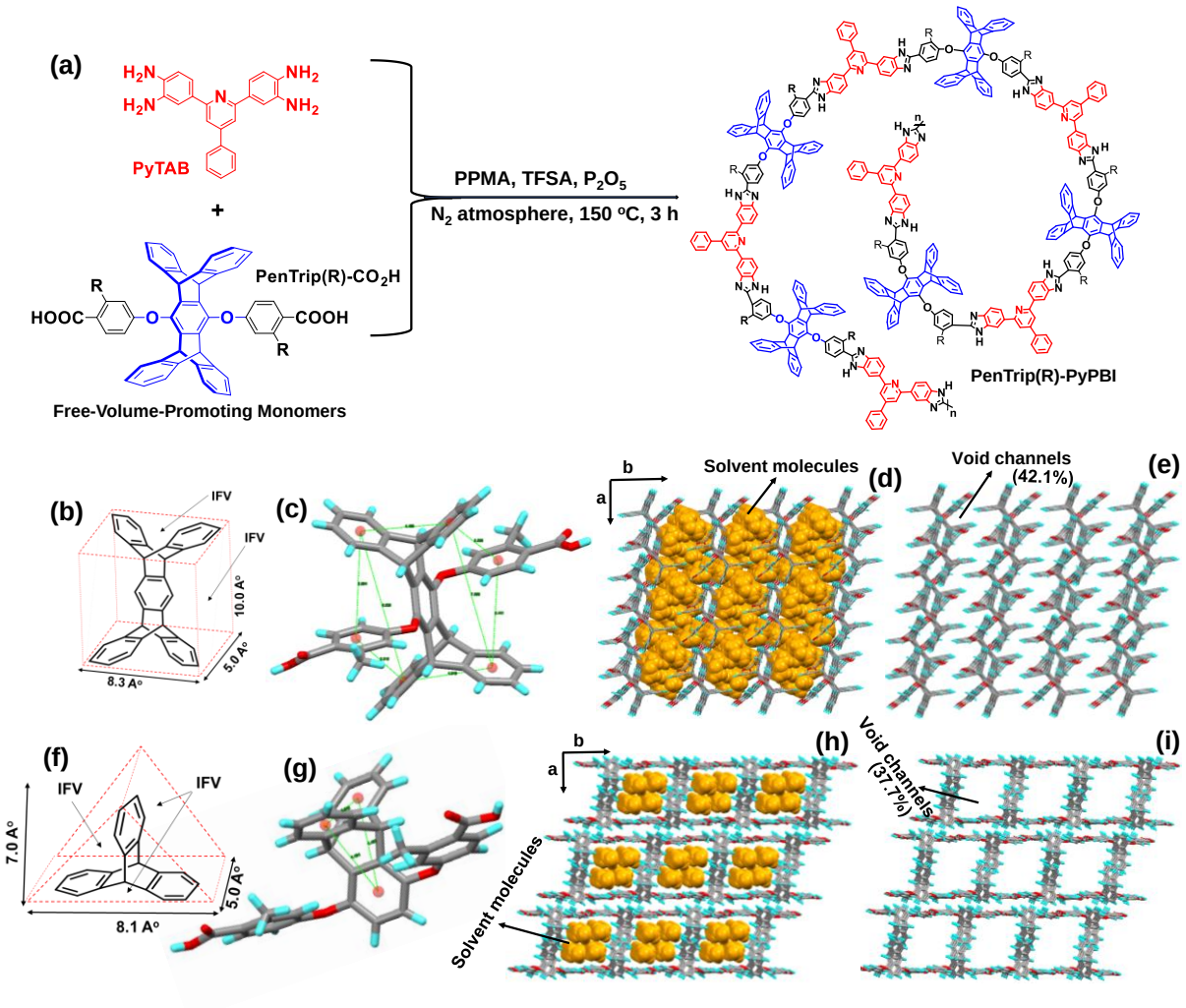

Figure 6.2. Strategy for preparing stable microporous amorphous 3D iptycene-based PyPBIs. (**a**) Condensation of 3D iptycene-based diacids and PyTAB to produce a microporous amorphous iptycene-based PyPBIs. (**b**) Illustration of internal free volume (IFV) of

pentiptycene. (**c**) X-ray crystal structures of PenTrip(CH_3)-COOH and crystallographic packing 3D structure (**d** & **e**) showing uniform void channels highlighted with and without solvent molecules, respectively; 1,4-dioxane (yellow orange) solvent molecules viewed in the *ab*-plane. (**f**) Illustration of internal free volume (IFV) of triptycene. (**g**) X-ray crystal structure of Trip(CH_3)-COOH and crystallographic packing 3D structures (**h** & **i**) showing uniform void channels highlighted with and without solvent molecules, respectively; hexane (yellow orange) solvents in this case viewed in the *ab*-plane. Red, grey and light blue colours correspond to oxygen, carbon and hydrogen atoms, respectively.

6.3.2. Synthesis and structural confirmation of monomers and polymers

In this work, we targeted the synthesis of two series of triptycene and pentiptycene-containing arylether dicarboxylic acids with systematically varied substituted groups ca. H and CH_3 named as Trip-COOH, Trip(CH_3)-COOH, PenTrip-COOH and PenTrip(CH_3)-COOH, respectively with high purity and yields. To our knowledge, Trip(CH_3)-COOH, PenTrip-COOH and PenTrip(CH_3)-COOH diacids had never been reported, though Trip-COOH is reported.[41] Under the optimized conditions **(Appendix IV Table 6.2)**, we have achieved the Trip(CH_3)-COOH, PenTrip-COOH and PenTrip(CH_3)-COOH diacids synthesis in high yield on a multi-gram scale from a triethylene glycol acid hydrolysis as shown in **Scheme 6.1**. To our delight, the reaction was relatively clean and the products diacids were obtained as the major product in >80% yield (see **Appendix IV Table 6.2**, entry 8). It is important to note that the monomers **3 a**, **b** and **7 a**, **b** exhibits good solubility in triethylene glycol which makes the synthetic conditions of diacids mild and facile route. The multistep synthetic strategy of diacids is schematically depicted in **Scheme 6.1**. The slow evaporation of the solution of Trip-COOH (CCDC No. 2070384), Trip(CH_3)-COOH (CCDC No. 1951204), PenTrip-COOH (CCDC No. 2099945) and PenTrip(CH_3)-COOH (CCDC No. 2070350) produced high-quality colorless needle-shaped crystals at room temperature (**Scheme 6.1**), which are unambiguously confirmed by single-crystal X-ray diffraction (SCXRD) and a variety of spectroscopic techniques. The particulars of structural refinement and data collection for four diacids are provided in **Appendix IV Table 6.1 (a)** and **Appendix IV Table 6.1(b)**. The complete characterization data of these diacid monomers are shown in the supporting information and

all the NMR (both ^{1}H and ^{13}C) and FT-IR spectra are shown in **Appendix IV Figures 6.2–6.17.**

With the 3D non-planar diacid building in hand, we further executed the synthesis of the first 3D iptycene-based porous PBI polymers by reacting Trip-COOH, Trip(CH_3)-COOH, PenTrip-COOH and PenTrip(CH_3)-COOH diacids with pyridine functionalized tetraamine (PyTAB)[15] under polycondensation reaction conditions as shown in [**Figure 6.1(a)** & **(b)**]. However, we found aromatic-rich iptycene-containing dicarboxylic acid non-planar molecule is insoluble in common polymerization solvents probably due to an anomalous C-H…π stacking interactions and stronger hydrogen bonding networks between the adjacent molecules (carboxyl···carboxyl) (**Appendix IV Figure 6.22** and **6.23**). Therefore, it is a critical task to find a suitable synthetic process to make the iptycene-based polybenzimidazoles. Hence, we are endeavoured to screen various polycondensation conditions including solvents, temperatures, and reaction time (**Appendix IV Table 6.3**) and finally under a certain condition (last entry in **Appendix IV Table 6.3**) obtained four amorphous porous polymer networks, termed as Trip-PyPBI, Trip(CH_3)-PyPBI, PenTrip-PyPBI and PenTrip(CH_3)-PyPBI in a reaction medium comprising of a mixture of CF_3SO_3H, CH_3SO_3H and P_2O_5 followed by heating at 140 °C for 3 hours **(Figure 6.1b)**. To our surprise, when a reaction medium containing a mixture of CF_3SO_3H, CH_3SO_3H and P_2O_5 were used as polymerization solvent, polymers with high molecular weight (estimated from higher inherent viscosity) are obtained (see **Appendix IV Table 6.3**, entry 9). With this optimized condition, we examined the generality of this polymerization method (**Appendix IV Table 6.3**, entry 9), firstly we synthesized the desired model derivatives (**M1** and **M2**) by condensation of commercially available o-phenylenediamine (OPDA) and iptycene-based diacids (Trip-COOH and PenTrip-COOH) with moderate to good yields (>90%) (**Figure 6.1a**, top row). Noteworthy, the synthesis of two model compounds greatly influences us to go further with the similar synthetic path. Therefore, we ascertained from our above observations that the CF_3SO_3H–catalyzed PPMA (mixture of P_2O_5 and CH_3SO_3H) is the appropriate choice of solvent for 3D iptycene-based PyPBI polymers. Both the synthesis and characterization were done multiple times to confirm the reproducibility of the results. The polymer molecular weight was determined from inherent viscosity (IV) measurements by following earlier reported procedure for PBI and values are tabulated in **Appendix IV Table 6.4**. The viscosity average molecular weight was obtained from the Mark−Houwink–Sakurada equation.[42,43] The synthesized polymers are

having very good molecular weight as seen from **Appendix IV Table 6.4** which endures the formation of flexible membranes with enough mechanical strength for the fabrication of PA doped PBI PEM. We also made a non-iptycene-based PBI (**Appendix IV Scheme 6.1** denoted as Ph-PyOPBI) according to the method reported in our previous studies[18] for the purpose of comparison in evaluating the properties and performance of hierarchically structured 3D iptycene-based PyPBI membranes reported in this study.

The evolution of formed benzimidazole linkage in 3D iptycene-based PyPBI polymers are monitored by the FT-IR, ^{1}H-NMR, solid-state ^{13}C NMR and X-ray photoelectron spectroscopy (XPS). **Figure 6.3a** compares the IR spectra of monomers and all the aryl ether-linked iptycene-based PyPBI polymers. Important characteristic stretching modes of the polymer structure, indicated by dotted lines and marked with different colour rectangles, are clearly visible in the spectra which have been previously discussed in the literature as signature IR frequencies for PBI polymers.[13,15] After the polymerization, the characteristic stretching mode (3375 cm^{-1}) of amino groups from PyTAB monomer and the mode (1696 cm^{-1}) of carboxylic acid group (C=O) from iptycene-based diacids was greatly attenuated, which indicates the formation of the imidazole rings. Besides, the appearances of new peaks at 1594 cm^{-1} and 1469 cm^{-1} originated from the C=N and C=C stretching modes demonstrates the successful benzimidazole ring formation. Additionally, the prominent characteristic vibration modes between 1240 and 1280 cm^{-1} corresponding to asymmetric and symmetric Ar-O-Ar linkage stretching modes reveals the preservation of arylether functional groups during the polymerization consistent with those in model compounds **M1** and **M2** (IR peaks at 1255 cm^{-1} and 1030 cm^{-1}, **Appendix IV** Figures **6.19** and **Appendix IV 6.21**).[44] In addition, a distinguished characteristic modes of methyl groups are found at around 2965-2850 cm^{-1} in the Trip(CH_3)-PyPBI and PenTrip(CH_3)-PyPBI polymers.

The ^{1}H NMR spectra further supported the effective formation of benzimidazole linkages in all these polymers as seen from **Figure 6.3b**. The chemical shift of the typical imidazole NH and iptycene scaffold bridgehead carbon (marked with light green colour circle) attached proton of all these polymers is centred at 13.23 and 5.99 ppm, respectively which are well consistent with those in the model compounds (**M1** and **M2**) NMR peaks at 13.4 ppm and 6.1 ppm (**Appendix IV** Figures **6.18** and **Appendix IV 6.20**). Aromatic protons chemical shifts appear at around 7.1-8.71 ppm. Notably, in the case of Trip(CH_3)-PyPBI and PenTrip(CH_3)-PyPBI spectra, analogously to the aromatic ring protons, one additional identical downfield

signal at 2.2 ppm is also clearly visible compared to other iptycene-based polymers which is ascribed to the protons of the *ortho*-methyl groups (highlighted in the magnified view). Solid-state ^{13}C NMR spectra further confirms the characteristic resonance signals of benzimidazole group and iptycene scaffold bridgehead carbons for Trip-PyPBI and PenTrip-PyPBI polymers at 110-152 and ~50 ppm, respectively (**Appendix IV Figure 6.24**). Similar spectral features are reported in literature and agrees well with our model compounds (**M1** and **M2**) (**Appendix IV** Figures **6.18** & **Appendix IV 6.20**).[25, 30]

Furthermore, the XPS tests were performed on the four iptycene-based PyPBIs to investigate the differences in their surface functional groups. The XPS survey spectra (**Figure 6.3c)** and an elemental content (atomic percent) table (**Appendix IV Table 6.5**) shows that the three predominant peaks of C 1s (284.8 eV), N 1s (401.08 eV) and O 1s (540.58 eV) for all polymers indicating the existence of C, N, and O elements in the 3D iptycene-PyPBIs. We further investigate the types of carbon and nitrogen atoms in PyPBIs by fitting the high-resolution. The C 1s peaks at 284.8 and 287.6 eV are assigned to C=C and C-C bonds for PenTrip(CH_3)-PyPBI (**Figure 6.3d**) and Trip(CH_3)-PyPBI [**Appendix IV** Figure **6.25 (c)**], respectively and peaks at 285.2 eV are assigned to C=C bonds for PenTrip-PyPBI (Figure **6.3f**) and Trip-PyPBI [**Appendix IV** Figure **6.25 (a)**]. The two typical N 1s peaks at 399.45 and 401.08 eV are allocated to pyridinic-N and imidazole-N bonds for all 3D iptycene-PyPBI [Figure 6.3e, g and **Appendix IV Figure 6.25 (b, d)**], respectively. These binding energies of 3D iptycene-PyPBIs were matched well with those of PBI in previous literature.[20] In light of all these spectral results, undoubtedly the formation of arylether-linked iptycene-based pyridine-functionalized oxypolybenzimidazoles is proved.

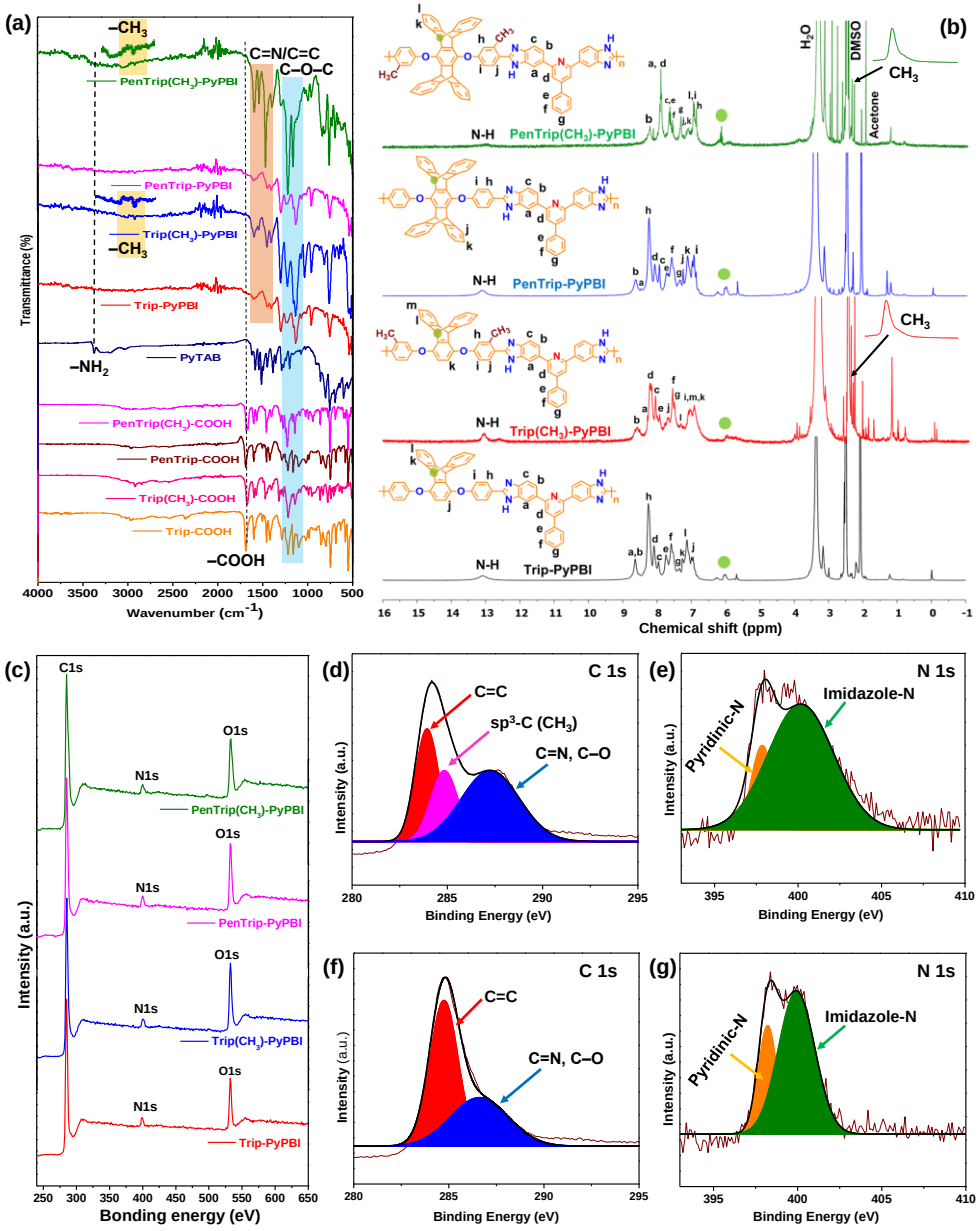

Figure 6.3. Fourier transform infrared spectra (**a**) and ^{1}H NMR spectra recorded in DMSO-d_6 (**b**) of all the synthesized polymers. All the monomers FT-IR spectra are also included for comparison. XPS full spectra (**c**) of iptycene-based PyPBIs and high resolution XPS spectra of C1s, N1s band of PenTrip(CH_3)-PyPBI (**d** and **e**) and PenTrip-PyPBI (**f** and **g**).

6.3.3. Solubility behaviour of 3D iptycene-PyPBI

It is well known that solubility of the PBIs in solvents including polar solvent is poor due to the rigid structure and strong intra and intermolecular H-bonding interactions between imidazole groups of PBI.[13] However, it is important to note here that the high molecular weight

iptycene-based PyPBIs shows good dissolution in NMP, DMAc and DMSO at room temperature even up to concentrations of 2 wt% (**Appendix IV Table 6.4**). This good solubility behaviour is ascribed to the rational design of PBI structures consisting of the flexible main arylether chain and the bulky 3D iptycene rings which perturb the dense packing and interchain interactions, and hence create larger free volume leading to enhanced solubility. Thus, the improvement of solubility leads to the formation of strong, homogeneous transparent iptycene-based PyPBI membranes readily by solution casting method as depicted in **Figure 6.1(d)**.

6.3.4. Polymer chain packing and microporosity

The PXRD patterns of the 3D iptycene-based PyPBI polymers are shown in **Appendix IV Figure 6.26**. The broad halos of the diffraction pattern indicate the complete amorphous nature of the polymers. The inclusion of bulky rigid iptycene motifs in the backbone is expected to reduce the interchain interactions leading to the loss of crystallinity and enhancement in amorphous nature is observed. The d-spacing corresponding to peak at ~24° 2θ is due to the face-to-face packing as mentioned noted by several authors earlier.[16, 22]

It has been observed that polymer of intrinsic microporosity (PIM) derived from iptycene-based monomers have reasonable surface areas with inherent hierarchical porosity for applications in gas separation membranes.[30, 45] However, void space and functionality of pore surface are important structural factors need to be designed for proton-conductive frameworks with the impregnation of conducting media. This prompted us to investigate the permanent intrinsic microporosity through BET surface area measurements of all as-synthesized iptycene-based PyPBIs. We used the most commonly used gas probe, i.e., nitrogen (N_2) to measure the porosity and surface area of the resultant polymer networks at 77 K and the isotherms are shown in **Figure 6.4a**. These isotherms indicated a typical microporous Type-II N_2 sorption isotherm for these polymers.[46] The obtained BET surface area of Trip-PyPBI, Trip(CH_3)-PyPBI, PenTrip-PyPBI and PenTrip(CH_3)-PyPBI are 34, 37, 41 and 50 $m^2\ g^{-1}$, respectively, which are superior to that of Ph-PyOPBI (12 $m^2\ g^{-1}$) and earlier reported conventional PBI polymer like m-PBI (16 $m^2\ g^{-1}$).[47] This could be ascribed mainly to the internal molecular free-volume of iptycene units as discussed in **Figure 6.1**. However, it is also interesting to highlight the change in BET surface area, pore size and pore volume on altering the backbone structure (**Table in Figure 6.4c**). Again, these observations indicate the presence of much larger internal molecular

free-volume of bulky methyl substituted pentiptycene than that of triptycene and hence attributing to a great potential of pentiptycene moieties in constructing highly porous materials. The pore size distribution (PSD) (**Figure 6.4b**) was estimated by the density functional theory (DFT) method based on the N_2 sorption isotherms and reveals that these polymeric networks have pores that are microporous (pore width <12 Å).[30] This observation proves the presence of microporous nature of the synthesized iptycene-based PyPBIs, and no macropores (i.e., pore width greater than 50 nm) are observed in the iptycene-based polymer networks. It is evident that the infusion of 3D and shape-persistent bridged bicyclics iptycene ring synergistically contributed to the effective disruption of tight chain packing and generating large micropores within the membranes which may enable fast proton transport in these polymer membranes.

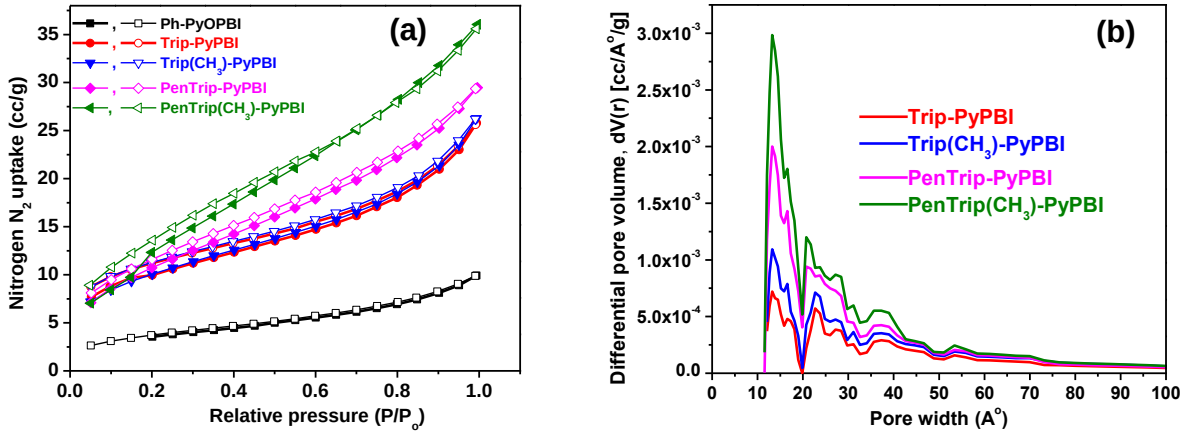

(c)

Sample identity	BET surface area ($m^2\ g^{-1}$)	Total pore volume ($cm^3\ g^{-1}$)	Average pore size (Å)
Ph-PyOPBI	12	-	-
Trip-PyPBI	34	6.9×10^{-4}	12.01
Trip(CH_3)-PyPBI	37	10.9×10^{-4}	12.5
PenTrip-PyPBI	41	19.5×10^{-4}	12.8
PenTrip(CH_3)-PyPBI	50	29.9×10^{-4}	13.01

Figure 6.4. (**a**) The N_2 sorption isotherms at 77 K and **(b)** pore size distribution of iptycene-based PyPBIs along with Ph-PyOPBI. (**c**) A table showing various data obtained from BET study. Adsorption and desorption isotherm are indicated using filled and empty symbol, respectively.

6.3.5. Morphology of the membranes

We used field emission scanning electron microscope (FESEM), atomic force microscopy (AFM) and high-resolution transmission electron microscopy (HR-TEM) techniques to understand the microscopic morphological features of the as-prepared hierarchical membrane structures. It should be noted that the internal microstructure morphology has a significant influence on the performance of PEMs. FESEM cryo-fractured cross-sectional images of the membranes are shown in **Figure 6.5a**. All the 3D iptycene-based PyPBI membranes display a ripple-spongy-like network structure consisting of microcavities which increases with an increase in inflexible bridged bicyclic aromatic units (as we go from left to right in the **Figure 6.5a**). This may be due to the "inter molecular free volume" of iptycene-aromatic segments. This spongy-like feature is more visible in pentiptycene-based PyPBI membranes which shows various improvement in the physical properties of the membrane such as stability, mechanical property and phosphoric acid absorption etc.(discussed in later section). Furthermore, the AFM and TEM images (**Figure 6.5b** & **6.5c**,**d**) also show that the iptycene-based membrane possesses an ordered columnar void channel structural arrays which are absent in case of Ph-PyOPBI membrane (**Appendix IV Figure 6.27**). AFM topographic height images (**Figure 6.5b**) revealed similar surface morphology with cylindrical microdomains cavities in a few micrometers for all membranes that are almost absent in the case of Ph-PyOPBI membrane [**Appendix IV Figure 6.27 (b)**]. The incorporation of ladder-type bulky units reduces the root mean square (RMS) roughness and promotes self-aggregation and which in turn produces a phase separated morphology in the membranes. The bright region is due to the hydrophobic iptycene PyPBI chain-rich domain while the dark region can be assigned to the hydrophilic region formed by the clustering of long ether-bonded pyridinium and imidazolium groups. HR-TEM images (**Figure 6.5c** & **d**) reveals that abundant and evenly distributed interconnected sphere-like narrow channels (white portion, indicated by yellow markings) are present in the iptycene-based PyPBI membranes but in absent Ph-PyOPBI membrane [**Appendix IV Figure 6.27 (c)**].[30, 34] Notably, the pores with an average diameter of 2 nm is seen in iptycene-based PyPBIs (yellow highlights in **Figure 6.5d** at high-resolution, indicating a distinct hierarchical microstructures formed in these samples which agrees well with the BET microcavity size estimations discussed in the previous section. To our knowledge, these sizes are smaller than those from porous PBI materials reported so far. Thus,

by combining the morphological results along with BET, we can conclude the presence of sphere-like pore network and large free volume, which will probably facilitate proton hopping between adjacent H_3PO_4 molecules and can be boost the final PEM performance in this class of materials.

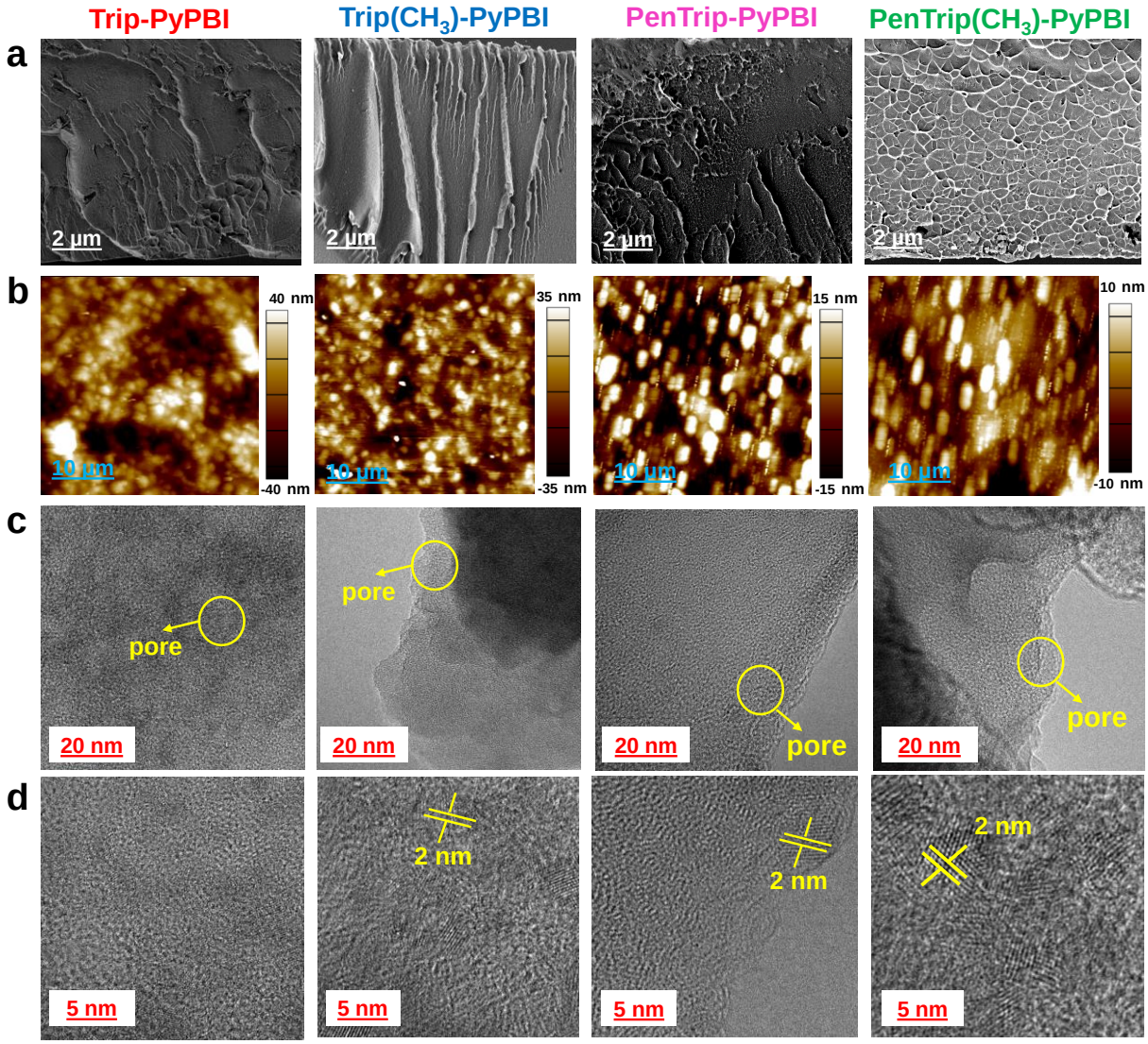

Figure 6.5. Microscopic morphologies of all the polymer membranes. Each column is identified with different polymer as noted at the top. (**a**) Cross-sectional FESEM, (**b**) AFM height and (**c** & **d**) HR-TEM images with scale bar 20 and 5 nm, respectively.

6.3.6. Chemical stability screening

Membranes with good chemical stability are required in PEMFC as mechanical stress imposed in the membrane-electrode-assembly (MEA) fabrication and oxidative environment

created during the electrochemical operation process. Therefore, we examined the oxidative (chemical) stability by immersing the as-prepared iptycene-based PyPBIs membranes in 3% hydrogen peroxide (H_2O_2) solution containing 4 ppm $FeSO_4$ (Fenton reagent) at 70 °C for 6 days (see the experimental procedure in the Supporting Information). We measured the weight loss as a function of time and observed that no substantial weight loss during the degradation experiment as compared to pristine Ph-PyOPBI [**Figure 6.6(a)**]. This may be due to the formation of supramolecular interlocked structures and the presence of π-π interactions because of iptycene units, which prevent the polymer backbones from the attack by the radicals generated from Fenton's reagent. Among the four 3D iptycene-based membranes, the PenTrip(CH_3)-PyPBI polymer based membrane degradation is the lowest and almost negligible (<4%). This low rate of degradation of PenTrip(CH_3)-PyPBI membrane is related to strong supramolecular face to face π-π stacking interactions induced by pentriptycene units[31] and the methyl groups on the phenyl linkers cause inductive effect that weaken the polarisation of imidazole (C=N) units and soften the interlayer electrostatic repulsion, yielding stable network of this polymer.[48] After the stability test for 6 days as discussed above, the membranes were washed, dried, and then FT-IR spectra was recorded. Surprisingly, all the characteristic stretching bands are retained (**Appendix IV Figure 6.28**) demonstrating prolonged integrity of the benzimidazole linkages and robustness of the frameworks even in this oxidative chemical environment. We were also curious about the porous structures of iptycene-based polymers after testing with Fenton's reagent. However, it is noteworthy that N_2 adsorption isotherms (**Figure 6.6b**) at 77K after 6 days Fenton's reagent treatment, are very close to those of as-synthesized materials (discussed in previous section, **Figure 6.4a**) which further confirmed that the porosity is intact in the membrane. We further investigated the stability of iptycene-based PyPBIs by immersing into concentrated (85 wt%) H_3PO_4 solution at 120 ^oC for 1 week. **Figure 6.6c** reveals that the iptycene-based PyPBIs membranes did not exhibit any significant changes in H_3PO_4 solution. This can be clearly observed from the picture of the membranes in the solution where no sign of broken membrane or a change in the solution colour are seen. Also, after the removal from the solution the membranes were subjected to bending, twisting and folding by applying forces but we did not observe any breakage in the membrane rather they remain flexible as seen from the picture (**Figure 6.6c** upper panel**)**. We also noted the weight loss of the membranes after 1 week of PA soaking at 120 ^oC and displayed them as the remaining weight (%) along with pristine Ph-PyOPBI (**Figure 6.6d**). There is negligible weight

loss for all iptycene-based PyPBI membranes-only 3 to 4 % weight is lost even after 1 week of treatment in PA at 120 °C however, only 87% is remaining in case of Ph-PyOPBI. This series of experimental results suggested that flexible unsymmetrical bulky 3D iptycene type structure in the backbone of PyPBI greatly increases the chemical stability in both oxidative environment and in concentrated PA medium even at higher temperature like 120 ^{o}C for 1week.

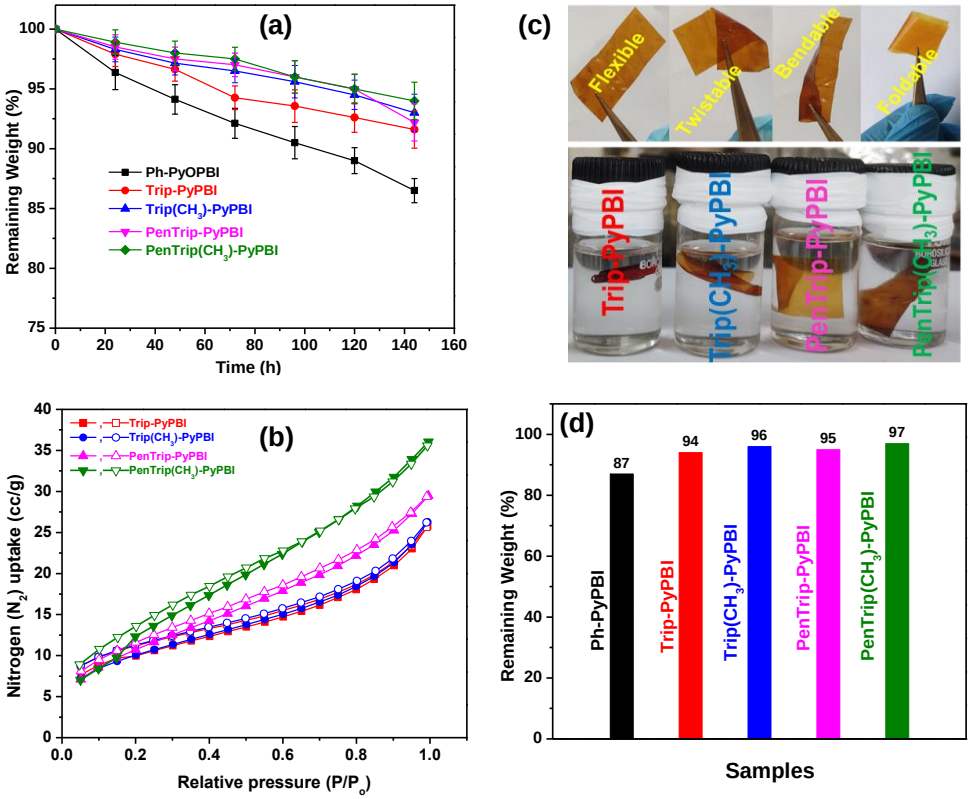

Figure 6.6. **a**) Chemical stability of all the membranes in 3% H_2O_2 containing 4 ppm Fe^{2+} at 70 °C. (**b**) N_2 adsorption-desorption isotherms at 77K for iptycene-based PyPBIs after being soaked in Fenton's reagent (washed and dried before conducting the measurement). Adsorption and desorption isotherm are indicated using filled and empty symbol, respectively. **(c)** Demonstration of the robustness of the freestanding PA-doped iptycene-based PyPBI membranes after the solubility test and (**d**) membrane remaining weight after the solubility test soaked in PA at 120 °C for 1 week.

6.3.7. Thermal stability and thermomechanical properties

The durability of a working HT-PEMFC depends upon the thermal and mechanical characteristics of the PEM and hence optimization of the thermomechanical properties of

PEMs are necessary. The undoped iptycene-based membranes showed almost no mass loss up to 350 ºC, 5% mass loss observed at 523-536 ºC and char yields are more than 80% at 700 ºC for all the cases (**Figure 6.7a**). All the samples exhibit comparable thermal stability with the reported Ph-PyOPBI.[15] In comparison to those of undoped membranes, the PA-doped membranes display two step mass losses: a loss which began at about 200 °C is due to the release of water from H_3PO_4 and the creation of pyrophosphoric acid and higher ordered phosphate species and the second mass loss above 450 ºC is ascribed to degradation of the PBI main chains.

Furthermore, DMA measurements of the membranes were conducted from 100−400 °C and results are presented as temperature-dependent storage modulus (E′), loss modulus (E″), and tan delta (δ) plots (**Figure 6.7)**. It is clearly observed from **Figure 6.7b** that the E′ of the iptycene-based PyPBI membranes are superior to that of the Ph-PyOPBI membrane at all temperatures and also the value of E′ increases with increasing bulky pendant iptycene with ortho substituted methyl on phenylene units. The improved storage modulus in iptycene-based PyPBI membranes is credited to the very special molecular configurations of iptycenes that enables strong supramolecular interactions via a chain-threading and interlocking mechanism.[30, 31, 39] In addition, a large increase in the glass transition temperature (T_g) of the iptycene-based PyPBIs relative to the non-iptycene Ph-PyOPBI is also observed. It could be seen from **Figure 6.7 (c, d)** that the loss modulus and tan delta curves for the iptycene-based PyPBIs are much more intense than those of the non-iptycene Ph-PyOPBI, demonstrating their improved dampening properties. Among the all iptycene-based PyPBI polymers, PenTrip-PyPBI polymer displays significantly higher T_g value at 410 °C. The observed increase in T_g indicates that the bulky shape of pentiptycene units effectively increase the polymer chain rigidity.[38, 39] On the other hand, the strong supramolecular interlocking steric interactions between adjacent chain benzene rings of pentiptycene units might also help to obtain higher glass transition temperatures. In addition, we cross-examine the stress-strain behaviour of the membranes after PA loading using a universal testing machine (UTM) (**Appendix IV Figure 6.29**). Tensile strength and elongation at break, obtained from the stress vs strain plot, of the PA-loaded 3D iptycene-based PyPBI membranes show higher or comparable elongation than the PA-doped Ph-PyOPBI. Our results clearly demonstrates the effect of molecular level change in achieving high mechanical strength. From these TGA and DMA results, it can be

resolved that all the iptycene-based PyPBI membranes made in this work meet the thermomechanical stability requirements for the use in HT-PEMFC.

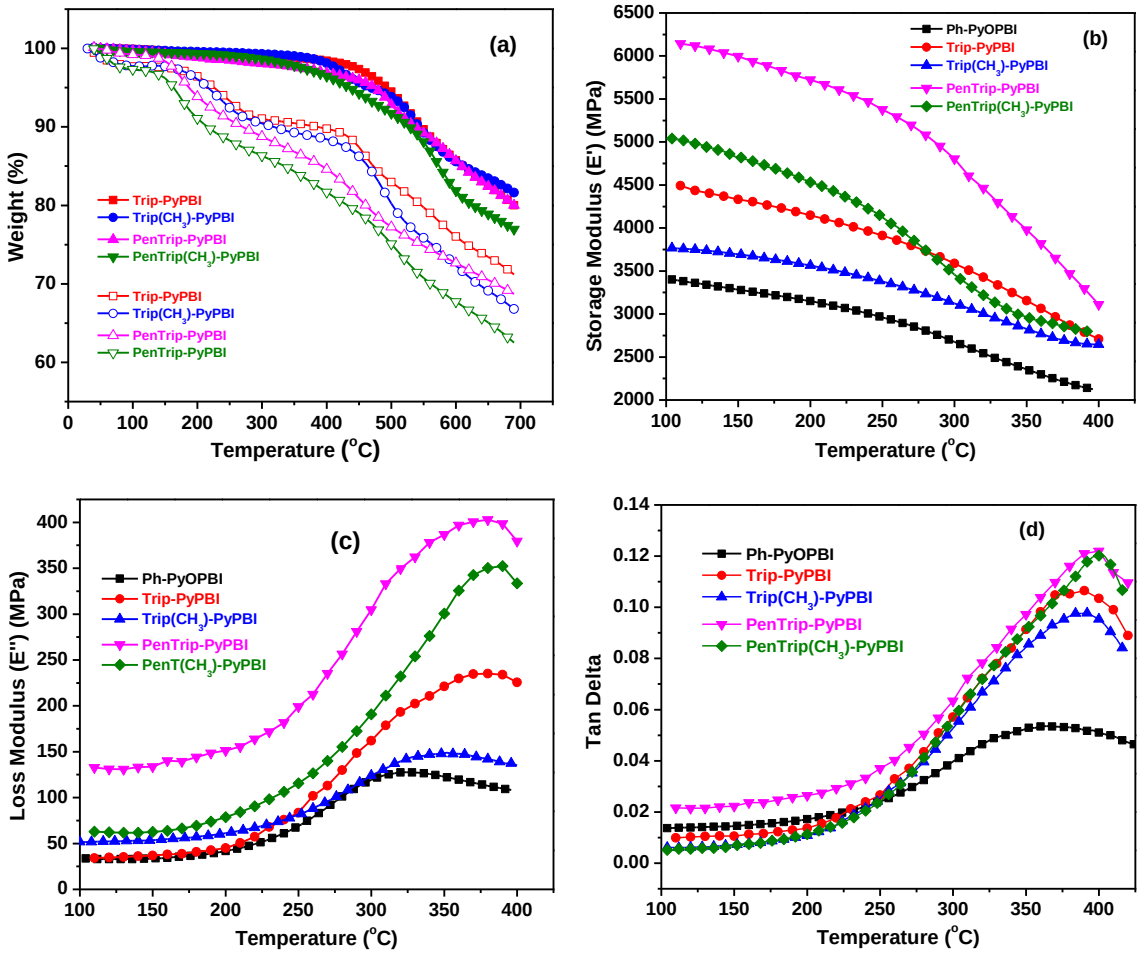

Figure 6.7. (**a**) TGA curves of undoped (filled symbols) and PA-doped (unfilled symbols) iptycene based PyPBIs measured under N_2. DMA plots of undoped membranes: (**b**) storage modulus (E'), (**c**) loss modulus (E'') and (**d**) Tan δ plots against temperature.

6.3.8 Phosphoric acid loading and dimensional stability of membranes

The phosphoric acid (PA) doping level (ADL) and swelling behaviours of the iptycene-based PyPBI membranes were measured and compared with that of Ph-PyOPBI membrane based on a standard titration protocol (see Supporting Information) The ADL (PA moles per PBI repeat unit) of all the prepared membranes are presented as a function of doping time in **Figure 6.8a** and the PA uptake (in weight %) is also shown in **Appendix IV Figure 6.30**. The ADL and PA uptake of Trip-PyPBI, Trip(CH_3)-PyPBI, PenTrip-PyPBI and PenTrip(CH_3)-

PyPBI could easily reach up to 20 (446 wt %), 25 (489 wt %), 28 (573 wt %) and 32 (600 wt %), respectively, which are much higher than the Ph-PyOPBI 18.20 (410 wt %). This is owing to the fact that the open space between the benzene blades of iptycene moieties, known as "internal molecular free volume", which induces significant amount of permanent microvoid space that facilitated the adsorption of PA molecules. Also, the ample of multiple inherently strong proton accepting and donating functionalities such as arylether (–O–), pyridinic nitrogen (pyri-N) and imidazole aligned across the membranes of PyPBI provides sites for anchoring the H_3PO_4 network through strong hydrogen bonding of P=O···H–N, O–H···N=C and O–H···O–C interactions.[2] The bulky iptycene scaffold prohibits the polymers from packing efficiently, leading to void space in the ladder-type PyPBIs backbone as discussed in the earlier section and hence facilitated adsorption of more PA compared to conventional Ph-PyOPBI in a concentrated PA aqueous solution. Furthermore, in the comparison of Trip(CH_3)-PyPBI with PenTrip(CH_3)-PyPBI show that the later membrane could absorb more PA, which is attributed to the high degrees of internal free void space of pentiptycene units as indicated in earlier section. FTIR study proves the presence of PA as seen from the new stretching and in-plane bending vibration modes of the P=O, P–O bond of phosphate anions ($H_2PO_4^-$) anion at 990 and 497 cm^{-1},[20, 49] respectively (**Figure 6.8c**). Noticeably, the shifting of vibration band of the C=N bond to 1648 cm^{-1} indicating that the nitrogen atom of the C=N chemical linkage forms strong H-bonding interactions with PA in the channels (vide infra).[20, 48] In addition, the successful loading of PA were further confirmed by TGA analysis (**Figure 6.7a**) and their degradation temperature is above 200 ^oC, which is consistent with literature results.[18] These results and analyses unambiguously proved the presence of multiple hierarchical interactions between the walls of the current PBIs with the PA molecules.

It has been identified that the extreme swelling of PEM increases the ionic channels and thereby reduces the membrane stability. The high rigidity of the backbone can help in reducing the chain mobility and suppressing the excessive membrane swelling and hence can help in developing a well-defined microphase separated morphology which facilitates the proton transport and improves membrane stability. **Figure 6.8b** shows that the all these iptycene-based membranes exhibit excellent dimensional stability with low swelling ratios despite of their relatively high PA uptake (**Appendix IV Figure 6.30**). We believe that the

supramolecular interlocking interactions and π-π stacking owing to the iptycene units in the hydrophobic blocks are responsible in defeating the undesired excessive acid-swelling in PEM.

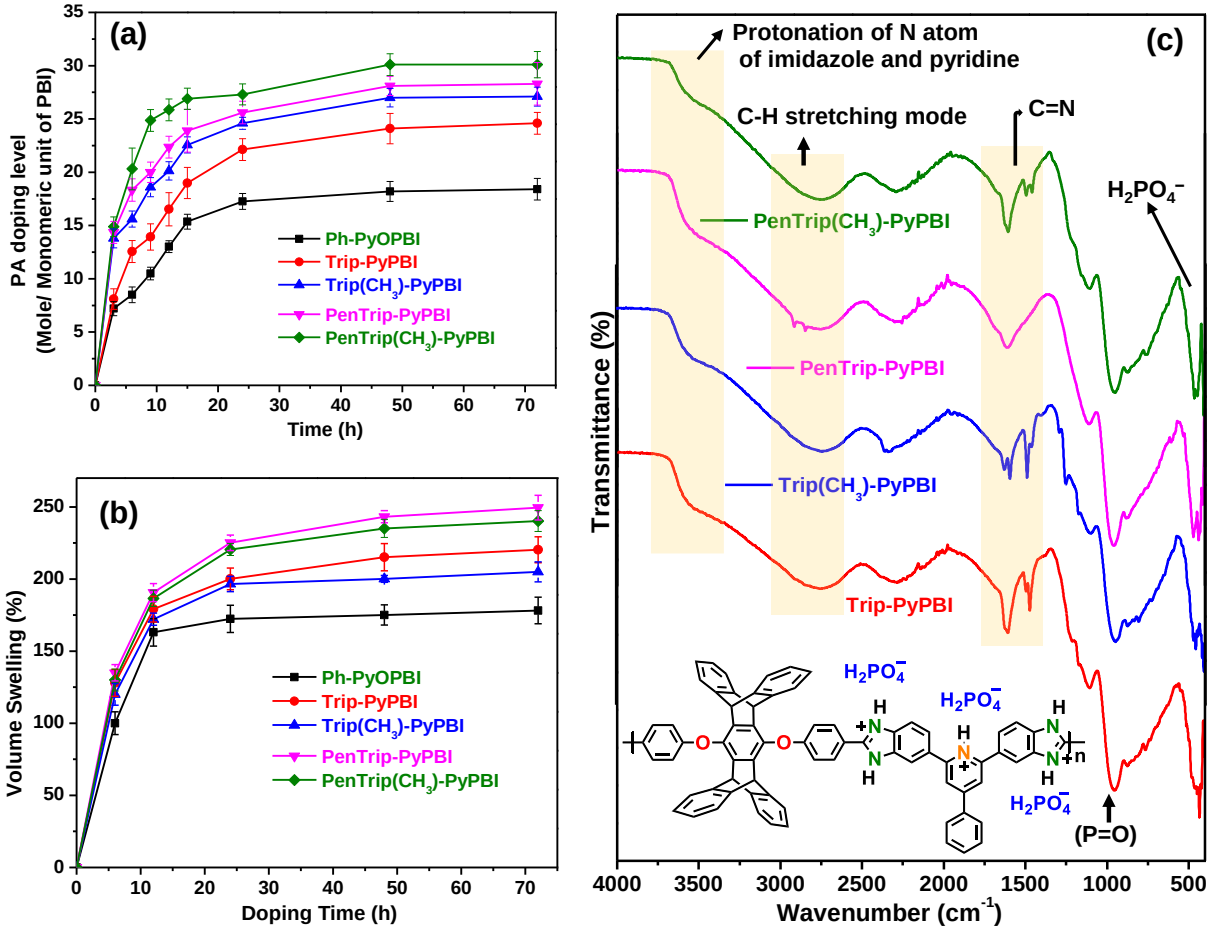

Figure 6.8. (**a**) Acid doping level (ADL) and (**b**) swelling volume of iptycene based-PyPBI membranes as a function of doping time and (**c**) IR spectra of iptycene-based PyPBIs after the treatment under acid conditions for 1 week. ADL is measured as moles of phosphoric acid (PA) per polymer repeat unit.

6.3.9. Proton conductivity

The preeminent thermal stability and structural insight motivated us to evaluate the proton conductivities of these 3D iptycene-based PEMs after loading with H_3PO_4. We used electrochemical impedance spectroscopy (EIS) to measure the proton conductivities of iptycene-based PEMs. Membranes developed in this work were dipped into 85 wt % PA for 72 h and dried in vacuum oven at 120 ^oC for 2 h prior to fixing into a four-point probe conductivity test cell (see Supplementary Information for details). Proton conductivity of the

membranes are generally expected to increase with the increasing PA content (loading) of the membranes and our current results are matching well with this trend. **Figure 6.9a** displays substantial improvement in proton conductivity as a function of temperature for different structure. The proton conductivity (σ) values are 0.24, 0.19, 0.16 and 0.13 S cm^{-1} at 180 °C in PenTrip(CH_3)-PyPBI, PenTrip-PyPBI, Trip(CH_3)-PyPBI and Trip-PyPBI, respectively. In contrast the proton conductivity of Ph-PyOPBI is only 0.06 S cm^{-1} at 180 °C which is significantly less compared to all other ladder-type iptycene-based PyPBI polymer PEMs. The highest proton conductivity value of 0.24 S cm^{-1} is obtained with a 600 wt% (ADL 32) H_3PO_4 loading, which is nearly 4 orders of magnitude higher than that of the Ph-PyOPBI and removes the maximum proton conductivity barrier of all PBI systems under anhydrous condition.[5-23] We believe that the reasons behind this kind of high conductivities of iptycene-based polymers are many folds and these are firstly, there are stronger multiple hierarchical interactions (P=O···H–N, O–H···N=C and O–H···O–C) between pyridine-functionalized oxypolybenzimidazole pore walls with the H_3PO_4 networks allow the membranes to hold large amount of PA which can initiate the formation of continuous proton-conducting paths.[16, 44] Secondly, the strong supramolecular edge-to-face π-π stacking interactions brought by 3D iptycene units are helpful in stopping the membrane swelling while retaining the favourable PA uptake needed for maintaining high proton conductivity in the membranes.[29] Thirdly, the significantly improved proton conductivity can be credited to the highly interconnected intrinsic microporous nature of iptycene-based PyPBI membrane, which enables the high loading of H_3PO_4 and interconnected continuous channels drives the formation of long-range ordered proton-conducting pathways for fast transport.[44] The subtle difference in proton conductivity values for various structures suggest that more facile proton transfer pathways are created among the bulky pendant fused arene rings containing iptycene-based PyPBI-H_3PO_4 adducts than Ph-PyOPBI because of the formation of strong hydrogen-bonding and packing through π-π interactions. Hence, the above discussion clearly attributes to the fact that the intrinsic microporosity has enormous effect in improving the performance of the membrane.

Subsequently, we monitored the long-term proton conductivity stability of all the acid-loaded membranes by keeping the membrane at 160 °C and maintain the conductivity after every 6 hours interval over 72 hours in order to mimic an operating PEMs environment. The proton conductivity initially shows drops in all the samples as shown in **Figure 6.9b** because of the removal of water molecules and some unstable acid and the local dimensional changes

in the membrane. Though initial drop in proton conductivities of these membranes is observed, the conductivities of the Trip-PyPBI, Trip(CH_3)-PyPBI, PenTrip-PyPBI and PenTrip(CH_3)-PyPBI membranes are much greater than a representative Ph-PyOPBI. Remarkably, the conductivity does not show an obvious change even after 40 hours (**Figure 6.9b**) indicating the excellent stability of proton conductivity and long-term thermal durability of the iptycene-based PyPBI membrane. Moreover, we found the structural integrity of PEMs are well maintained after these tests (**Appendix IV Figure 6.31**), again indicating the good stability of the prepared membrane. Furthermore, PA retention ability of the membranes were demonstrated by exposing them to water vapour at 100 °C for a period of 3 h and monitoring the remaining weight after every 30 min. It was found that all the membranes exhibit improved acid retention capacity (as high as 65.5 wt%) as compare to Ph-PyOPBI (~27 wt%) (**Appendix IV Figure 6.32**). the 3D iptycene-based porous PyPBI membranes show much better performance with regard to proton conductivities, ADL and especially conductivity stability compared to recently reported membranes especially traditional membranes[3] and porous PBI membranes,[27] as shown in **Appendix IV Table 6.6**. This comparison clearly indicates that the design and fabrication of the membranes with microporous structures can greatly facilitate the performance of HT-PEMFCs. The reproducibility of these resulted was consistent up to three experiments. Based on the above experimental results, we propose such high conductivity and retention stability is mainly due to the intriguing structural advantages such as abundant microporosity, excellent thermal-chemical stability and the ample multiple proton acceptor and proton donor functionalities are synergistically distributed on the channel surfaces and pointed inward, which provided a large number of continuous proton hopping highway and thereby facilitates the proton conducting process (**Figure 6.9c**). Hence, it is worth noting that the data clearly prove that the presence of pendant iptycene units in the backbone improves the acid retention capacity and stability of the membrane.

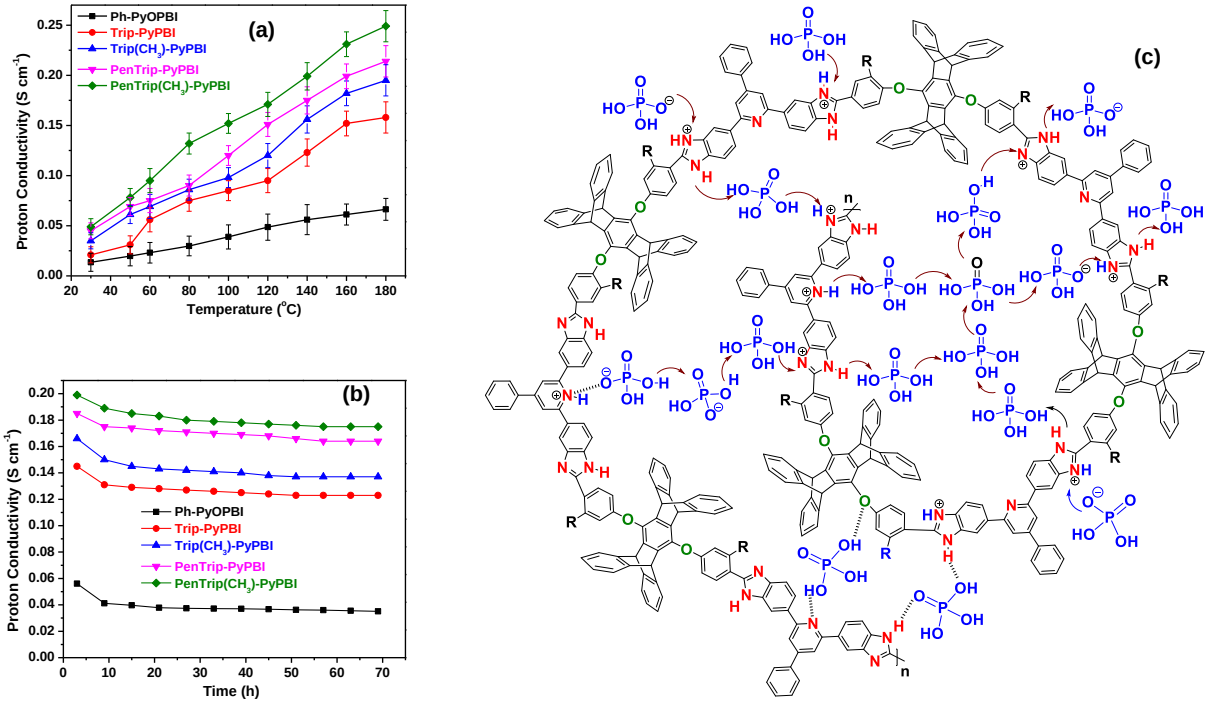

Figure 6.9. (**a**) Proton conductivity of PA-loaded iptycene-based PyPBI membranes as a function of temperature in a non-humidification environment and (**b**) conductivity stability of the membranes at 160 °C without humidification and (**c**) proposed multipoint bonding interaction pattern of PA molecules and proton transport with microporous iptycene-based pyridine functionalized-polybenzimidazole (IPyPBI) membrane.

6.3.10. Fuel cell performance test

The single cell performance of PA-loaded pristine Ph-PyOPBI and the microporous 3D iptycene-based PyPBI membranes were measured at 160 °C with unhumidified hydrogen and oxygen in ambient pressure. The polarization and power density curves of the MEA (membrane electrode assembly) made from the membranes developed in this work are shown in **Figure 6.10**. It shows that the MEA with the porous 3D iptycene-based PyPBI membranes exhibit a peak power density (PPD) in the range of 0.19−0.28 W cm^{-2}, which are much higher than that of the MEA with the pristine Ph-PyOPBI (0.13 W cm^{-2}). The open circuit voltages (OCV) of all MEAs are found to be greater than 0.9 V suggesting minimal fuel gas permeability through the membrane. This indicates that the 3D iptycene-based PyPBI membranes can deliver better fuel cell performance compared to the Ph-PyOPBI due to their continuous and well intergrown

structure with reasonably low gas cross-over and enhanced proton conductivity. Although the performance of the 3D iptycene-based PyPBI membranes are close to those of conventional PBI based PEMs but it is indeed quite promising since this is the first reported 3D iptycene-based PyPBI membranes. We disassembled the single cells and the tested membranes were taken out from the MEA to verify the physical condition of the membrane after performance analysis. Interestingly, we did not observe any physical damage in case of 3D iptycene-based PyPBI membranes even after completion of the fuel cell test (**Appendix IV Figure 6.33**). Currently we are working towards achieving better fuel cell performance by systematic optimizations of various parameters including thickness of carbon paper, catalysts type and loading, operating temperature, ionomer binder development and overall MEA fabrication process.

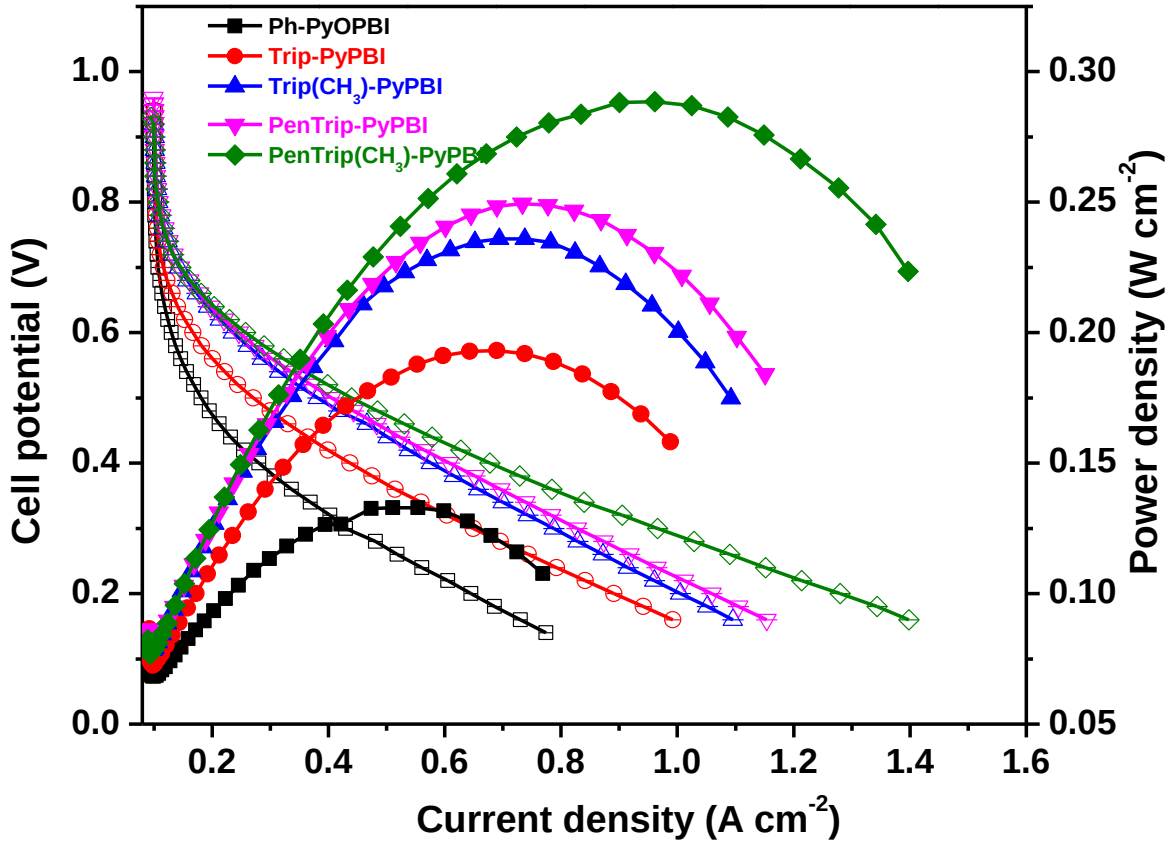

Figure 6.10. HT-PEMFC performance of PA-doped Ph-PyOPBI and 3D iptycene-based PyPBI membranes at 160 °C without humidification.

6.3.11. Photophysical Properties

Absorption peaks at around 280–345 nm obtained from the dilute solution of PBI have been assigned to the π-π* electronic transitions.[49, 51] Earlier, we have shown that the absorption maxima (λ_{max}) of longer wavelength π-π* transition is very responsive to the overall electronic conjugation in the PBI backbone and can be tuned easily by changing the chemical structure of the PBI chains.[16] The absorption spectra of iptycene-based PyPBIs are shown in **Appendix IV Figure 6.4a**. In case of Ph-PyOPBI, the absorption spectrum shows the highest intensity band at 325 nm with shoulder band at 270 nm where the highest intensity broad absorption band for the new polymers reported herein (iptycene-based PyPBIs) are observed in the range of 280–380 nm and these are assigned to π-π* transitions in the peripheral nonconjugated phenylene rings of iptycene and adjacent conjugated aromatic rings situated in the polymer chain. One shoulder bands is also observed around at 280 nm in addition to the highly intense band. These data indicated a bathochromic shift for iptycene-based PyPBIs with respect to Ph-PyOPBI. In iptycene-based PyPBIs, the extent of homoconjugation in the bridging chromophore is significantly higher which is responsible for the observed bathochromic shift.

Appendix IV Figure 6.4b shows the fluorescence emission spectra of all the polymers recorded from DMSO dilute solution. The emission peaks of the polymers are located at around 400−420 nm. A dramatically redshift and a significant increase in the fluorescence intensity relative to Ph-PyOPBI are observed for all iptycene-based PyPBI samples. Presumably, this is because of the incorporation of electron-donor methyl substituents at the *ortho* position of phenylenes and an increase in the structure rigidity favours increase conjugation and hence an increase in the fluorescence intensity. Thus, the fluorescence properties of polymers are because of the presence of interchain π-stacking interactions in the polymer chain and the increase in the luminescence intensity relative to the iptycene precursor is because of an increase in the structure rigidity.

6.4. Conclusion

In conclusion, we have shown a facile strategy for designing three-dimensional (3D) iptycene-based pyridine-functionalized oxypolybenzimidazoles (IPyPBIs) with inherent yet well-ordered micropores (~12.1 Å) to achieve fast and also stable proton conductivity under anhydrous condition over a wide range of temperature up to 180 °C. The hierarchical

microporous IPyPBIs networks are thermally and mechanically stable to aid the spatial quarantine of PA in the micropores. The pore walls trigger multiple H-bonding interactions with PA networks in order to stabilize and activate (via protonation deprotonation process) the proton exchange membranes. This structural alignment not only offers uniform pathways to achieve ultrafast proton conductivity at a high PA-doping level, but also locks the polymer framework to achieve stable performance at high temperatures. The IPyPBIs allow the combination of anhydrous conductivity, performance stability and high peak power density in one system–a set of fascinating features which are highly desired for HT-PEMFC performance. Owing to these unique structural features, we envisaged that 3D iptycene-based PBIs offer a path to design well defined super hierarchical microporous PBI materials for proton conductivity and in various areas including adsorption, separation, energy conversion, and catalysis.

Appendix IV

Detailed procedures describing the synthesis and characterization, including intermediates, monomers, model compounds and polymer synthesis, X-ray crystallographic data, XPS, PXRD, PA uptake and acid leaching are included in the Appendix IV (page no. 175-221).

REFERENCE

1. Haider, R.; Wen, Y.; Ma, Z.-F.; Wilkinson, D. P.; Zhang, L.; Yuan, X.; Song, S.; Zhang, J. *Chem. Soc. Rev.* **2021**, *50*, 1138-1187.
2. Quartarone, E.; Mustarelli, P. *Energy Environ. Sci.* **2012**, *5*, 6436-6444.
3. Aili, D.; Yang, J.; Jankova, K.; Henkensmeier, D.; Li, Q. *J. Mater. Chem. A* **2020**, *8*, 12854-12886.
4. Lee, A. S.; Choe, Y.-K.; Matanovic, I.; Kim, Y. S. *J. Mater. Chem. A* **2019**, *7*, 9867−9876.
5. Peng, J.; Wang, P.; Yin, B.; Fu, X.; Wang, L.; Luo, J.; Peng, X. *J. Membr. Sci.* **2021,** *640*, 119775.
6. Wang, P.; Peng, J.; Yin, B.; Fu, X.; Wang, L.; Luo, J.-L.; Peng, X. *J. Mater. Chem. A* **2021,** *9*, 26345-26353.

7. Wang, L.; Liu, Z.; Ni, J.; Xu, M.; Pan, C.; Wang, D.; Liu, D.; Wang, L. *J. Membr. Sci.* **2019,** *572*, 350-357.
8. Wang, P.; Liu, Z.; Li, X.; Peng, J.; Hu, W.; Liu, B. *Chem. Commun.* **2019,** *55*, 6491-6494.
9. Yin, B.; Liang, R.; Liang, X.; Fu, D.; Wang, L.; Sun, G. *Small* **2021,** *17*, 2103214.
10. Hu, M.; Ni, J.; Zhang, B.; Neelakandan, S.; Wang, L. *J. Power Sources* **2018,** *389*, 222-229.
11. Sannigrahi, A.; Ghosh, S.; Maity, S.; Jana, T. *Polymer* **2011**, 52, 4319-4330.
12. Singha, S.; Jana, T. *Polymer* **2014**, 55, 594-601.
13. Ghosh, S.; Sannigrahi, A.; Maity, S.; Jana, T. *J. Phys. Chem. C* **2011**, 115, 11474-11483.
14. Maity, S.; Jana, T. *ACS Appl. Mater. Interfaces* **2014**, 6, 6851-6864.
15. Maity, S.; Jana, T. *Macromolecules* **2013**, 46, 6814−6823.
16. Sana, B.; Jana, T. *Polymer* **2018**, *137*, 312−323.
17. Harilal; Nayak, R.; Ghosh, P. C.; Jana, T. *ACS Appl. Polym. Mater*. **2020**, *2*, 3161−3170.
18. Harilal; Shukla, A.; Ghosh, P. C.; Jana, T. *ACS Appl. Energy Mater.* **2021**, *4*, 1644-1656.
19. Maity, S.; Jana, T. *Polym. Int.* **2015**, 64, 530-540.
20. Li, J.; Wang, J.; Wu, Z.; Tao, S.; Jiang, D. *Angew. Chem., Int. Ed.* **2021**, *133*, 13028-13033.
21. Lee, S.; Nam, K.-H.; Seo, K.; Kim, G.; Han, H. *Polymers* **2020**, *12*, 1604.
22. Shen, C.-H.; Jheng, L.-C.; Hsu, S. L.-C.; Tse-Wei Wang, J. *J. Mater. Chem*. **2011**, *21*, 15660−15665.
23. Eguizábal, A.; Sgroi, M.; Pullini, D.; Ferain, E.; Pina, M. P. *J. Membr. Sci*. **2014**, *454*, 243−252.
24. Nam, K.-H.; Seo, K.; Lee, S.; Han, H. *ACS Sustain. Chem. Eng.* **2020**, *8*, 16156-16163.
25. Klumpen, C.; Winterstein, S.; Papastavrou, G.; Senker, J. *J. Mater. Chem.* **2018**, *6*, 21542-21549.
26. Chen, Y.; Thorn, M.; Christensen, S.; Versek, C.; Poe, A.; Hayward, R. C.; Tuominen, M. T.; Thayumanavan, S. *Nat. Chem.* **2010**, *2*, 503-508.
27. Li, J.; Li, X.; Yu, S.; Hao, J.; Lu, W.; Shao, Z.; Yi, B. Manage. **2014**, *85*, 323−327.

28. Yu, S.; Xiao, L.; Benicewicz, B. C. *Fuel Cells* **2008**, *8*, 165− 174.
29. Mecerreyes, D.; Grande, H.; Miguel, O.; Ochoteco, E.; Marcilla, R.; Cantero, I. *Chem. Mater.* **2004**, *16*, 604-607.
30. Zhao, Y.-C.; Cheng, Q.-Y.; Zhou, D.; Wang, T.; Han, B.-H. *J. Mater. Chem.* **2012**, *22*, 11509-11514.
31. Wang, T.; Li, T.; Aboki, J.; Guo, R. *Front. Chem.* **2020**, *8*, 674.
32. Aboki, J.; Jing, B.; Luo, S.; Zhu, Y.; Zhu, L.; Guo, R. *ACS Appl. Mater. Interfaces* **2018,** *10*, 1173-1186.
33. Moh, L. C.; Goods, J. B.; Kim, Y.; Swager, T. M. *J. Membr. Sci.* **2018**, *549*, 236-243.
34. Gong, F.; Zhang, S. *J. Power Sources* **2011**, *196*, 9876-9883.
35. Kim, Y.; Wang, Y.; France-Lanord, A.; Wang, Y.; Wu, Y.-C. M.; Lin, S.; Li, Y.; Grossman, J. C.; Swager, T. M. *J. Am. Chem. Soc.* **2019,** *141*, 18152-18159.
36. Gong, F.; Mao, H.; Zhang, Y.; Zhang, S.; Xing, W. *Polymer* **2011,** *52*, 1738-1747.
37. Luo, S.; Liu, J.; Lin, H.; Kazanowska, B. A.; Hunckler, M. D.; Roeder, R. K.; Guo, R. *J. Mater. Chem. A* **2016,** *4*, 17050-17062.
38. Pournaghshband Isfahani, A.; Sadeghi, M.; Wakimoto, K.; Shrestha, B. B.; Bagheri, R.; Sivaniah, E.; Ghalei, B. *ACS Appl. Mater. Interfaces* **2018,** *10*, 17366-17374.
39. Swager, T. M. *Acc. Chem. Res.* **2008,** *41*, 1181-1189.
40. Tsui, N. T.; Paraskos, A. J.; Torun, L.; Swager, T. M.; Thomas, E. L. *Macromolecules* **2006,** *39*, 3350-3358.
41. Hsiao, S.-H.; Wang, H.-M.; Chou, J.-S.; Guo, W.; Tsai, T.-H. *J. Polym. Res.* **2012,** *19*, 1-10.
42. Kim, H. J.; An, S. J.; Kim, J. Y.; Moon, J. K.; Cho, S. Y.; Eun, Y. C.; Yoon, H. K.; Park, Y.; Kweon, H. J.; Shin, E. M. *Macromol. Rapid Commun.* **2004**, *25*, 1410-1413.
43. Yuan, Y.; Johnson, F.; Cabasso, I. *J. Appl. Polym. Sci.* **2009**, *112*, 3436−3441.
44. Chen, J.-C.; Chen, P.-Y.; Lee, S.-W.; Liou, G.-L.; Chen, C.-J.; Lan, Y.-H.; Chen, K.-H. *React. Funct. Polym.* **2016**, *108*, 122-129.
45. Rabbani, M. G.; Reich, T. E.; Kassab, R. M.; Jackson, K. T.; El-Kaderi, H. M. *ChemComm* **2012**, *48*, 1141-1143.
46. Sing, K. S. *Pure Appl. Chem.* **1985**, *57*, 603.
47. Zhou, S.; Guan, J.; Li, Z.; Huang, L.; Zheng, J.; Li, S.; Zhang, S. *J. Mater. Chem. A* **2021,** *9*, 3925-3930.

48. Tao, S.; Zhai, L.; Wonanke, A. D.; Addicoat, M. A.; Jiang, Q.; Jiang, D. *Nat. Commun.* **2020**, *11*, 1-8.
49. Berber, M. R.; Nakashima, N. *ACS Appl. Mater. Interfaces* **2019**, *11*, 46269-46277.
50. Sannigrahi, A.; Arunbabu, D.; Sankar, R. M.; Jana, T. *Macromolecules* **2007,** *40*, 2844-2851.
51. Ghosh, S.; Sannigrahi, A.; Maity, S.; Jana, T. *J. Phys. Chem. B* **2010**, *114*, 3122-3132.

Chapter 7

SUMMARY and CONCLUSIONS

7.1 SUMMARY

This thesis entitled ***"Novel Polybenzimidazoles for the Development of Proton Exchange Membrane Fuel Cells"*** describes the synthesis and characterization of various novel polybenzimidazoles for the development of proton exchange membrane fuel cells (PEMFCs). The whole thesis work comprises of total seven chapters that starts with an introductory chapter then materials and methods followed by four working chapters. A brief summary of each chapter is as follows.

CHAPTER 1

This chapter deals with a brief introduction of fuel cell, various types of fuel cells, working principle of PEMFC, properties of PEM and their types, including PA doped PBI membrane and fabrication methods. Furthermore, we have discussed brief introduction of polybenzimidazoles (PBIs), types and importance of PBI in terms of PEM. Finally, this chapter describes the scope of the thesis work.

CHAPTER 2

This chapter describes the details of materials that were used for all the working chapters and details of experimental procedures, various instrumentation methods used for characterization of samples and property evaluation of all polybenzimidazole derivatives and proton exchange membranes.

CHAPTER 3

Despite several unique advantages, high-temperature proton-exchange membrane fuel cells (HT-PEMFCs) based on polybenzimidazole (PBI) membranes suffer from various drawbacks like weak chemical resistance, poor mechanical strength, acid leaching, etc., which eventually reduces the performance of the cell. In order to minimize these drawbacks and to improve the cell performance, in this work we have developed proton-exchange membranes (PEMs) in which pyridine-bridged-oxypolybenzimidazole (PyOPBI) and brominated polyphenylene oxide (BrPPO) were chemically cross-linked by an ex situ methodology. Three cross-linked membranes **P1**, **P2**,

and **P3** consisting of 12.5, 25.0, and 37.5 wt % BrPPO, respectively, with respect to PyOBI were successfully fabricated and PEM properties were studied. These membranes showed much improved acid stability, oxidative stability, mechanical strength, and strong resistance to swelling in concentrated phosphoric acid (PA) solution. They were found to be completely stable in 85% PA whereas uncross-linked PyOPBI membranes readily dissolved in 60% PA. The reason for such stability has been ascribed to the cross-linked network structure of the membrane. The **P1** membrane exhibited remarkably high proton conductivity (0.123 S cm^{-1}) whereas the pristine PyOPBI membrane showed a conductivity of 0.008 S cm^{-1} at 180 ºC. The single cell measurement under anhydrous conditions at 160 °C of membrane electrode assembly (MEA) obtained from the P1 membrane displayed good fuel cell efficiencies with power density 290 mW cm^{-2} and current density 848.7 mA cm^{-2} at 0.3 V whereas under the identical measurement conditions, MEA of the pristine PyOPBI membrane showed 96.4 mW cm^{-2} power density and 321.5 mA cm^{-2} current density at 0.3 V. All these results indicated that cross-linked membranes have great potential to be used in the HT-PEMFC.

CHAPTER 4

Although pyridine bridged oxypolybenzimidazole (PyOPBI) membranes are considered to be promising hightemperature proton exchange membrane (HT-PEM) materials that have the potential to overcome many obstacles such as solubility, membrane processability, cost, etc., of the mainstream conventional polybenzimidazole (PBI)-based HT-PEM, the weak structural stability of PyOPBI in concentrated phosphoric acid (PA) and poor dimensional and mechanical stability have been the crucial issues restraining the performance. To mitigate these bottlenecks, in this work, we successfully synthesized three types of PyOPBIs with flexible aryl ether backbones and bulky substituents by polycondensation reaction of various aryl diacids and pyridine-bridged tetraamine 2,6-bis(3′,4′-diaminophenyl)-4-phenylpyridine (PyTAB) in Eaton's reagent followed by casting as HT-PEMs. Three designed bulky substitute containing PyOPBI membranes showed considerably high PA loading capacity (16−22 mol of PA/repeat unit) and proton conductivity (0.04−0.078 S/cm) at 180 °C as compared to earlier reported unsubstituted PyOPBI membranes (14 mol of PA/repeat unit and 0.007 S/cm at 180 °C). In addition, the obtained

membranes showcased good chemical, mechanical, thermal, and long-term conductivity stabilities and outstanding stability in concentrated PA. The pendent groups and the bulkiness of the backbone are believed to be the cause behind better stability and facilitating proton transport that results in higher proton conductivity. The single cell made from the membrane electrode assembly of these bulky substituted PyOPBI membranes displayed a peak power density in the range of 144−240 mW cm^{-2} under H_2/O_2 at 160 °C, which is considerably higher than that for unsubstituted PyOPBI membrane (90.4 mW cm^{-2}). Overall, the current results provide an effective strategy to explore the benefits of structural modulation of PyOPBI using various structurally divergent diacids to enhance HT-PEM properties and suggest a scalable route for the advancement of PBI-based HT-PEM fuel cells.

CHAPTER 5

The development of phosphoric acid (PA)-loaded polybenzimidazole (PBI) proton exchange membranes (PEMs) possessing high proton-conductivity and stability (both chemically and dimensionally) is highly desirable but remains an unmet challenge. A novel series of random copolymers of pyridine-functionalized bulky fluorophenylene-containing flexible arylether polybenzimidazoles were designed and synthesized in good yields with different molecular weights, and casted into high-proton conductive membranes for the use in high-temperature PEM fuel cell (HTPEMFC). These membranes showed hydrophilic-hydrophobic microphase-separated structures, confirmed by transmission electron microscopy (TEM), owing to the combination of rigid and numerous heteroatoms including C, N, O and F which were integrated into polymer skeletons. The copolymer backbone with a microphase-separated path endowed the membranes with high PA-loading capacity (up to 25.4 mol of PA/repeat unit) and high efficiency proton transmission. Noticeably, the constructed co-network membranes exhibited the high proton conductivity (up to 0.17 S cm^{-1} at 180 °C) under anhydrous conditions and the H_2/O_2 single-cell membrane electrode assembly (MEA) based on copolymer (Co-P3) PEM exhibited a maximum peak power density (PPD) of 332 mW cm^{-2} at a current density of 722 mA cm^{-2} at 160 °C which are much better than that of both homo PA-loaded PyOPBI membranes (108 mW cm^{-2} with a current density of 209 mA cm^{-2}) and Ph(CF_3)-PyOPBI (239 mW cm^{-2} at current density of 629

mA cm^{-2}) under the identical measurement conditions. In addition, these membranes showcased considerable performance in oxidative and thermal-mechanical stability. Overall, the current results demonstrate that the combination of pendant rigid and flexible random co-structures are promising membrane materials for the use in HT-PEMFC.

CHAPTER 6

The preparation of polymeric anhydrous proton conducting membrane is critical to the development of high-temperature proton-exchange membrane (HT-PEM) for the use in fuel cell and remains a significant scientific challenge till date. Polybenzimidazole (PBI) is a highly stable engineered plastic with excellent thermochemical stability and this specificity triggers a wide range of research to explore the suitability of PBI as HT-PEM. Nevertheless, such material encounters challenging issues owing to leaching of phosphoric acid (PA), a proton carrier, slow and low proton transport. Herein, we demonstrated a feasible strategy to address these key issues by rational design and synthesis of a new class of three-dimensional (3D) iptycene-based ladder-like porous pyridine-bridged oxypolybenzimidazoles (IPyPBIs) as self-standing, highly flexible HT-PEM *via* a facile polycondensation between newly designed Y and H-shaped scaffold of iptycene-containing arylether diacids and pyridine functionalized tetraamine building blocks. The as-synthesized polymers possess high molecular weights, excellent thermal-chemical stability, hierarchical intrinsic-porosity (ca. 12.1 Å) and good solubility in a wide range of organic solvents and thus excellent processability for PEM fabrication readily. Furthermore, the IPyPBIs walls found to trigger multiple hydrogen-bonding interactions with PA molecules to lock and stabilize the PA network inside the pores, thereby favouring superior PA-holding capability (as high as 32 mols of PA/repeat unit) in resulting membranes. Consequently, these PA-loaded IPyPBI HT-PEMs exhibited stable ultrahigh proton conductivities (up to 0.24 S cm^{-1}at 180 ^{o}C and 0% humidity) and crossed the upper proton conductivity (0.1 S cm^{-1}) limit of traditional PA-loaded PBI. This work paved the way for the realization of the targeted properties of PBIs through predesign and functionalization of the pore surface, and highlighted the great potential of microchannels forming PBIs as a rigid platform for fast proton transportation.

CHAPTER 7

This chapter deals with summery and conclusion of the whole thesis work in addition future scopes of these work are also outlined.

7.2 Conclusions

In conclusion, we have successfully synthesized various types of polybenzimidazoles and utilized as efficient proton exchange membrane materials for HT-PEMFCs. Here are some conclusive points those are drawn based on the work carried out for this thesis work (Chapter 3 to Chapter 6).

1. Various cross-linked membranes of PyOPBI with polymeric crosslinker have been prepared and explored for their potential use as PEM.

2. The universal testing machine (UTM) analysis of these membranes concluded that the phosphoric acid (PA) loaded cross-linked membranes have high mechanical strength than PA-loaded pristine PyOPBI.
3. Morphology of the cross-linked PEMs exhibited a honeycomb network structure which helped in accommodate more content of PA and eventually led to higher proton conductivities and fuel cell performance.
4. Three types of arylether functionalized pendant-type polybenzimidazoles (PBIs) derivatives have been synthesized from arylether backbones containing diacid monomers.
5. These arylether pendant-type PBI membranes are showed higher stability towards PA compared to pristine PyOPBI due to the higher rate of dynamic hydrogen bonding ability with imidazole and acid molecules.
6. Proton conductivity and fuel cell performance of the arylether pendant-type PBI PEMs are higher than the pristine PyOPBI.
7. A series of sterically hindered pyridine-functionalized arylether-linked random copolymers with systematically varied composition have been synthesized from different diacid monomers through a sustainable approach for the development efficient proton exchange membranes (PEMs)
8. These copolymer PEMs showed higher acid doping level (ADL), good proton conductivity and single cell performance compared to homo polymer PEMs.

9. A new class of three-dimensional (3D) iptycene-based (i.e., triptycene and pentiptycene) ladder-like porous pyridine-bridged oxypolybenzimidazoles (IPyPBIs) have been synthesized from newly designed Y and H-shaped scaffold of iptycene-containing arylether diacids building blocks via a facile polycondensation.
10. Porosity and microrphology of the IPyPBI PEMs exhibited a ripple-spongy-like network structure consisting of microcavities which facilitate proton hopping between adjacent H_3PO_4 molecules and eventually led to higher proton conductivities and fuel cell performance.
11. Pentiptycene-based PBI PEMs showed higher ADL, conductivity and mechanical stability compared to the triptycene-based PBI PEMs due to the "internal molecular free volume" and the ample of multiple inherently strong proton accepting and donating functionalities.
12. This macromolecular architecture concept (chapter 6) would inspire the rational construction of a new generation of porous polybenzimidazole loaded with electrolyte for advanced energy applications.

7.3. Scope for future work

The current thesis has addressed three important aspects of Polybenzimidazole: microporous polybenzimidazole PEMs, pendant-type polybenzimidazole PEMs and cross-linked polybenzimidazole PEMs. We believe the findings of this thesis will have great impact on the future development of polybenzimidazole (PBI) chemistry in general, especially the use of PBI as HT-PEM. We believe the potential and scope of future work of this thesis are enormous. Few of these are listed below

1. Efforts can be made to cross-link PyPBI with different functionalized polymeric crosslinkers and study their properties and application for HT-PEM fuel cells.
2. The results in chapter 4 allow for the production and rigorous testing of robust pendant-type of PyPBI membranes for further development for PEMFC application and offer a platform that can enable the targeted design of new class of PEMs.
3. Efforts can be made to develop various multi-functionalized PBIs by making new type of tetraamine monomer derivatives.

4. Attempts must be made to synthesize new pendant-type of PyPBI by developing new dicarboxylic acid monomers (DCAs).
5. Synthesis of block copolymers and random copolymers can be done from functionalized PyPBI polymers.
6. The findings in the chapter 6 may help in opening paths towards new microporous conducting material concept for fuel cell application, which should focus on the choice of monomer structure.
7. Efforts can also be made to study the prospects of IPyPBI based composite with different nanofillers and blends with various polymers as PEM in HT-PEMFCs.
8. Another focus of future studies can be the optimization of IPyPBI membranes for PEMFCs application by increasing mechanical strength like by covalent cross-linking.

Appendix

Appendix I

Synthesis of BrPPO copolymer

In a typical synthesis, PPO (2 g, 10 mmol), AIBN (0.083 g, 0.49 mmol) and brominating agent NBS (1.21 g, 6.6 mmol) were dissolved in chlorobenzene (20 mL) and the solution was refluxed for 3h under N_2 atmosphere. After cooling to room temperature, the homogeneous solution was precipitated into a 10-fold excess of methanol. The polymer was filtered and washed with methanol, and the residue subsequently re-dissolved in chloroform (50 mL) and again precipitated into a 10-fold excess of methanol. The resulting BrPPO polymer was dried at 60 °C under vacuum overnight.

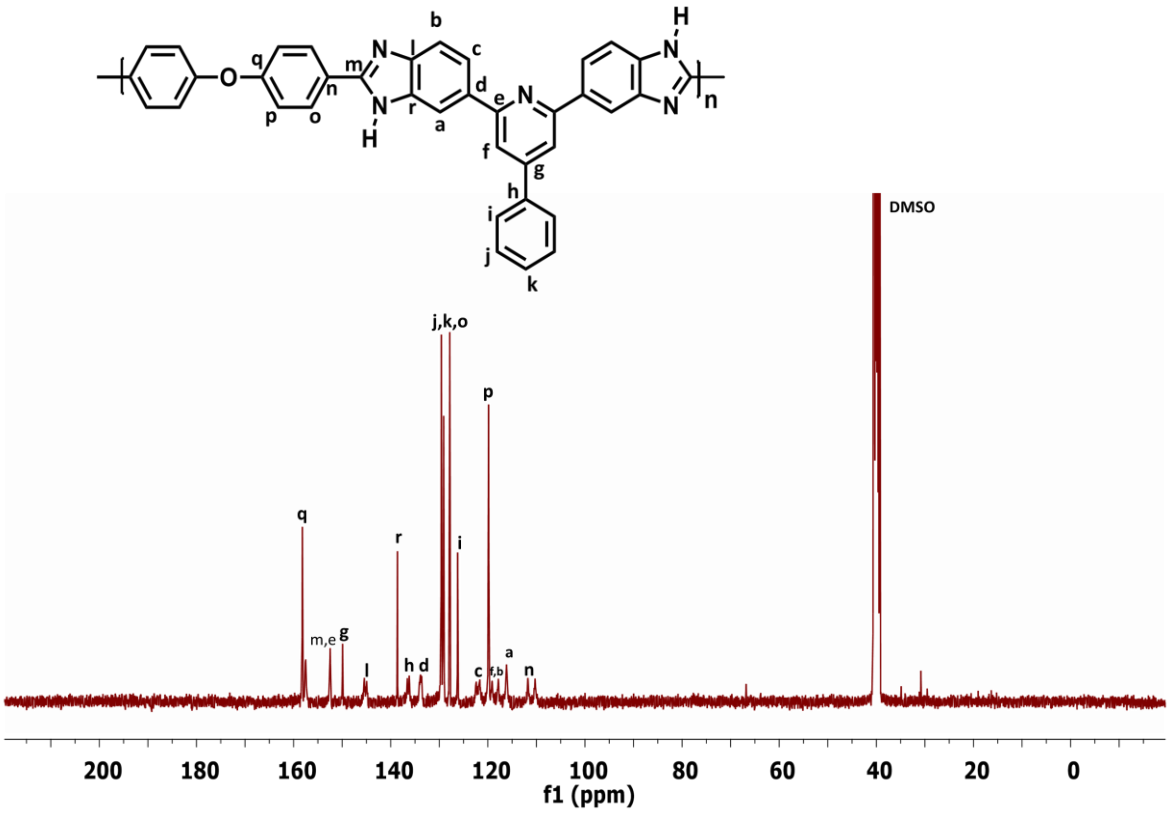

Appendix-I Figure 3.1. ^{13}C NMR spectrum of PyOPBI along with structure of the polymer and peak identification.

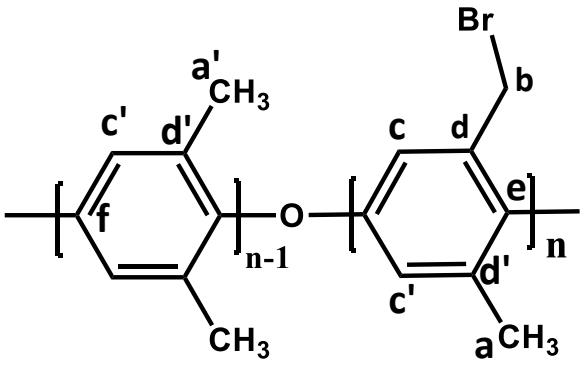

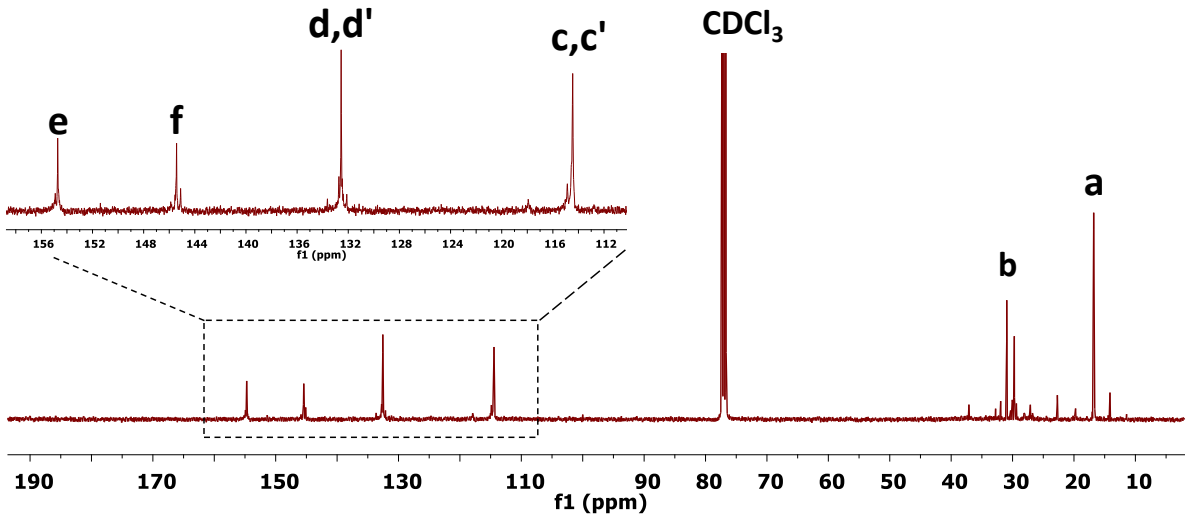

Appendix-I Figure 3.2. ^{13}C-NMR spectrum of BrPPO along with peak assignments.

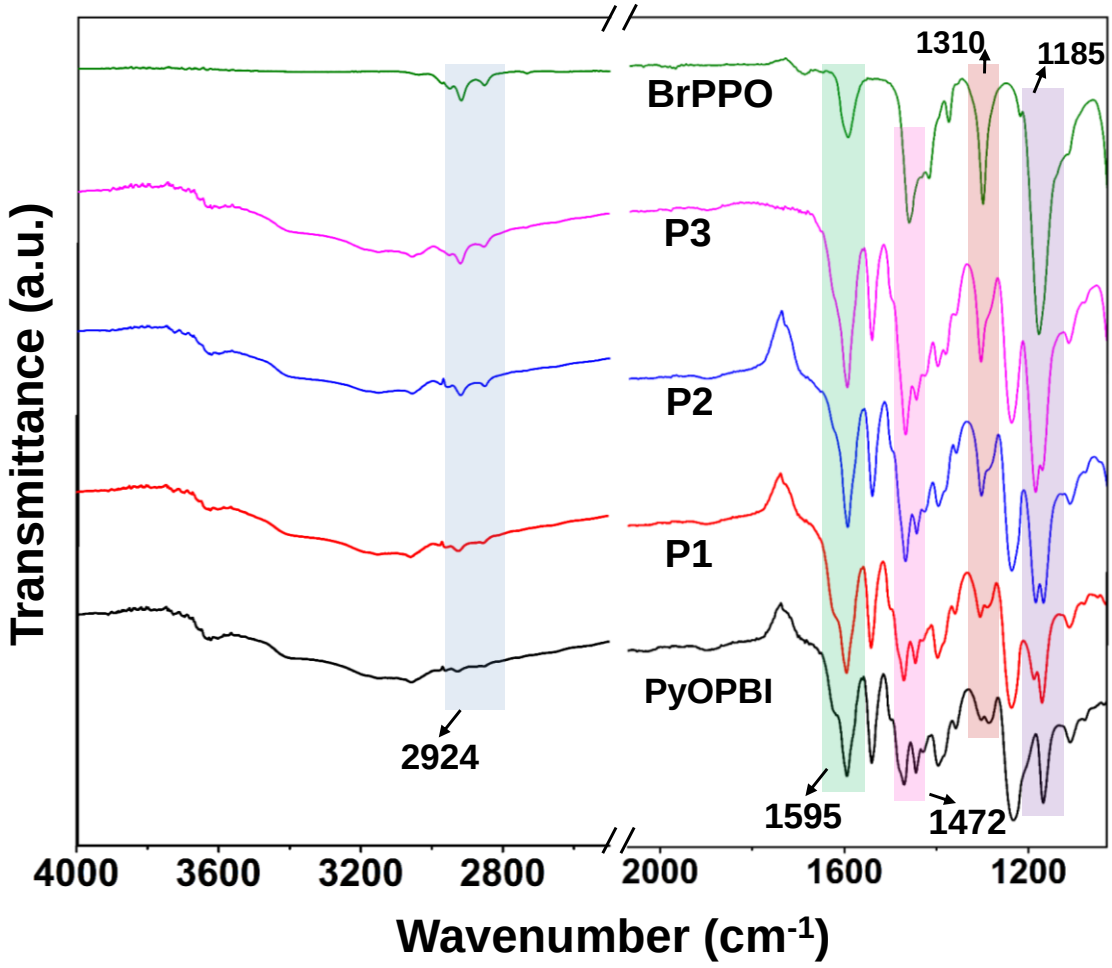

Appendix-I Figure 3.3. ATR-FTIR spectra of PyOPBI, cross-linked membranes and BrPPO. The important peaks are highlighted in the figure.

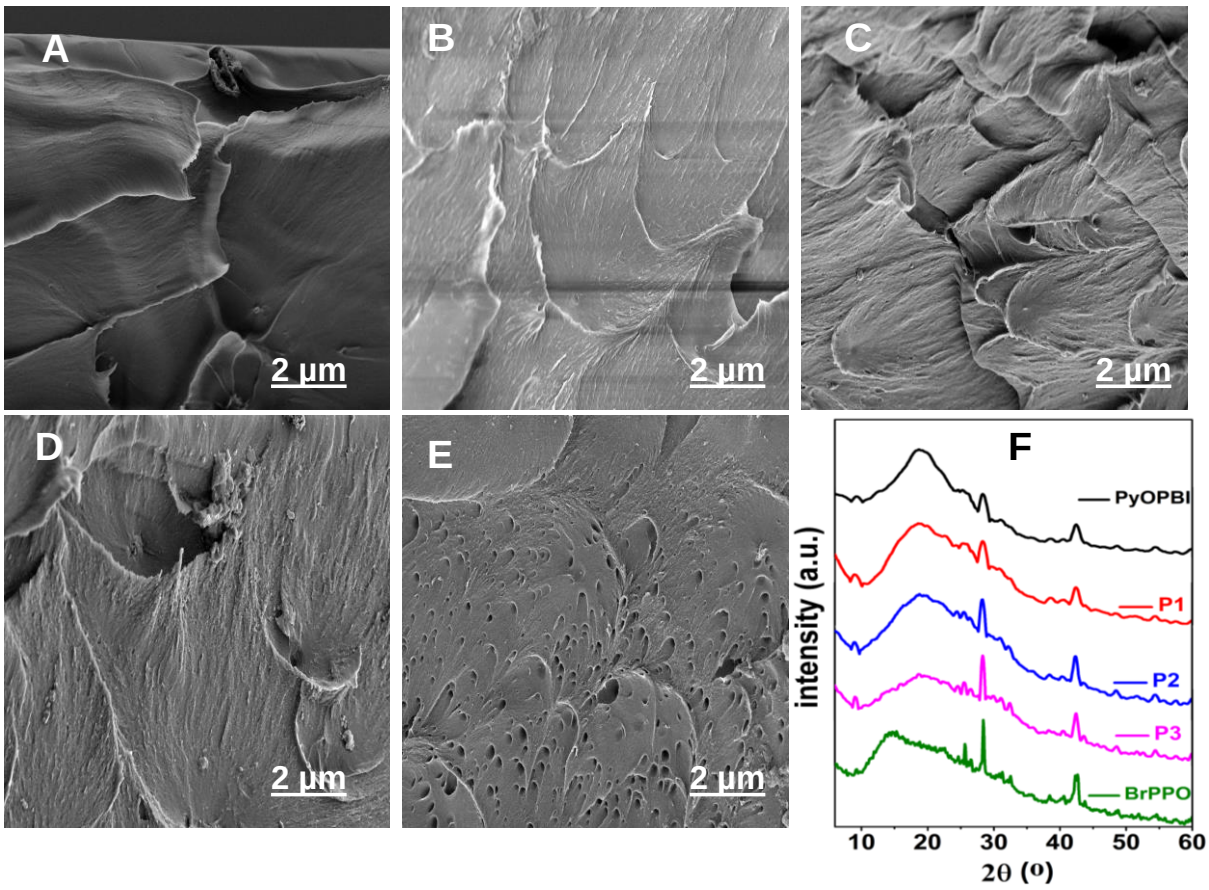

Appendix-I Figure 3.4. FESEM cross-section morphology of PyOPBI (A), P1 (B), P2 (C), P3 (D), BrPPO (E) and PXRD pattern (F) of PyOPBI, Br-PPO and cross-linked membranes.

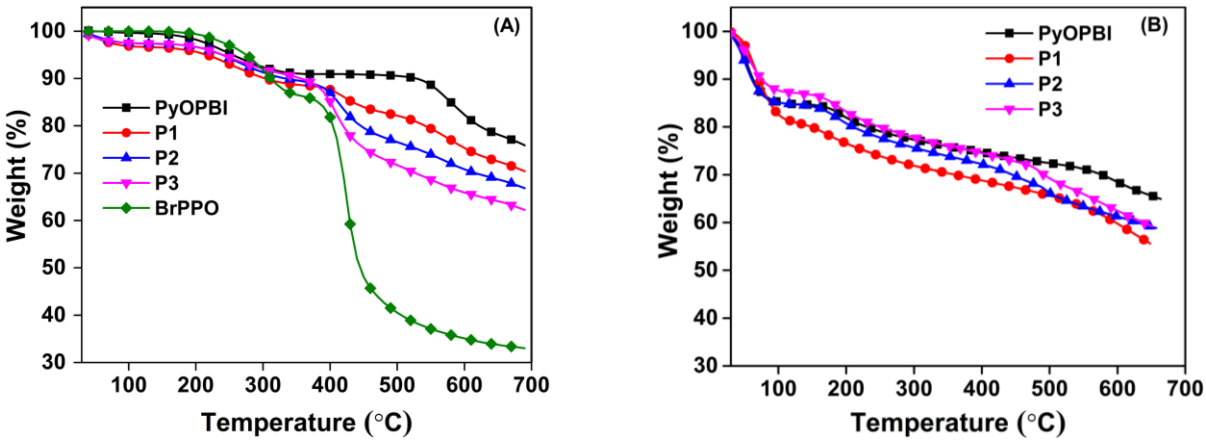

Appendix-I Figure 3.5. TGA curves of undoped (A) and PA doped (B) membranes.

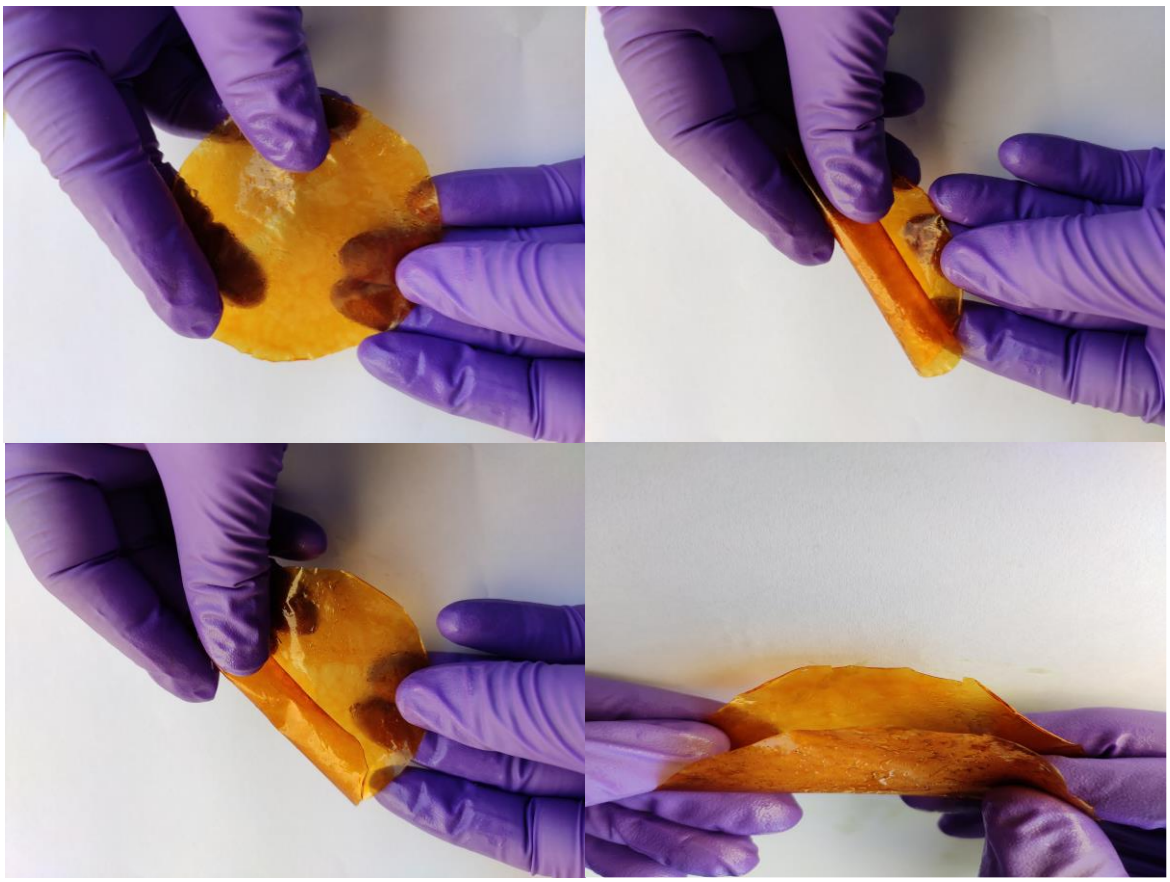

Appendix-I Figure 3.6. Few pictures of PA loaded CrLPyOPBI membranes. Membranes were rolled in different ways to show the flexibility of the membranes.

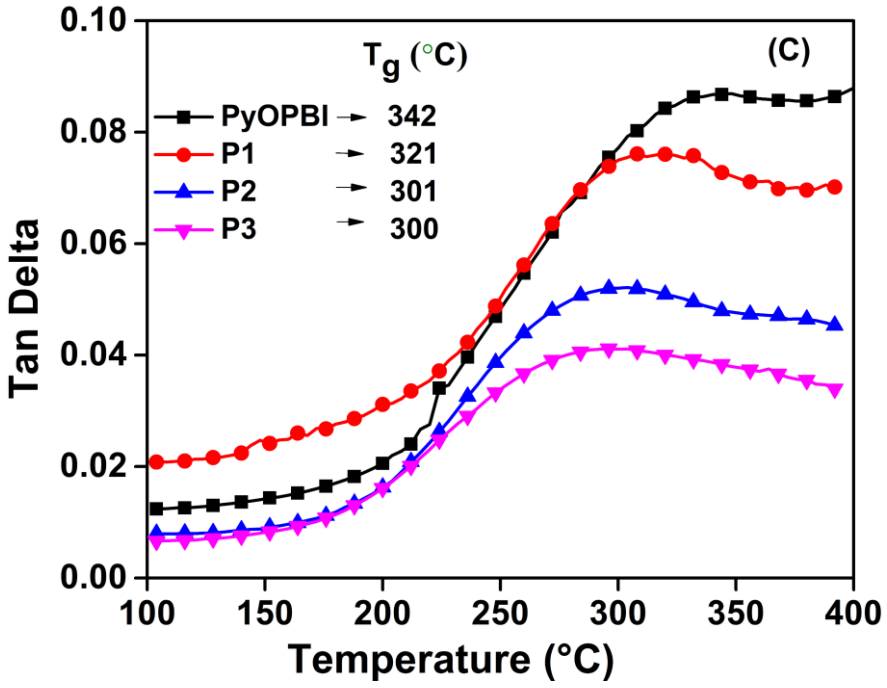

Appendix-I Figure 3.7. Thermo-mechanical properties (temperature dependent tan δ plots) of PyOPBI and cross-linked membranes from DMA. The T_g values obtained from tan δ are shown inside the figure.

APPENDIX-II

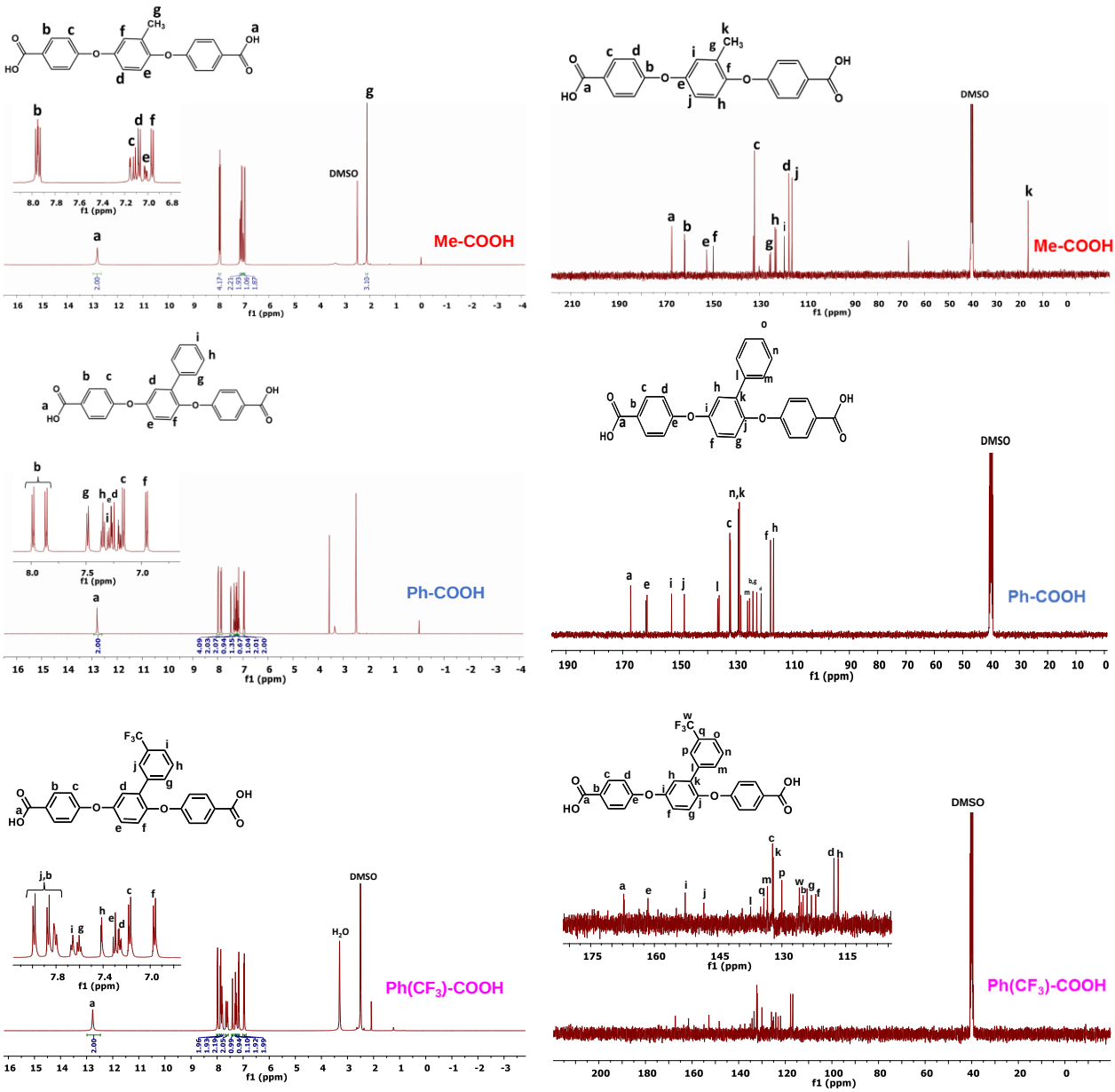

Appendix-II Figure 4.1: ^{1}H and ^{13}C NMR spectra of Me-COOH, Ph-COOH and Ph(CF_3)-COOH acid monomers.

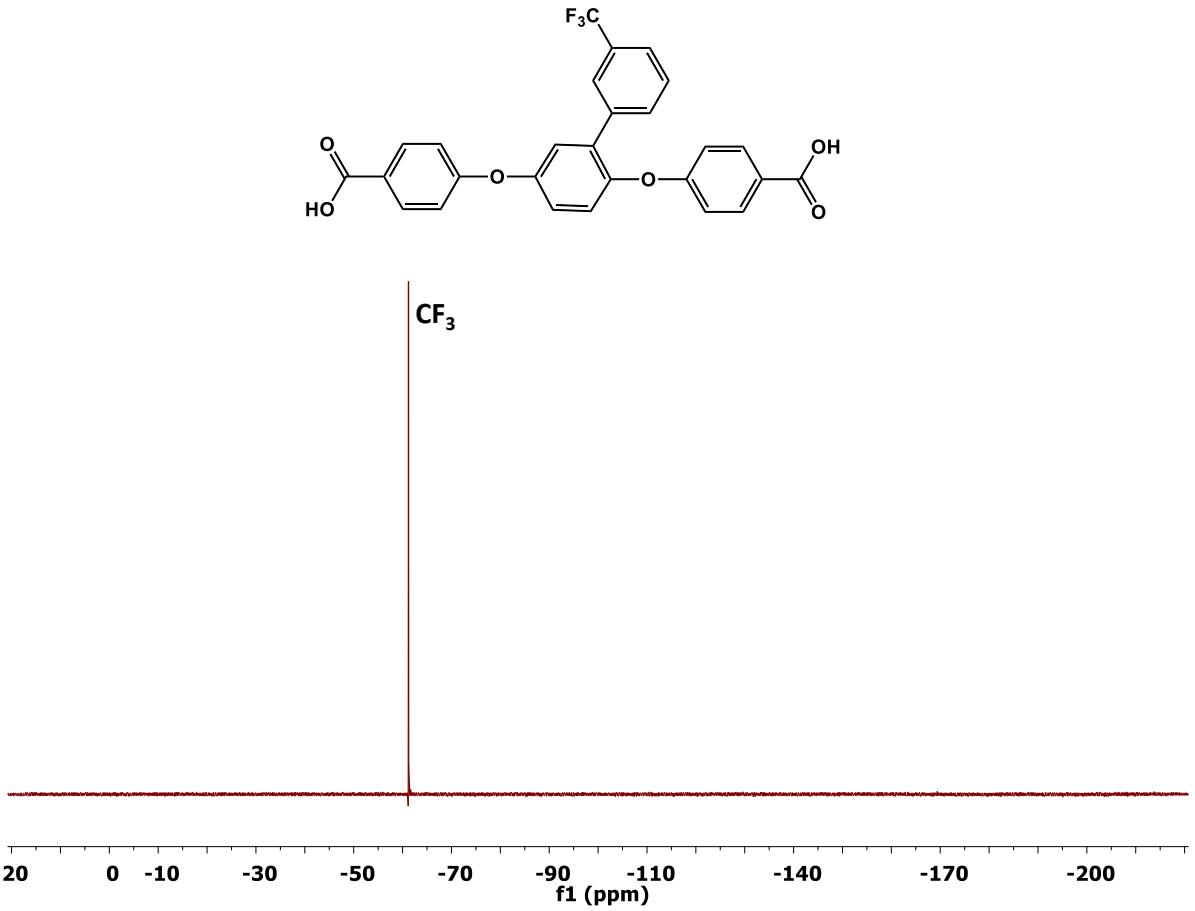

Appendix-II Figure 4.2: ^{19}F NMR spectrum of Ph(CF_3)-COOH acid monomer.

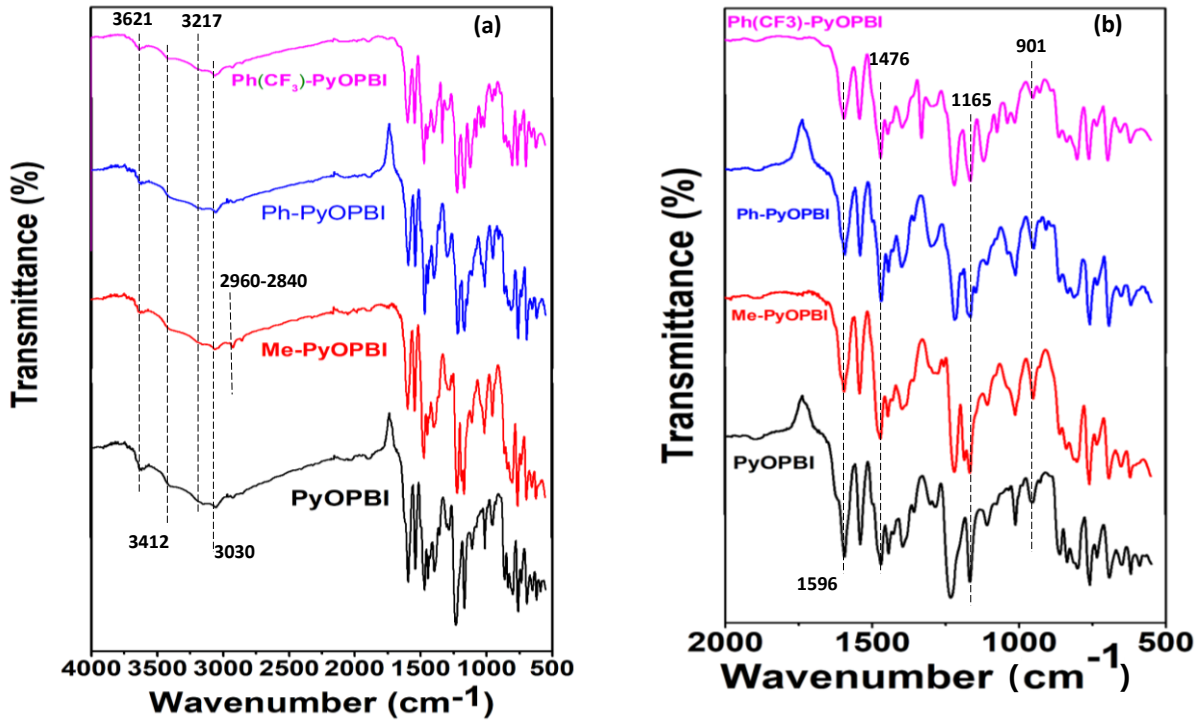

Appendix-II Figure 4.3. FT-IR spectra of the synthesized PyOPBIs (a) and the magnified portion of these spectra in the region 2000 to 500 cm^{-1} (b).

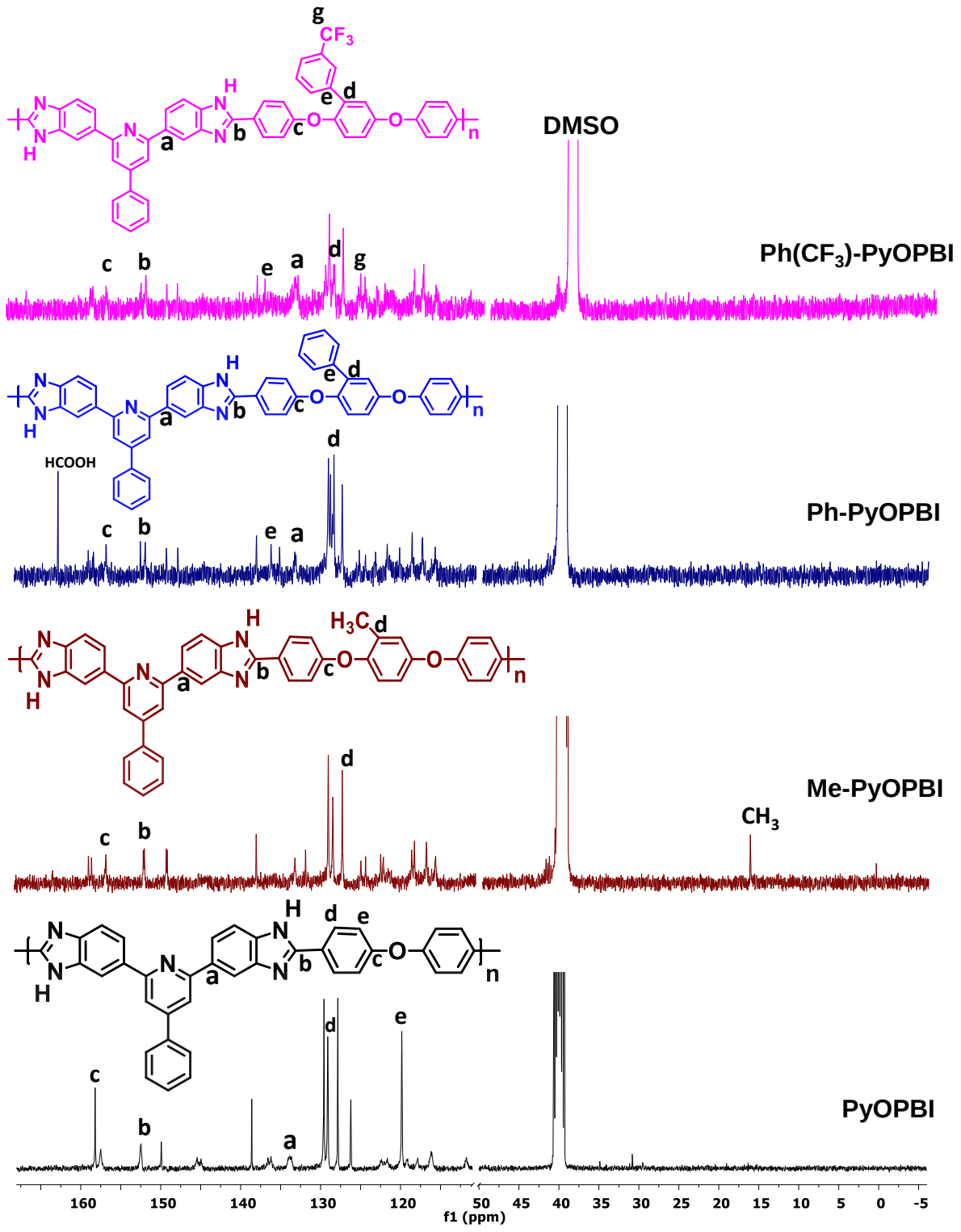

Appendix-II Figure 4.4. ^{13}C NMR spectra of PyOPBI, Me-PyOPBI, Ph-PyOPBI and Ph(CF_3)-PyOPBI recoded in DMSO-*d*6.

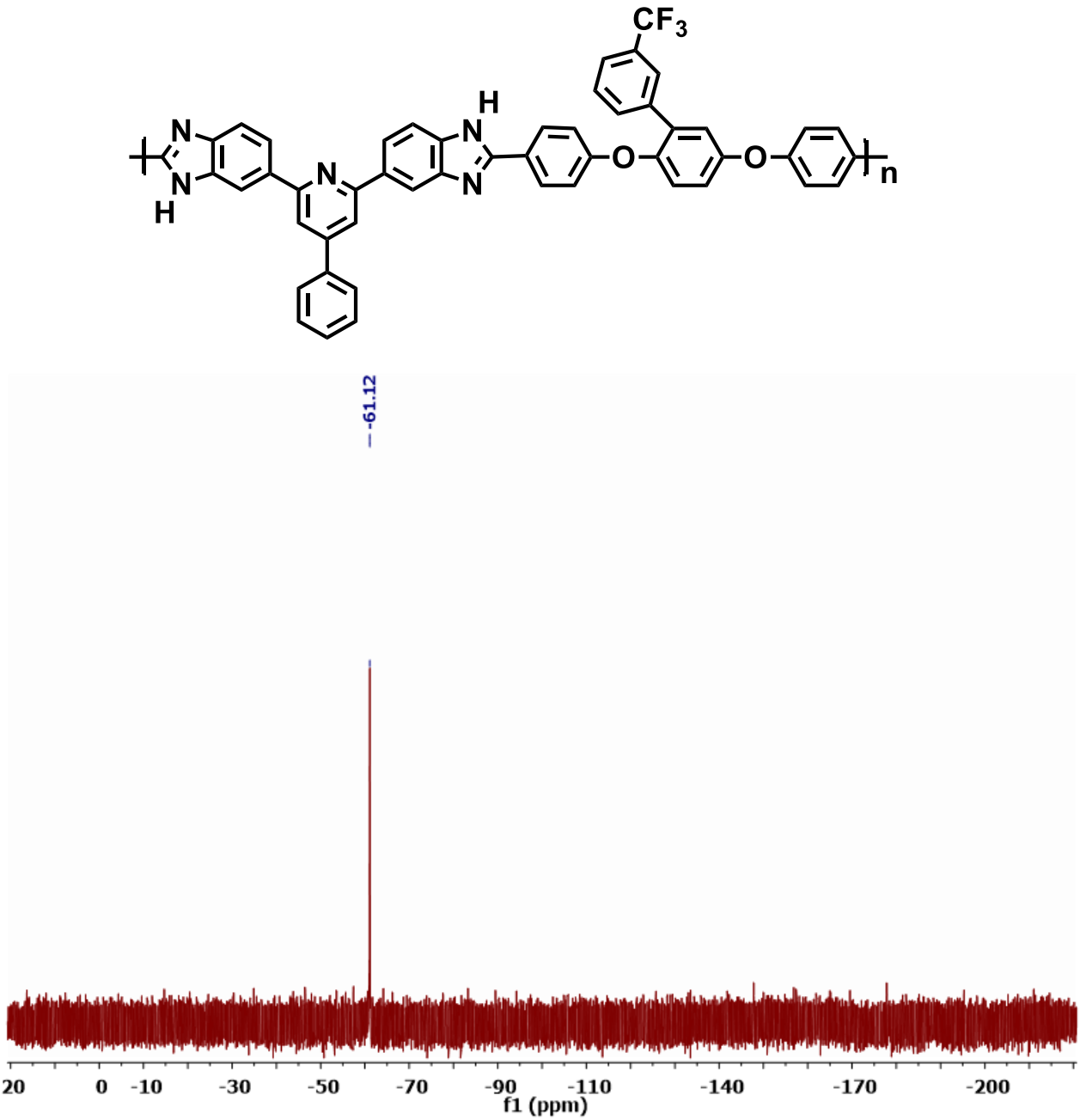

Appendix-II Figure. 4.5: ^{19}F NMR spectrum of Ph(CF_3)-PyOPBI polymer.

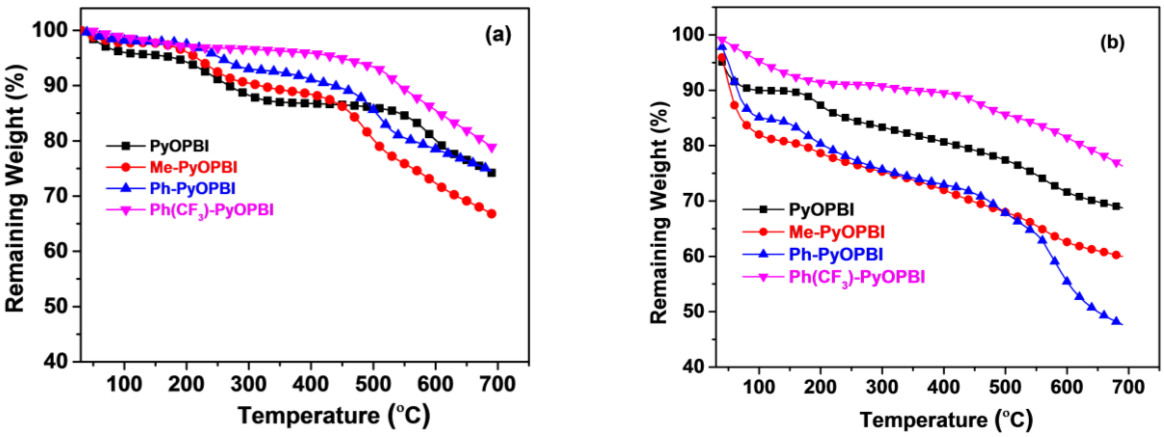

Appendix-II Figure 4.6. TGA curves of undoped (a) and PA doped (b) membranes under N_2.

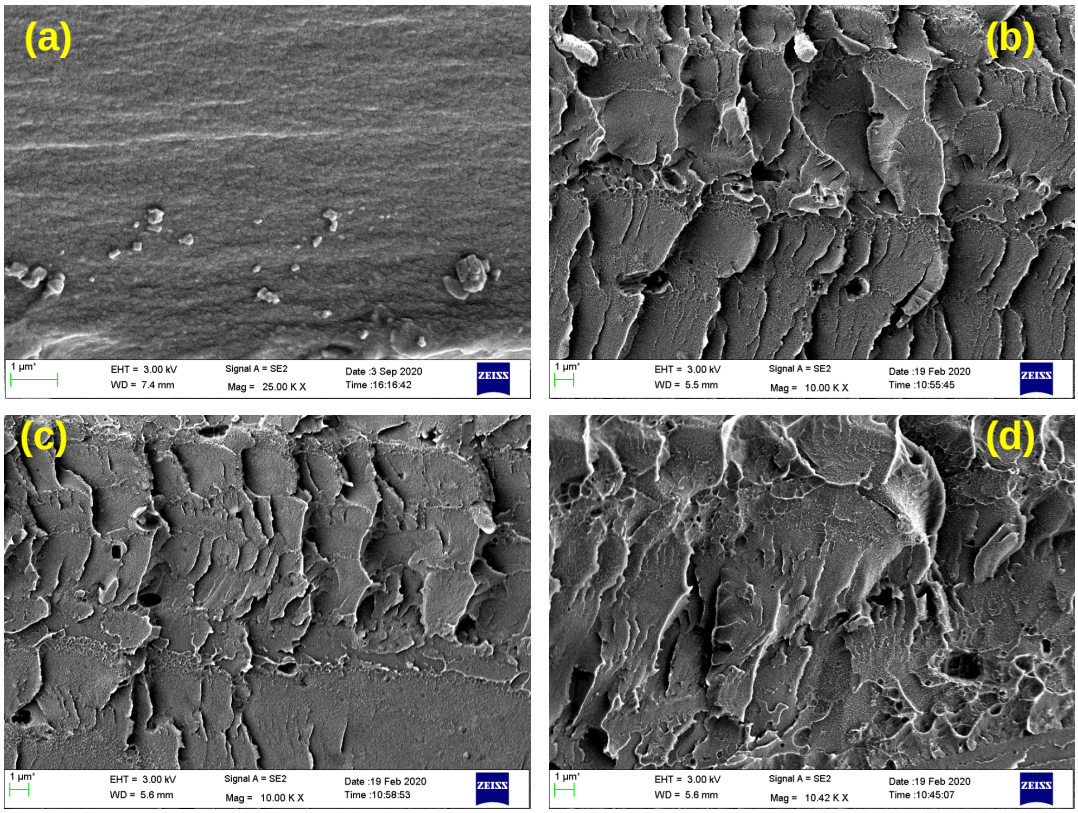

Appendix-II Figure 4.7. FESEM cross-section morphology of PyOPBI (a), Me-PyOPBI (b), Ph-PyOPBI (c), Ph(CF_3)-PyOPBI (d) membranes.

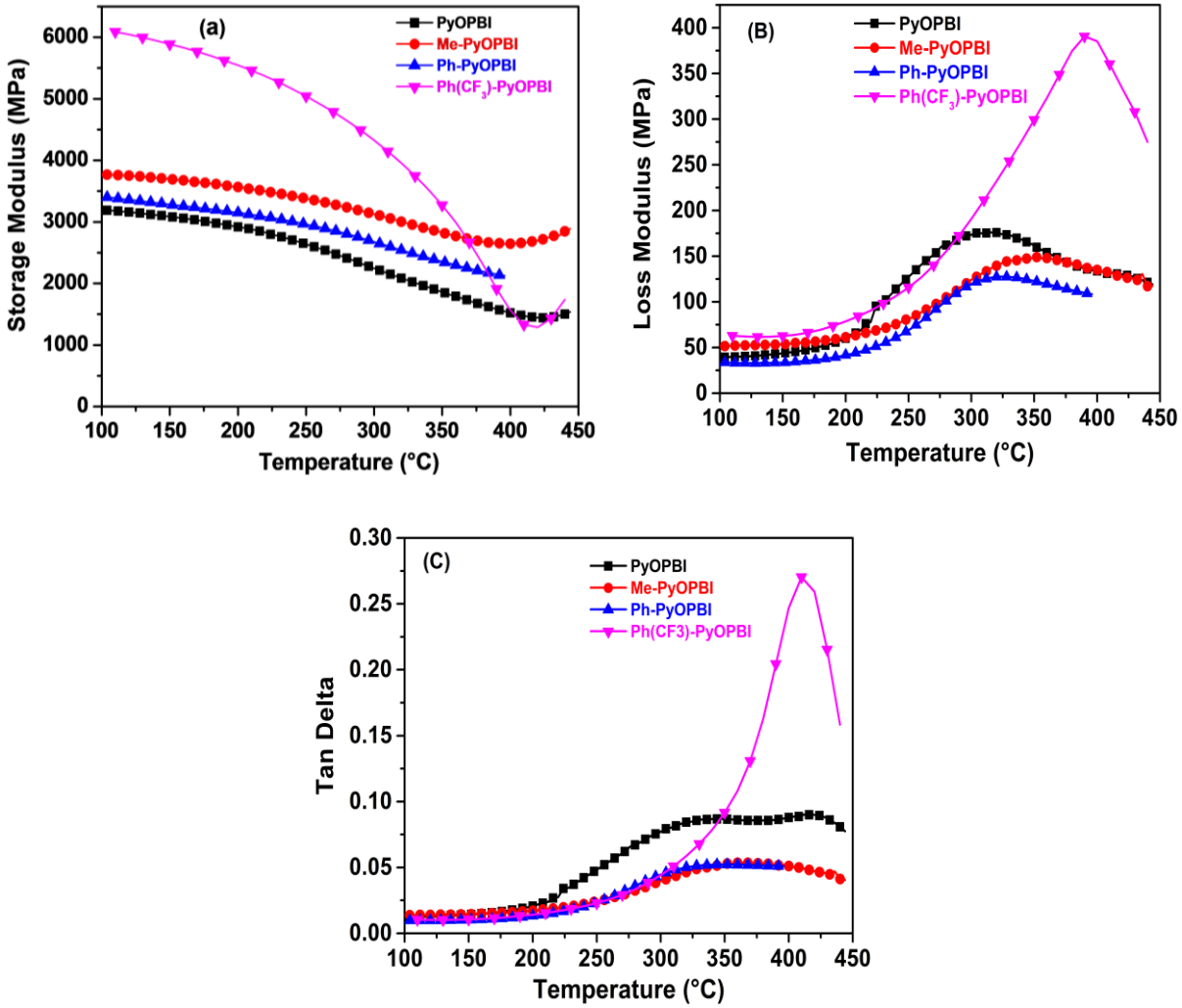

Appendix-II Figure 4.8. Thermomechanical properties of PyOPBI, Me-PyOPBI, Ph-PyOPBI and Ph(CF_3)-PyOPBI membranes obtained from DMA analysis. (a) Storage modulus (E'), (b) loss modulus (E'') and (c) Tan δ plots against temperature.

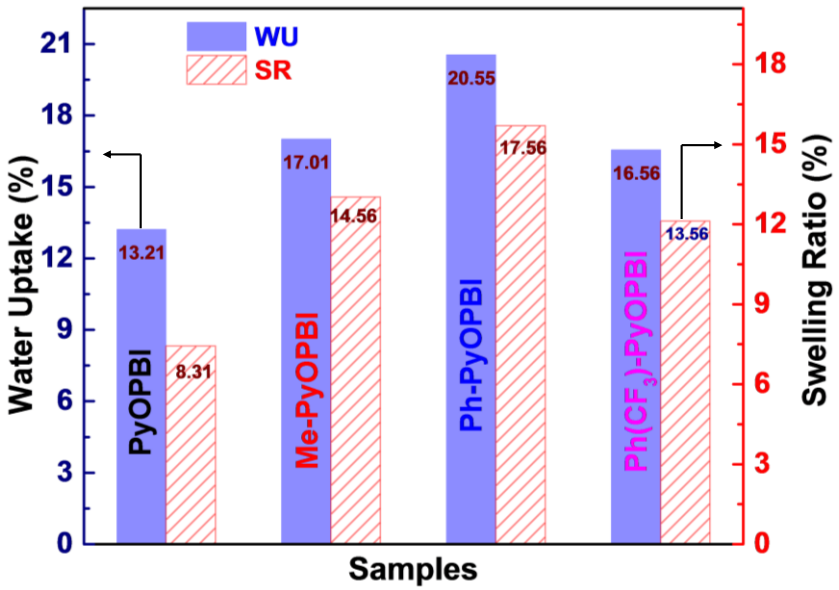

Appendix-II Figure 4.9. The water uptake (WU) and swelling ratio (SR) of different pendant-type PyOPBI membranes.

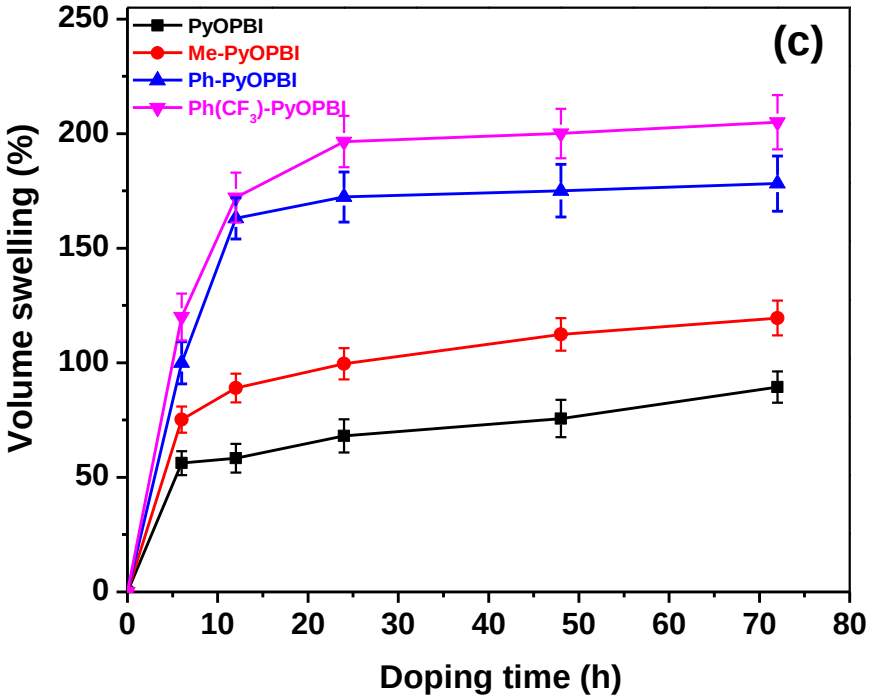

Appendix-II Figure 4.10. The volume swelling ratio of different pendant-type PyOPBI membranes.

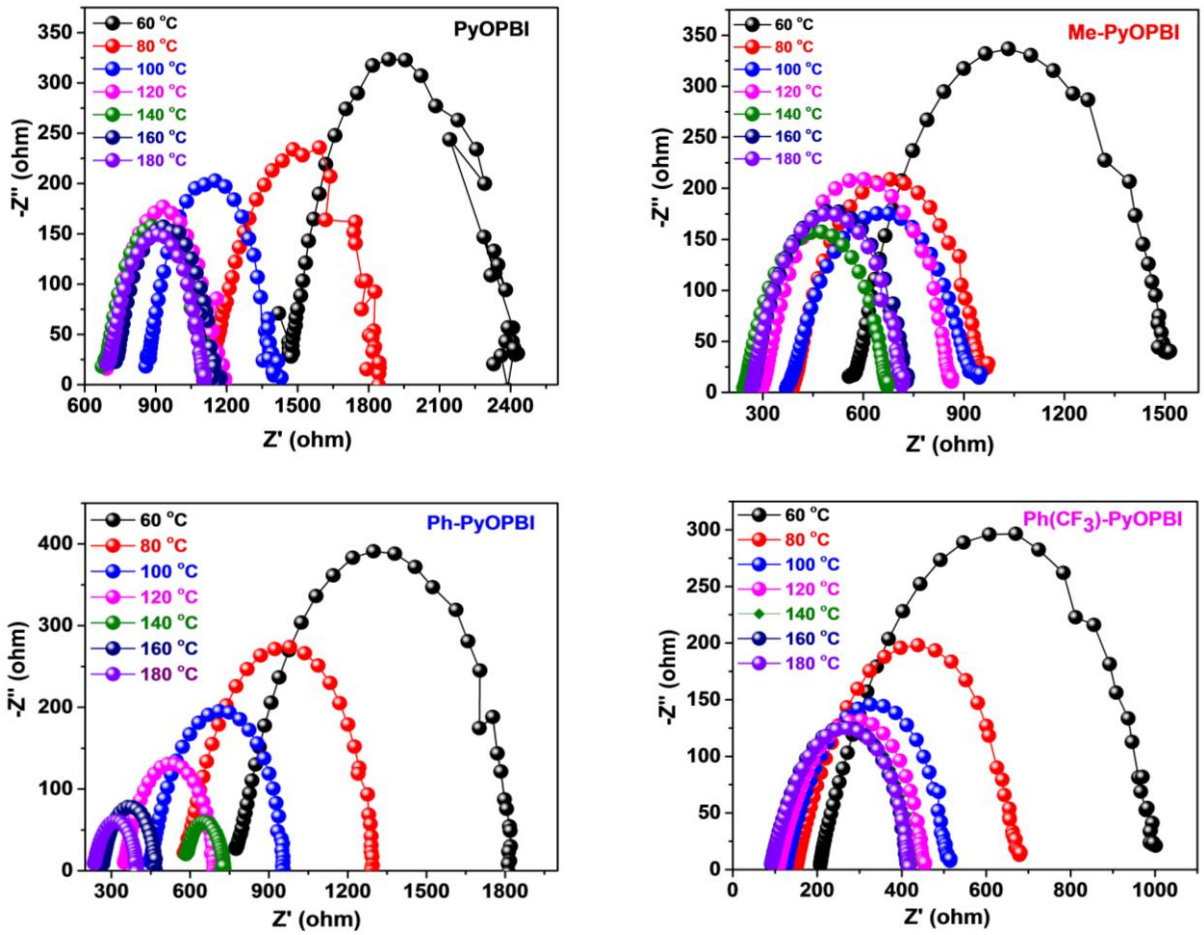

Appendix-II Figure 4.11. Typical Nyquist plots at different temperatures for PyOPBI, Me-PyOPBI, Ph-PyOPBI and Ph(CF_3)-PyOPBI.

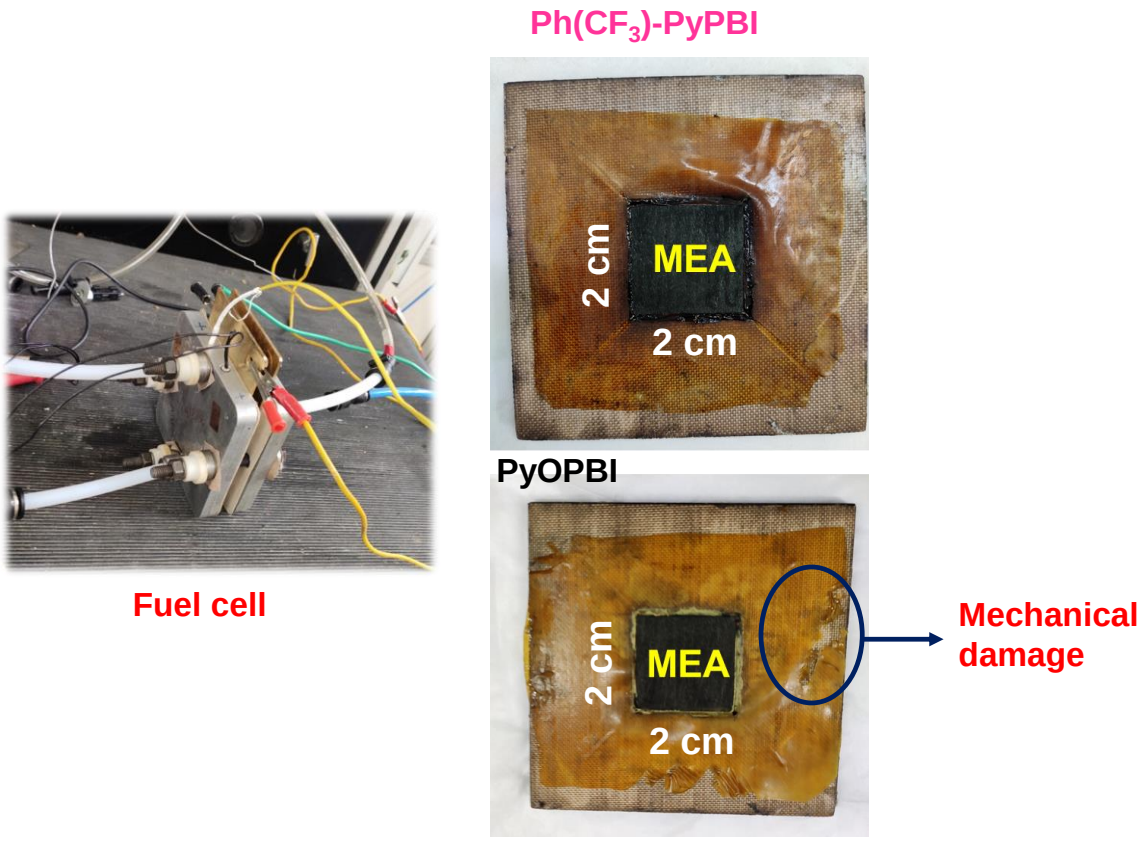

Appendix-II Figure 4.12. Photos of fuel cell, Ph(CF_3)-PyOPBI and PyOPBI assembled MEA after single cell test.

Appendix-III

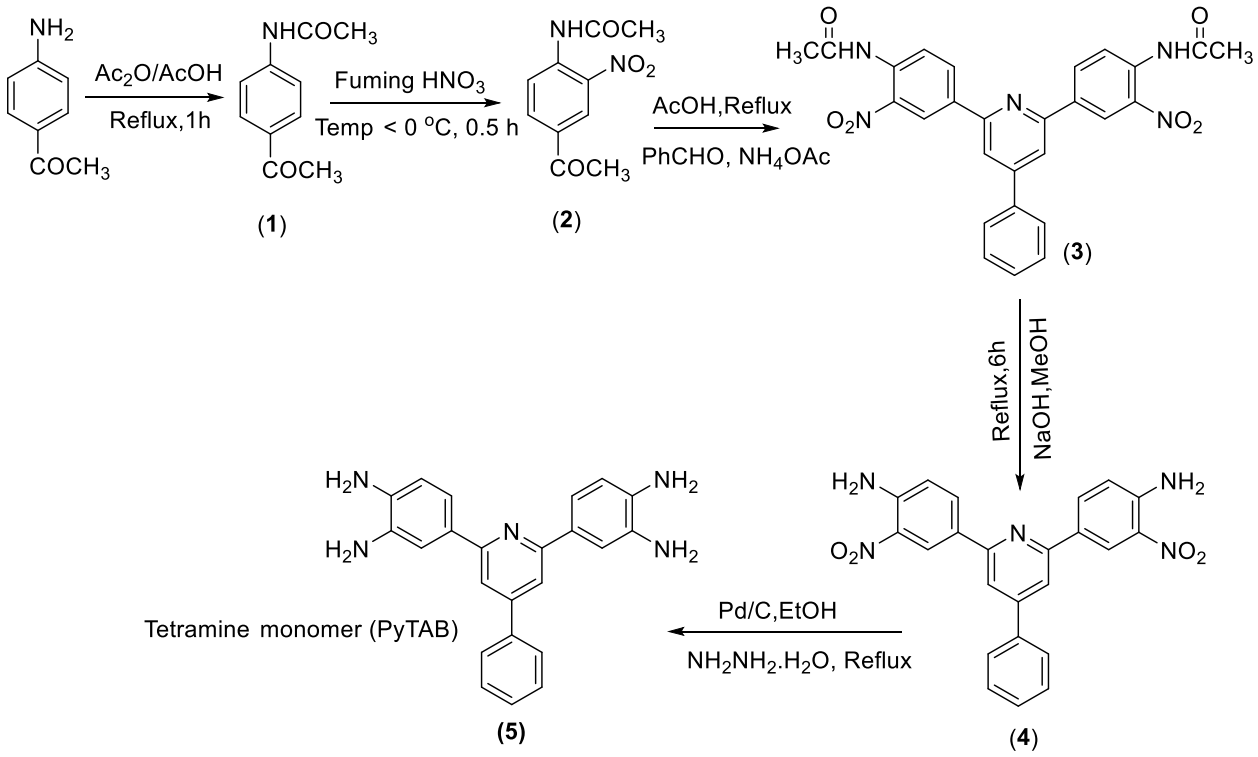

Appendix-III Scheme 5.1. Synthesis pathway of the aromatic pyridine functionalized tetraamine (PyTAB) monomer.

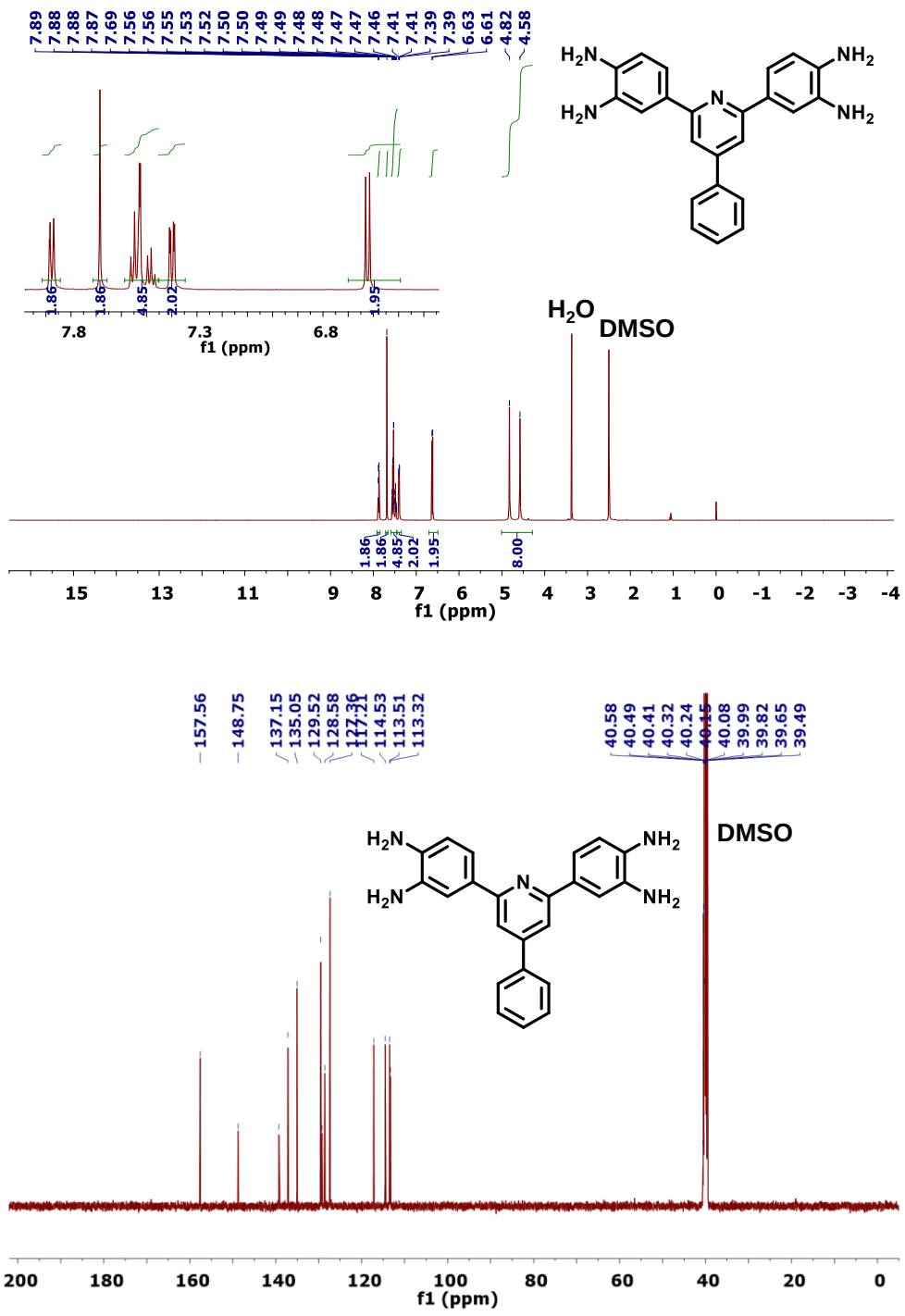

Appendix-III Figure 5.1. ^{1}H NMR and ^{13}C NMR spectra of PyTAB. DMSO-d_6 is used as NMR solvent.

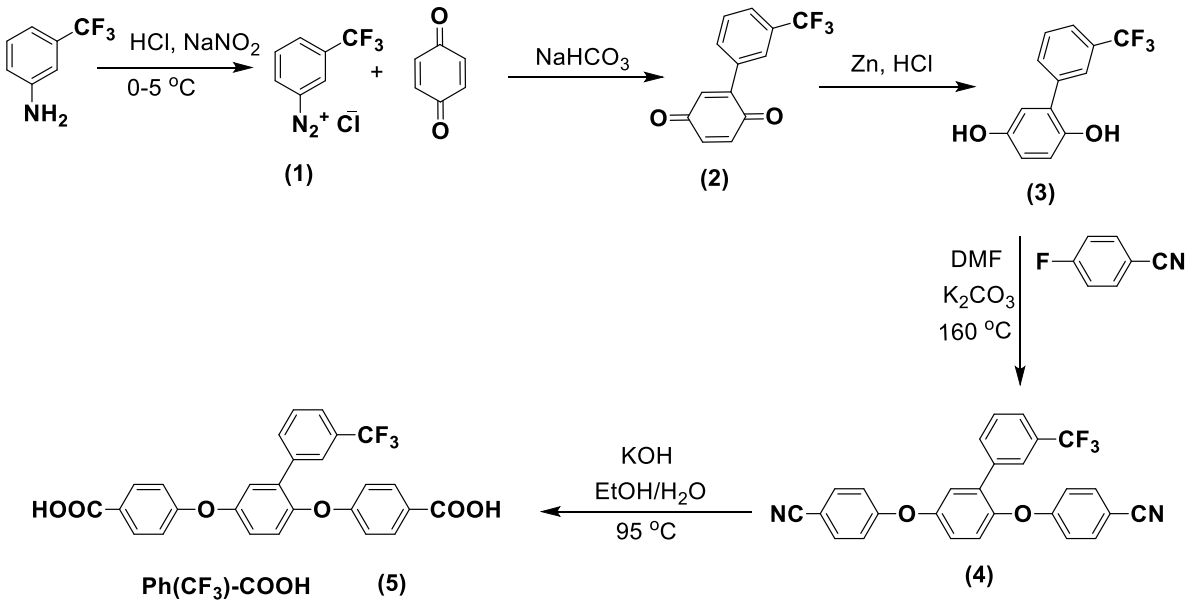

Appendix-III Scheme 5.2. Scheme used for synthesizing (3-trifluoro methyl)phenyl arylether dicarboxylic acid [Ph(CF_3)-COOH] monomer.

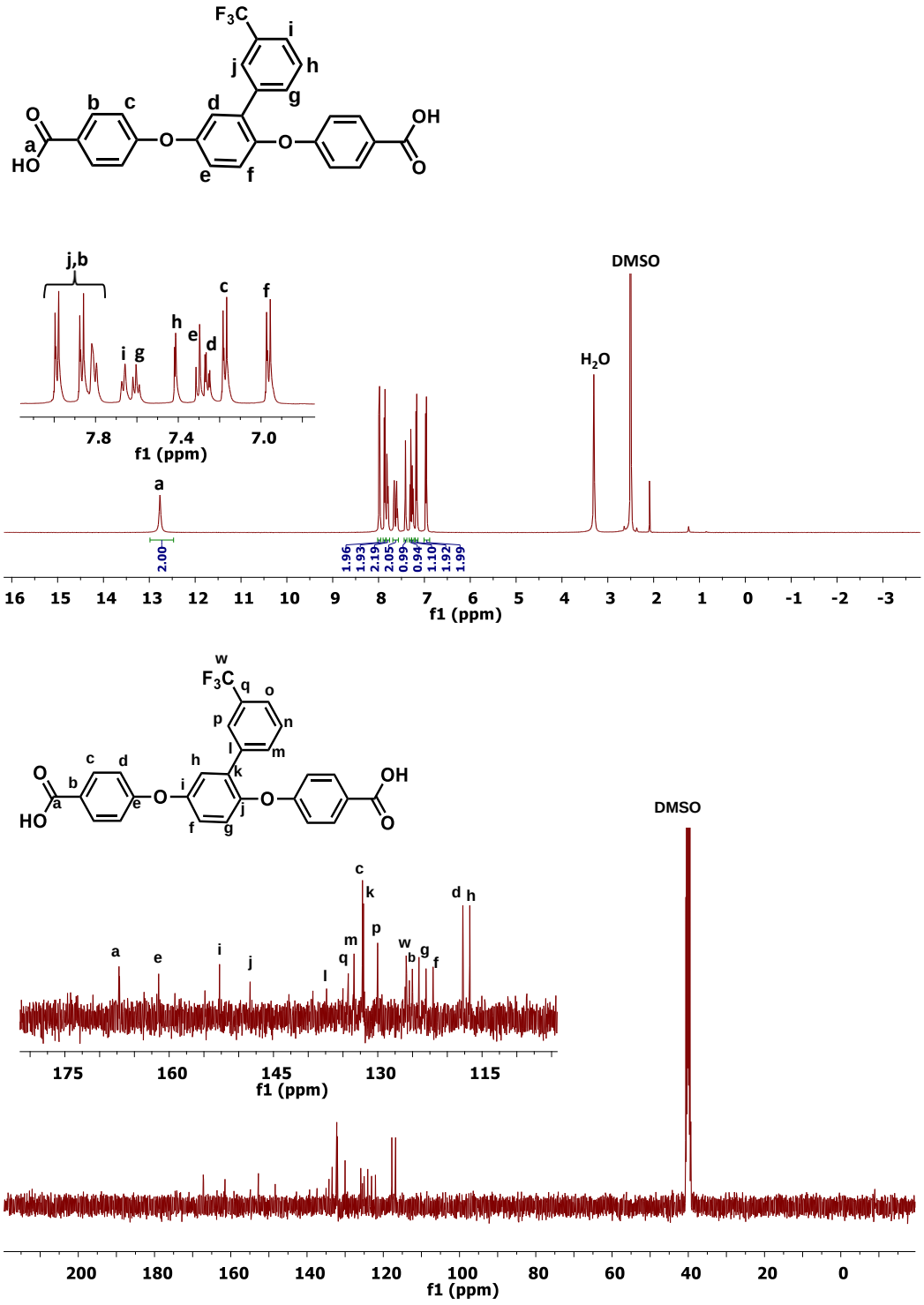

Appendix-III Figure. 5.2: ^{1}H and ^{13}C NMR spectrum of Ph(CF_3)-COOH. DMSO-d_6 is used as NMR solvent.

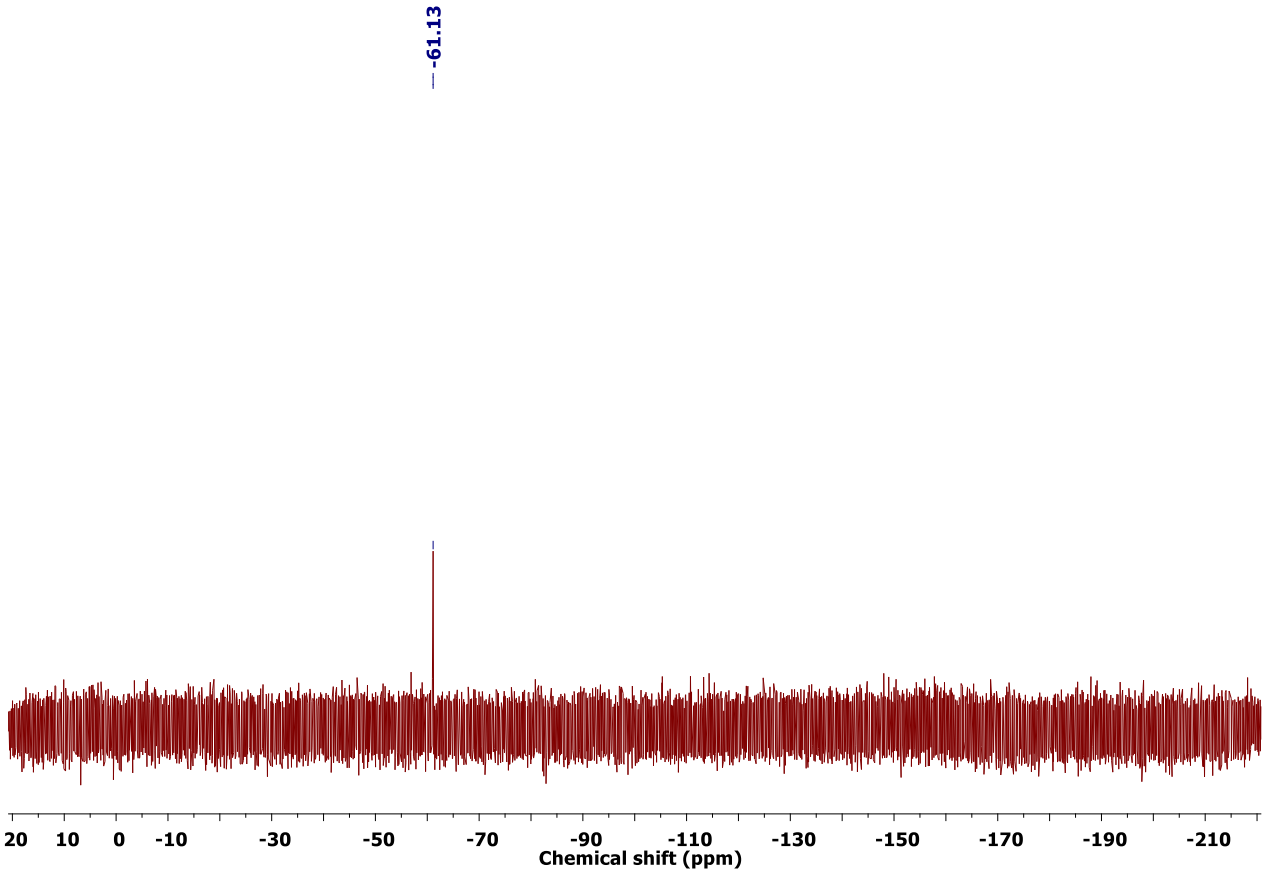

Appendix-III Figure. 5.3: ^{19}F NMR spectrum of **Co-P1** polymer. DMSO-*d*$_6$ is used as NMR solvent.

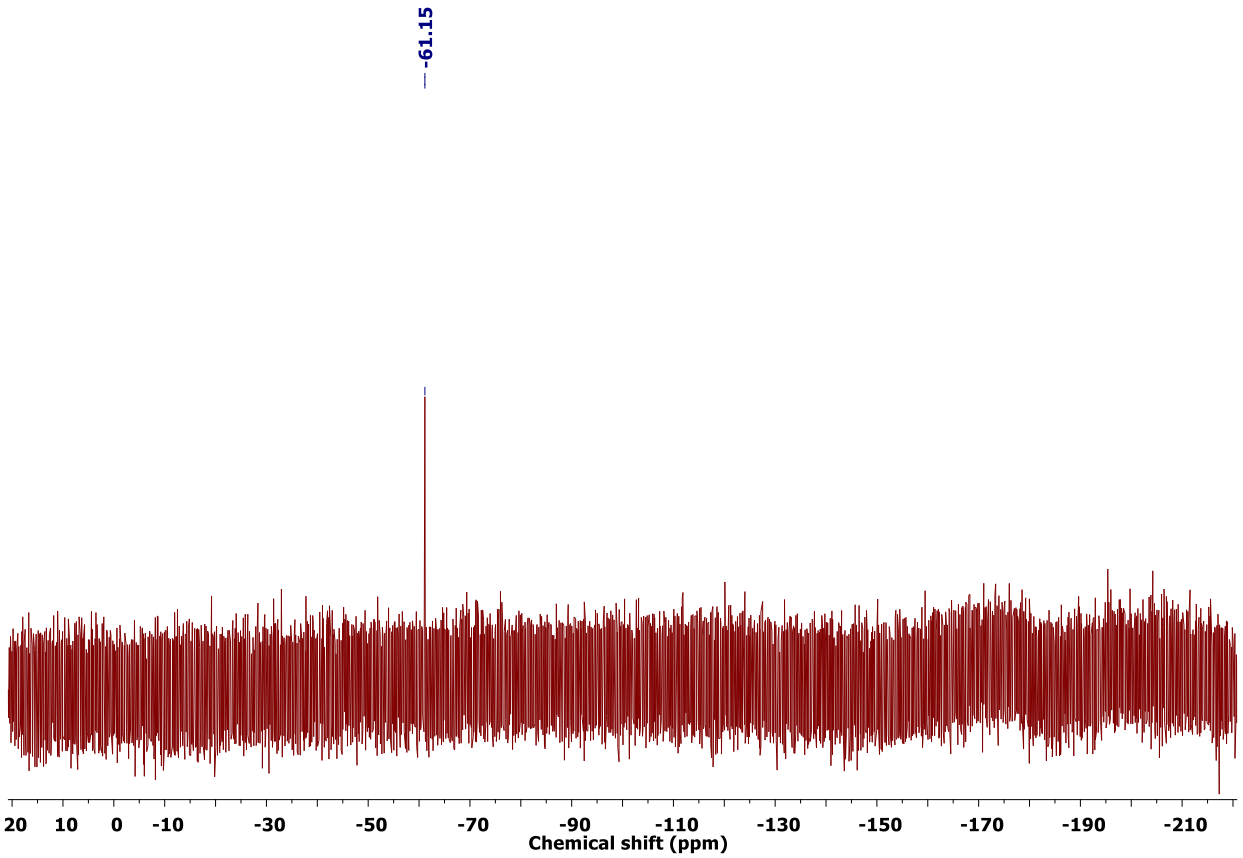

Appendix-III Figure. 5.4: ^{19}F NMR spectrum of **Co-P2** polymer. DMSO-*d*$_6$ is used as NMR solvent.

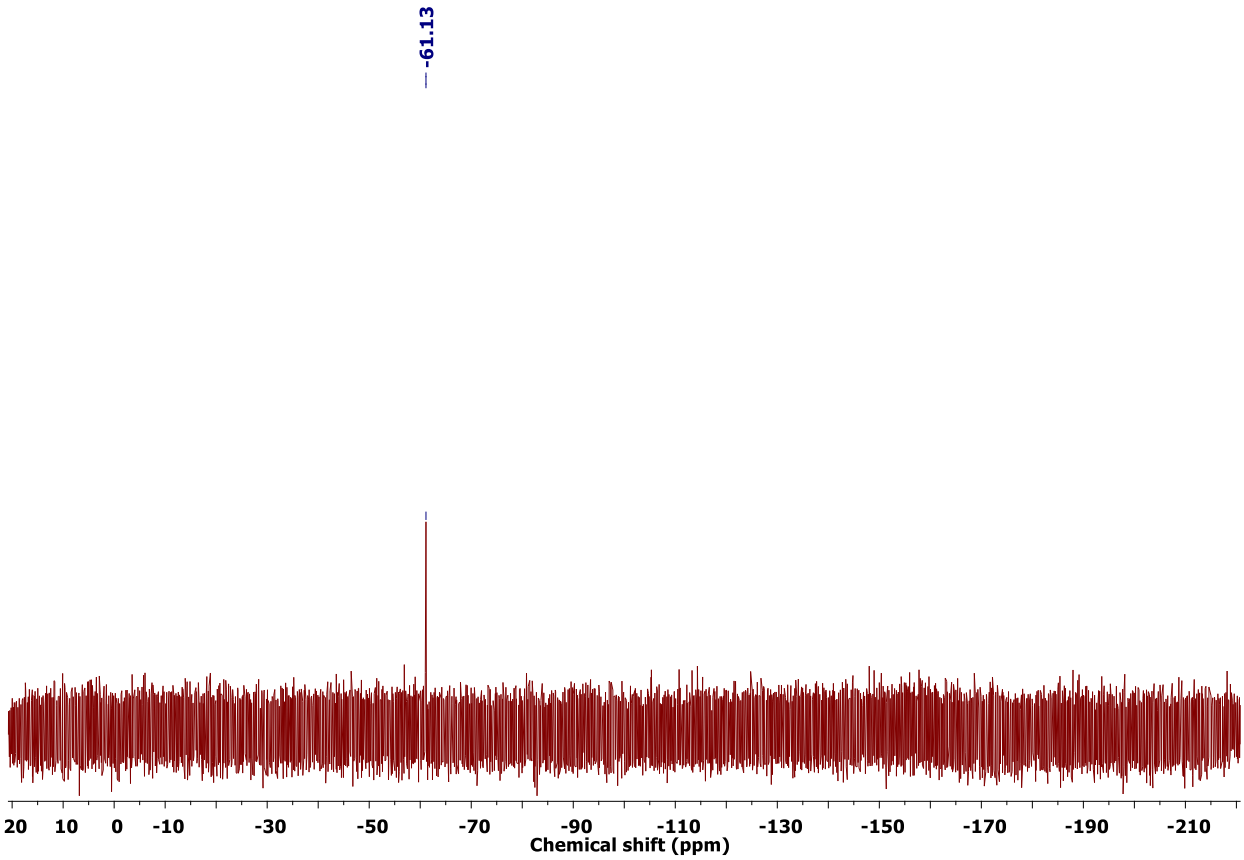

Appendix-III Figure. 5.5: ^{19}F NMR spectrum of **Co-P3** polymer. DMSO-d_6 is used as NMR solvent.

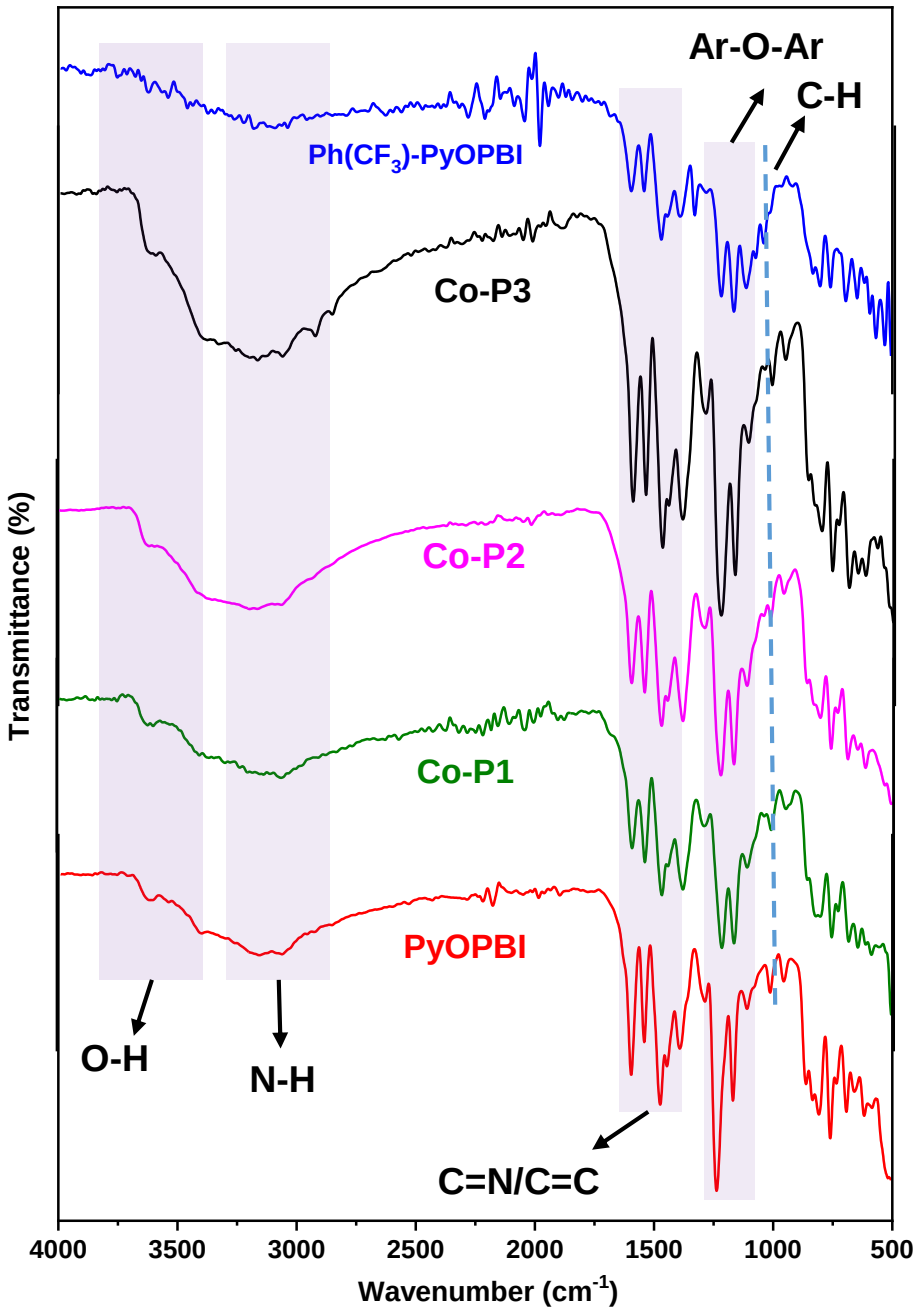

Appendix-III Figure 5.6. FT-IR spectra of the synthesized homo PyOPBI, Ph(CF_3)-PyOPBI and copolymers (Co-P1, Co-P2 and Co-P3).

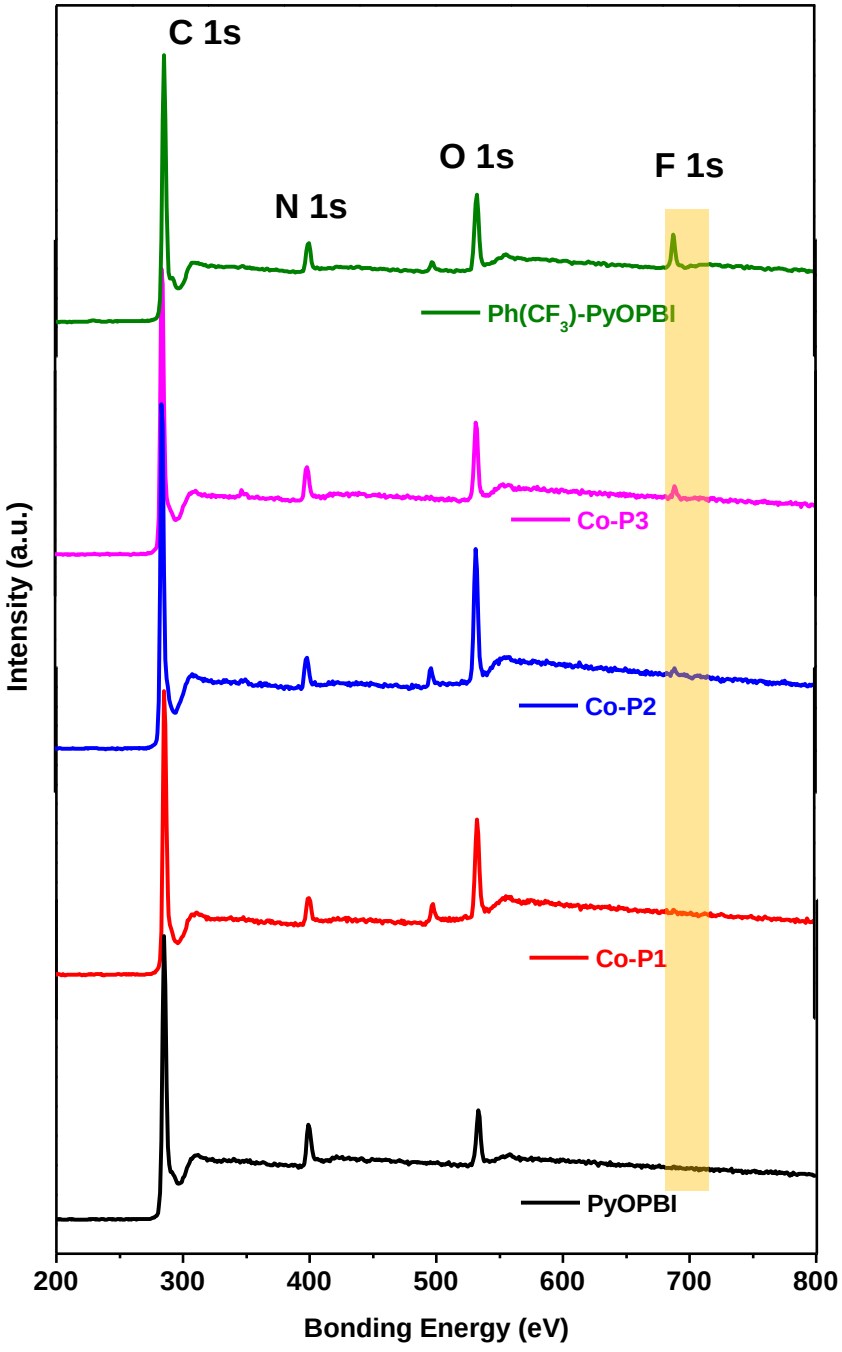

Appendix-III Figure 5.7. XPS full spectra of homo PyOPBI, Ph(CF_3)-PyOPBI and copolymers.

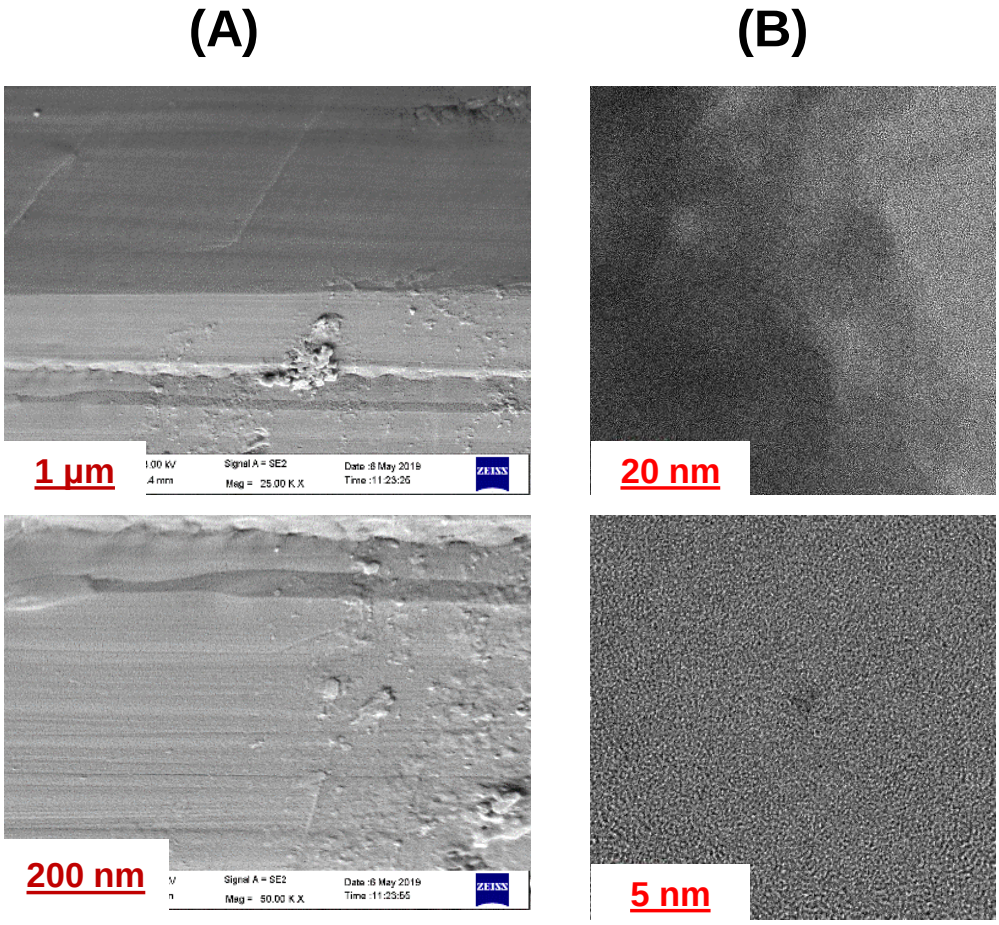

Appendix-III Figure 5.8. Microscopic morphologies PyOPBI membrane. (**A**) Cross-sectional SEM images with scale bar 1µm and 200 nm, respectively and (**B**) HR-TEM images with scale bar 20 and 5 nm.

Appendix-III Table 5.1. Atomic contents of C, O, N and F as obtained from XPS study and polarity ratio for Co-P1, Co-P2 and Co-P3.

Samples	**C 1s** (atomic %)	**N 1s** (atomic %)	**O 1s** (atomic %)	**F 1s** (atomic %)	Polarity ratio (%)
Co-P1	86.96	5.01	7.79	0.24	15.01
Co-P2	84.06	6.2	9.43	0.31	18.96
Co-P3	81.37	6.4	10.72	1.51	22.89

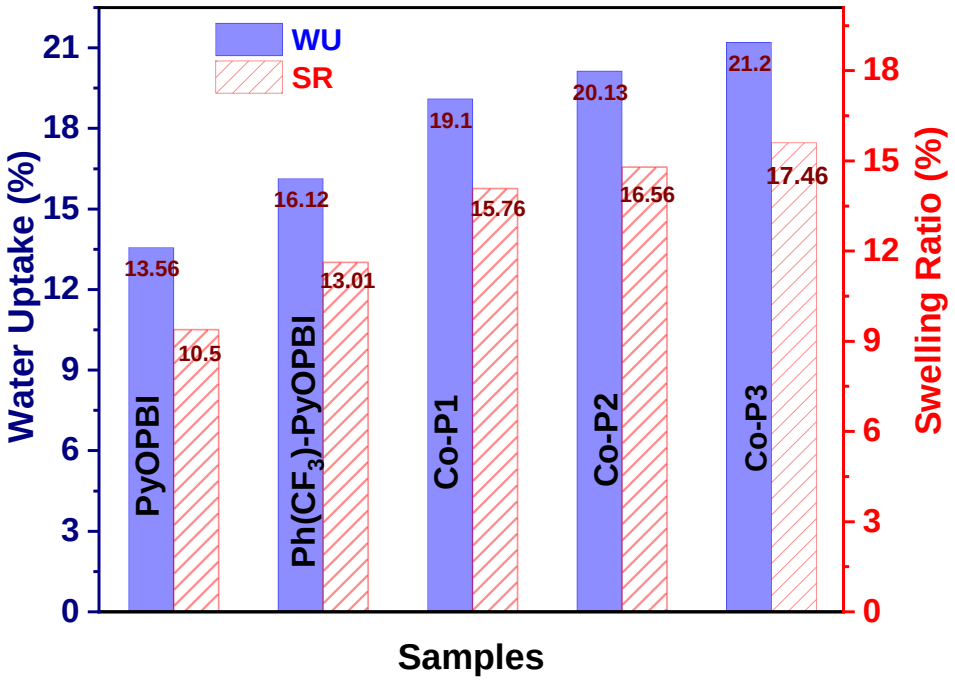

Appendix-III Figure 5.9. The water uptake (WU) and swelling ratio (SR) of different homo and copolymer membranes.

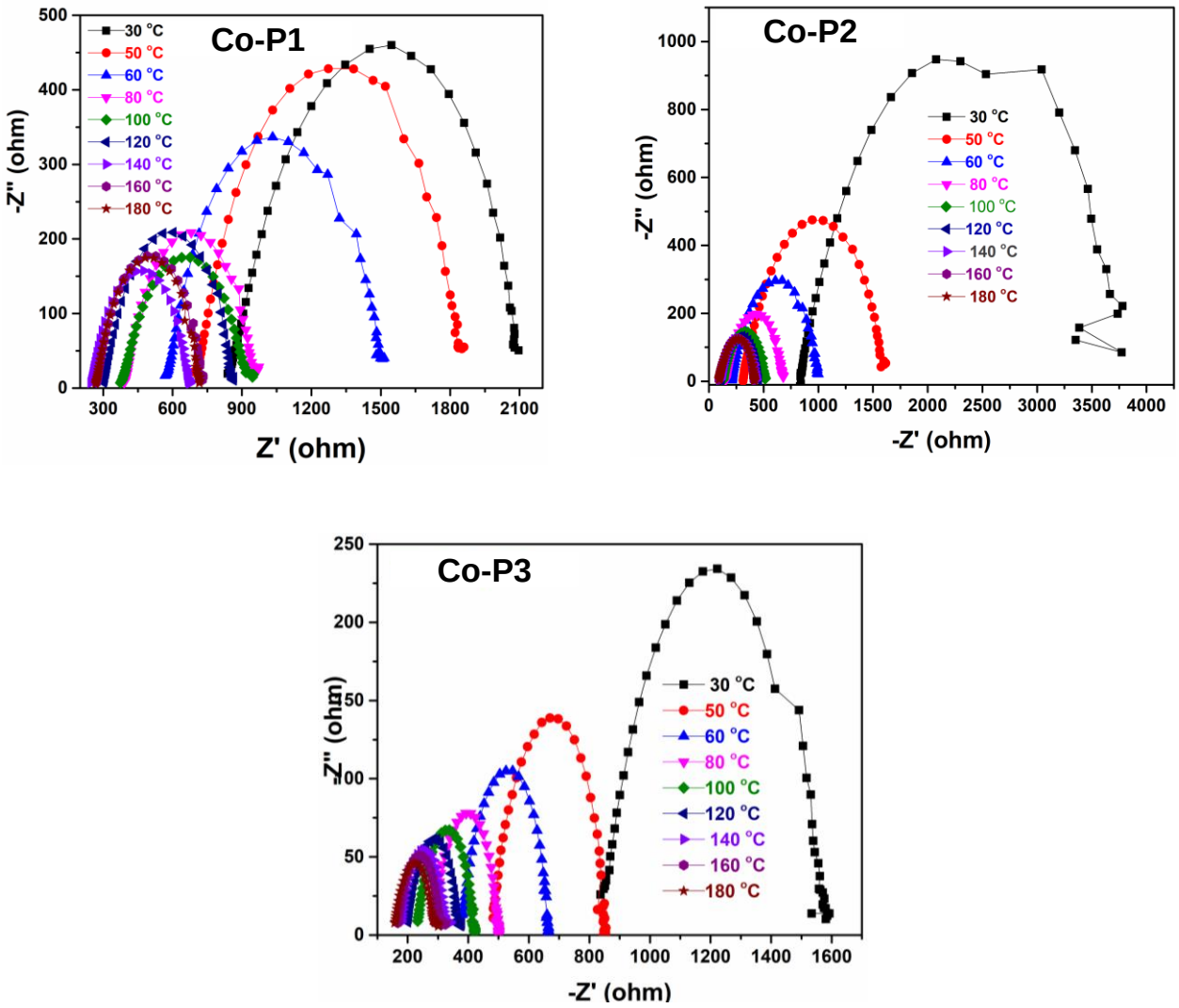

Appendix-III Figure 5.10. Typical Nyquist plots at different temperatures for Co-P1, Co-P2 and Co-P3.

Appendix-IV

Synthesis of pentiptycene quinone (1)

Compound (**1**) was synthesized using modified literature procedure. A mixture of anthracene (0.04 mol, 7.1 g), p-benzoquinone (0.024 mol, 2.6g) and tetra-chloro-1,4-benzoquinone (0.04 mol, 9.8 g) in 250 mL of glacial acetic acid (AcOH) was refluxed for 16 h. After cooling to room temperature, the solid was filtered, washed several times with diethyl ether and AcOH and then dried under reduced pressure at room temperature to get 8.4 g (yield = 91%) of pentiptycene quinone as a yellow solid. The structure was confirmed by ^{1}H and ^{13}C NMR ($CDCl_3$) as shown in **Appendix-IV Figure 6.2**.

Synthesis of pentiptycene hydroquinone (2)

Compound (**2**) was synthesized using modified literature procedure. 8.1 g (0.018 mol) of the synthesized pentiptycene quinone (**1**) was dissolved in 170 mL of DMF followed by the addition of 0.125 mol (10.5 g) of sodium bicarbonate and 0.061 mol (10.5 g) of sodium dithionite. The mixture was stirred at 100°C for 18 h during which time three additional portions of 10.5 g of sodium bicarbonate were added for further reduction. The solution was cooled to room temperature and poured into 500 mL of water. The white precipitated pentiptycene diol was collected, washed several times with water and dried under reduced pressure (yield = 98%). ^{1}H and ^{13}C NMR ($CDCl_3$) of the synthesized compound are shown in **Appendix-IV Figure 6.3**.

Synthesis of pentiptycene containing dicyano compounds (3a and **b)**

Compound 3a: The detailed synthetic route for the synthesis of 1,4-bis(cyanophenoxy) pentiptycene (PenTrip–CN) **3a** is elaborated here as a representative one. Similar procedure was followed for **3b** with appropriate reactant as shown in **Scheme 6.1** in the main article. Pentiptycene hydroquinone **2** (7.1 g, 15.1 mmol) and 4-fluoro benzonitrile (4.33 g, 35.7 mmol) were dissolved in dry DMF (40 mL) in a 100 mL two-necked round-bottom flask followed by the addition of K_2CO_3 (4.03 g, 29.1 mmol) under N_2 atmosphere. After refluxing at 150 ^oC under N_2 atmosphere for 6 h, the solvent (DMF) was removed under vacuum and the resultant solid dicyano compound was obtained and washed with acetone and deionized (DI) water extensively and dried at 100 ^oC in a vacuum oven overnight to obtain a white powder as the dicyano compound **3a (**PenTrip-CN**)** (9.1 g, yield 90%) m.p [melting point obtained from differential scanning calorimetry at a heating rate of 2 $^oC\ min^{-1}$]: 491 ^oC. **^{1}H NMR** (400 MHz, $CDCl_3$) δ [ppm]: 7.66 (d, *J* = 8.8 Hz, 4H), 7.29 (s, 1H), 7.09 (dd, *J* = 5.2, 3.3 Hz, 8H), 6.94 (dd, *J* = 5.3, 3.1 Hz, 8H), 6.88 (d, *J* = 8.8 Hz, 4H), 5.39 (s, 4H) (**Appendix-IV Figure 6.4**). **^{13}C NMR** (101 MHz, $CDCl_3$) δ [ppm]: 162.02, 144.08, 141.06, 137.86, 134.55, 125.54, 123.83, 118.90, 116.51, 105.88, 77.36, 77.04, 76.72, 48.18 (**Appendix-IV Figure 6.4**). **HRMS** (m/z) for $C_{48}H_{28}N_2O_2$ [$M+Na^+$]: Calcd 687.1901; Found 687.1903. **IR (ATR)** [wavenumber (ν), cm^{-1}] = 3018, 2224, 1600, 1500, 1457, 1297, 1228, 1164, 987, 826, 739, 595 (**Appendix-IV Figure 6.5**).

Compound 3b: It should be noted that a similar procedure was followed for the synthesis of the 1,4-bis(cyanophenoxy) 2-methyl pentiptycene product [PenTrip(CH_3)-CN] **3b** (yield 87%), mp: 444 ^oC by DSC at 2 °C/min. **^{1}H NMR** (400 MHz, $CDCl_3$) δ [ppm]: 7.57 (d, *J* = 8.6 Hz, 2H), 7.29 (s, 1H), 7.10 (dd, *J* = 5.2, 3.2 Hz, 8H), 6.94 (dd, *J* = 5.3, 3.1 Hz, 8H), 6.75 (d, *J* = 1.9 Hz, 2H), 6.64 (dd, *J* = 8.5, 2.3 Hz, 2H), 5.39 (s, 4H), 2.49 (s, 6H) (**Appendix-IV Figure 6.6**). **^{13}C NMR** (101 MHz, $CDCl_3$) δ [ppm]: 161.79, 144.87, 144.15, 141.05,

137.72, 134.76, 125.46, 123.86, 118.27, 117.31, 113.74, 106.39, 77.35, 77.04, 76.72, 48.19, 20.66 (**Appendix-IV Figure 6.6**). **HRMS** (m/z) for $C_{50}H_{32}N_2O_2$ [M+1]: Calcd 693.25; Found 693.2544. **IR (ATR)**: ν [cm^{-1}] = 3084, 2225, 1611, 1576, 1498, 1437, 1322, 1302, 1227, 1170, 1117, 1044, 994, 961, 918, 890, 837, 790, 740, 707, 636, 594 (**Appendix-IV Figure 6.7**).

Synthesis of pentiptycene containing diacid monomers (4c and **d)**

Monomer 4c: We screened various synthetic conditions which include solvents, temperature and reaction time (**Appendix-IV Table 6.2**) to make the diacid monomers in good yield. 4,4'-((5,7,12,14-tetrahydro-5,14:7,12-bis([1,2]benzeno)pentacene-6,13-diyl)bis(oxy))dibenzoic acid **(**PenTrip-COOH**) 4c** was finally obtained under optimal synthetic condition as discussed below. The dicyano-para product **3a** (20 g, 0.1 mmol) and triethylene glycol (250 mL) were placed in a 500 mL one-neck round-bottomed flask equipped with a magnetic stirrer and the mixture was refluxed at 200 °C for approximately 10 h to form a homogeneous solution. The resulting clear solution was cooled down to room temperature and aqueous KOH solution (44 g KOH in 200 ml H_2O) was added. Furthermore, the reaction mixture was refluxed under stirring for approximately 24 h at 100 °C. The mixture was allowed to cool to room temperature and the solution was slowly acidified with concentrated hydrochloric acid (HC1) through an addition funnel with ice bath until the solution reached a pH=l. Then, the mixture was stirred for another 1 hour. Thereafter, the white precipitate was filtered and washed repeatedly with deionized (DI) water, and then dried for 24 h at 140 °C until constant weight. The obtained white powder was recrystallized twice with dioxane to afford PenTrip-COOH (**4c**) as colorless crystals (12.6 g, 80% yield; m.p 373 °C by DSC at 2 °C/min). **^{1}H NMR** (500 MHz, DMSO-d_6) δ [ppm]: 12.85 (s, 2H), 7.97 – 7.92 (m, 6H), 7.27 (dd, *J* = 5.3, 3.2 Hz, 6H), 7.00 (dd, *J* = 5.4, 3.1 Hz, 6H), 6.96 – 6.94 (m, 5H), 6.88 (s, 2H), 5.69

(s, 4H) (**Appendix-IV Figure 6.8**). **^{13}C NMR** (101 MHz, DMSO-d_6) δ [ppm]: 167.27, 162.26, 144.59, 141.57, 138.08, 132.26, 125.75, 125.60, 124.21, 115.99, 47.80 (**Appendix-IV Figure 6.8**). **HRMS** (m/z) for $C_{48}H_{30}O_6$ [M+1]: calcd 703.20; found, 703.2122. **IR (ATR)**: ν [cm^{-1}] = 2978, 1689, 1603, 1459, 1422, 1219, 1161, 989, 798, 747, 580, 550. The structure of PenTrip-COOH (**4c**) was also determined and confirmed by single crystal x-ray diffraction (SCXRD) analysis and the obtained structure is shown in **Scheme 6.1** in the main article. The crystallographic data are shown in **Appendix-IV Table 6.1(a)**.

Monomer 4d: The synthetic procedure 4,4'-((5,7,12,14-tetrahydro-5,14:7,12-bis([1,2]benzeno)pentacene-6,13-diyl)bis(oxy))bis(2-methylbenzoic acid) (PenTrip(CH_3)-COOH) **4d** was the same as that of PenTrip-COOH (**4c**) except that in this case PenTrip(CH_3)-CN (**3b**) intermediate was used for the acid hydrolysis. The resulting monomer was obtained as white solid and then crystallized from dioxane to afford PenTrip(CH_3)-COOH (**4d**) as colorless crystals (12.6 g, 80% yield, m.p: 377 °C by DSC at 2 °C/min). **^{1}H NMR** (400 MHz, DMSO) δ [ppm]: ^{1}H NMR (400 MHz, DMSO-d_6) δ 12.78 (s, 2H), 7.91 (d, *J* = 8.7 Hz, 2H), 7.17 – 7.11 (m, 8H), 6.93 (dd, *J* = 5.3, 3.1 Hz, 8H), 6.65 (dd, *J* = 8.6, 2.3 Hz, 2H), 6.55 (d, *J* = 2.1 Hz, 2H), 5.54 (s, 4H), 2.40 (s, 6H) (**Appendix-IV Figure 6.9**). **^{13}C NMR** (101 MHz, DMSO-d_6) δ [ppm]: 168.38, 160.98, 144.58, 142.96, 141.44, 138.04, 125.71, 124.77, 124.29, 118.60, 113.30, 47.80, 22.21 (**Appendix-IV Figure 6.9**). **IR (ATR):** ν [cm^{-1}] = 2980, 1681, 1600, 1459, 1227, 1142, 990, 860, 752, 691, 580, 447. The structure of PenTrip(CH_3)-COOH (**4d**) was also determined and confirmed by single crystal x-ray diffraction (SCXRD) data [**Scheme 6.1** and **Appendix-IV Table 6.1(a)**].

Synthesis of triptycene quinone (5)

Triptycene quinone (**5**) was prepared according to the published literature.[3] A typical reaction is as follows: anthracene (10.12 g, 56.67 mmol), p-benzoquinone (7.37 g, 68.14 mmol) and xylenes (70.8 mL) were added into a round-bottom flask with a stir bar. The mixture was refluxed at 140 ^{o}C under stirring in a nitrogen atmosphere for six hours. The mixture was allowed to cool to room temperature and then filtered. The obtained solid was then washed three times with hot water (500 mL). The quinone product (**5**) (13.02 g, 80% yield) was collected and dried at 60 ^{o}C under vacuum overnight. The structure was confirmed by ^{1}H and ^{13}C NMR ($CDCl_3$) spectra (**Appendix-IV Figure 6.10)**.

Synthesis of triptycene hydroquinone (6)

To synthesize triptycene hydroquinone (**6**), the quinone product (**5**) (13.02 g, 45.4 mmol) and glacial acetic acid (165 mL) were added into a round-bottom flask with a stir bar. The mixture was brought to reflux at 118 ^{o}C under a nitrogen atmosphere. Hydrobromic acid (HBr, 48%) (0.7 mL) was added to the flask and the mixture was allowed to reflux for an additional 30 minutes. A light tan precipitate was formed. The mixture was allowed to cool to room temperature and then filtered. The resulting hydroquinone product (**6**) (11.71 g, 90% yield) was dried under vacuum at 60 ^{o}C for 9 hours. The structure was confirmed by ^{1}H and ^{13}C NMR spectra as shown in **Appendix-IV Figure 6.11**.

Synthesis of triptycene containing dicyano compounds (7a and **7b)**

Compound 7a and **7b**: The dicyano compounds 1,4-bis(cyanophenoxy) triptycene (Trip-CN) **7a** and 1,4-bis(cyanophenoxy) 2-methyle triptycene (Trip(CH_3)-CN) **7b** were synthesized following the similar procedure used for **3a** and **3b**. The resulting mixtures were poured into the acetone and water (v/v = 1:1), filtered, washed and dried under vacuum at 100 ^{o}C overnight giving a white powder as dicyano compounds **7a** and **7b**, respectively. **7a** (Trip-

CN): (Yield: 90%), mp. 330 °C by DSC at 2 °C/min. **^{1}H NMR** (400 MHz, DMSO-d_6) δ [ppm]: 7.80 (s, 1H), 7.78 (s, 1H), 7.25 (dd, *J* = 5.3, 3.2 Hz, 4H), 7.03 (dd, *J* = 5.4, 3.2 Hz, 4H), 6.93 (s, 2H), 6.86 (d, *J* = 2.5 Hz, 2H), 6.84 (d, *J* = 2.5 Hz, 1H), 6.81 (d, *J* = 2.4 Hz, 1H), 5.61 (s, 2H), 2.40 (s, 6H) (**Appendix-IV Figure 6.12**). **^{13}C NMR** (101 MHz, $CDCl_3$) δ [ppm]: 162.02, 144.08, 141.06, 137.86, 134.55, 125.54, 123.83, 118.90, 116.51, 105.88, 48.18 (**Appendix-IV Figure 6.12**). **HRMS** for $C_{34}H_{20}N_2O_2$ [M+NH_4^+]: Calcd 506.19; Found 506.1883. **IR (ATR)**: ν [cm^{-1}] = 3071, 2222, 1600, 1502, 1470, 1232, 1210, 1161, 991, 828, 791, 730, 635, 539 (**Appendix-IV Figure 6.13**).

Compound 7b: Yield 90%. mp: 317 ºC by DSC at 2 °C/min. **^{1}H NMR** (400 MHz, DMSO-d_6) δ[ppm]: 7.80 (s, 1H), 7.78 (s, 1H), 7.25 (dd, *J* = 5.3, 3.2 Hz, 4H), 7.03 (dd, *J* = 5.4, 3.2 Hz, 4H), 6.93 (s, 2H), 6.86 (d, *J* = 2.5 Hz, 2H), 6.84 (d, *J* = 2.5 Hz, 1H), 6.81 (d, *J* = 2.4 Hz, 1H), 5.61 (s, 2H), 2.40 (s, 6H) (**Appendix-IV Figure 6.14**). **^{13}C NMR** (101 MHz, DMSO-d_6) δ 161.60, 146.11, 144.83, 144.37, 140.00, 135.32, 128.99, 125.92, 124.55, 120.32, 118.40, 115.03, 106.15, 48.00, 20.52 (**Appendix-IV Figure 6.14**). **HRMS** (m/z) for $C_{36}H_{24}N_2O_2$: Calcd 516.16; Found 516.1689. **IR (ATR)**: ν [cm^{-1}] = 3071, 2212, 1599, 1566, 1466, 1281, 1240, 1211, 1161, 1098, 1016, 946, 863, 814, 736, 699, 635, 585 (**Appendix-IV Figure 6.15**).

Synthesis of triptycene containing diacid monomers (8c and **8d)**

Monomers 8c and **8d**: The diacid compounds 4,4'-((9,10-dihydro-9,10-[1,2]benzenoanthracene-1,4-diyl)bis(oxy))dibenzoic acid (Trip-COOH) **8c** and 4,4'-((9,10-dihydro-9,10-[1,2]benzenoanthracene-1,4-diyl)bis(oxy))bis(2-methylbenzoic acid) (Trip(CH_3)-COOH) **8d** were synthesized following the similar procedure used for PenTrip-COOH (**4c**) and PenTrip(CH_3)-COOH (**4d**). The resulting mixtures were acidified with HCl at pH l and the white precipitate was filtered, washed with water, dried at 140 °C, and then

crystallized from dioxane to afford Trip-COOH (**8c**) and Trip(CH_3)-COOH (**8d**) as colorless crystals, respectively. **8c** (Trip-COOH) (6.0 g, 80% yield; mp 385–388 °C, by DSC at 2 °C/min). **^{1}H NMR** (500 MHz, DMSO-d_6) δ [ppm]: 12.85 (s, 2H), 8.06 – 7.88 (m, 4H), 7.27 (dd, *J* = 5.3, 3.2 Hz, 4H), 7.07 – 6.98 (m, 4H), 7.00 – 6.92 (m, 4H), 6.88 (s, 2H), 5.69 (s, 2H) (**Appendix-IV Figure 6.16**). **^{13}C NMR** (126 MHz, DMSO-d_6) δ [ppm]: 167.29, 161.95, 146.58, 144.63, 144.45, 139.82, 132.18, 125.87, 125.72, 124.47, 120.10, 117.74, 116.83, 47.63 (**Appendix-IV Figure 6.16**). **HRMS** (m/z): [M]+ calcd. for $C_{34}H_{22}O_6$, 526.14; found, 526.2264. **IR (ATR):** ν [cm^{-1}] = 2960, 1687, 1600, 1458, 1421, 1286, 1218, 1161, 1099, 851, 798, 746, 686, 549, 500, 458, 420. The structure of Trip-COOH was also determined by single crystal x-ray diffraction (SCXRD) data [**Scheme 6.1**, **Appendix-IV Table 6.1(b)**].

8d (Trip(CH_3)-COOH)**:** Yield: 80%, m.p 323 °C by DSC at 2 °C/min. **^{1}H NMR** (500 MHz, DMSO-d_6) δ [ppm]: 12.68 (s, 2H), 7.88 (d, *J* = 8.6 Hz, 2H), 7.26 (dd, *J* = 5.3, 3.2 Hz, 4H), 7.10 – 6.93 (m, 6H), 6.85 (d, *J* = 4.6 Hz, 2H), 6.73 (ddd, *J* = 19.0, 10.0, 3.6 Hz, 4H), 5.65 (s, 2H), 2.45 (s, 6H) (**Appendix-IV Figure 6.17**). **^{13}C NMR** (126 MHz, DMSO-d_6) δ [ppm]: 168.34, 146.50, 144.56, 133.46, 125.81, 124.51, 120.00, 119.50, 114.15, 47.74, 22.07 (**Appendix-IV Figure 6.17**). **HRMS** (m/z) for $C_{36}H_{26}O_6$ [M+1]: calcd, 554.1815; found, 554.1815. **IR (ATR):** ν [cm^{-1}] = 2919, 2847, 1671, 1596, 1471, 1319, 1216, 1141, 990, 862, 777, 741, 710, 618, 509, 438. The structure of Trip(CH_3)-COOH (**8d**) was also determined and confirmed by single crystal x-ray diffraction (SCXRD) data [**Scheme 6.1** and **Appendix-IV Table 6.1(b)**].

Synthesis of model compounds

Compound M1: A 25 mL three neck round-bottom flask was charged with 2.0 g (2.8 mmol) of purified PenTrip(CH_3)-COOH and 0.6 g (5.5 mmol) of o-Phenylenediamine (OPDA)

in a reaction medium consisting of a mixture of PPMA (1:1 mixture of P_2O_5 and CF_3SO_3H) and CH_3SO_3H (TFSA) under inert atmosphere. Afterward, the mixture was stirred using overhead mechanical stirrer and gradually heated up to 100 °C for 2 h and another 1 h stirring was continued at 140 °C under nitrogen atmosphere. Thereafter, a homogeneous solution was obtained immediately and a viscosity increase was observed. After the complete reaction, a dark brown colour viscous solution was slowly poured into deionized (DI) water with stirring and the collected precipitated model compounds (**M1**) was filtrated and washed with copious amount of DI water several times. The residual phosphoric acid in the product powder was neutralized with 10 wt % sodium hydrogen carbonate ($NaHCO_3$) solution at 40 °C overnight and the **M1** was washed thoroughly with DI water until the wash water pH reached 7.0 and then dried under reduced pressure at 100 °C for 24 h to get 2.1 g (95% yield) of a dark brown solid (**see Figure 6.1a** in the main article). **^{1}H NMR** (400 MHz, DMSO-d_6) δ [ppm]: 13.57 (s, 1H), 8.23 (s, 2H), 8.05 (s, 2H), 7.94 (d, 6H), 7.78 (s, 2H), 7.62 (t, 3H), 7.37 (s, 2H), 7.23 (d, 6H), 6.99 (s, 2H), 6.16 (s, 2H) (**Appendix-IV Figure 6.18**). **^{13}C CP-MAS solid-state NMR** (400 MHz) δ [ppm]: 151.32, 146.57, 141.48, 138.44, 136.88, 131.63, 130.04, 128.07, 127.35, 126.48, 125.48, 124.96, 124.26, 122.28, 120.94, 119.94, 49.45 (**Appendix-IV Figure 6.18**). **IR (ATR)**: ν [cm^{-1}] = 3065 (imidazole ring N−H vibration), 1601-1472 (C=N, C=C vibration), 1304 (in-plane benzimidazole ring vibration), 1226-1168 (asymmetric C−O vibration) (**Appendix-IV Figure 6.19**).

Compound M2: The procedure (see **Figure 6.1a** in the main article) to prepare **M2** was similar to that used for **M1**. **^{1}H NMR** (500 MHz, DMSO-d_6) δ [ppm]: 13.48 (s, 1H), 8.28 (d, 2H), 8.08 (d, 4H), 7.96 (m, 8H), 7.80 (d, 2H), 7.54 (d, 4H), 7.48 (d, 4H), 7.29 (d, 2H), 7.03 (d 2H), 6.75 (m, 4H), 6.08 (s, 4H) (**Appendix-IV Figure 6.20**). **^{13}C CP-MAS solid-state NMR** (400 MHz) δ [ppm]: 151.32, 146.57, 140.95, 138.44, 136.88, 131.63, 130.04, 128.07, 127.35,

126.48, 125.48, 124.96, 124.26, 122.28, 120.94, 119.94, 118.22, 116.58, 112.84, 49.45 (**Appendix-IV Figure 6.20**). **IR (ATR)**: ν [cm^{-1}] = 2924 (imidazole ring N−H vibration), 1602-1456 (C=N, C=C vibration), 1410-1304 (in-plane benzimidazole ring vibration), 1212-1133 (asymmetric C−O vibration) (**Appendix-IV Figure 6.21**).

Appendix-IV Table 6.1 (a). Crystallographic data and structure refinement for PenTrip-COOH and PenTrip(CH_3)-COOH.

Sample code	**PenTrip-COOH (4c)**	**PenTrip(CH_3)-COOH (4d)**
Crystal system	monoclinic	triclinic
Space group	P 1 21/c 1	P-1
Chemical formula	C_{52} H_{38} O_8	C_{70} H_{70} O_{16}
Formula weight	790.82	1167.26
Radiation (Å)	MoKα (λ = 0.71073)	MoKα (λ = 0.71073)
a (Å)	18.5689(4)	12.9173(3)
b (Å)	15.4573(4)	13.0433(2)
c (Å)	18.2748(5)	19.2711(3)
α (°)	90	107.7810(10)
β (°)	100.328(2)	97.242(2)
γ (°)	90	97.459(2)
Volume/(Å^3)	5160.3(2)	3018.03(10)
Z	4	2
Temperature (K)	293(2)	107(7)
Independent reflections	10813	11458
Data/restrains/ parameters	10813/2/541	11458/0/782
D_{calcd} [g cm^{-3}]	1.018	1.284
F(000)	1656.0	1236.0
R factor [I >2 σ(I)]	R_1 = 0.0606, wR_2 =0.1871	R_1 = 0.0722, wR_2 = 0.1786
R factor (all data)	R_1 =0.0905 wR_2 = 0.2030	R_1 = 0.1310, wR_2 = 0.2202
GoF	1.100	1.057
CCDC number	2099945	2070350

Appendix-IV Table 6.1 (b). Crystallographic data and structure refinement for Trip-COOH and Trip(CH_3)-COOH.

Sample code	Trip-COOH (8c)	Trip(CH_3)-COOH (8d)
Crystal system	triclinic	monoclinic
Space group	P-1	C 2/c
Chemical formula	C_{44} H_{42} O_{11}	C_{48} H_{50} O_6
Formula weight	746.77	722.88
Radiation (Å)	MoKα (λ = 0.71073)	MoKα (λ = 0.71073)
a (Å)	8.37800(10)	32.9760(19)
b (Å)	13.2003(3)	7.9644(3)
c (Å)	17.8121(5)	31.495(2)
α (°)	72.054 (2)	90
β (°)	84.683(2)	112.675(7)
γ (°)	83.825(2)	90
Volume/(Å^3)	1859.47(7)	7632.3(8)
Z	2	8
Temperature (K)	293(2)	293(2)
Independent reflections	6553	6725
Data/restrains/ parameters	6553/0/498	6725/0/ 573
D_{calcd} [g cm^{-3}]	1.334	1.258
F(000)	788.0	3088.0
R factor [I >2 σ(I)]	R_1 = 0.0464, wR_2 = 0.1217	R_1 = 0.1006, wR_2 = 0.2565
R factor (all data)	R_1 = 0.0589, wR_2 = 0.1313	R1 = 0.1598, wR_2 = 0.2865
GoF	1.092	0.976
CCDC number	2070384	1951204

Appendix-IV Table 6.2. Synthetic conditions that were screened for synthesizing PenTrip-COOH.

Entry	Reactant (6.98 g)	Base (4 eq.)	Solvent	Temp. (°C)	Reaction Time	Yield of PenTrip-CO_2H (%)
1	PenTrip-CN	KOH	EtOH+H_2O (1/1 by vol.)	90	48 h, reflux	2
2	PenTrip-CN	KOH	EtOH+MeOH+H_2O (1/1/1 by vol.)	85	72 h, reflux	0
3	PenTrip-CN	KOH	MeOH+H_2O (1/1 by vol.)	65	48 h, reflux	1
4	PenTrip-CN	NaOH	EtOH+H_2O (1/1 by vol.)	90	48 h, reflux	0
5	PenTrip-CN	NaOH	EtOH+MeOH+H_2O (1/1/1 by vol.)	85	24 h, reflux	0
6	PenTrip-CN	tBuOK	EtOH+H_2O (1/1 by vol.)	95	48 h, reflux	5
7	PenTrip-CN	tBuOK	EtOH+MeOH+H_2O (1/1/1 by vol.)	85	24 h, reflux	10
8	PenTrip-CN	KOH	Triethylene glycol	200	48 h, reflux	89
9	PenTrip-CN	NaOH	Triethylene glycol	200	48 h, reflux	65

Appendix-IV Table 6.3. Screening of conditions for PenTrip-PyPBI synthesis.

Entry	Reactant 1 (5 mmol)	Reactant 2 (5 mmol)	Solvent	Temp. (°C)	Time and atmosphere	Observation and yield of PenTrip-PyPBI
1	PenTrip-CO_2H	PyTAB	PPA+P_2O_5 [a]	220	24 h, N_2	0 (%)
2	PenTrip-CO_2H	PyTAB	PPA+NMP	190	24 h, N_2	0 (%)
3	PenTrip-CO_2H	PyTAB	PPMA	160	8 h, N_2	10 (%)
4	PenTrip-CO_2H	PyTAB	PPMA+P_2O_5 [a]	160	16 h, N_2	8 (%)
5	PenTrip-CO_2H	PyTAB	PPMA+NMP[b] +P_2O_5	150	16 h, N_2	15 (%)
6	PenTrip-CO_2H	PyTAB	CH_3SO_3H	140	16 h, N_2	0 (%)
7	PenTrip-CO_2H	PyTAB	CF_3SO_3H+P_2O_5	140	2.5 h N_2	Viscous but not soluble
8	PenTrip-CO_2H	PyTAB	PPMA+ CF_3SO_3H	140	3 h, N_2	Viscous, easy to stir, 80 (%)
9	PenTrip-CO_2H	PyTAB	PPMA+ CF_3SO_3H+ P_2O_5 [c]	140	3 h, N_2	Viscous, easy to stir, 98 (%)

[a] The content of added P_2O_5 was calculated for a total PPA concentration of 128 wt%.

[b] The added P_2O_5 content is equal to 5 wt% of PPA.

[c] The added content P_2O_5 content is equal to 5 wt% of PPA.

Appendix-IV Table 6.4. Inherent viscosity, viscosity average molecular weight ($\overline{M_v}$) and solubility results of the iptycene-based PyPBI polymers.

Sample code	I.V (dL/g)	$\bar{M}_v^a$ (kDa)	DMSO	DMAc	MSA	DMF	FA
Trip-PyPBI	1.32	9.4	+ +	+ +	+ +	+ +	+ +
Trip(CH_3)-PyPBI	2.00	9.7	+ +	+ +	+ +	+ +	+ +
PenTrip-PyPBI	1.77	9.3	+ +	+ +	+ +	+ +	+ +
PenTrip(CH_3)-PyPBI	2.11	12.9	+ +	+ +	+ +	+ +	+ +

+ + completely Soluble at room temperature up to 2 wt%.

[a] $\overline{M_v}$ obtained from Mark–Houwink–Sakurada equation $[\eta]= K\bar{M}_v^a$ where K = 5.2×10^{-5} dL/g and a = 0.92 and $[\eta] = \frac{\eta_{sp}+3\ln\eta_{rel}}{4C}$ where η_{sp} = 1-η_{rel} and $\eta_{rel} = {}^{t}/_{t_o}$ where t and t_o are the time flow for the polymer solution and solvent, respectively.[6]

Appendix-IV Table 6.5. Atomic elemental contents (C, O and N) of 3D iptycene-based PyPBIs calculated by XPS.

.

Samples	**C 1s** (atomic %)	**N 1s** (atomic %)	**O 1s** (atomic %)
Trip-PyPBI	83.82	4.18	11.99
Trip(CH_3)-PyPBI	88.58	2.91	8.51
PenTrip-PyPBI	89.18	2.29	8.49
PenTrip(CH_3)-PyPBI	89.75	1.91	8.34

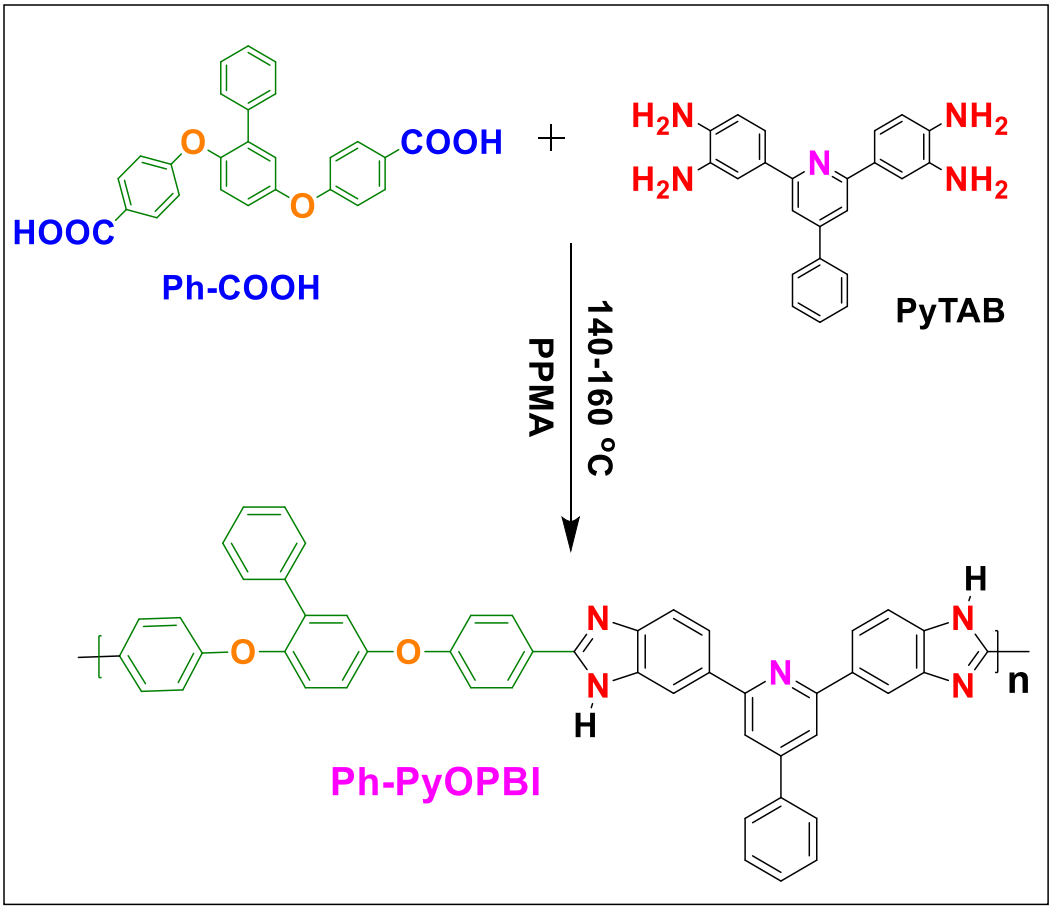

Appendix-IV Scheme 6.1. Synthesis of Ph-PyOPBI polymer.

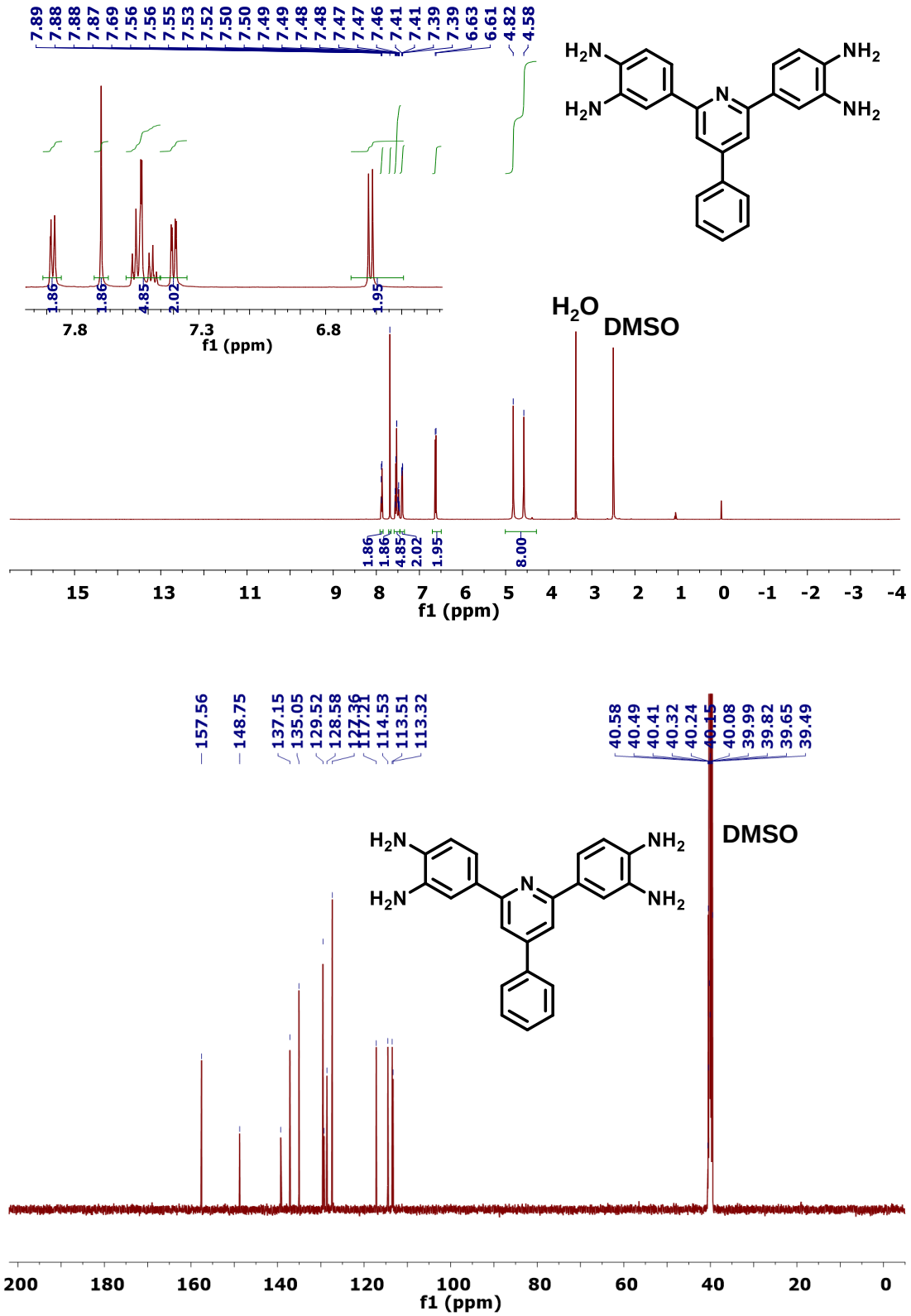

Appendix-IV Figure 6.1. ^{1}H NMR and ^{13}C NMR spectra of PyTAB. DMSO-d_6 is used as NMR solvent.

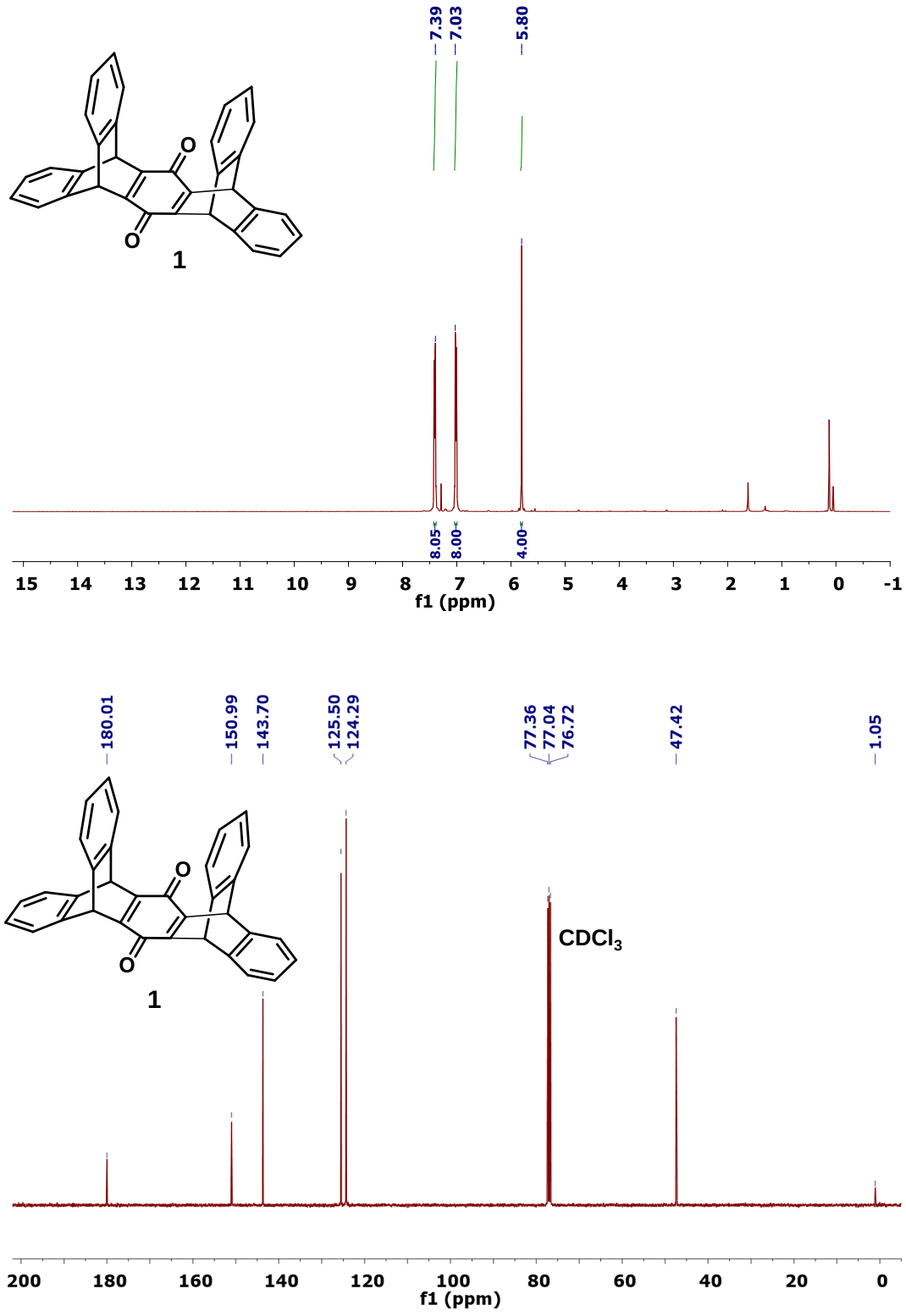

Appendix-IV Figure 6.2. ^{1}H and ^{13}C NMR spectra of pentiptycene quinone (**1**). NMR solvent: $CDCl_3$

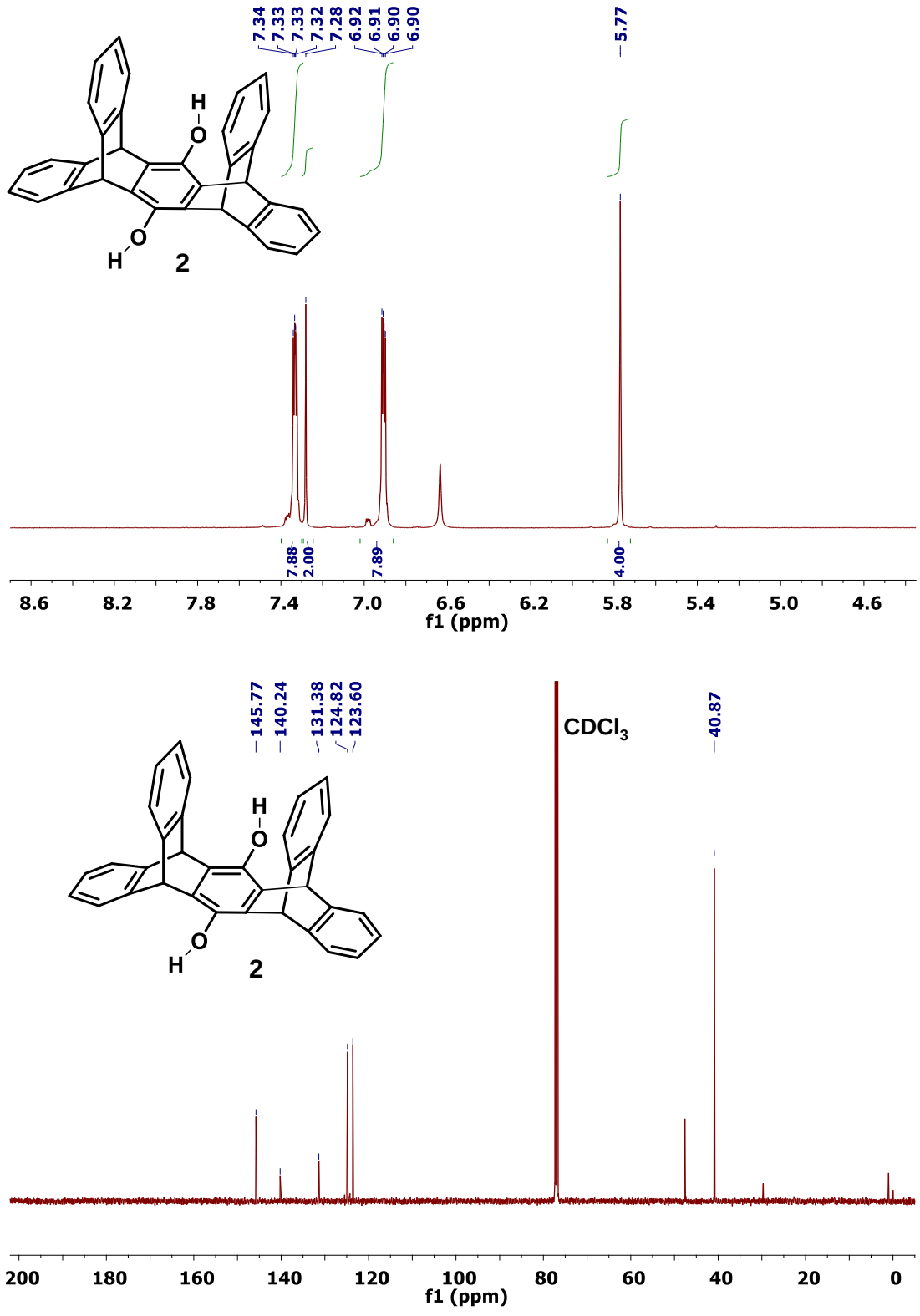

Appendix-IV Figure 6.3. ^{1}H and ^{13}C NMR spectra of pentiptycene hydroquinone (**2**). NMR solvent: $CDCl_3$.

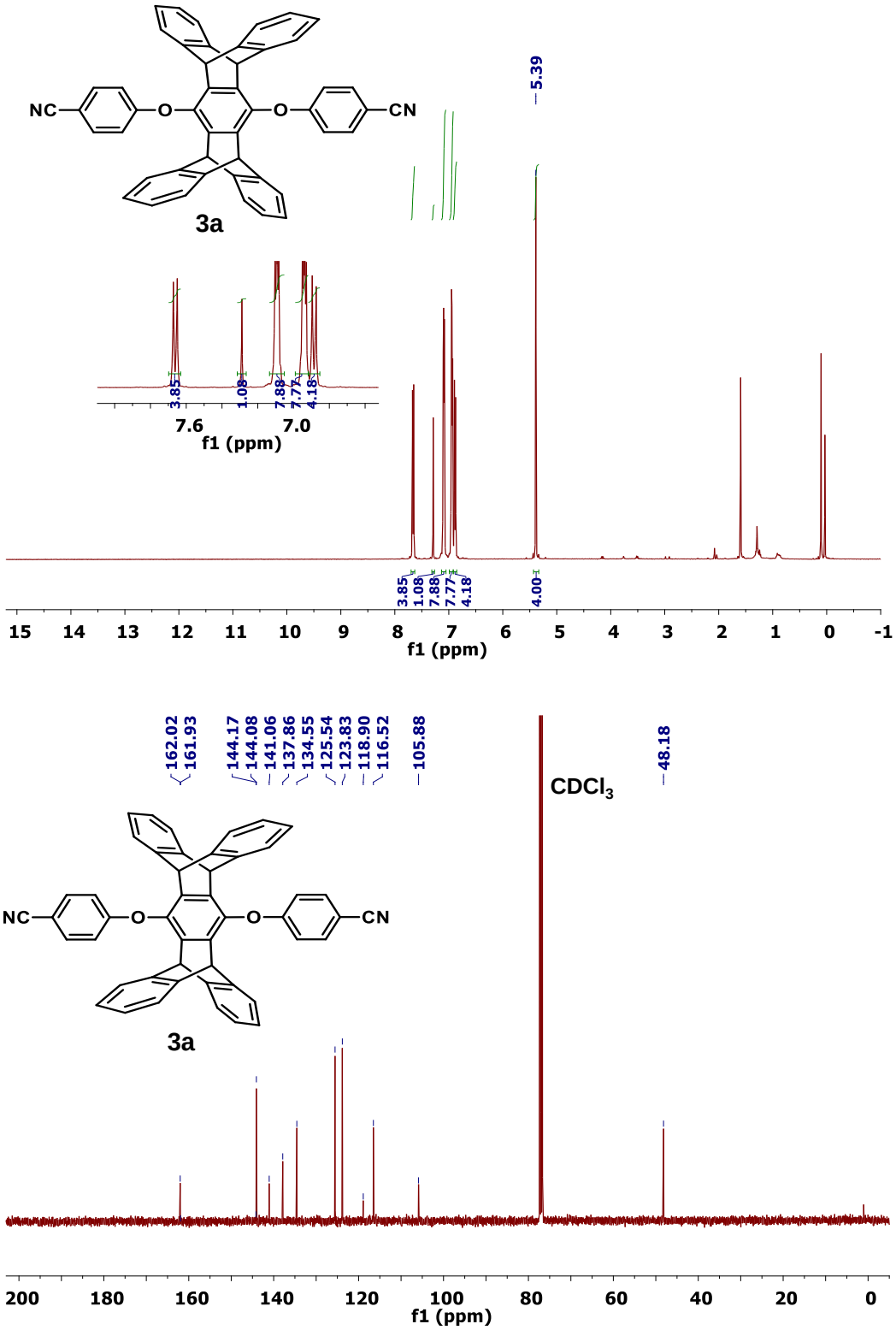

Appendix-IV Figure 6.4. ^{1}H and ^{13}C NMR spectra of PenTrip–CN (**3a**). NMR solvent: $CDCl_3$.

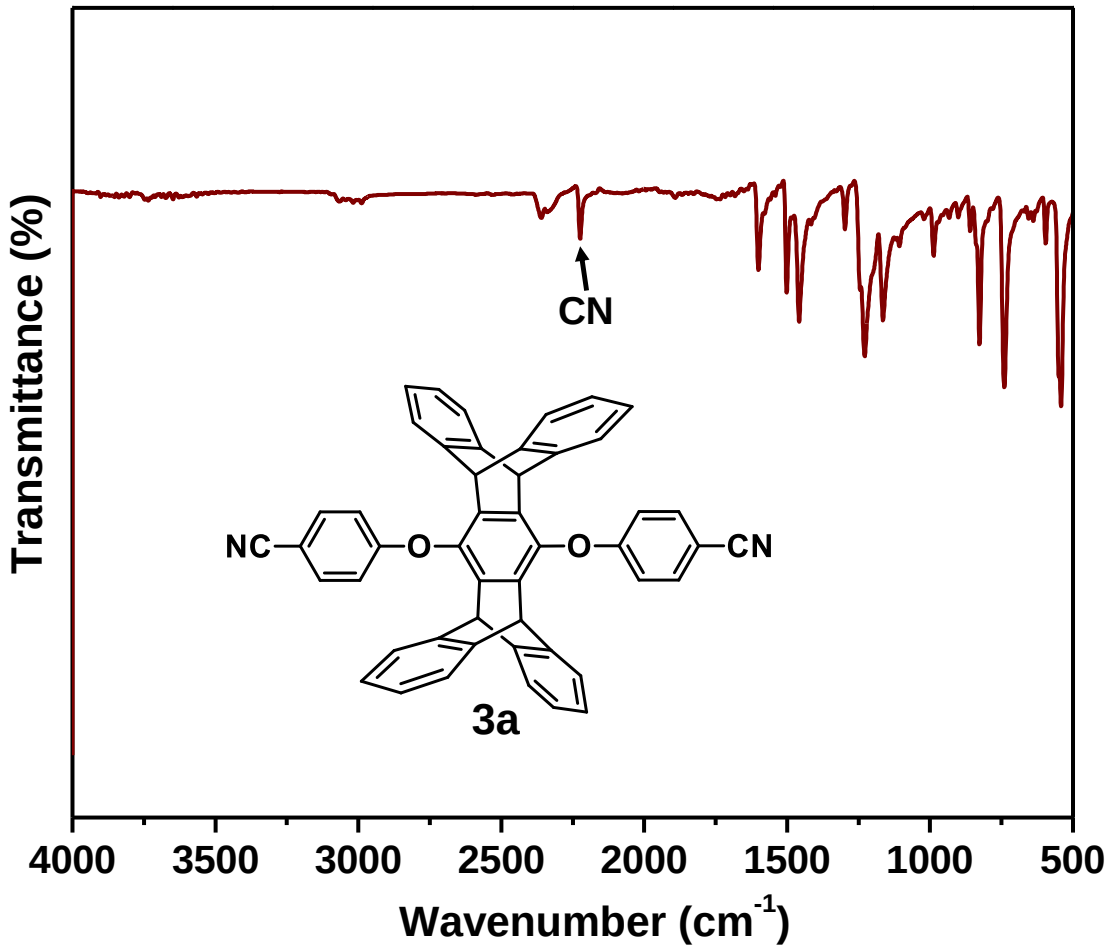

Appendix-IV Figure 6.5. FTIR spectra of PenTrip–CN (**3a**).

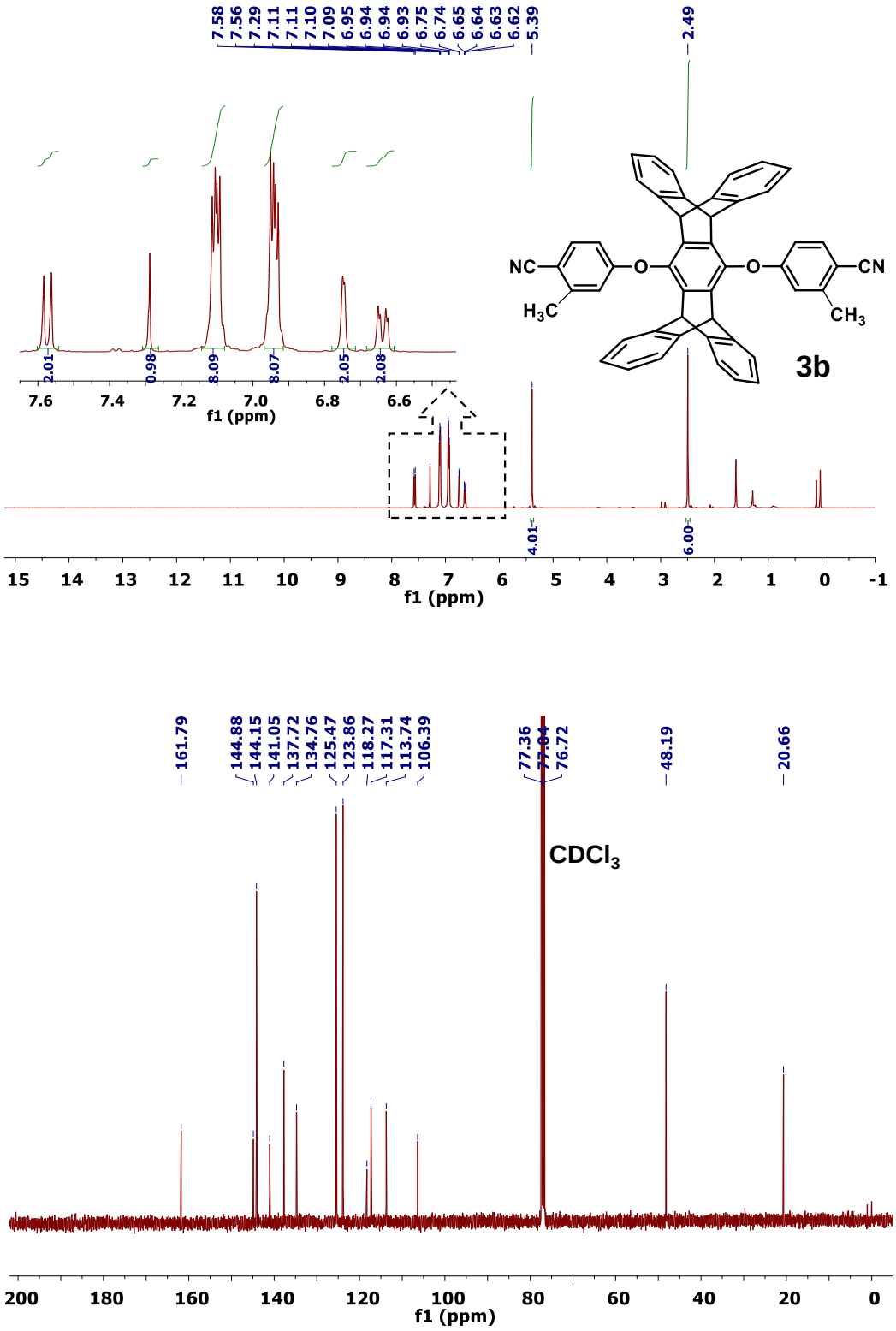

Appendix-IV Figure 6.6. ^{1}H and ^{13}C NMR spectra of PenTrip(CH_3)–CN (**3b**). NMR solvent: $CDCl_3$.

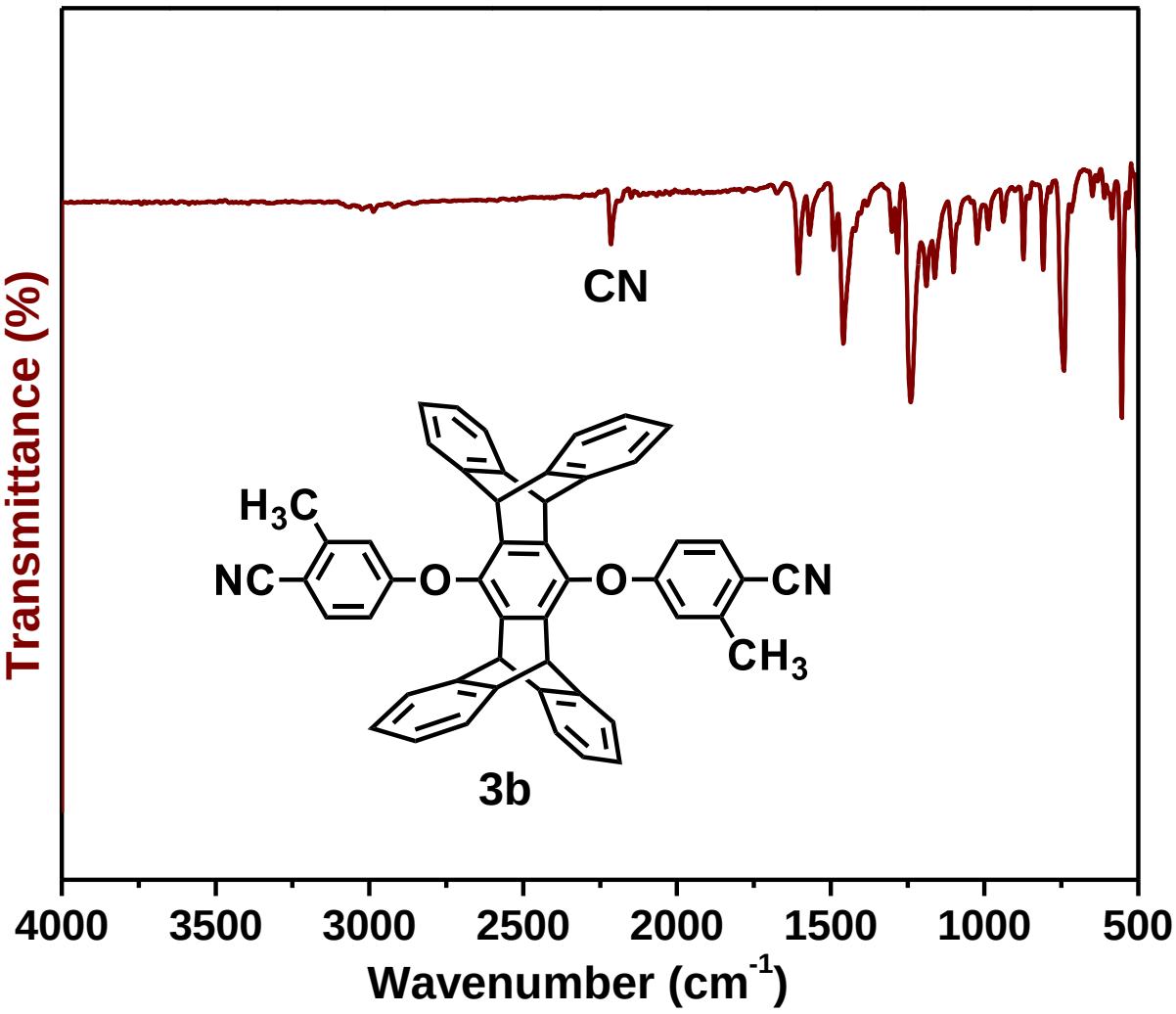

Appendix-IV Figure 6.7. FTIR spectra of PenTrip(CH_3)–CN (**3b**).

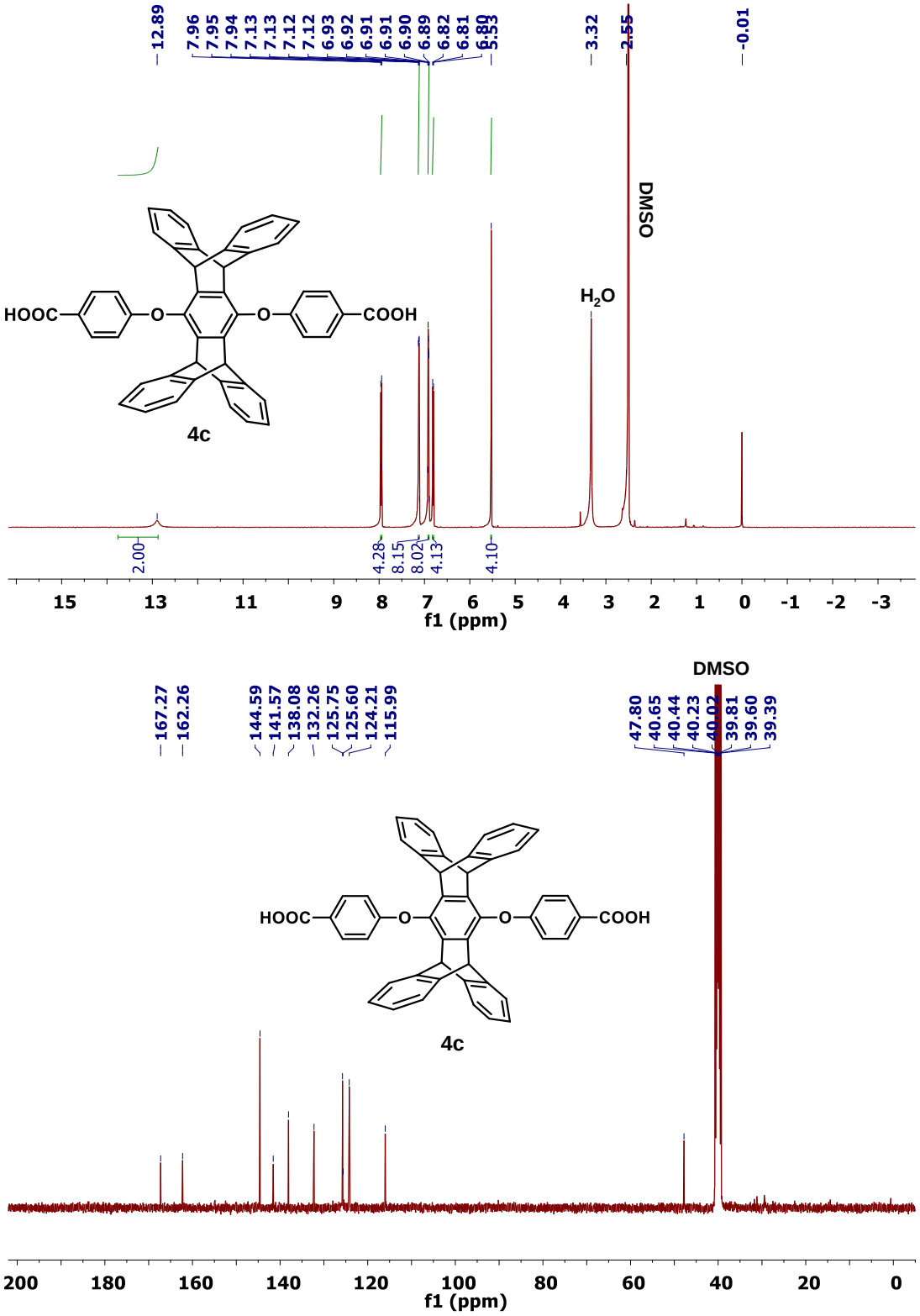

Appendix-IV Figure 6.8. ^{1}H and ^{13}C NMR spectra of PenTrip–COOH (**4c**). NMR solvent: DMSO-*d*$_6$.

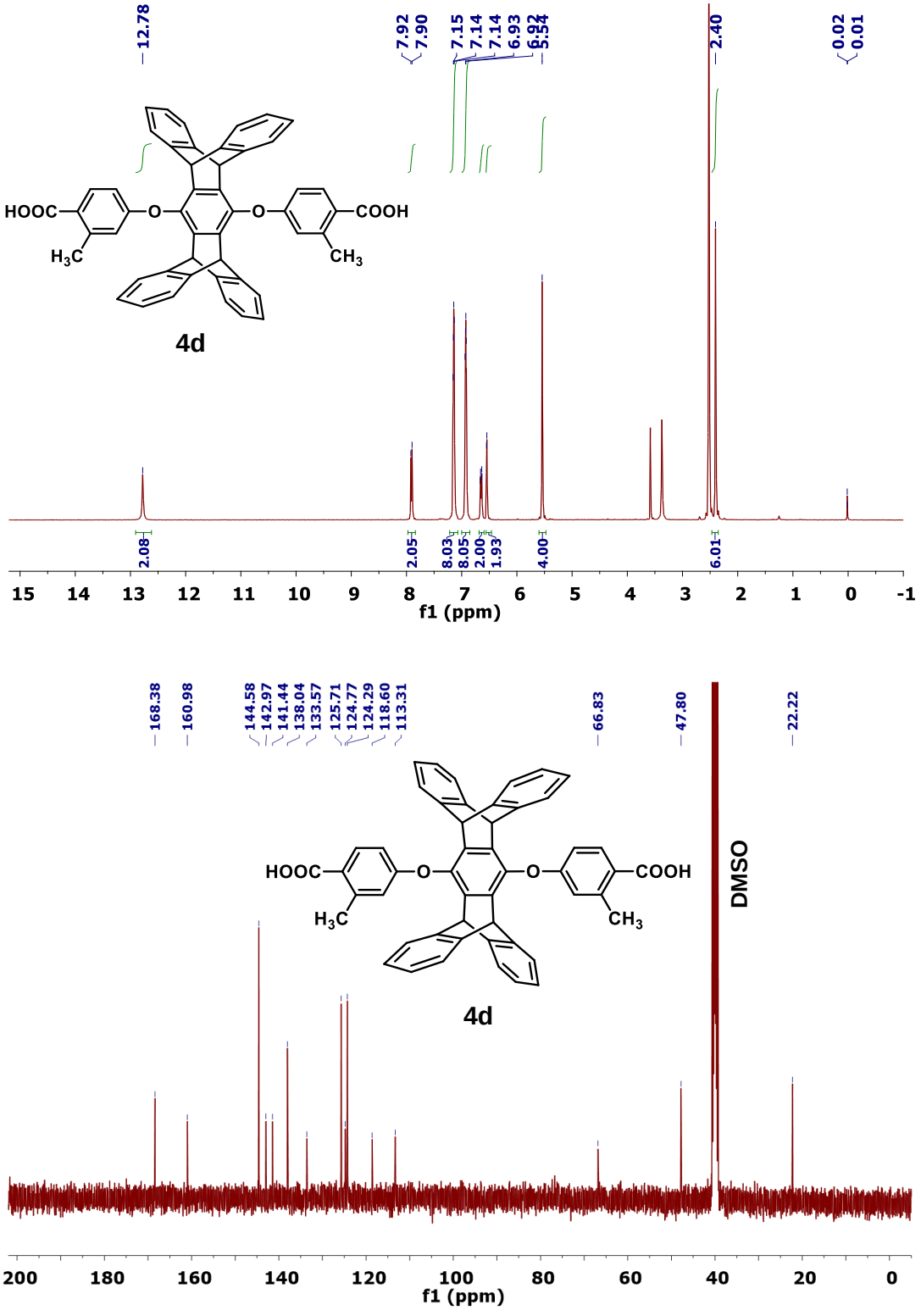

Appendix-IV Figure 6.9. ^{1}H and ^{13}C NMR spectra of PenTrip(CH_3)–COOH (**4d**). NMR solvent: DMSO-*d*$_6$.

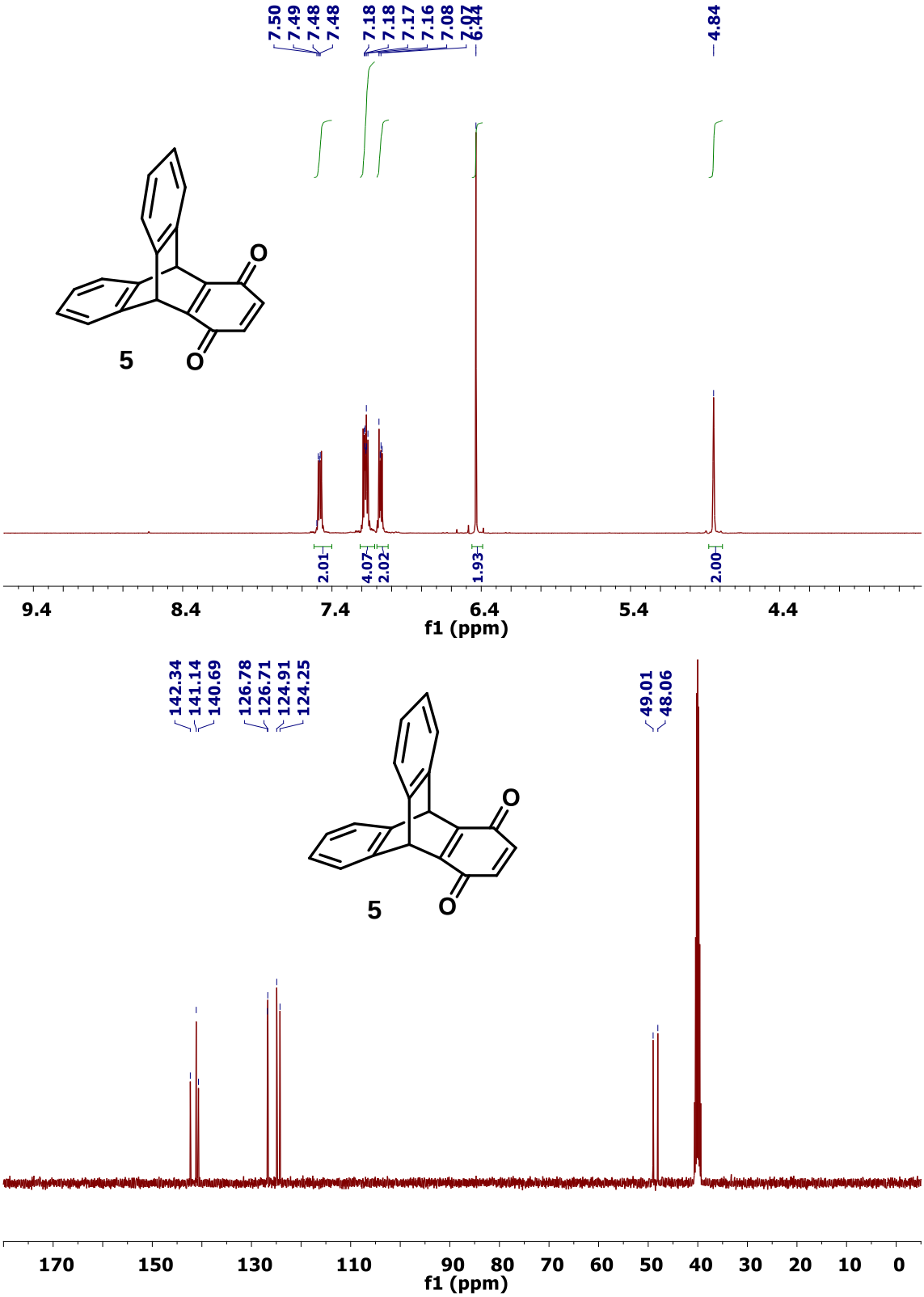

Appendix-IV Figure 6.10. ^{1}H and ^{13}C NMR spectra of triptycene quinone (**5**). NMR solvent: DMSO-d_6.

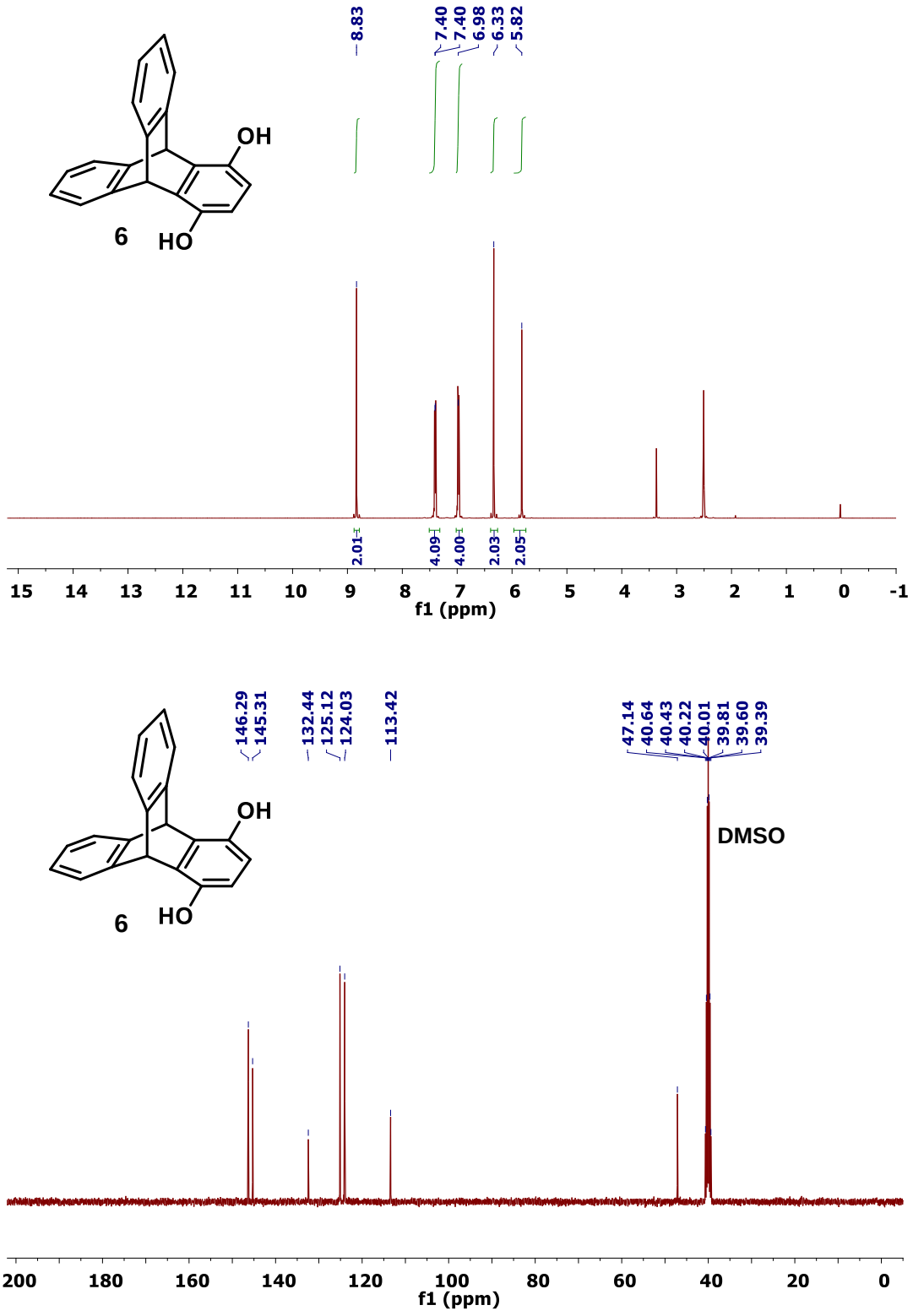

Appendix-IV Figure 6.11. ^{1}H and ^{13}C NMR spectra of triptycene hydroquinone (**6**). NMR solvent: DMSO-d_6.

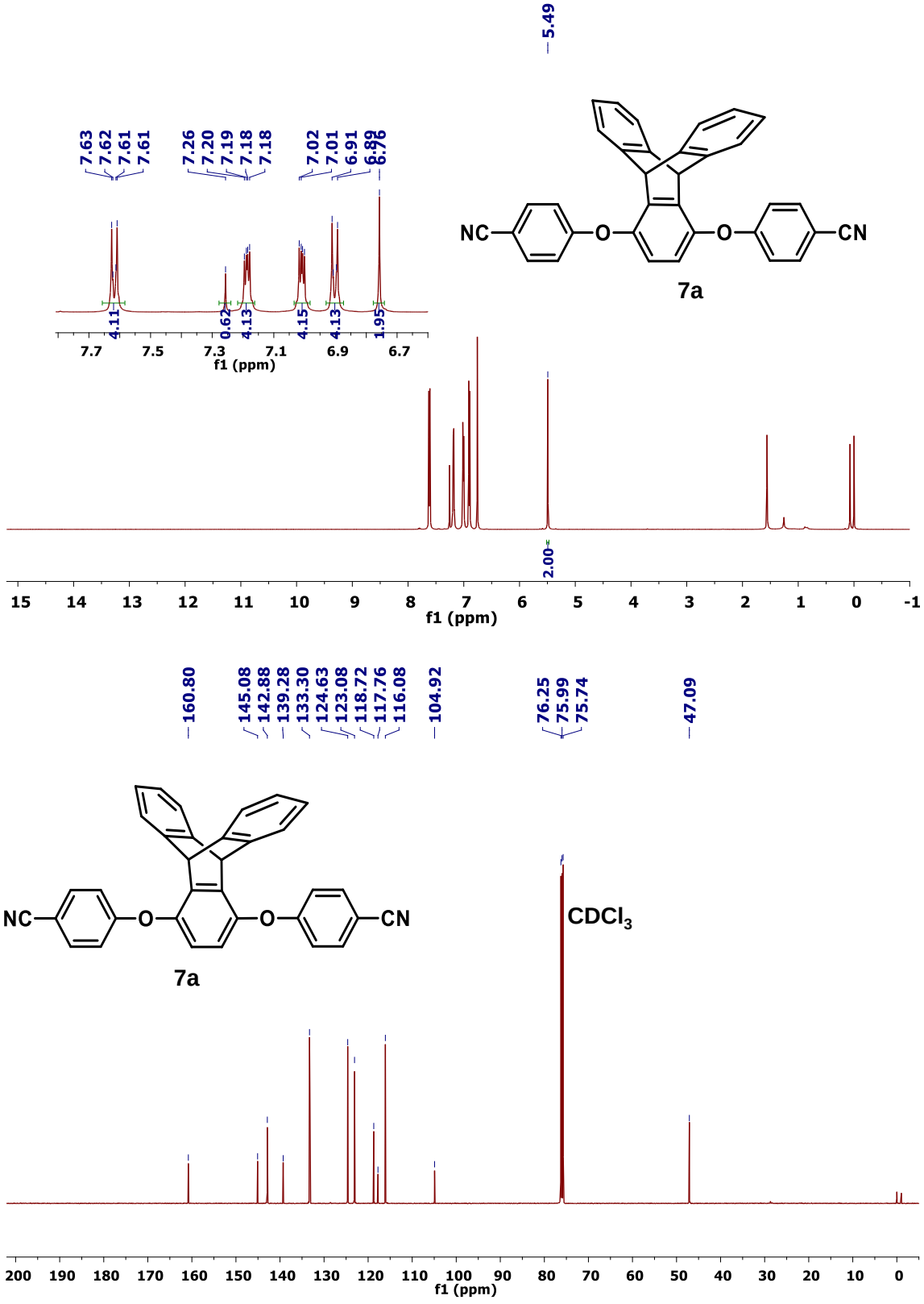

Appendix-IV Figure 6.12. ^{1}H and ^{13}C NMR spectra of Trip–CN (**7a**). NMR solvent: $CDCl_3$.

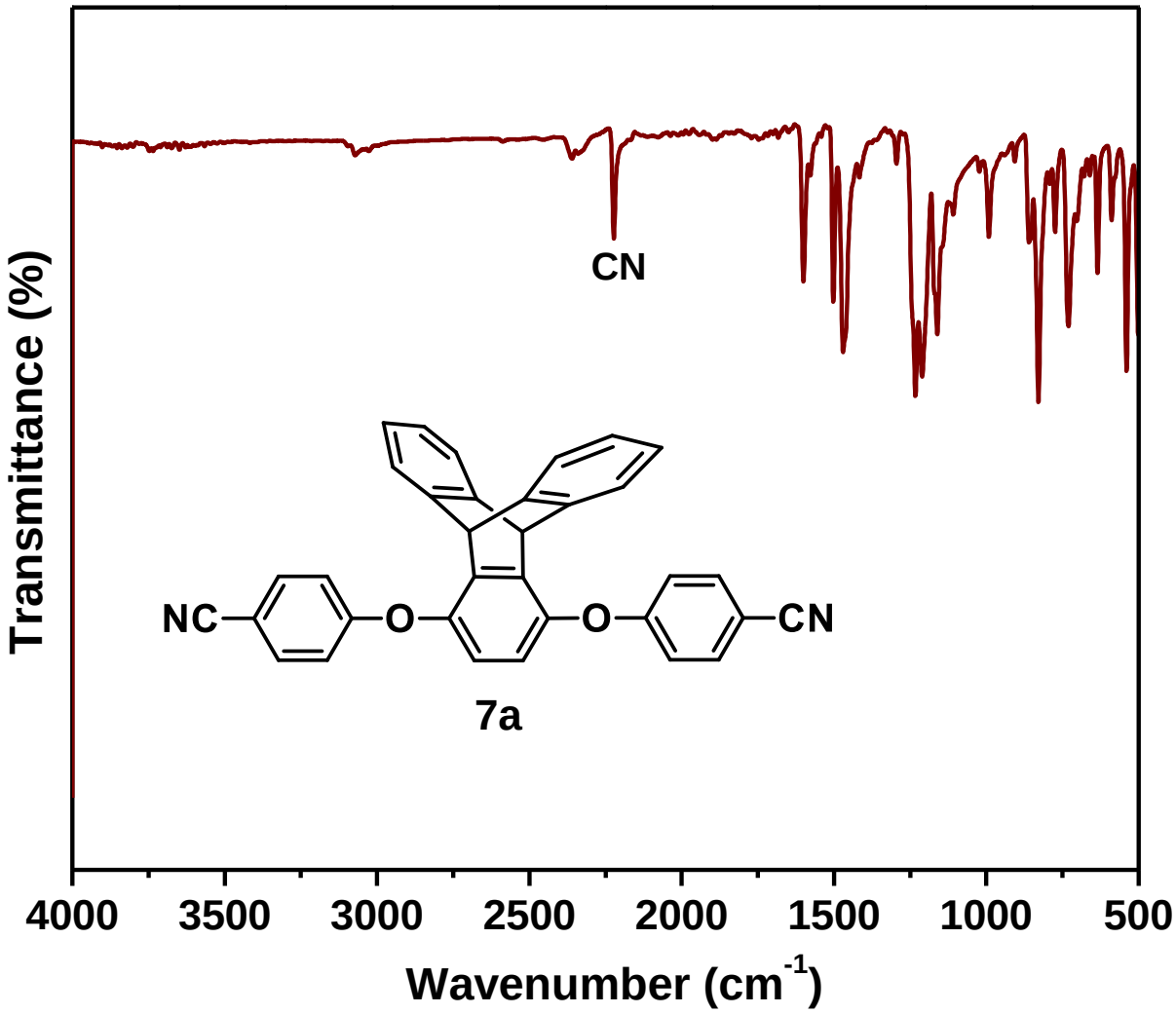

Appendix-IV Figure 6.13. FT-IR spectra of Trip–CN compound (**7a**).

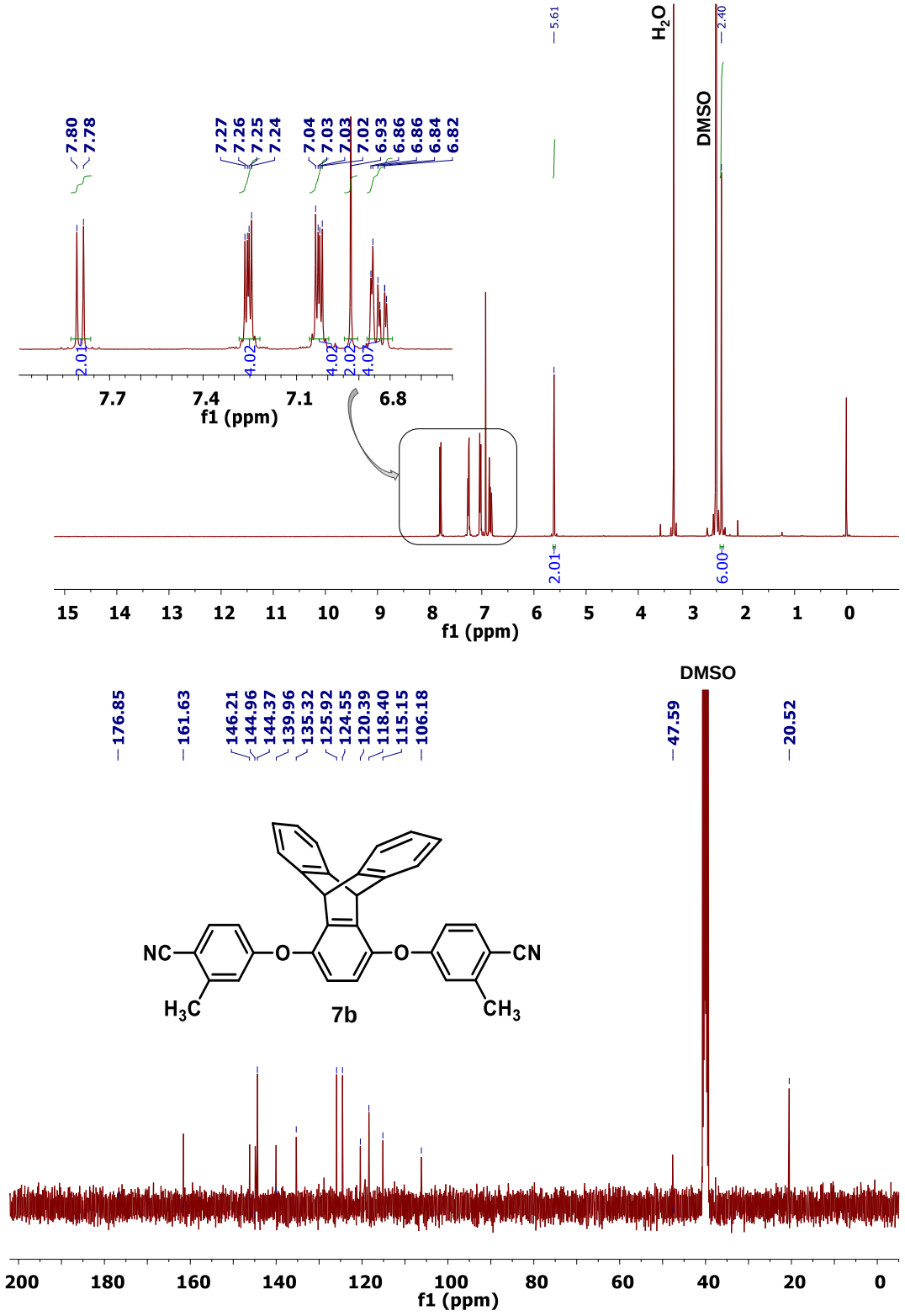

Appendix-IV Figure 6.14. ^{1}H and ^{13}C NMR spectra of Trip(CH_3)–CN (**7b**). NMR solvent: DMSO-d_6.

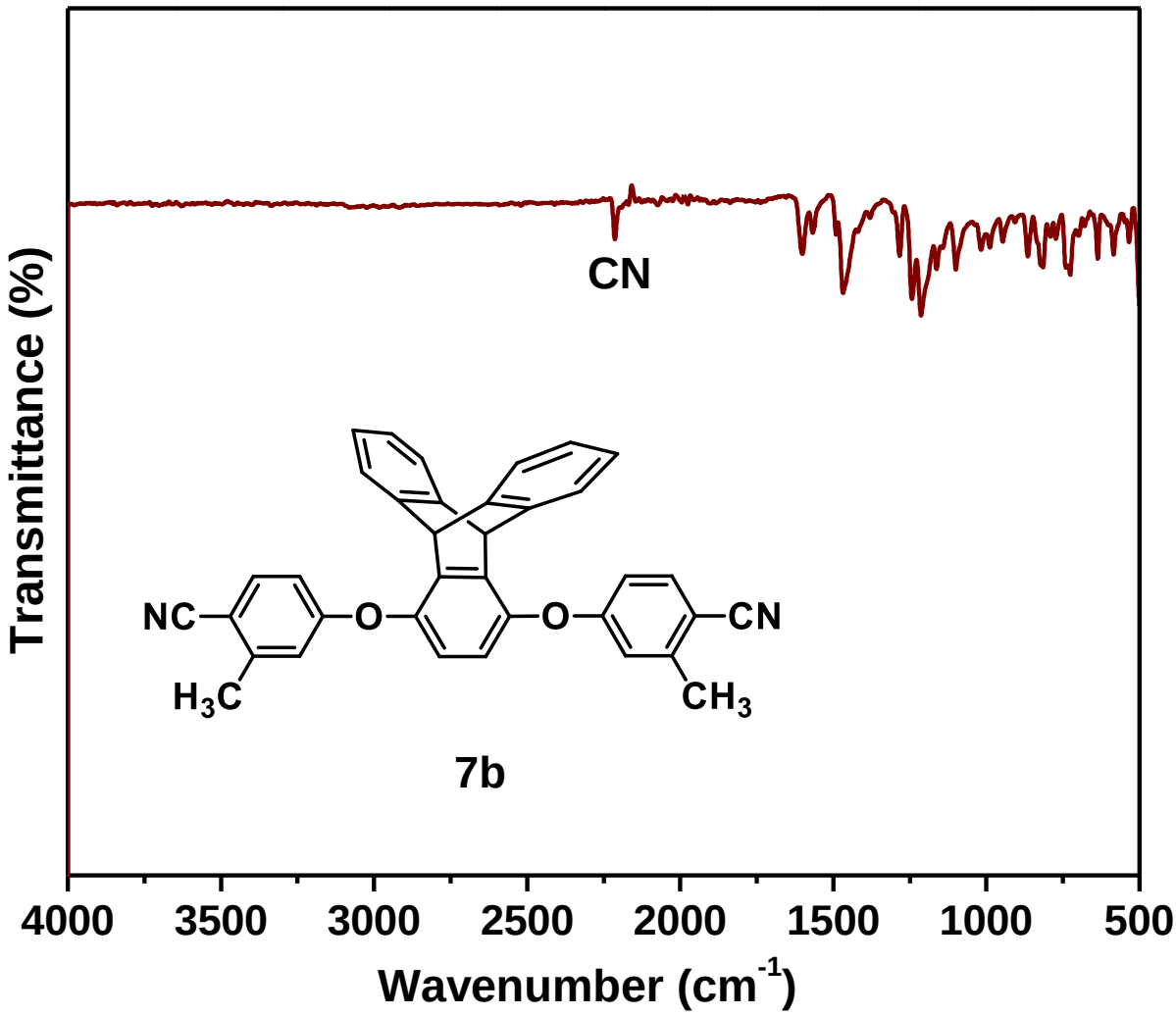

Appendix-IV Figure 6.15. FT-IR spectra of Trip(CH_3)–CN compound (**7b**).

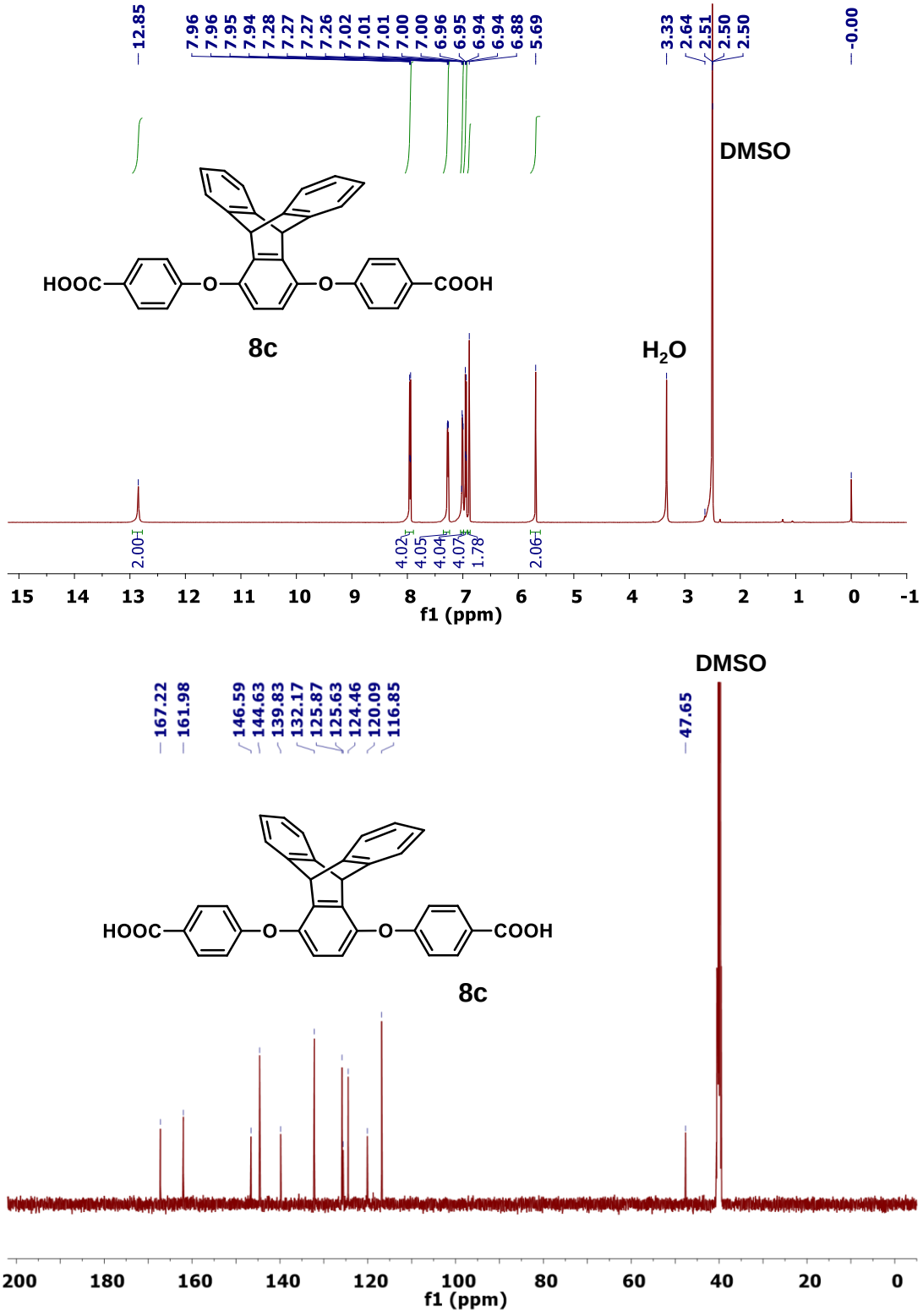

Appendix-IV Figure 6.16. ^{1}H and ^{13}C NMR spectra of Trip–COOH (**8c**). NMR solvent: DMSO-d_6.

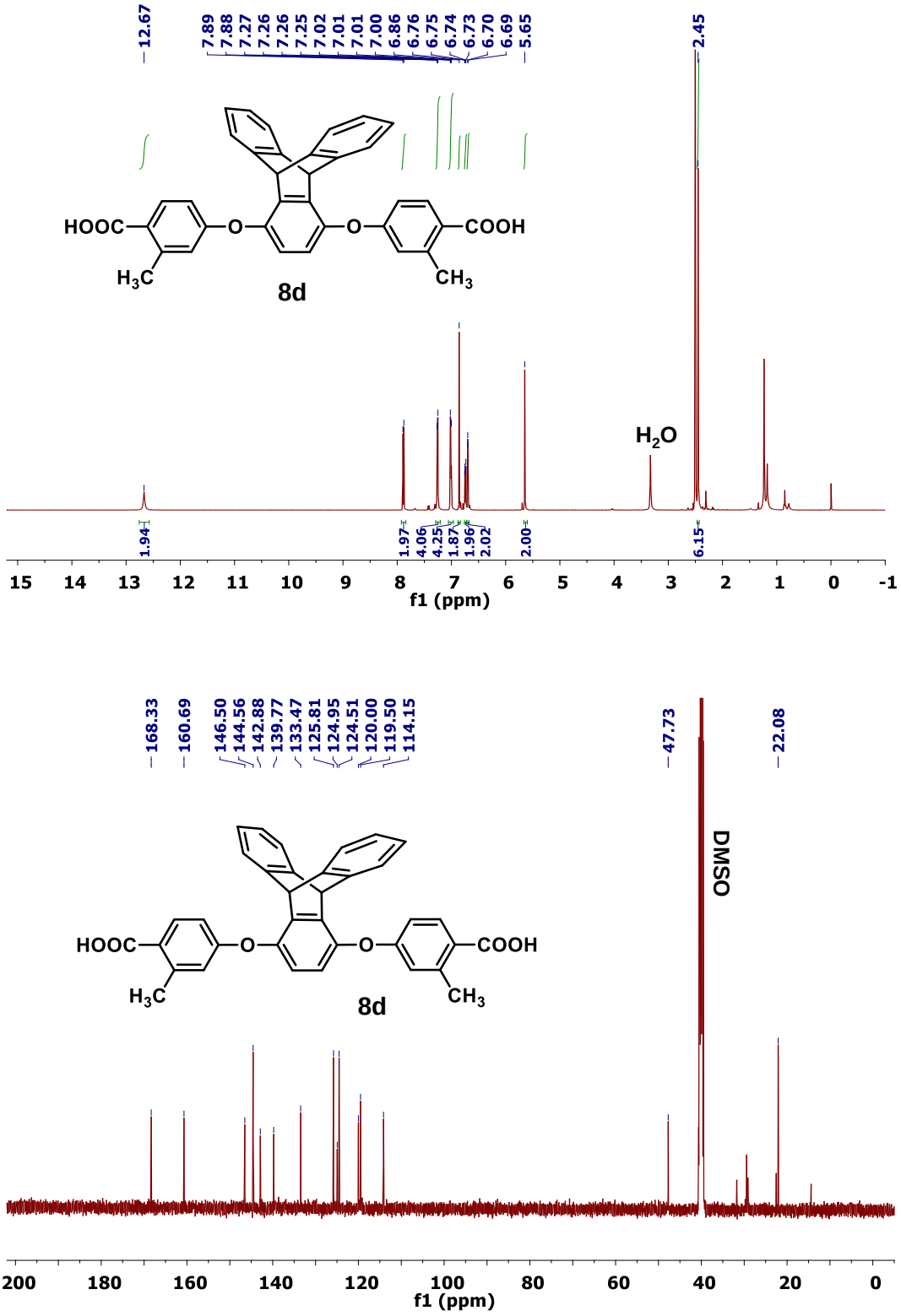

Appendix-IV Figure 6.17. ^{1}H and ^{13}C NMR spectra of Trip(CH_3)–COOH (**8d**). NMR solvent: DMSO-d_6.

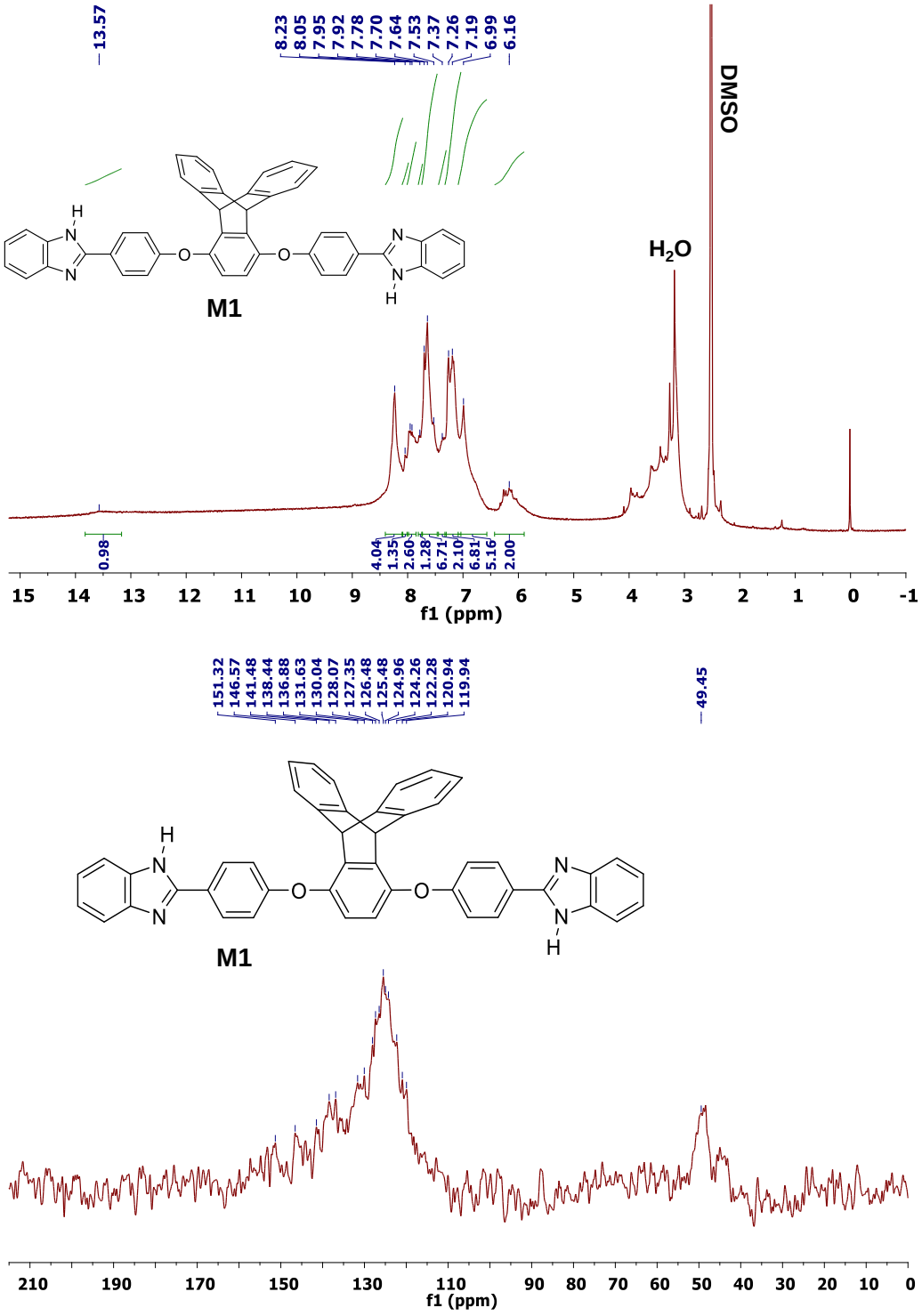

Appendix-IV Figure 6.18. ^{1}H NMR spectra (solvent: DMSO-d_6) and ^{13}C CP-MAS solid-state NMR spectra of model compound (**M1**).

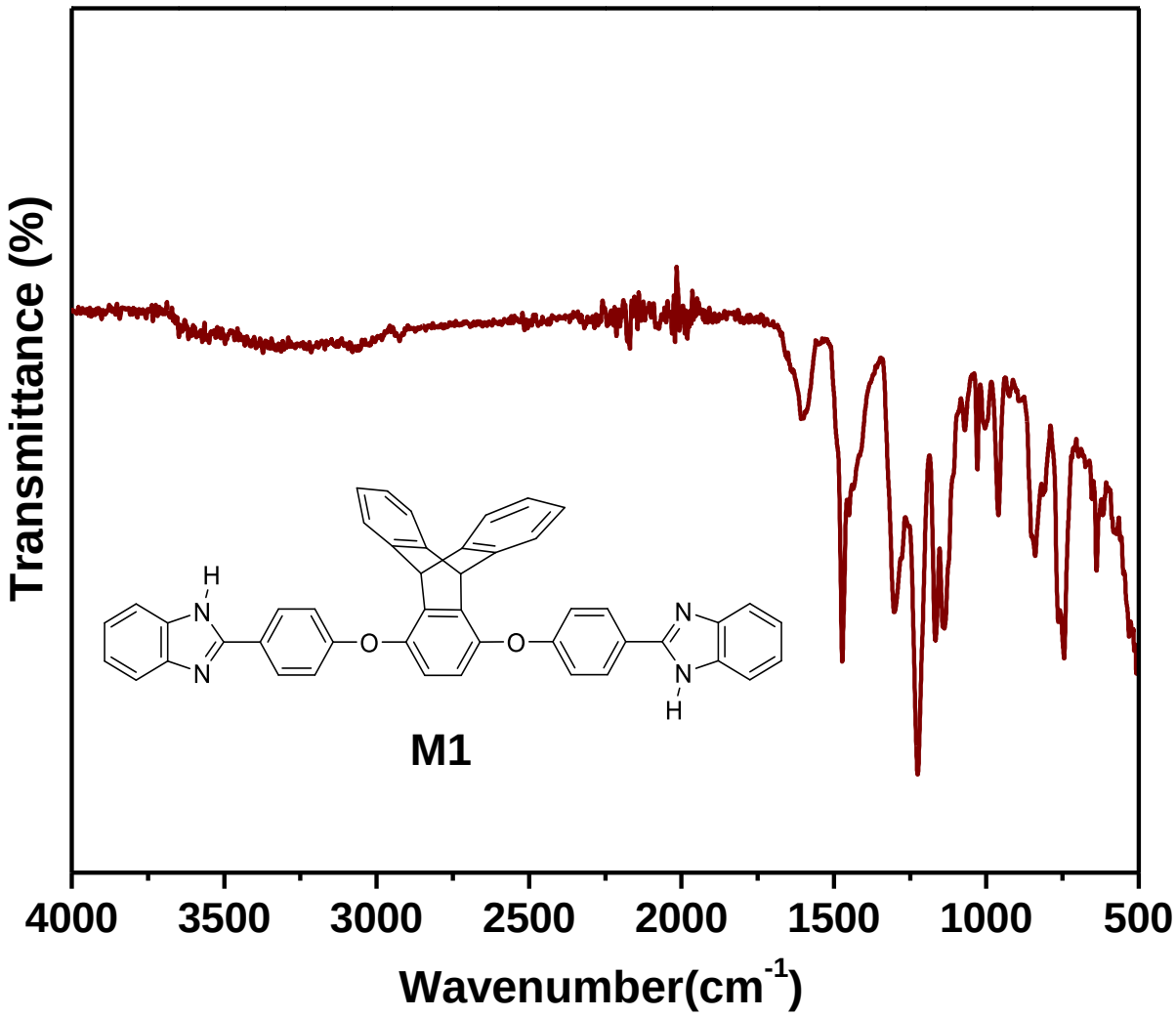

Appendix-IV Figure 6.19. FTIR spectra of model compound (**M1**).

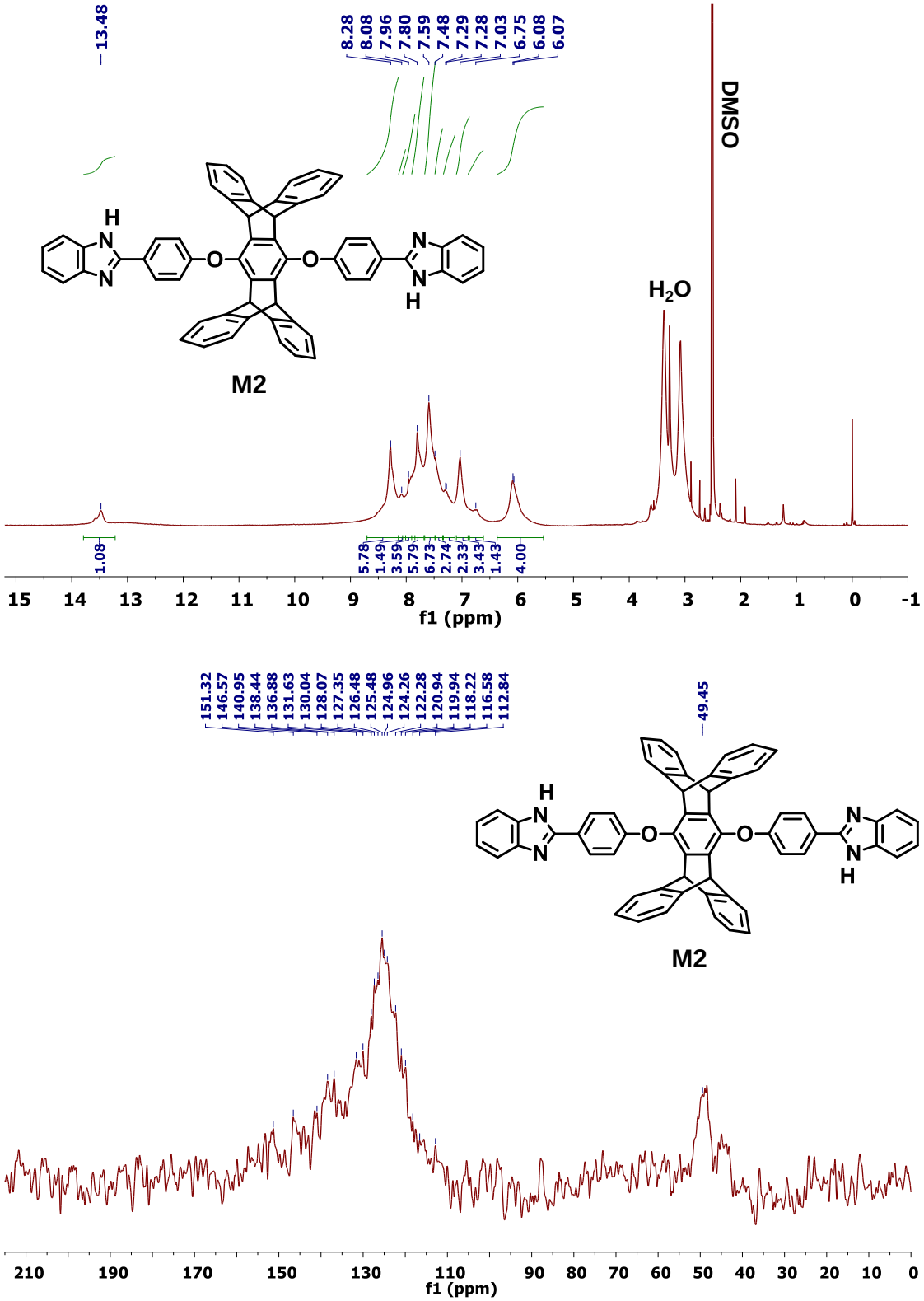

Appendix-IV Figure 6.20. ^{1}H NMR spectra (solvent: DMSO-d_6) and ^{13}C CP-MAS solid-state NMR spectra of model compound (**M2**).

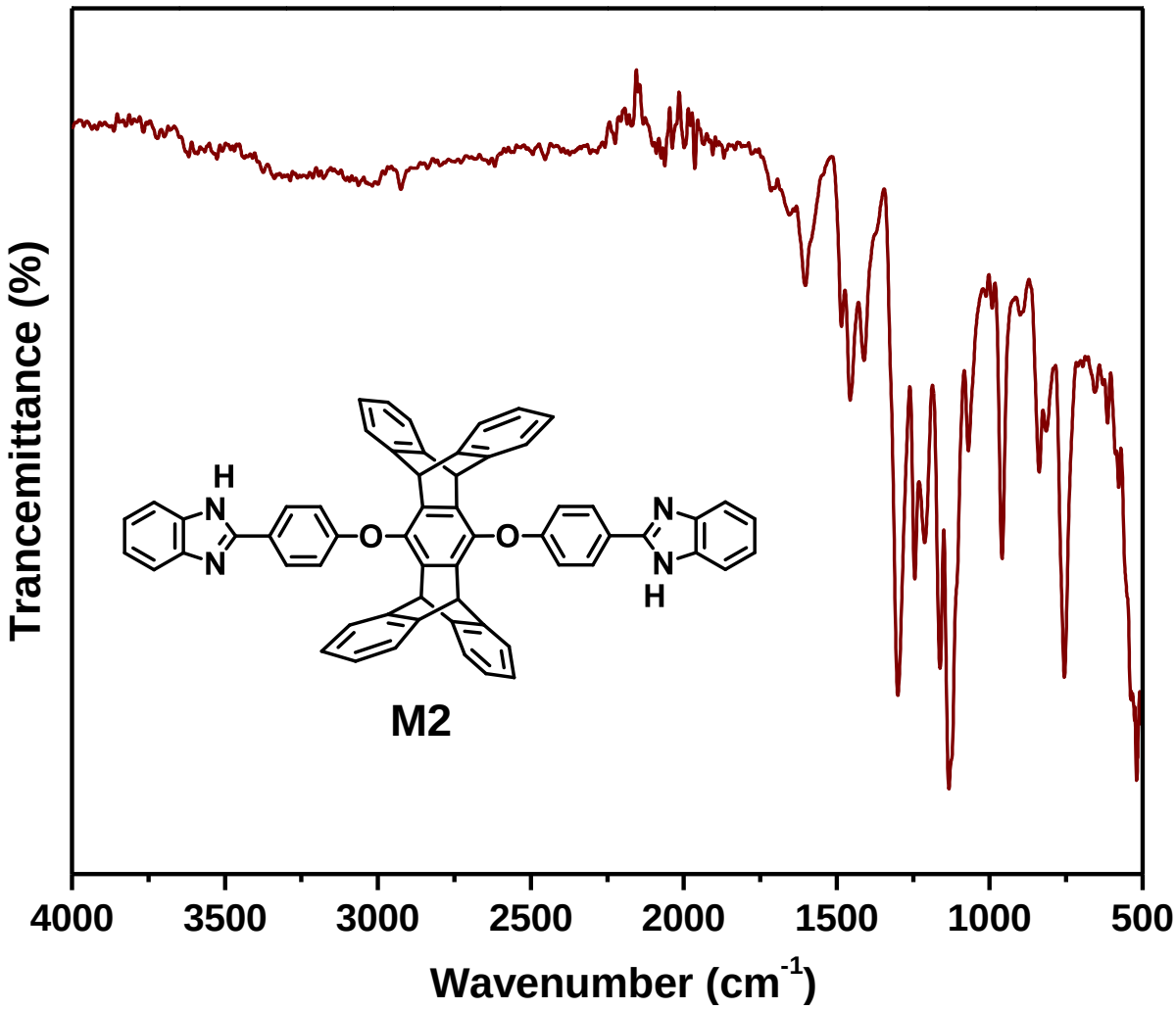

Appendix-IV Figure 6.21. FTIR spectra of the model compound (**M2**).

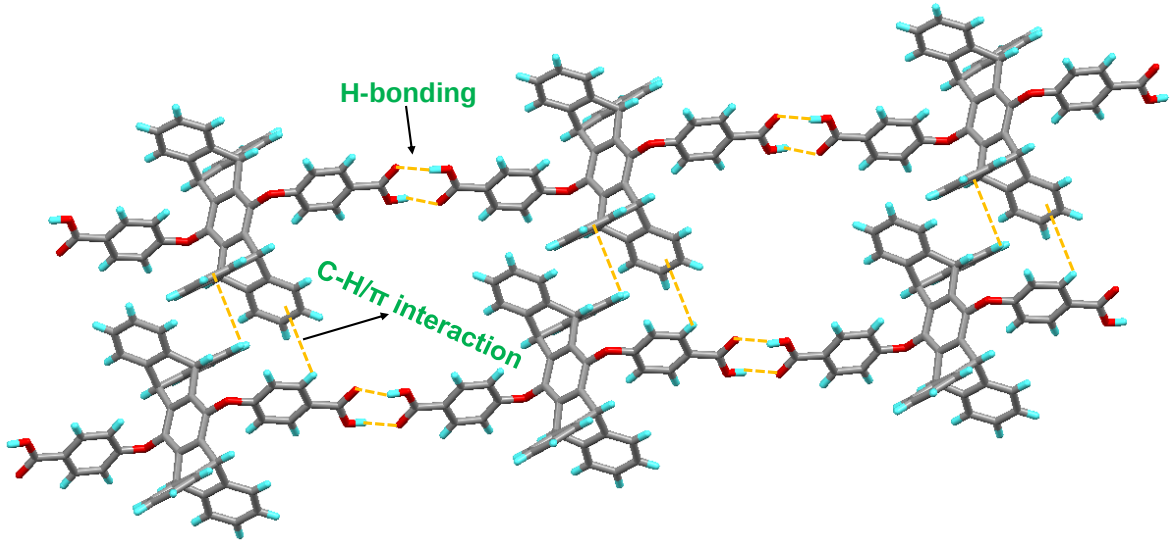

Appendix-IV Figure 6.22. Adjacent building blocks of PenTrip-COOH forms the extended network and are held together by intermolecular hydrogen bonding (orange) involving the carboxylic groups and C-H…π stacking interactions. Grey-carbon, light blue-hydrogen, red-oxygen.

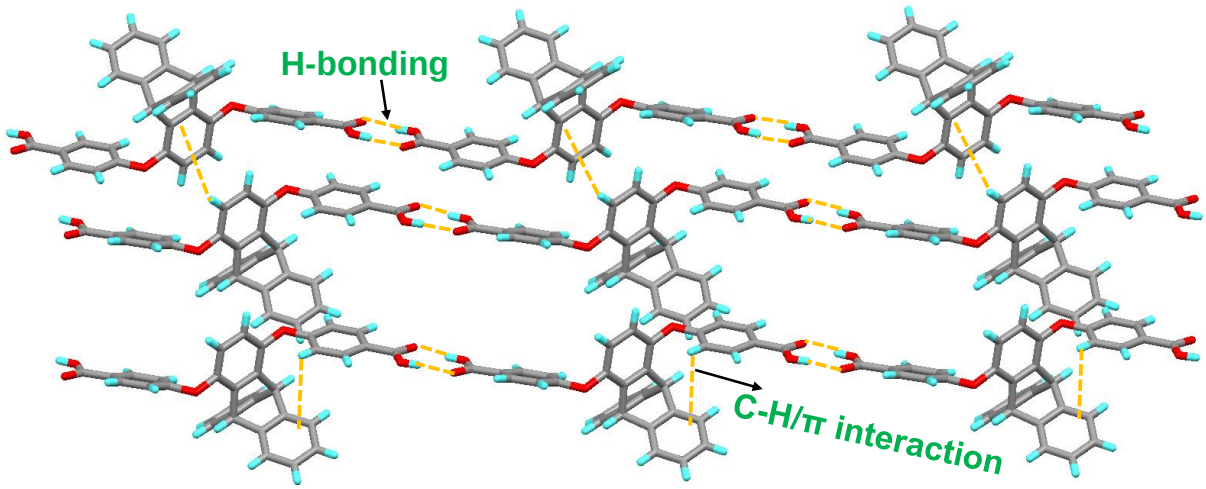

Appendix-IV Figure 6.23. Adjacent building blocks of Trip-COOH forms the extended network and are held together by intermolecular hydrogen bonding (orange) involving the carboxylic groups and C-H…π stacking interactions. Grey-carbon, light blue-hydrogen, red-oxygen.

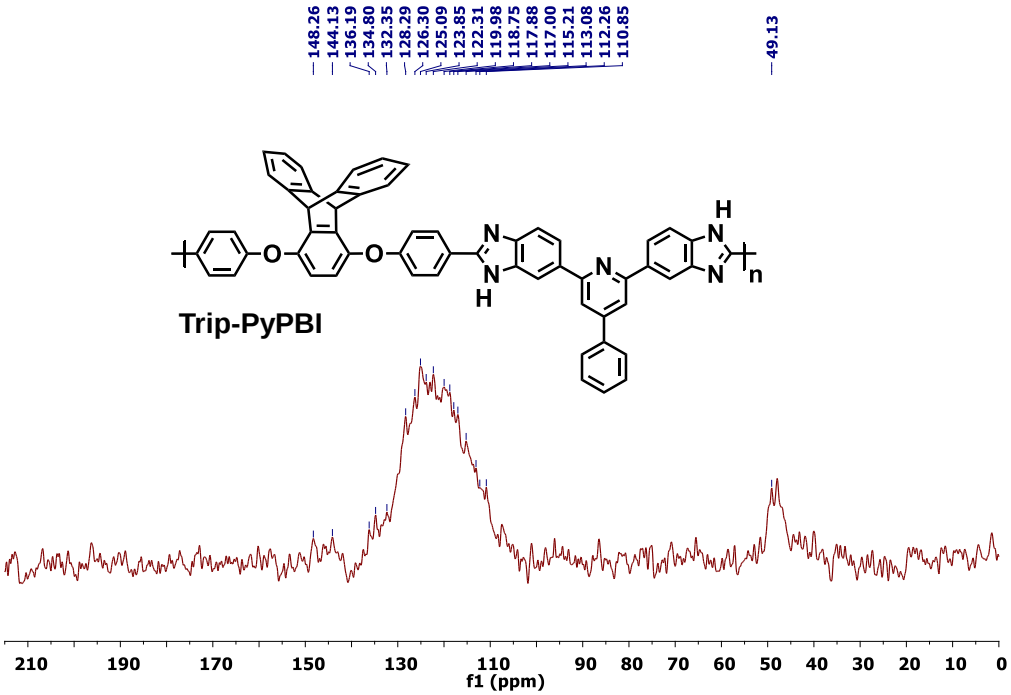

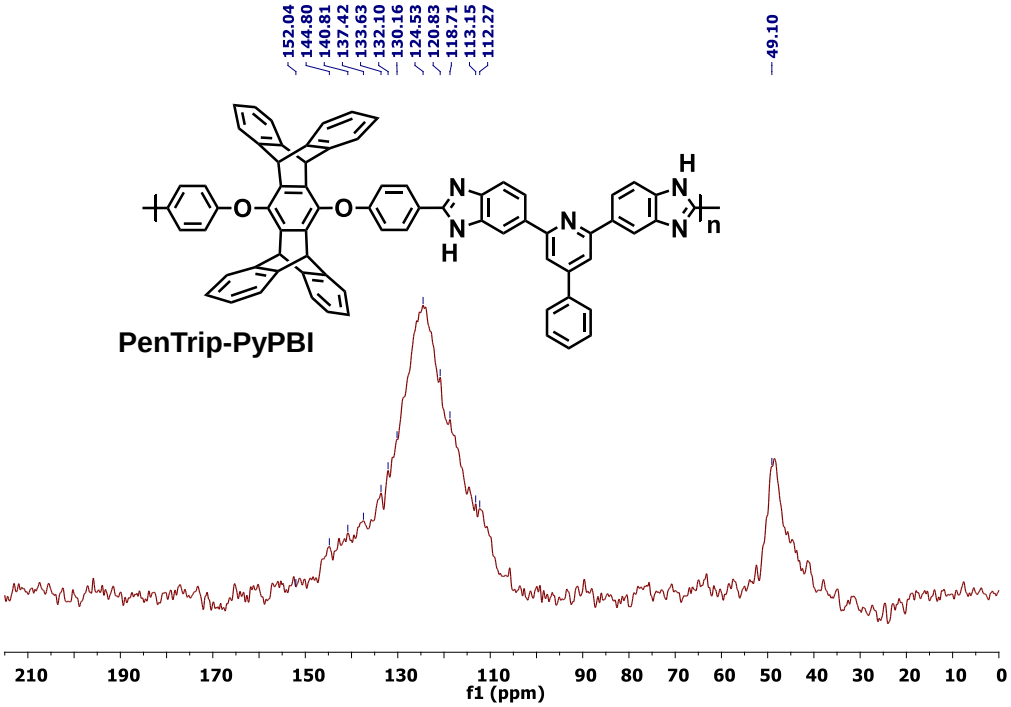

Appendix-IV Figure 6.24. ^{13}C CP-MAS solid-state NMR spectra of Trip-PyPBI and PenTrip-PyPBI.

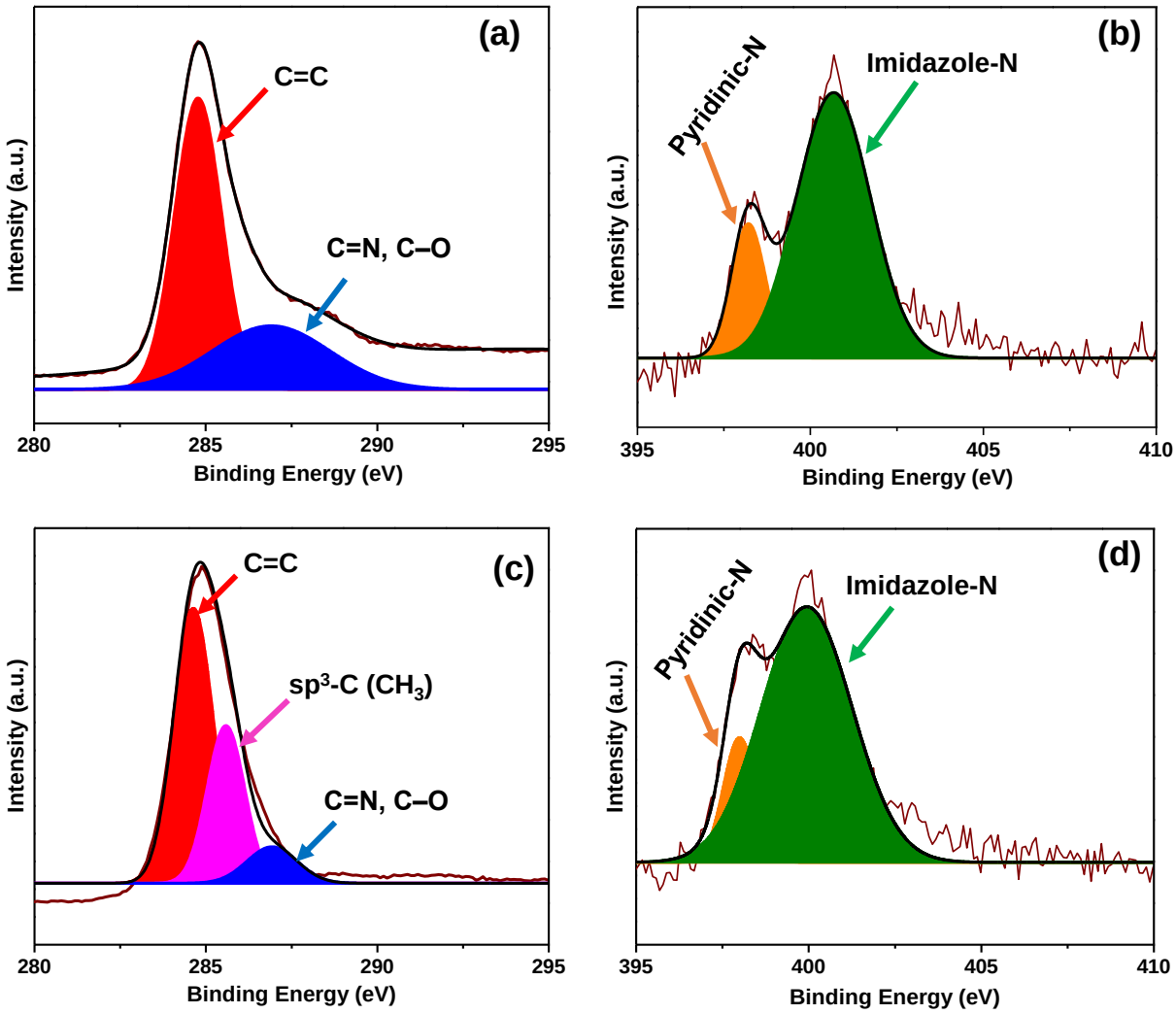

Appendix-IV Figure 6.25. XPS spectra of C1s, N1s band of Trip-PyPBI (**a** & **b**) and Trip(CH_3)-PyPBI (**c** & **d**).

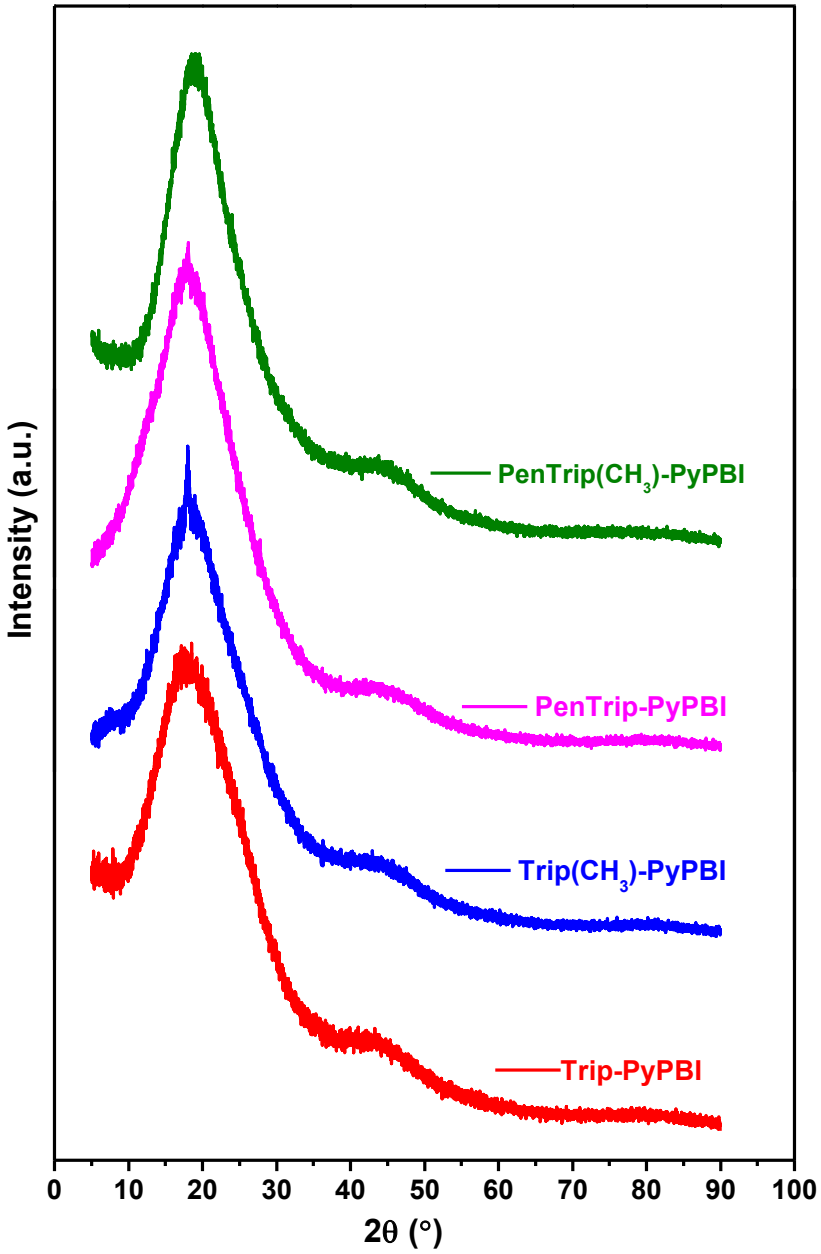

Appendix-IV Figure 6.26. PXRD patterns of iptycene-based PyPBIs.

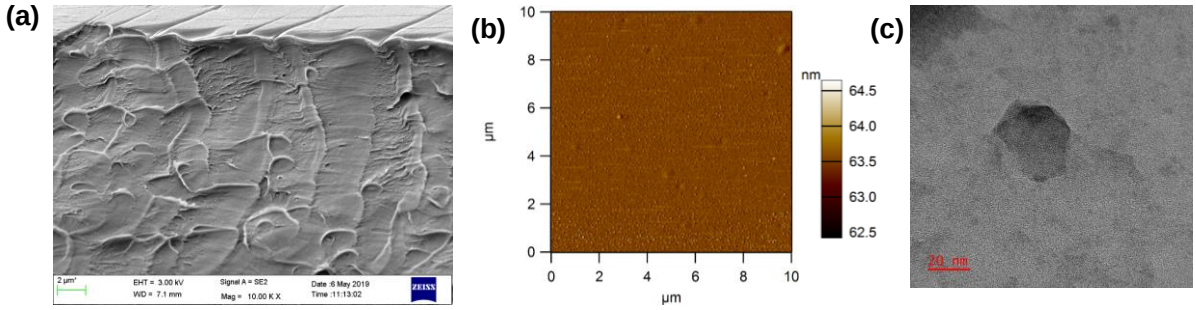

Appendix-IV Figure 6.27. Microscopic morphologies Ph-PyOPBI membrane. (**a**) Cross-sectional FESEM, (**b**) AFM height and (**c**) HR-TEM Scale bar = 20 nm image.

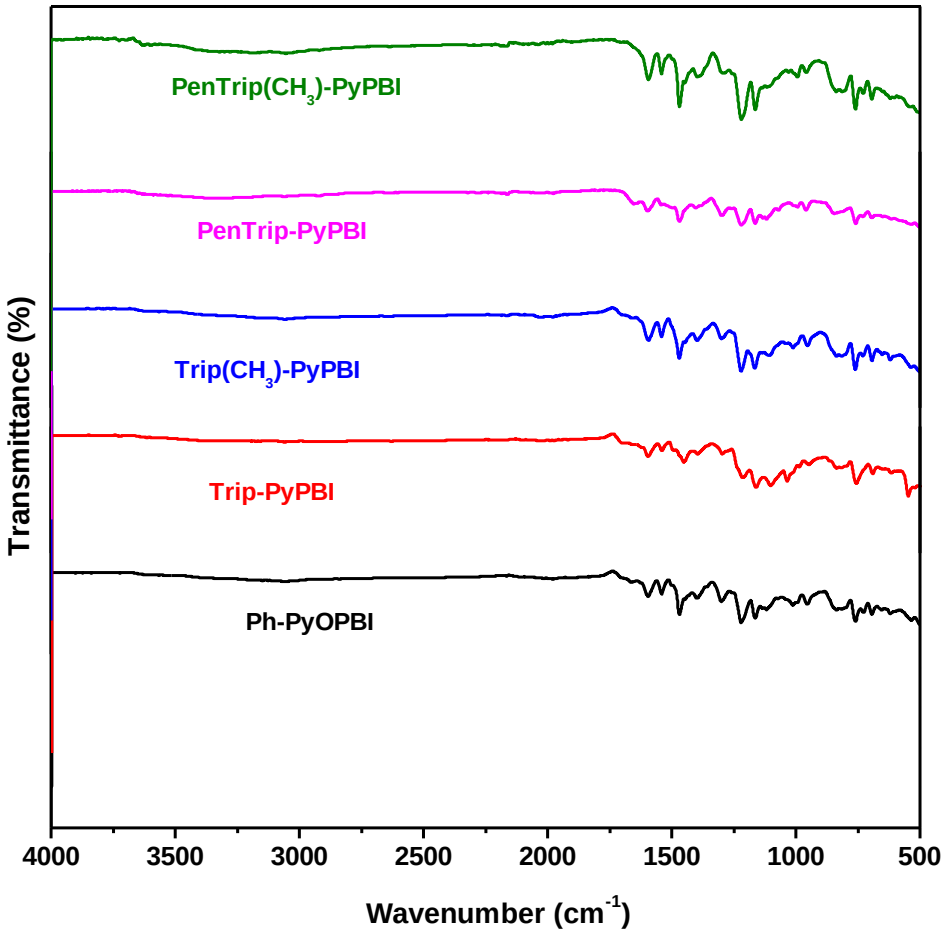

Appendix-IV Figure 6.28. FTIR spectra of Ph-PyOPBI and iptycene-based PyPBIs after the treatment under harsh conditions for 6 days.

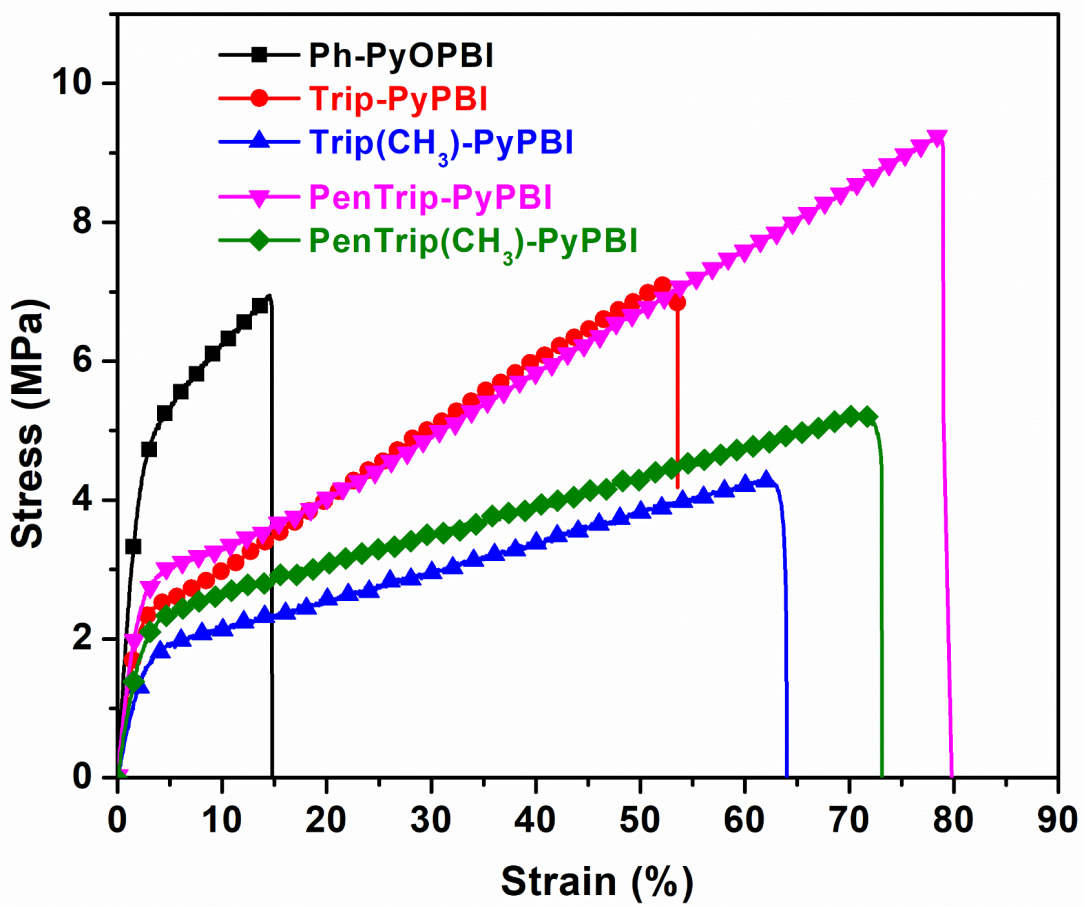

Appendix-IV Figure 6.29. Stress−strain plots of doped Ph-PyOPBI and 3D iptycene-based PyPBI membranes.

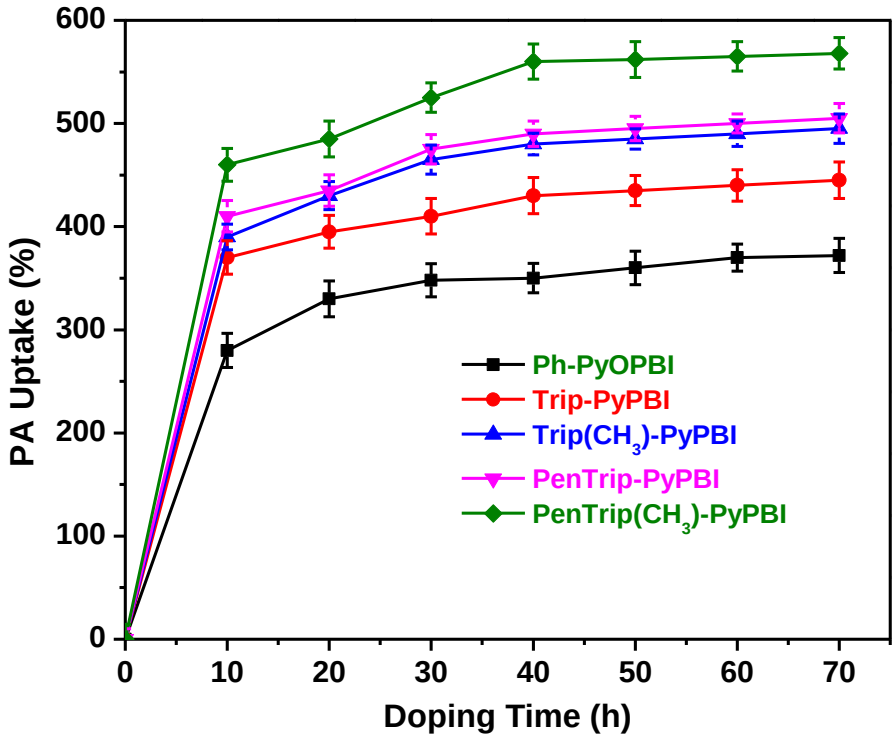

Appendix-IV Figure 6.30. The PA uptake of different iptycene-based PyPBI membranes along with Ph-PyOPBI.

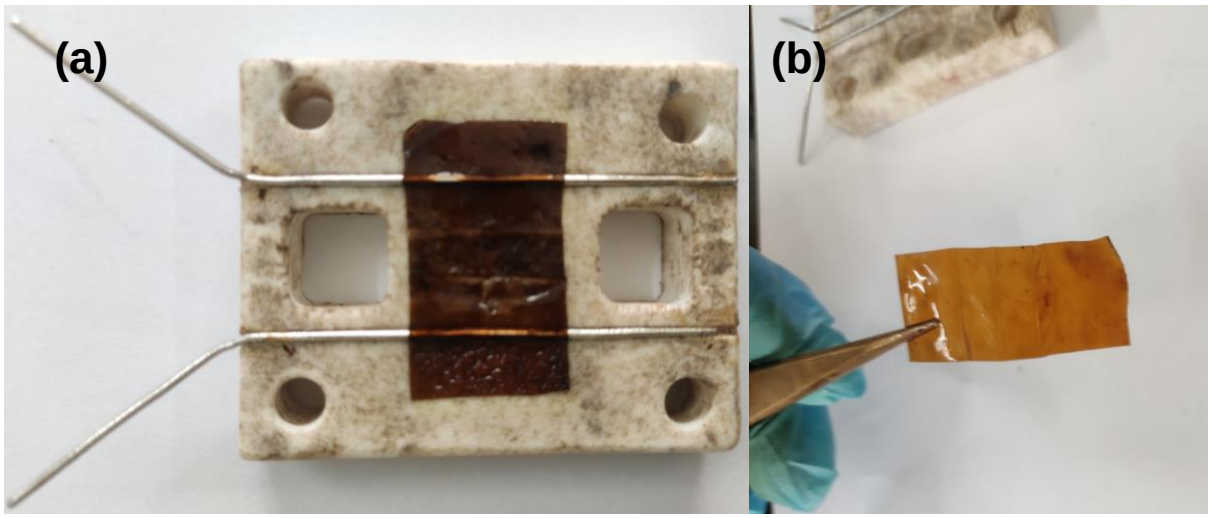

Appendix-IV Figure 6.31. The PA-doped membrane mechanical integrity of PenTrip(CH_3)-PyPBI after proton conductivity measurement at 180 ^oC for 72 h. (**a**) Membrane in the cell with electrodes after measurement and (**b**) membrane taken out of the cell but still remain flexible to handle.

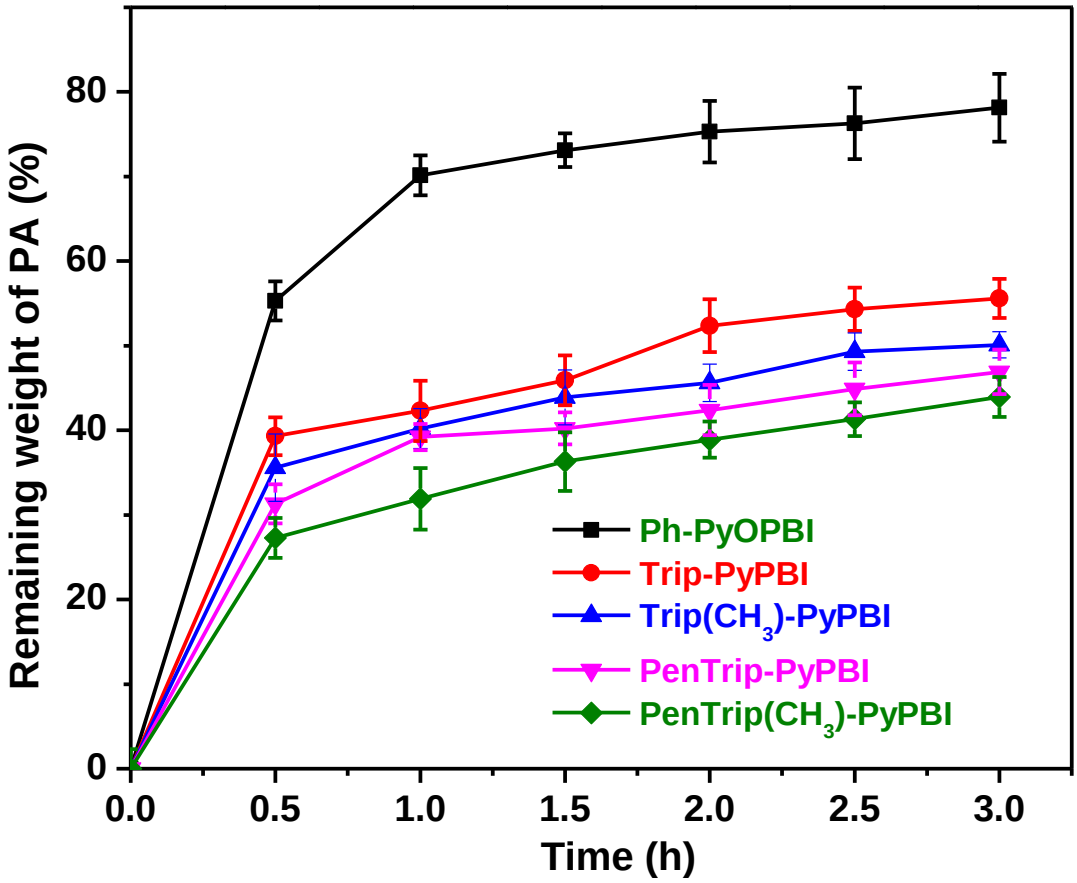

Appendix-IV Figure 6.32. PA stability of different iptycene-based PyPBI membranes under the water vapour at ~100 °C.

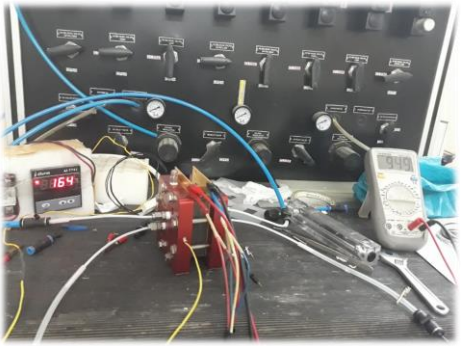

Fuel Cell

Trip(CH_3)-PyPBI

PenTrip(CH_3)-PyPBI

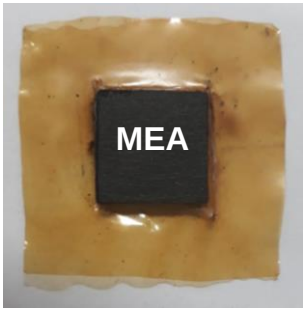

Appendix-IV Figure 6.33. Photos of fuel cell, Trip(CH_3)-PyPBI and PenTrip(CH_3)-PyPBI assembled MEA after single cell test.

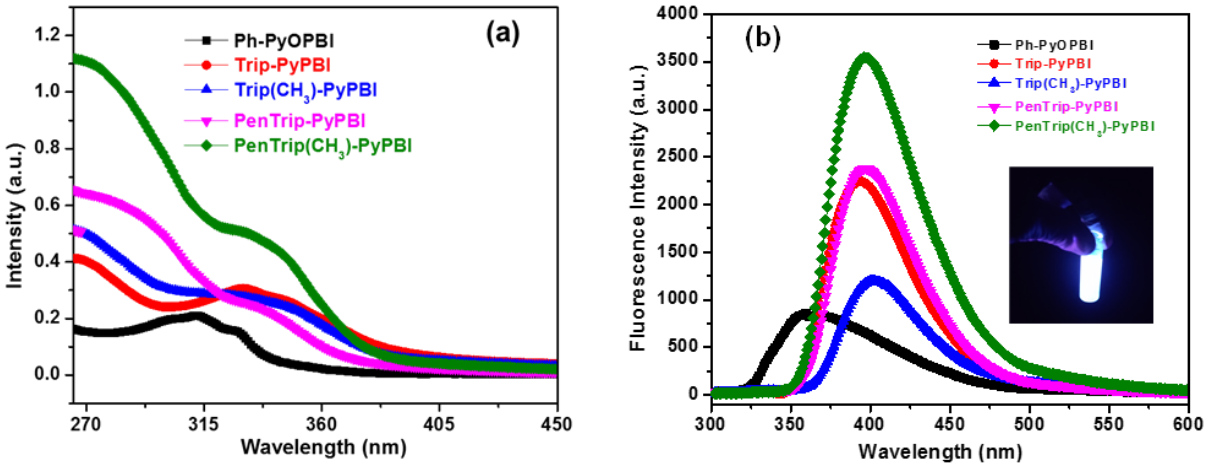

Appendix-IV Figure 6.34. (**a**) Absorption spectra and (**b**) Fluorescence emission spectra of iptycene-based PyPBIs in DMSO dilute solution. Emission photographs of the corresponding solutions under 365 nm irradiation is also shown in the inset. Spectra were recorded by exciting the sample at 360 nm. Concentration of the solution was 2×10^{-5} M where molarity is calculated by considering repeat unit as 1 mol.

PUBLICATIONS and PRESENTATIONS

PUBLICATIONS

Thesis Chapter Publications

1. **Harilal**; Nayak, R.; Ghosh, P. C.; Jana, T., Cross-Linked Polybenzimidazole Membrane for PEM Fuel Cells.
   ACS Appl. Polym. Mater. 2020**,** 2, 3161-3170.
2. **Harilal**; Shukla, A.; Ghosh, P. C.; Jana, T., Pyridine-Bridged Polybenzimidazole for Use in High-Temperature PEM Fuel Cells.
   ACS Appl. Energy Mater. 2021 *4* (2), 1644-1656.
3. **Harilal,** R. Bhattacharyya, P. C. Ghosh, T. Jana, Rational Design of Microporous Polybenzimidazole Framework for Efficient Proton Exchange Membrane Fuel cell.
   *(Communicated to **J. Mater. Chem. A**)*
4. **Harilal,** A. Shukla, P. C. Ghosh, T. Jana, Copolymers of Pyridine-bridged Polybenzimidazole for the use in High Temperature PEM Fuel Cell. *(Communicated to **ACS Appl. Polym. Mater.**)*

Other Publications

5. Manojkumar, P.; **Harilal**; Mahipal, V.; Suresh, G.; Venkatesh, N.; Ramesh, M.; Parthasarathy, T., Exploring the charge transfer dynamics of hydrogen bonded crystals of 2-methyl-8-quinolinol and chloranilic acid: synthesis, spectrophotometric, single-crystal, DFT/PCM analysis, antimicrobial, and DNA binding studies. ***RSC Advances*** 2021, *11* (63), 39994-40010.
6. S.Ghosh, **Harilal**, A.Das, T.Jana, Solvent Induced Porous Polybenzimidazole Membrane for the use in Fuel Cell.
   (***Manuscript under preparation***)
7. A.Gorre, **Harilal**, T.Jana, Cross-Linkable Polymeric Ionic Liquid Improve Acid Retention and Conductivity Stability in PBI based PEMs.
   (***Manuscript under preparation***)

Note: Only publications 1, 2, 3 and 4 are included in this thesis as chapter 3, 4, 5 and 6, respectively.

PRESENTATIONS

1. **Poster presented** on "Cross-Linked Polybenzimidazole as Proton Exchange Membranes" at 15th international conference on Polymer Science and Technology conducted by the society for polymer science (India) (**SPSI MACRO, 2018**) at IISER-Pune, Pune, Maharashtra, India.

2. **Poster presented** on "Cross-Linked Polybenzimidazole as Proton Exchange Membrane" during 16th annual in-house symposium (**CHEMFEST, 2019**) at School of Chemistry, University of Hyderabad, Hyderabad, India.

3. **Oral talk presented** on "Pyridine bridged Polybenzimidazole Membrane: Synthesis and PEM Properties" 17th annual in-house symposium (**CHEMFEST, 2020**) at School of Chemistry, University of Hyderabad, Hyderabad, India.

Novel Polybenzimidazoles for the Development of Proton Exchange Membrane Fuel Cells

by Harilal .

Submission date: 30-Jan-2022 09:50AM (UTC+0530)
Submission ID: 1750847007
File name: Harilal-Thesis.pdf (11.95M)
Word count: 40470
Character count: 212876

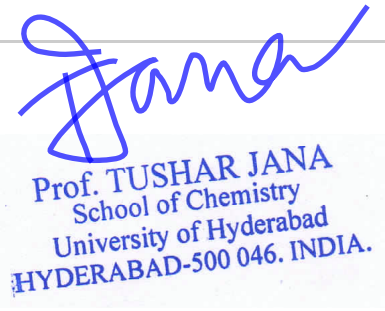

Novel Polybenzimidazoles for the Development of Proton Exchange Membrane Fuel Cells

ORIGINALITY REPORT

41%	4%	39%	3%
SIMILARITY INDEX	INTERNET SOURCES	PUBLICATIONS	STUDENT PAPERS

PRIMARY SOURCES

1	Harilal, Avanish Shukla, Prakash Chandra Ghosh, Tushar Jana. "Pyridine-Bridged Polybenzimidazole for Use in High-Temperature PEM Fuel Cells", ACS Applied Energy Materials, 2021 Publication	21%
2	Harilal, Ratikanta Nayak, Prakash Chandra Ghosh, Tushar Jana. "Cross-Linked Polybenzimidazole Membrane for PEM Fuel Cells", ACS Applied Polymer Materials, 2020 Publication	8%
3	Harilal (*), Ratikanta Nayak, Prakash Chandra Ghosh, Tushar Jana. "Cross-linked Polybenzimidazole Membrane for PEM Fuel Cells", ACS Applied Polymer Materials, 2020 Publication	5%
4	Submitted to Associatie K.U.Leuven Student Paper	1%
5	Submitted to University of Hyderabad, Hyderabad	<1%

Prof. TUSHAR JANA
School of Chemistry
University of Hyderabad
HYDERABAD-500 046. INDIA.

Student Paper

6 Fengxiang Liu, Shuang Wang, Hao Chen, Jinsheng Li, Xue Tian, Xu Wang, Tiejun Mao, Jingmei Xu, Zhe Wang. "Cross-Linkable Polymeric Ionic Liquid Improve Phosphoric Acid Retention and Long-Term Conductivity Stability in Polybenzimidazole Based PEMs", ACS Sustainable Chemistry & Engineering, 2018 <1%
Publication

7 Alberto Coralli, Bernardo J.M. Sarruf, Paulo Emílio V. de Miranda, Luigi Osmieri, Stefania Specchia, Nguyen Q. Minh. "Fuel Cells", Elsevier BV, 2019 <1%
Publication

8 Rizwan Haider, Yichan Wen, Zi-Feng Ma, David P. Wilkinson, Lei Zhang, Xianxia Yuan, Shuqin Song, Jiujun Zhang. "High temperature proton exchange membrane fuel cells: progress in advanced materials and key technologies", Chemical Society Reviews, 2021 <1%
Publication

9 Sudhangshu Maity, Tushar Jana. "Soluble Polybenzimidazoles for PEM: Synthesized from Efficient, Inexpensive, Readily Accessible Alternative Tetraamine Monomer", Macromolecules, 2013 <1%
Publication

10	pubs.rsc.org Internet Source	<1 %
11	Xiaobai Li, Hongwei Ma, Yanchao Shen, Wei Hu, Zhenhua Jiang, Baijun Liu, Michael D. Guiver. "Dimensionally-stable phosphoric acid–doped polybenzimidazoles for high-temperature proton exchange membrane fuel cells", Journal of Power Sources, 2016 Publication	<1 %
12	www.freepatentsonline.com Internet Source	<1 %
13	www.ncbi.nlm.nih.gov Internet Source	<1 %
14	"High Temperature Polymer Electrolyte Membrane Fuel Cells", Springer Nature, 2016 Publication	<1 %
15	pubs.acs.org Internet Source	<1 %
16	Hongwei Zhang, Pei Kang Shen. "Recent Development of Polymer Electrolyte Membranes for Fuel Cells", Chemical Reviews, 2012 Publication	<1 %
17	Tao Wang, Tianyun Li, Joseph Aboki, Ruilan Guo. "Disulfonated Poly(arylene ether sulfone) Random Copolymers Containing Hierarchical	<1 %

Iptycene Units for Proton Exchange Membranes", Frontiers in Chemistry, 2020
Publication

18	Balakondareddy Sana, Tushar Jana. "Polymer electrolyte membrane from polybenzimidazoles: Influence of tetraamine monomer structure", Polymer, 2018 Publication	<1 %
19	Li Wang, Yingnan Wu, Mingliang Fang, Jiale Chen, Xiaoting Liu, Bibo Yin, Lei Wang. "Synthesis and preparation of branched block polybenzimidazole membranes with high proton conductivity and single-cell performance for use in high temperature proton exchange membrane fuel cells", Journal of Membrane Science, 2020 Publication	<1 %
20	Rambabu Koyilapu, Shuvra Singha, S.N.Raju Kutcherlapati, Tushar Jana. "Grafting of vinylimidazolium-type poly(ionic liquid) on silica nanoparticle through RAFT polymerization for constructing nanocomposite based PEM", Polymer, 2020 Publication	<1 %
21	www.s-mot.com Internet Source	<1 %
22	Peng Wang, Jinwu Peng, Bibo Yin, Xian-Zhu Fu, Lei Wang, Jing-Li Luo, Xiaojun Peng.	<1 %

"Phosphoric acid doped polybenzimidazole with leaf-like three-layer porous structure as high-temperature proton exchange membrane for fuel cell", Journal of Materials Chemistry A, 2021
Publication

23	upcommons.upc.edu Internet Source	<1 %
24	Balakondareddy Sana, Anupam Das, Manju Sharma, Tushar Jana. "Alkaline Anion Exchange Membrane from Alkylated Polybenzimidazole", ACS Applied Energy Materials, 2021 Publication	<1 %
25	Fuel Cells, 2013. Publication	<1 %
26	Submitted to Jawaharlal Nehru Technological University Student Paper	<1 %
27	Li, Q.. "High temperature proton exchange membranes based on polybenzimidazoles for fuel cells", Progress in Polymer Science, 200905 Publication	<1 %
28	Yağmur Özdemir, Necati Özkan, Yılser Devrim. "Fabrication and Characterization of Cross-linked Polybenzimidazole Based Membranes	<1 %

for High Temperature PEM Fuel Cells", Electrochimica Acta, 2017
Publication

29	Tiejun Mao, Hao Chen, Jinsheng Li, Fengxiang Liu, Xu Wang, Shuang Wang. "Hydroxy-Polybenzimidazole Electrolyte with Excellent Stability for High Power Density All-Solid-State Supercapacitors", ACS Applied Energy Materials, 2020 Publication	<1 %
30	Submitted to University of Birmingham Student Paper	<1 %
31	Xiaobai Li, Peng Wang, Zhenchao Liu, Jinwu Peng, Chengying Shi, Wei Hu, Zhenhua Jiang, Baijun Liu. "Arylether-type polybenzimidazoles bearing benzimidazolyl pendants for high-temperature proton exchange membrane fuel cells", Journal of Power Sources, 2018 Publication	<1 %
32	www.ros.hw.ac.uk Internet Source	<1 %
33	patents.justia.com Internet Source	<1 %
34	María Cabrero Antonino. "Metal-Organic Frameworks as Heterogenous Photocatalysts	<1 %

for the Production of Solar Fuels", Universitat Politecnica de Valencia, 2021
Publication

35	Zhang, Na, Baolong Wang, Chengji Zhao, Yurong Zhang, Fanzhe Bu, Ying Cui, Xuefeng Li, and Hui Na. "Dual cross-linked organic-inorganic hybrid polymer electrolyte membranes based on quaternized poly(ether ether ketone) and (3-aminopropyl)triethoxysilane", Journal of Power Sources, 2015. Publication	<1 %
36	repositorio-aberto.up.pt Internet Source	<1 %
37	Jiangpeng Ni, Meishao Hu, Dong Liu, Huixiong Xie, Xiongzhi Xiang, Lei Wang. "Synthesis and properties of highly branched polybenzimidazoles as proton exchange membranes for high-temperature fuel cells", Journal of Materials Chemistry C, 2016 Publication	<1 %
38	Submitted to Curtin University of Technology Student Paper	<1 %
39	Ki-Ho Nam, Kwangwon Seo, Sangrae Lee, Haksoo Han. "Sulfur-Doped Hierarchically Porous Open Cellular Polymer/Acid Complex Electrolyte Membranes for Efficient Water-	<1 %

Free Proton Transport", ACS Sustainable Chemistry & Engineering, 2020
Publication

40	Tiejun Mao, Hao Chen, Jinsheng Li, Fengxiang Liu, Xu Wang, Shuang Wang. "Hydroxypolybenzimidazole Electrolyte with Excellent Stability for High Power Density All-Solid-State Supercapacitors", ACS Applied Energy Materials, 2020 Publication	<1 %
41	159.226.64.105 Internet Source	<1 %
42	Submitted to Indian Institute of Technology, Kharagpure Student Paper	<1 %
43	Sudhangshu Maity, Arindam Sannigrahi, Sandip Ghosh, Tushar Jana. "N-alkyl polybenzimidazole: Effect of alkyl chain length", European Polymer Journal, 2013 Publication	<1 %
44	Submitted to University of Science and Technology Student Paper	<1 %
45	Submitted to Imperial College of Science, Technology and Medicine Student Paper	<1 %

46	Mohamed R. Berber, Naotoshi Nakashima. "Tailoring Different Molecular Weight Phenylene–Polybenzimidazole Membranes with Remarkable Oxidative Stability and Conductive Properties for High-Temperature Polymer Electrolyte Fuel Cells", ACS Applied Materials & Interfaces, 2019 Publication	<1 %
47	Sandip Ghosh, Arindam Sannigrahi, Sudhangshu Maity, Tushar Jana. "Role of Solvent Protic Character on the Aggregation Behavior of Polybenzimidazole in Solution", The Journal of Physical Chemistry B, 2010 Publication	<1 %
48	Xiaobai Li, Hongwei Ma, Peng Wang, Zhenchao Liu, Jinwu Peng, Wei Hu, Zhenhua Jiang, Baijun Liu, Michael D. Guiver. "Highly Conductive and Mechanically Stable Imidazole-Rich Cross-Linked Networks for High-Temperature Proton Exchange Membrane Fuel Cells", Chemistry of Materials, 2020 Publication	<1 %
49	Zhang, Hongwei, and Pei Kang Shen. "Recent Development of Polymer Electrolyte Membranes for Fuel Cells", Chemical Reviews, 2012. Publication	<1 %

50	Submitted to Kwangwoon University Graduate School Student Paper	<1 %
51	Xue Tian, Shuang Wang, Jinsheng Li, Fengxiang Liu, Xu Wang, Hao Chen, Hongzhe Ni, Zhe Wang. "Composite membranes based on polybenzimidazole and ionic liquid functional Si–O–Si network for HT-PEMFC applications", International Journal of Hydrogen Energy, 2017 Publication	<1 %
52	www.beilstein-journals.org Internet Source	<1 %
53	Sara Nasiri Sovari, Natasa Radakovic, Paul Roch, Aurélien Crochet, Aleksandar Pavic, Fabio Zobi. "Combatting AMR: a molecular approach to the discovery of potent and non-toxic rhenium complexes active against C. albicans-MRSA co-infection", Cambridge University Press (CUP), 2021 Publication	<1 %
54	etd.ohiolink.edu Internet Source	<1 %
55	Sannigrahi, Arindam, Dhamodaran Arunbabu, R. Murali Sankar, and Tushar Jana. "Tuning the Molecular Properties of	<1 %

Polybenzimidazole by Copolymerization", The Journal of Physical Chemistry B, 2007.
Publication

56	kluedo.ub.uni-kl.de Internet Source	<1 %
57	tel.archives-ouvertes.fr Internet Source	<1 %
58	Maity, Sudhangshu, and Tushar Jana. "Soluble Polybenzimidazoles for PEM: Synthesized from Efficient, Inexpensive, Readily Accessible Alternative Tetraamine Monomer", Macromolecules, 2013. Publication	<1 %
59	Sana, Balakondareddy, and Tushar Jana. "Polybenzimidazole composite with acidic surfactant like molecules: A unique approach to develop PEM for fuel cell", European Polymer Journal, 2016. Publication	<1 %
60	www.faqs.org Internet Source	<1 %
61	Tae-Ho Kim. "Proton-Conducting Zirconium Pyrophosphate/Poly(2,5-benzimidazole) Composite Membranes Prepared by a PPA Direct Casting Method", Macromolecular Chemistry and Physics, 11/05/2007 Publication	<1 %

62	scholarbank.nus.edu.sg Internet Source	<1 %
63	Isadora Maria de Oliveira. "Alquinos calcogênicos: Síntese e aplicações em reações multicomponentes para a obtenção de núcleos quinolínico, propargilaminas e ésteres vinil β-borilados", Universidade de Sao Paulo, Agencia USP de Gestao da Informacao Academica (AGUIA), 2020 Publication	<1 %
64	idus.us.es Internet Source	<1 %
65	utexas.influuent.utsystem.edu Internet Source	<1 %
66	www.csv.warwick.ac.uk Internet Source	<1 %
67	www.netl.doe.gov Internet Source	<1 %
68	www.scribd.com Internet Source	<1 %
69	Juan Antonio Asensio, Eduardo M. Sánchez, Pedro Gómez-Romero. "Proton-conducting membranes based on benzimidazole polymers for high-temperature PEM fuel cells. A chemical quest", Chemical Society Reviews, 2010	<1 %

Publication

70	Subhabrata Mukhopadhyay, Anupam Das, Tushar Jana, Samar K. Das. "Fabricating a MOF Material with Polybenzimidazole into an Efficient Proton Exchange Membrane", ACS Applied Energy Materials, 2020 Publication	<1 %
71	doi.org Internet Source	<1 %
72	patentscope.wipo.int Internet Source	<1 %
73	worldwidescience.org Internet Source	<1 %
74	www.escience.cn Internet Source	<1 %
75	"Electrocatalysis of Direct Methanol Fuel Cells", Wiley, 2009 Publication	<1 %
76	Submitted to University College London Student Paper	<1 %
77	www.readbag.com Internet Source	<1 %

Exclude quotes On Exclude matches < 14 words

Exclude bibliography On